GRAPHENE OXIDE QUANTUM DOTS-BASED NANOCOMPOSITES FOR WASTEWATER TREATMENT

by

SESETHU CHARMAINE TSHANGANA

submitted in accordance with the requirements for the degree of

DOCTOR OF PHILOSOPHY

in the subject

CHEMISTRY

at the

UNIVERSITY OF SOUTH AFRICA

Supervisor: Prof Alex Tawanda Kuvarega
Co-supervisors: Dr Adolph Anga Muleja
Prof Edward Nxumalo

January 2022

DECLARATION

Name   : Sesethu Charmaine Tshangana

Student number   : 44963262

Degree   : PhD in Chemistry

Exact wording of the title of the thesis as appearing on the electronic copy submitted for examination:

GRAPHENE OXIDE QUANTUM DOTS-BASED NANOCOMPOSITES FOR WASTEWATER TREATMENT

I declare that the above thesis is my own work and that all the sources that I have used or quoted have been indicated and acknowledged by means of complete references.

I further declare that I submitted the thesis to originality checking software and that it falls within the accepted requirements for originality.

I further declare that I have not previously submitted this work, or part of it, for examination at Unisa for another qualification or at any other higher education institution.

___**S.C Tshanagana**_____   on this   _**15**__ day of____**January 2022**_____

       (Candidate)

ABSTRACT

The presence of new emerging pollutants in freshwater systems poses potentially serious threats to human health, food production, ecosystems and hinder economic growth. Emerging personal care products and pharmaceuticals, pesticides, wide range of industrial chemicals, as well as climate change, all pose new threats to water quality. With largely long-term effects on people, the environment and ecosystems being unclear. The main aim of the thesis was to synthesize graphene oxide quantum dots (GQDs) using a facile one-pot method through the pyrolysis of citric acid and deploy them in the removal of emerging wastewater pollutants.

GQDs were initially applied alone as photocatalysts in the photodegradation of pollutants in real wastewater spiked with an organic dye (Brilliant black). The photodegradation and removal efficiency of the GQDs were improved by conjugating differently shaped zinc oxide (ZnO) nanoparticles to the GQDs. The design strategy and approach were based on the GQDs to acting as reservoirs for the photogenerated electrons that could subsequently enhance the lifetime of the electrons, exploiting the ability of GQDs to absorb light as well as the $\pi \rightarrow \pi^*$ transition in GQDs that allow more harvesting of sunlight. Upon conjugation of the GQDS with ZnO, there was a significant decrease in the band gaps, along with an improvement in photocatalytic efficiency. The conjugates of ZnO-GQDs showed enhanced bacterial inhibition against the bacterial strains tested (*Bacillus cereus* (*B. cereus*), *Pseudomonas aeruginosa* (*P. aeruginosa*), *Staphylococcus aureus* (*S. aureus*) and *Escherichia coli* (*E. coli*)). When PAA was employed as a synergistic oxidant on the GQDs; radicals that were not prone to quenching in complex water matrices were produced (acetylperoxyl and peroxyl radicals $CH_3C(=O)OO\bullet$ and $CH_3C(=O)O\bullet$). PAA exhibited disinfectant capabilities that were not entirely dependent on pH and did not generate toxic disinfection by-products (DBPs) in the treated effluent. To mitigate the limitations of a slurry photocatalytic system, the GQDs were embedded in polyethersulfone (PES), and the fabricated membranes were tested in a hybrid-filtration-advanced oxidation processes where the performance of the fabricated membrane was compared to that of a commercial membrane and water quality parameters were evaluated to determine the quality of the water.

GQDs were found to be promising materials for conjugation with other photocatalysts to form heterojunctions with increased photocatalytic activity under visible light irradiation. When embedded in polymeric membranes, the activity of the GQDs was not lost and the membrane could perform a dual AOPs/filtration function. This is important for the application of the membranes in real wastewater treatment applications etc.

DEDICATION

This work is dedicated to my angels in heaven; my late father **Claiment Zamuxolo Tshangana** and my older sister **Nolundi Vuyisile Tshangana**. My greatest cheerleaders and my biggest support who unfortunately did not live to see the completion of this doctoral degree.

Throw the biggest party in heaven!!! **I AM OFFICIALLY A DOCTOR!!!**

To my angels on earth; **Oswald, Munesu and Mufaro Mkhondo**, without you guys none of this would have been possible. I love you guys to the moon and back!!

ACKNOWLEDGEMENTS

"…And I'll testify of the battles you've won, how you were my portion when there wasn't enough, I'll testify of the seas that we have crossed. The waters you parted and the waves I have walked. Singing "oh my God did not fail"…"

The story I will tell- Maverick City ft N.Raine

I would like to extend my sincerest gratitude to the following people and institutions, without whom the completion of this program would not have been possible:

PUBLICATIONS AND PRESENTATIONS

The work presented in this thesis has been presented at several conferences and symposia. Parts thereof have also been submitted or published in international peer-reviewed journals and are summarized in this section.

Publications

1. **<u>Charmaine Tshangana,</u>** Alex Kuvarega, Bhekie Mamba and Adolph Muleja. The synergistic effect of peracetic acid activated by graphene oxide quantum dots in the inactivation of *E. coli* and organic dye removal. *Journal of Environmental Science and Health, Part A* **(2022) 1.** https://doi.org/10.1080/10934529.2022.2056385

2. **<u>Charmaine Tshangana,</u>** Adolph Muleja and Bhekie Mamba. Photocatalytic activity of graphene oxide quantum dots in an effluent from a South African wastewater treatment plant. *Journal of Nanoparticle Research, 24(2) (2021) 1.* https://doi.org/10.1007/s11051-022-05422-6

3. **<u>Charmaine. S. Tshangana</u>**, Adolph. A Muleja, Alex. T. Kuvarega, Tshepo. J. Malefetse and Bhekie. B. Mamba., The applications of graphene oxide quantum dots in the removal of emerging pollutants in water: An overview. *Journal of Water Process Engineering 43 (2021) 102249*. https://doi.org/10.1016/j.jwpe.2021.102249

4. **<u>Charmaine Tshangana</u>**, Mandla Chabalala, Adolph Muleja, Edward Nxumalo and Bhekie Mamba. Shape-dependant photocatalytic and antimicrobial activity of ZnO nanostructures when conjugated to graphene quantum dots. *Journal of Environmental Chemical Engineering 8 (2020) 103930*. https://doi.org/10.1016/j.jece.2020.103930

5. **<u>Charmaine Tshangana,</u>** Adolph A. Muleja, Edward N. Nxumalo and Sabelo D. Mhlanga. Poly (ether) sulfone electrospun nanofibrous membranes embedded with

graphene oxide quantum dots with antimicrobial activity. ***Environmental Science and Pollution Research 27 (2020) 26845***. https://doi.org/10.1007/s11356-020-09080-w

6. **<u>Charmaine Tshangana,</u>** Patrick Mubiayi, Alex Kuvarega, Bhekie Mamba and Adolph Muleja. Effective treatment of Sulfasalazine and *Staphylococcus aureus* in municipal wastewater through graphene oxide quantum dots and peracetic acid. **<u>Submitted</u> for publication in *Journal of Water Processing Engineering*.**

7. **<u>Charmaine Tshangana,</u>** Oranso Mahlangu, Alex Kuvarega, Bhekie Mamba and Adolph Muleja. Development of polyethersulfone/GQDs hybrid-filtration-advanced oxidation processes and its application in the degradation of dyes and pharmaceuticals. **<u>Submitted</u> for publication in *Journal of Membrane Science*.**

Publications under preparation

8. **<u>Charmaine Tshangana</u>**, Alex Kuvarega, Bhekie Mamba and Adolph Muleja. Graphene oxide quantum dots/ peracetic acid synergy in the photodegradation of tetracycline and ibuprofen.

Additional publications not directly linked to the thesis

9. Vimbainashe Chakachaka, **<u>Charmaine Tshangana</u>**, Oranso Mahlangu, Bhekie Mamba and Adolph Muleja. Interdependence of Kinetics and Fluid Dynamics in the Design of Photocatalytic Membrane Reactors. ***Membranes, 12*(8) (2022) *745***. https://doi.org/10.3390/membranes12080745

10. Adolph Muleja, **<u>Charmaine Tshangana</u>**, Joshua Gorimbo, Ilunga Kamika and Bhekie Mamba. Antimicrobial activity of hydrogen treated cobalt supported natural zeolite from mining in South Africa. ***International Journal of Environmental Science and Technology (2022).*** https://doi.org/10.1007/s13762-022-04441-z

11. Muthumuni Managa, **Charmaine Tshangana**, Adolph Muleja, Bhekie Mamba and Tebello Nyokong. Porphryin-graphene oxide quantum dots conjugates in the photodegradation of ibuprofen. **Accepted** **for publication in** *Optical Materials*.

Conferences and symposium presentations

Oral presentations

1. **Charmaine Tshangana,** Patrick Mubiayi, Alex Kuvarega, Bhekie Mamba and Adolph Muleja. Effective treatment of Sulfasalazine and *Staphylococcus aureus* in municipal wastewater through graphene oxide quantum dots and peracetic acid. *Institute for Nanotechnology Water Sustainability (iNanoWS) Inaugural Launch, 30 September 2021, Virtual presentation.*

2. **Charmaine Tshangana,** Adolph Muleja. Graphene Quantum Dots Based ZnO Nanomaterials for Degradation of Pollutant and Microbial Deactivation in Wastewater Treatment Plant. *2020 Virtual AIChE Annual Meeting*.

3. **Charmaine Tshangana**, Mandla Chabalala, Adolph Muleja, Edward Nxumalo and Bhekie Mamba. Shape-dependant photocatalytic and antimicrobial activity of ZnO nanostructures when conjugated to graphene quantum dots. *Nanotechnology Young Researcher Symposium (NYRS), 12 November 2019, Pretoria, South Africa.*

4. **Charmaine S. Tshangana**, Adolph A. Muleja, Edward N. Nxumalo and Sabelo D. Mhlanga. Poly (ether) sulfone electrospun nanofibrous membranes embedded with graphene oxide quantum dots with antimicrobial activity. *US-Africa Forum on Nanotechnology Convergence, 11-15 August 2019, Muldersdrift, South Africa.*

5. **Charmaine Tshangana**, Edward Nxumalo and Sabelo Mhlanga. Modified electrospun nanofiber membranes for application in a novel solar-driven water purification system**.** *The 2nd African Membrane Society International Congress, 29 July 2018-1 August 2018, Florida, South Africa.*

Poster presentations

6. **<u>Charmaine Tshangana</u>,** Oranso Mahlangu, Alex Kuvarega, Bhekie Mamba and Adolph Muleja. Development of polyethersulfone/GQDs hybrid-filtration-advanced oxidation processes and its application in the degradation of dyes and pharmaceuticals. *UNISA CAES/CSET Innovation Day, Florida, South Africa.*

TABLE OF CONTENTS

CHAPTER 6 CONJUGATING ZNO NANOSTRUCTURES TO GRAPHENE OXIDE QUANTUM DOTS FOR ENHANCED PHOTOCATALYTIC AND ANTIMICROBIAL ACTIVITY

CHAPTER 7 THE SYNERGISTIC EFFECT OF PERACETIC ACID ACTIVATED BY GRAPHENE OXIDE QUANTUM DOTS IN THE INACTIVATION OF E. COLI AND ORGANIC DYE REMOVAL

LIST OF FIGURES

LIST OF TABLES

LIST OF SYMBOLS

ε %	porosity
δ	membrane thickness
ζ	zeta potential
H	electrolyte viscosity
ε	permittivity of water
ΔP	applied pressure
ρ_w	density of pure water

LIST OF ABBREVIATIONS

AFM	Atomic Force Microscopy
AOPs	Advanced Oxidative Processes
AR	Antibiotic Resistant
APTES	3-aminopropyl-triethoxysilane
BB	Brilliant Black
BPA	Bisphenol-A
BSA	Bovine Serum Albumin
BZF	Bezafibrate
CA	Citric Acid
CA	Clofibric Acid
CAP	Chloramphenicol
CB	Conduction Band
CBZ	Carbamazepine
CZ	Carbendazim
DBPs	Disinfection by-products
DCF	Diclofenac
DCP	Dichlorophenol
DFT	Density Functional Theory
DMF	Dimethylformamide
ECDs	Endocrine Chemical Disruptors
EDC	1-ethyl-3-(3- dimethylaminopropyl) carbodiimide hydrochloride
ECL	Electrochemiluminscence
EPs	Emerging pollutants
FBR	Fixed bed reactor

FT-IR	Fourier Transform Infrared Red
FWHM	Full Width Half Maximum
GAC	Granular Activated Carbon
GQDs	Graphene Oxide Quantum Dots
GO	Graphene Oxide
GSH	Glutathione
HOPG	Highly Oriented Pyrolytic Graphite
HR-SEM	High-Resolution Scanning Electron Microscope
HR-TEM	High-Resolution Transmission Electron Microscope
IBF	Ibuprofen
KEP	Ketoprofen
LA	Laser Ablation
LED	Light Emitting Diodes
LDHs	Layered Double Hydroxides
LSPR	Local Surface Plasmon Resonance
LUMO	Lowest Unoccupied Molecular Orbital
MB	Methylene blue
MB	Membrane bioreactor
MBR	Moving bed reactor
MH	Meuller-Hinton
MMM	Mixed-matrix membrane
MO	Methyl Orange
MOF	Metal Organic Frameworks
MPN	Most probable number
NA	Nutrient Agar
NAP	Naproxen
NF	Nanofiltration

NHS	N-hydroxysuccinimide
NIR	Near-infrared Region
NOM	Natural Organic Matter
NPs	Nanoparticles
PL	Photoluminescence
RhB	Rhodamine B
SSZ	Sulfasalazine
PAA	Peracetic Acid
PAH	Polycyclic Aromatic Hydrocarbon
PBS	Phosphate-buffered solutions
PDS	Persoxydisulfate
PDT	Photodynamic Therapy
PEI	Polyethyleneimine
PES	Polyether sulfone
PLAL	Pulsed laser ablation in liquid
PMR	Photocatalytic reactor membrane
PMS	Peroxymonosulfate
PVC	Polyvinyl Chloride
PVDF	Polyvinylidene Fluoride
PVP	Polyvinylpyrolidone
PZC	Isoelectric point
QY	Quantum yield
ROS	Reactive Oxygen Species
SMX	Sulfamethoxazole
TA	Tannic Acid
TC	Tetracycline
TEA	Triethanolamine

THMs	Trihalomethanes
TFN	Thin Film Nanocomposite
TMC	Trimesoyl Chloride
TPA	tri-n-propylamine
TPs	Transformation products
WHO	World Health Organization
WWTPs	Wastewater Treatment Plants
US	Ultrasound
UV	Ultraviolet
VB	Valence Band
XPS	X-ray Photoelectron Spectroscopy
XRD	X-ray diffraction
ZnO	Zinc Oxide
ZnO-F	Zinc Oxide flakes
ZnO-R	Zinc Oxide rods

CHAPTER 1
INTRODUCTION

1.1   Background and motivation

The global population is on a rapid increase and according to the most recent statistics, as of June 2021, the estimated number of people on earth was approximately 7.9 billion [1]. It is projected that by the year 2050 this proportion will likely increase to 9.7 billion. One of the consequences of a large population size is the strain on natural resources. Arguably one of the most affected natural resources is water. The available water resources are stretched to cater for a growing population. An increase in population size is also accompanied by inevitable water pollution emanating from anthropogenic, industrial, and agricultural activities. Consequently, the quality and availability of surface water and groundwater has continued to deteriorate. This reality is currently worsened by the shifts in temperatures and weather patterns through global warming, which has resulted in severe and unpredictable catastrophes in some regions of the globe.

The issue of water quality continues to plague South Africa and other countries worldwide. The effluents from wastewater treatment plants (WWTPs) have recently been reported to contain pharmaceutical metabolites, insecticides, additives, endocrine chemical disruptors (ECDs), and other waste discharges from industrial and agricultural waste [2-4]. The presence of these pollutants typically classified as "*emerging pollutants*" in wastewater effluents are predominantly due to the ineffectiveness of conventional WWTPs to efficiently remove them from the treatment train [5]. Therefore, emerging pollutants (EPs) find their way into the receiving streams where their fate is an environmental concern. EPs often get released into lakes, rivers, and dams, and some have been reportedly found in water sources designated for human consumption [6]. The spiraling negative effect this has on human life is irrefutable.

EPs can enter the environment through several pathways, including through various point and non-point sources. **Figure 1.1** presents simplified pathways that illustrate the origin of EPs and their occurrence in surface water as well as how these EPs can potentially end up in drinking water. The transport of EPs from diffuse sources to water bodies is influenced by

their properties such as polarity, volatility, adsorption properties as well as persistence in the environment. It has been shown that the concentration of EPs varies from the discharge point to the abstraction point. This difference is ascribed to; photolysis, sorption, dispersion, volatilisation, and biotransformation which contribute to reducing the initial concentrations or in the transformation of the pollutants. The fate of these EPs in water, however, is influenced mostly by their physicochemical properties such as: (i) the sediment-water partition coefficient (K_{oc}), (ii) the octanol-water partition coefficient (K_{ow}), (iii) the octanol-water distribution coefficient (D_{ow}), (iv) the degradation rate as well as (v) the flow rate of EPs [7]. The discharge of these contaminants into the environment has long-lasting negative effects such as bioaccumulation, endocrine disruption, persistence in the environment, microbial resistance as well as reproductive toxicity [8].
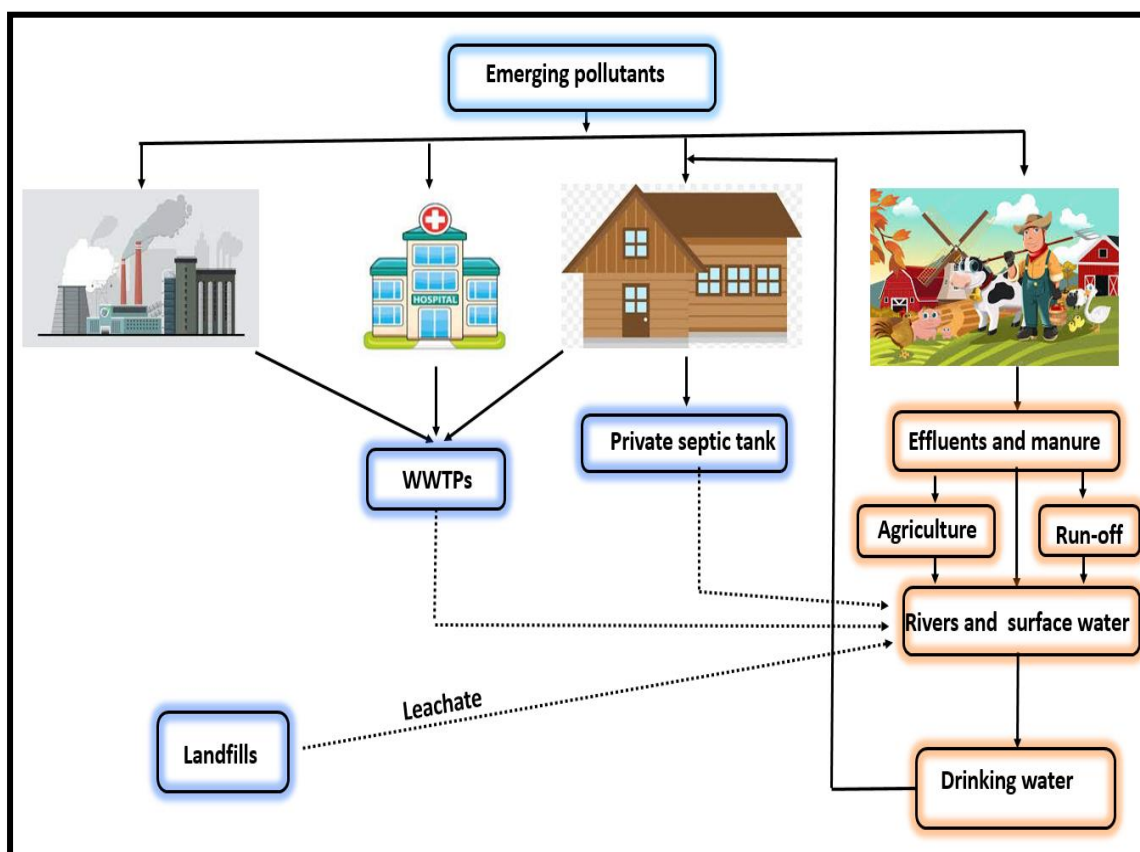
Figure 1.1: Pathways of EPs in the environment that results in their presence in drinking water.

Synthetic dyes are a notorious class of pollutants that also contribute to the pollution of water. Almost 15% of the dyes are discharged as effluents from textile industries. Some of the dyes end up in water sources and they include basic, acidic, azo, reactive, diazo, anthraquinone and disperse, sulphur, triarylmethane, as well as vat dyes [9]. Generally, dye wastes are among some of the most complex effluents in nature. This is due to the diverse chemical structures and properties of the textile effluent. In addition to being made up of organic compounds; heavy metals have also been detected in trace amounts in textile effluents [10]. The uncontrolled discharge of these textile effluents in the environment postures a great risk to public health. Despite being toxic, the synthetic dyes also give water a displeasing color which affects the aesthetic and taste of water. The degraded intermediates of synthetic dyes are reported to be teratogenic and carcinogenic thus posing a severe health risk to human health [11, 12].

Water-borne diseases are another cause of high morbidity that stems from consuming water that has high microbial content. This is especially true in Sub-Saharan Africa, where some communities still use surface water for their daily needs [13]. As per the World Health Organization (WHO) guidelines, there should be zero coliforms present in drinking water. To circumvent this, current WWTPs employ techniques such as ozonation, chlorination and ultraviolet (UV) treatment to disinfect the water [14]. These techniques unfortunately suffer from a few drawbacks; in the case of ozonation; undesirable harmful by-products such as bromates, and formaldehydes are often generated.

Chlorination may result in transformation by-products being formed and the generation of carcinogenic derivatives of chloramines have been reported during the disinfection process [15]. The high cost of the reactors used, and microbial resistance are some of the limitations associated with the use of UV treatment. In this regard, new cost-effective technologies that can disinfect water without the formation of transformation by-products are paramount.

1.1.1 Environmental considerations

The spread of EPs into the environment has been reported to be unavoidable due to ineffective treatment of wastewater. The presence of EPs in the environment has long-lasting negative effects albeit their occurrence at lower concentrations.

1.1.2 Effect on humans

EPs have potential long-lasting negative effects on humans. Some diseases that are related to the long-term exposure to EPs include cancers, immune suppression, obesity, neurotoxicity, birth defects, long duration toxicological effects, hormone and/or endocrine disruption [16]. Endocrine disrupting chemicals (EDCs) can mimic natural hormones in the body by inhibition or imitation and thus they end up blocking and producing antagonistic effects. They further deregulate ideal levels of the natural hormones causing disturbances in both male and female reproductive systems. Some diseases associated with exposure to EDCs include hormone-related cancer, diabetes, neurological disorders and growth and development abnormalities [17].

1.1.3 Effect on aquatic ecosystem

Long-term EP exposure is hazardous to the aquatic ecosystem as well as to humans. Shelley et al. [18] reported that a 96-hour exposure of sub-lethal concentration of atrazine affected the swimming and feeding behavior of rainbow trout. When exposed to high levels of EPs, goldfish showed a 113 bio-centration factor [19]. Diclofenac was shown to affect the organs of fishes and Nie et al. [20] reported that sulfamethoxazole impedes the photosynthesis process whereas ciprofloxacin showed toxicity to green algae. Feminization was also observed for fish in sewage treatment [21]. Fish are the most vulnerable to EPs because most of these EPs end up in their natural habitat.

1.1.4 Removal of emerging pollutants in wastewater

The removal efficiency of EPs by existing conventional WWTPs was demonstrated to be usually low or not attained at all. The low removal efficiency is ascribed to the biotransformation of upstream precursors or the transformation of conjugated forms to free forms of the precursors [22]. Prasse et al. [23] demonstrated that only a small fraction (less than 25%) removal efficiency was obtained for diclofenac and carbamazepine using ozonation. Gibbs et al. [24] found in their study that WWTPs were unable to efficiently remove bisphenol-A, caffeine, and carbamazepine. In another study, Nam et al. [25] reported a low (6%) removal for metoprolol from water using conventional techniques.

Figure 1.2 shows an illustration of a conventional wastewater treatment plant which is comprised of primary, secondary, and tertiary treatments. Solid wastes such as plastics, oils, fats, sand, and grit are separated in the primary treatment. The primary treatment is achieved through sedimentation and filtration processes, while biological degradation of organic substances occurs at the secondary treatment. Activated sludge, membrane bioreactor (MB), moving bed reactor (MBR) and fixed bed reactor (FBR) are few of the biological treatment techniques included in the secondary treatment [26]. Tertiary treatment is the final step which includes disinfection either by chlorination or UV irradiation. It is worth noting that biological and chemical degradation may result in transformation products (TPs) with more eco-toxicity than the parent compound. Another type of TPs are disinfection by-products (DBPs). When organic matter in the water combines with disinfectants like chlorine or ozone, DBPs are generated. As a result, one of the primary goals of this research was to study the synergy between peracetic acid (PAA) and graphene oxide quantum dots (GQDs) as a possible disinfectant that can efficiently treat wastewater without generating DBPs.
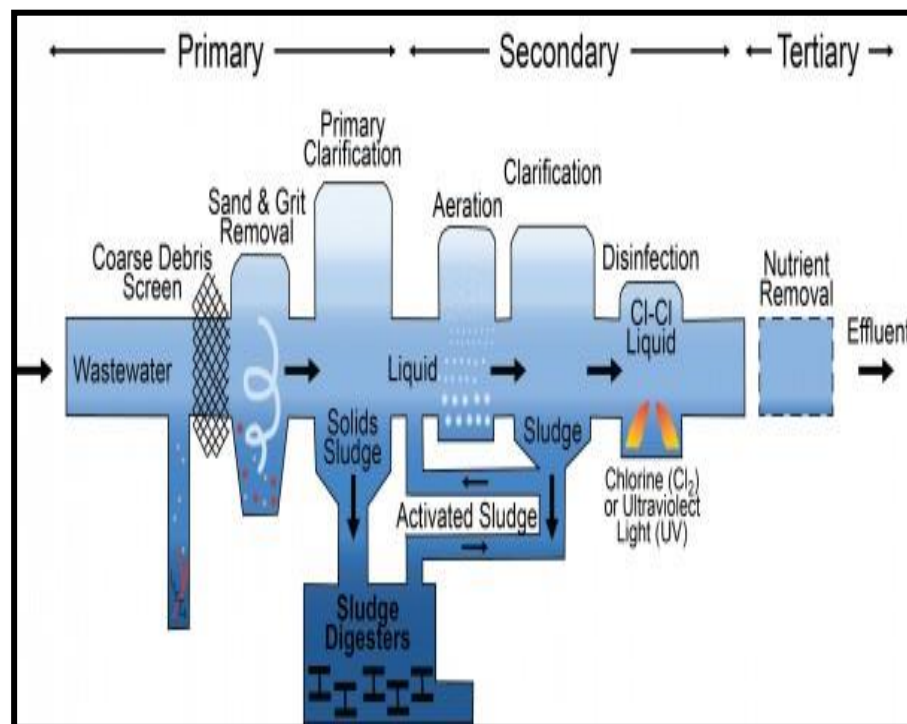
Figure 1.2:   Schematic representation of a typical wastewater treatment plant [38].

Conventional WWTPs are unable to remove EPs in wastewater due to the following reasons: (i) initial design and construction of WWTPs did not take into account the presence in wastewater of xenobiotics and EPs with complex structural properties; (ii) the typical concentration of biodegradable compounds that can be removed in a conventional WWTP are in the range of milligram per liter and a most probable number (MPN) of at least 10^6 MPN/100 mL, while the concentration of EPs that arrive at the WWTP is often in the range of 10^{-3}-10^{-6} mg L^{-1} [27,28]; (iii) often when EPs are subjected to available treatments in existing WWTPs, the EPs precursors will either bio-transform into their corresponding metabolites or the conjugated EPs will transform into free forms and generate several toxic by-products such as nitrosamines, iodinated trihalomethanes (THMs), carboxylic acids, esters, alcohols, hydroxy acids, aldehydes, ketones, halomethanes and keto acids as reported [29,30].

1.2 Research motivation

Treatment processes in conventional WWTP such as adsorption, chlorination, precipitation, and coagulation have proven to have low removal efficiencies for EPs. There is therefore a need for more research on developing effective strategies directed towards the removal of EPs and synthetic dyes in wastewater. The limitations of the existing technologies warrant the need to adapt, improve, or combine current WWTPs with advanced techniques to efficiently remove EPs from wastewater before they get discharged into receiving water bodies. Although advanced oxidative processes (AOPs) have proven to be favourable alternatives in the removal of EPs; the formation of undesirable and secondary toxic by-products remain a significant problem. Thus, in this work a comprehensive study was undertaken to understand of the degradation pathways, the fate and toxicity of the by-products formed during the degradation process of EPs using a combination nano-engineered material and AOPs. This will enable effective prediction of their effect in the receiving environment and prevent secondary pollution.

1.3 Justification of the study

The presence of EPs in surface water has resulted in the need for improved water treatment technologies to meet the quality needed for safe drinking water for human consumption. In this study, GQDs were employed in the photodegradation and removal of EPs from

wastewater. The photodegradation and removal efficiency of the GQDs was improved by conjugating with zinc oxide nanoparticles, through the synergy with PAA as well fabricating a mixed-matrix membrane (MMM) containing the GQDs.

1.3.1 Graphene oxide quantum dots

GQDs are an allotrope of carbon which are zero-dimensional (0D), fluorescent materials in the size range of 1-20 nm and exhibit the phenomena of quantum confinement and edge effects [31]. This phenomenon has given rise to the excellent optical and photoluminescence (PL) properties on GQDs. They have high electron mobility and can provide a direct path for transport of photo-generated charge carriers which in turn result in increased lifetimes of the electron-hole pairs as well their up-conversion behaviour [31, 32]. GQDs also have a large surface area, large diameter and bandgaps that can be customized by changing the shape, size, and chemistry of the edges. Compared to conventional quantum dots (QDs), GQDs are an eco-friendly alternative that combines advantages such as simple synthesis approach and reduced leaching possibility which often results in secondary pollution. In comparison to typical semiconductor QDs, GQDs offer photostability, green synthesis, biocompatibility, relative ease of surface functionalization, adjustable PL, and lower toxicity [33]. As a result of their interesting and unique properties, GQDs have also been applied in a plethora of applications such as sensing, photodynamic therapy, photovoltaics and AOPs.

1.3.2 Zinc oxide nanoparticles

Zinc oxide (ZnO) nanoparticles were selected to augment the performance of the GQDs as a photocatalyst owing to their low-cost of production, non-toxicity as well as their ability to absorb in the UV region [34]. The broad direct band gap width (3.37 eV), transparency in the visible range, high electron mobility, significant excitation binding energy (60 meV) and outstanding antibacterial and photocatalytic capabilities are all advantages of ZnO nanoparticles in environmental applications [34]. The conjugation of the ZnO with GQDs improves the carrier charge lifetime for increased photocatalytic performance. The improvement of the photocatalytic efficiency is obtained by delaying the rate of charge carrier recombination, extending the light absorption ability to the visible region, and enhancing pollutant adsorption, thus making GQDs-ZnO conjugates suitable candidates for water and wastewater treatment.

1.3.3 Peracetic acid as an oxidant

In AOPs, the highly reactive species generated *via* chemical and photochemical reactions are the main oxidising species responsible for the degradation of contaminants. The most used peroxides in AOPs as sources of reactive radicals have been persoxydisulfate (PDS), hydrogen peroxide (H_2O_2) and peroxymonosulfate (PMS). These peroxides are often activated either using transition metals, ultraviolet (UV) or by applying heat [35-37]. PAA ($CH_3C(O)OOH$) is a peroxide that has great potential of producing similar highly reactive species, it has also been considered as a possible replacement for chlorine-based oxidants in the wastewater treatment largely because it does not generate toxic by-products during the disinfection process [38]. In this study, the effect of combining GQDs and PAA in the inactivation of model microorganisms as well as in the removal of microbes in raw water is reported for the first time.

1.4 Limitations of slurry systems and the need for photocatalyst support

An ideal photocatalyst should be in the nano size range as this provides greater specific surface area. On the contrary, smaller photocatalyst size make it extremely difficult to recover the photocatalyst after use and may necessitate time-consuming high-cost post-treatment to remove suspended photocatalyst after use. The size of the synthesized GQDs employed in this work is smaller than 10 nm, hence it would be necessary to immobilize them onto a polymer and fabricate a photocatalytic mixed-matrix membrane (MMM). Membrane immobilized photocatalysts have been proven to be better than suspended photocatalysts in that they minimize membrane fouling, increase permeability and chemical inertness as well as the mechanical strength of the membrane [38]. The polymer used in this work was polyether sulfone (PES) and was selected based on the following merits: high strength, extremely broad temperature tolerances, good chemical resistance and high dimensional stability for incorporation of inorganic nanoparticles. Photocatalytic membranes offer cost-effective alternatives in water treatment as they combine advantages of ease of operation and low energy requirement. In this study the role of the photocatalytic membrane was to immobilize the GQDs and to act as a biocidal molecular separation barrier for the EPs.

Among the numerous techniques that have been investigated as possible approaches of producing membranes; electrospinning has been shown to be a cost-effective and versatile method to fabricate membranes [39]. Electrospinning is a process that utilizes high voltage electric field to produce continuous nanofibers in a non-woven form from polymer solutions (**Figure 1.3**). These fibres range from 80 nm diameter to several hundred nanometres [40]. It differs from traditional membrane fabrication methods in that; it provides relatively uniform pore size distribution that results in high interconnectivity of pores, large specific surface area and low density [39]. In addition, by adjusting and modifying electrospinning parameters, material selection, and post-processing treatment, the properties of nanofibers can be adjusted to meet specific needs.

The focus of the study will be assessing the potential applicability of GQD-based materials as alternative wastewater treatment materials that can be retrofitted to existing WWTPs treatment techniques.
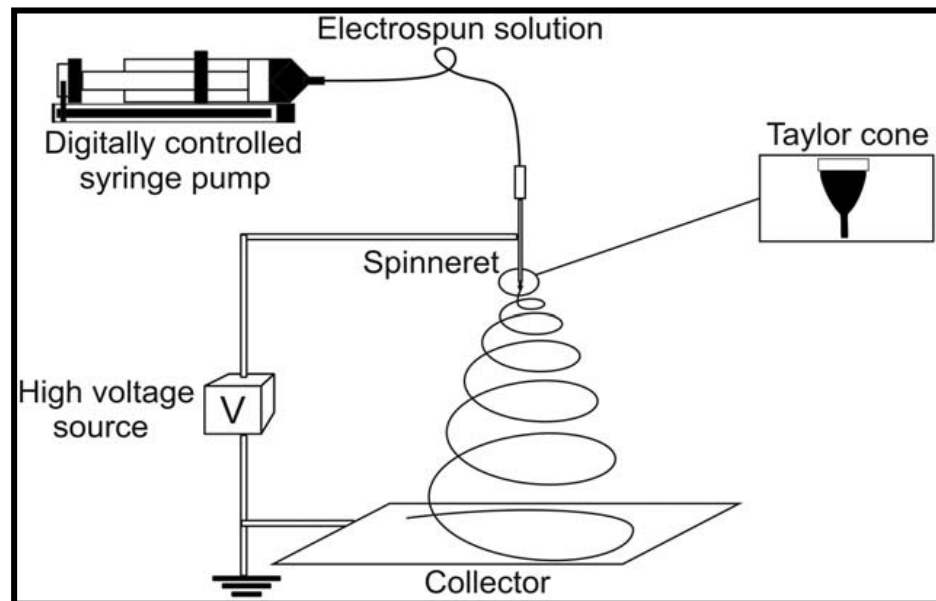
Figure 1.3:   Schematic diagram showing a mononozzle electrospinning setup [40].

1.5   Aims and objectives

This thesis seeks to address the limitations of existing wastewater technologies in removing EPs by employing GQDs, conjugates of ZnO and through the synergy between GQDs and PAA to enhance the photocatalytic efficiency of the GQDs. Additionally, the GQDs and GQDs-based nanocomposites were also used in the inactivation of microbes and further used to fabricate a photocatalytic MMM by embedding GQDs in a PES polymer. The resultant photocatalytic mixed-matrix membrane was used to demonstrate proof-of-concept and the membrane performance of the resultant membrane was compared to a commercially available membrane (Film Tec™NF270) and thereafter applied in low-pressure filtration system to treat raw wastewater.

This study seeks to answer the following research questions:

❖ Can GQDs efficiently degrade synthetic dyes, pharmaceutical drugs and inactivate microbes in raw wastewater under visible light irradiation?

❖ Is the photocatalytic efficiency of GQDs enhanced as a consequence of conjugating zinc oxide nanoparticles with GQDs and as a result of the synergy between PAA and GQDs?

❖ To what extent does the initial concentration of GQDs and the pollutants (synthetic dyes and pharmaceutical drugs), the pH, effect of water matrix have on the kinetics of the photodegradation process?

❖ Are the reaction intermediates formed during the photodegradation process toxic and mutagenic?

❖ Besides simply enhancing the inactivation of microbes, what role does peracetic acid play in the mechanism of inactivation of *E. coli* and *S. aureus*?

❖ Can a GQDs embedded PES photocatalytic membrane perform better in treating raw wastewater better than a commercial membrane (Film Tec™NF270)?

The aims of the study were achieved through the following research objectives:

(i) Synthesis of GQDs using a simple one-pot synthesis through pyrolysis of citric acid and synthesis of differently shaped ZnO nanoparticles *via* sol-gel method.

(ii) Characterisation of all the synthesized nanomaterials using various physico-chemical techniques such as Fourier transform infrared (FT-IR), Scanning electron microscopy (SEM), Transmission electron microscopy (TEM), Photoluminescence (PL), UV-Vis, Raman spectroscopy, etc.

(iii) Evaluation of the photocatalytic efficiency of GQDs in the photodegradation of synthetic dye namely: Brilliant Black in raw wastewater.

(iv) Conjugating GQDs to differently shaped ZnO nanoparticles and evaluating the performance in the degradation of pharmaceutical drugs, synthetic dyes as well as the inactivation of microorganisms.

(v) Embedding GQDs in a PES polymer and fabricating a photocatalytic mixed-matrix membrane and comparing the membrane performance against a commercial membrane (Film Tec™NF270).

(vi) Elucidating the degradation pathways of the selected model pollutants using LC-QTOF-MS.

(vii) Investigating the synergy of combining PAA with GQDs in the photodegradation of pharmaceutical dyes and inactivation of microorganisms.

(viii) Evaluating the toxicity of the degradation by-products formed using Ames test bioassay.

(ix) Modelling the degradation pathways as well as mechanisms of the inactivation of microorganisms.

A summary of the research outline of this thesis is presented in **Figure 1.4**.
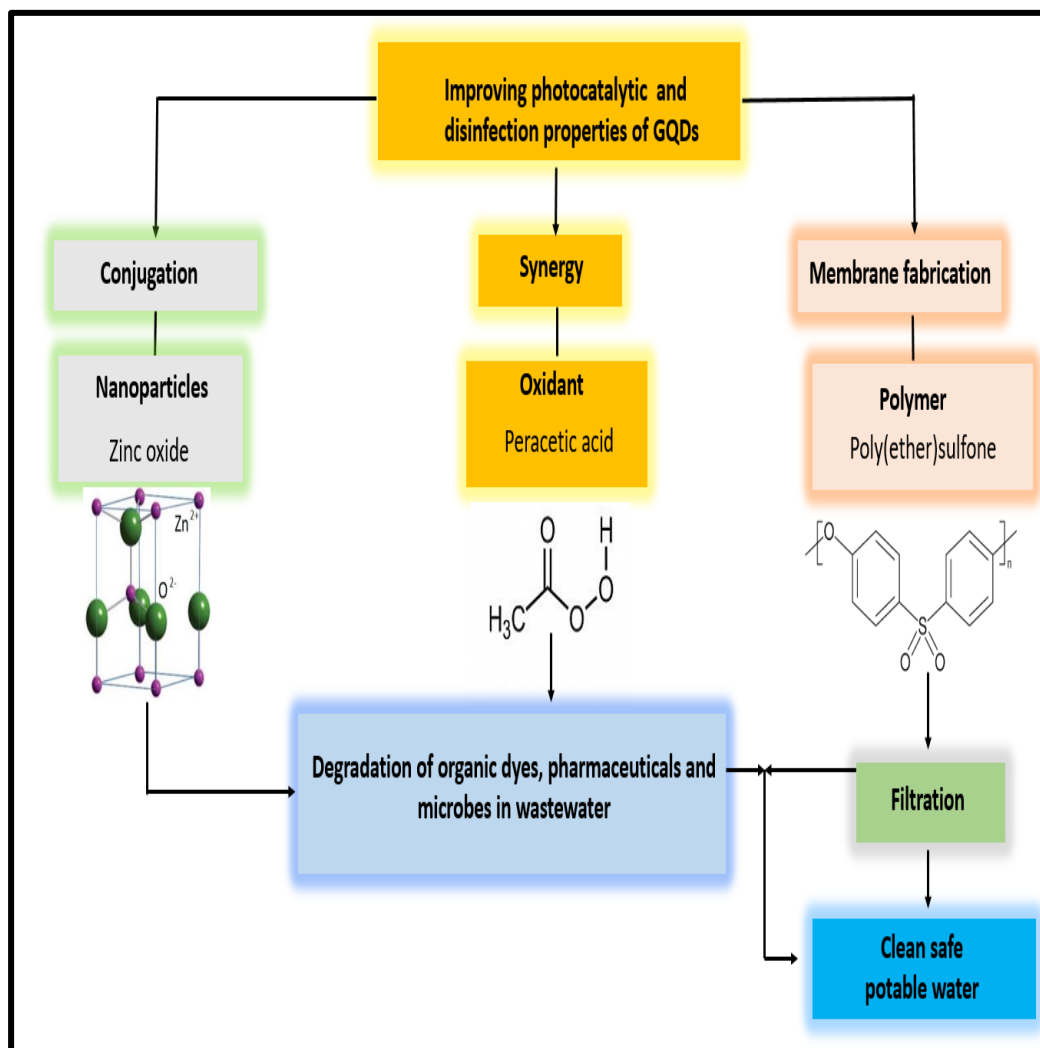
Figure 1.4:   Outline of the research objectives of this thesis.

1.6   Thesis outline

This section outlines the format of the thesis and gives a brief overview of what is entailed in each chapter.

Chapter 1:   introduces background, problem statement and research objectives of this study by highlighting issues relating to the global concerns of emerging pollutants found in water. The motivation and environmental consideration, justification, aims and objectives and a flow chart summarizing the research objectives of this study are clearly outlined in this chapter.

Chapter 2:   presents an overview of GQDs and ZnO as promising materials in environmental decontamination. The synthesis routes, characterisation and application of these materials is reviewed in detail. The recent applications of GQDs and ZnO in AOPs, membrane technology and other technologies in the removal of EPs are also discussed and this chapter. Inactivation of pathogens using PAA in combination of GQDs is also reviewed.

Chapter 3:   provides details on the experimental methodologies and characterisation techniques used throughout this study.

Chapter 4:   outlines the synthesis and characterisation of GQDs employed in this work.

Chapter 5:   reports on the removal of synthetic dyes in wastewater using GQDs as a photocatalyst.

Chapter 6:   provides results and discussion on studies on the effect of conjugating ZnO nanoparticles to GQDs in the enhancement of photocatalytic degradation of a synthetic dye (BB dye) as well as in the inactivation of microbes (*E. coli, S. aureus, B. cereus and P. aeruginosa).*

Chapter 7:   investigates and reports for the first time the synergistic effect of combining PAA with GQDs to enhance the photodegradation efficiency of BB dye and

delves into the disinfection potential of the resultant GQDs/PAA and studies the antimicrobial pathway of *E. coli.*

Chapter 8: evaluates the synergy between GQDs/PAA in the degradation of pharmaceutical products and the genotoxicity and mutagenic potential of the reaction by-products formed during the photodegradation process. Additionally, the chapter discusses the disinfection potential of GQDs/PAA against *S. aureus* and in real wastewater samples.

Chapter 9: presents the fabrication of membranes *via* electrospinning. The GQDs were embedded in the PES polymer to impart antibiofouling features of the membrane.

Chapter 10: discusses the integration of AOPs and membrane technologies in a hybrid system. The photocatalytic and the anti-biofouling properties of the membrane are investigated. To demonstrate proof-of-concept, the resultant membrane was used in a low-pressure raw wastewater filtration system and the performance of the membrane was tested against a commercial membrane (Film Tec™NF270).

Chapter 11: provides the overall conclusions drawn from the study as well as recommendations and future perspectives.

References

1. https://www.worldometers.info/world-population/ accessed on 29 June 2021.

2. de Sousa D.N.R, Mozeto, A. A, Carneiro, R. L., Fadini, P., *Environ. Sci. Pollut. Res.* 25 (5) (2018) 4607.

3. Rimayi C, Odusanya, D, Weiss, J.M, de Boer, J, Chimuka, L., *Sci. Total Environ.* 627 (2018) 1008.

4. Peng Y, Fang, W, Krauss, M, Brack, W, Wang, Z, Li, F, Zhang, X., *Environ. Pollut*. 241 (2018) 484.

5. Tran N.H, Reinhard, M, Gin, K.Y.H., *Water res.* 133 (2018) 182.

6. Luo Y, Guo, W, Ngo, H.H, Nghiem, L.D, Hai, F.I, Zhang, J, Liang, S, Wang, X.C., *Sci. Total environ.* 473 (2014) 619.

7. Stevens-Garmon J, Drewes, J.E, Khan, S.J, McDonald, J.A, Dickenson, E.R., *Water Res.* 45(11) (2011) 3417.

8. Mohapatra D.P, Kirpalani, D.M, *The Canadian J. Chem. Eng.* 97(10) (2019) 2621.

9. Ghaly A.E, Ananthashankar, R, Alhattab, M.V.V.R, Ramakrishnan, V.V., *J. Chem. Eng Process. Technol.* 5 (1) (2014)1.

10. Islam M.R, Mostafa, M.G., *J. Environ. Sci. Nat. Res.* 11(1-2) (2018) 131.

11. Bilal M, Iqbal, H.M, Hu, H, Wang, W, Zhang, X., *J. Environ. Man.* 188 (2017) 137.

12. Chatha S.A.S., Asgher, M, Iqbal, H.M., *Environ. Sci.Pollut. Res.* 24 (16) (2017) 14005.

13. WHO/UNICEF Joint Monitoring Programme for Water Supply and Sanitation "Report and MDG Assessment 2015" Available from: http://www.wssinfo.org/

14. Mezzanotte V., Antonelli, M., Citterio, S, Nurizzo, C., *Water Environ. Res*. *79* (12) (2007) 2373.

15. Li X.F., Mitch, W.A., *Environ. Sci. Techn.* (2018) 1681.

16. Marcoux M.A., Matias, M., Olivier, F, Keck, G., *Waste Man.*, *33* (11) (2013) 2147.

17. Bergman, Ǻ, Heindel, J. J., Jobling, S., Kidd, K. A., Zoeller, R. T. (2013). World Health Organization.

18. Shelley L. K., Ross, P. S., Miller, K. M., Kaukinen, K. H., Kennedy, C. J., *Aquatic Toxicol.* 124 (2012) 217.

19. Abdulrazaq A, Abdulkareem Abdulsalam, A. Larayetan Rotimi, A. Aliyu Abdulbasit, Okpanachi Clifford, O. Abdulazeez Abdulsalam, O. Nayo Racheal, A. Akor Joy, F. Omale Victor, Z. Mbese Johannes, Muhammad Bilal and Salehdeen Umar M (December 11th 2020). IntechOpen, 10.5772/intechopen.94447.

20. Nie X.P., Liu, B.Y., Yu, H.J., Liu, W.Q, Yang, Y.F., *Environ. Pollut. 172* (2013) 23.

21. Porseryd T, Larsson, J, Kellner, M, Bollner, T, Dinnétz, P, Hällström, I.P, *Aquatic Toxicol. 207* (2019)142.

22. Chen S, Zhou, Y, Meng, J, Wang, T, *Environ. Pollut.* 242 (2018) 2059.

23. Prasse C, Stalter, D, Schulte-Oehlmann, U, Oehlmann, J, Ternes, T.A., *Water res.* 87 (2015) 237.

24. Gibbs J., P.E. Stackelberg, E.T. Furlong, M.T. Meyer, S.D. Zaugg, R.L. Lippincott., *Sci. Total Environ.* 373 (2007) 240.

25. Nam S.W, Jo, B.I, Yoon, Y, Zoh, K.D, *Chemosphere* 95 (2014).

26. Gogoi A, Mazumder, P, Tyagi, V.K, Chaminda, G.T, An, A.K. Kumar, M., *Groundwater Sustain. Dev.* 6 (2018)169.

27. Center for Sustainable Systems, University of Michigan. 2020. "U.S. Wastewater Treatment Factsheet." Pub. No. CSS04-14.

28. Ziylan A, Ince, N.H., *J. hazard. Mater. 187*(1-3) (2011) 24.

29. Le-Minh N., Khan, S.J., Drewes, J.E, Stuetz, R.M., *Water res. 44* (15) (2010) 4295.

30. Ben W., Zhu, B., Yuan, X., Zhang, Y., Yang, M, Qiang, Z., *Water res. 130* (2018) 38.

31. Von Gunten U., *Water res.* 37 (7) (2003)1469.

32. Benítez-Martínez S, Valcárcel, M., *TrAC. 72* (2015) 93.

33. Li L., Wu, G., Yang, G., Peng, J., Zhao, J, Zhu, J.J., *Nanoscale 5* (10) (2013) 4015.

34. Rahimi K., Yazdani, A, Ahmadirad, M., *Mat. Res. Bull. 98* (2018)148.

35. Kołodziejczak-Radzimska A, Jesionowski, T., *Materials* 7 (4) (2014) 2833.

36. Keyikoglu R., Karatas, O., Khataee, A., Kobya, M., Can, O.T., Soltani, R.D.C, Isleyen, M., *Sep. Pur. Technol. 247* (2020) 116925.

37. Chen J., Zhang, L., Huang, T., Li, W., Wang, Y., Wang, Z. *J. Hazard. Mater. 320* (2016) 571.

38. Jazić J.M., Đurkić, T., Bašić, B., Watson, M., Apostolović, T., Tubić, A, Agbaba, *J. Environ. Sci. Water Res. Technol. 6* (10) (2020) 2800.

39. Kitis M., *EnviroN. Intern*. 30(1) (2004) 47.

40. Kuvarega A.T, Mamba B.B. (2016). Wenbin Cao (*Ed*), InTech, Croatia, ISBN 978-953-51-4661-2.

CHAPTER 2
LITERATURE REVIEW

2.1   Introduction

Recent literature on several aspects based on this study is outlined in this chapter. The literature review examines water pollution due to continuous discharge of pollutants from various sources. The shortcomings of currently wastewater treatment approaches are discussed, as well as the necessity for new treatment technology. Photocatalysis as a potential technology for wastewater treatment is also explored. Several synthetic processes for GQDs that influence their structure and morphology, are reviewed. Surface modification and functionalization of GQDs for conjugation with zinc oxide for enhanced efficiency towards removal of contaminants is discussed. Synergy achieved by using oxidants like PAA is also highlighted in this chapter. In addition, an overview of the most promising wastewater treatment technologies using GQDs-based nanocomposites are provided.

2.2 Water pollution by emerging pollutants

One of the primary global challenges of the twenty-first century is the rise in water pollution levels because of rapid industrialization. EPs are discharged into the aquatic environment as a result of typical WWTPs' partial and inadequate wastewater treatment [1]. EPs are found in the environment in amounts ranging from ng/L to g/L. The chemical composition of EPs allows them to accumulate in the endocrine systems of animals and/or humans, as well as travel through the food chain dynamically [2]. This movement through the food chain has toxicological effects on living organisms. While several review articles have successfully documented the occurrence, behaviour, environmental risks and impact of EPs, there is currently no comprehensive database on their toxicity [3, 4]. This is likely because EPs are more alkaline, polar, and more acidic compared to their natural counterparts. In this regard, the complex physico-chemical properties of EPs make it difficult to accurately predict their behaviour when they are discharged into the environment.

There are several possible scenarios that have been proposed when EPs get discharged into water; (i) they can transform into more toxic forms, (ii) if more than one kind of EPs is present in the water matrix, they can generate synergistic or antagonistic interactions yielding what is known the "*cocktail effect*", or (iii) EPs can be adsorbed and accumulate on sediments and eventually get transported into water bodies that provide drinking water for humans [5, 6]. In this context, new and innovative water treatment methods that can effectively remove EPs from water are required to meet the quality requirements for safe drinking water for humans.

2.3 Limitations of current treatment processes

Ideally, WWTPs should be able to achieve complete removal of all toxic organic pollutants in the water without forming undesirable and harmful by-products. The choice of a suitable treatment process for wastewater is informed by the type of the pollutants that are present in the water, secondly on the permissible contamination level in the treated water as guided by the World Health Organization (WHO) and other regulatory bodies and finally the cost related to the process [7]. To date, several treatment processes have been reported; each with varying degree of success coupled with a few shortcomings. **Table 2.1** gives a brief summary of the current treatment processes and their shortcomings.

19

Table 2.1: Summary of treatment processes used to remove EPs and the limitations associated with each process.

Treatment process	Brief description	Limitations	Ref.
Air stripping	Removes volatile organic pollutants	Does not completely destroy the organic pollutants but transfers the pollutants from one phase to another.	[8]
Granular activated carbon (GAC)	Removes organic pollutants from wastewater	The used carbon needs to be regenerated or incinerated.	[9]
Chlorination	Water disinfection	Potentially forms toxic disinfection by-products.	[10]
Ozonation	Water disinfection	Ozone may potentially generate cancer-causing agents.	[11]
Incineration	Incineration of organic waste	Releases harmful gasses in the atmosphere.	[12]

2.4 Advanced oxidation processes (AOPs)

AOPs have emerged as technologies that can overcome most of the shortcomings listed above (**Table 2.1**). AOPs refer to the multitude of oxidation processes that typically take place in aqueous media and are often characterized by the generation of non-selective and oxidative species such as the $\bullet OH$, H_2O_2, O_3 and $O^{\bullet 2-}$ radicals. AOPs are non-selective, as a result they are able to degrade a range of organic contaminants, which are then reduced to less hazardous intermediates or mineralized to innocuous by-products like CO_2 or H_2O [13]. AOPs also provide a platform for combining water disinfection and pollutant photodegradation into a single treatment step and thus ultimately improving the cost-effectiveness of the treatment process [14].

The principle of AOPs is comprised of several steps as illustrated in **Figure 2.1**. The process is initiated by the formation of reactive oxidative radicals, usually from an external stimulus such as light irradiation (**Figure 2.1a**). Secondly, the reactive oxidative radicals will react with toxic organic pollutants in water and yield intermediates that are mostly biodegradable, however and in other instances recalcitrant by-products may form (**Figure 2.1b**). AOPs can be heterogeneous or homogeneous depending on the type of reaction between the reactants and the photocatalyst. The adsorption and desorption of the reactants on the active sites determine the removal efficiency of contaminants in heterogeneous processes. The interactions of the chemical reagents with the target molecules will drive the removal efficiency of contaminants in homogenous processes [13]. Finally, the biodegradable intermediates will react with the reactive oxidative radicals to achieve complete mineralisation by producing H_2O, CO_2 and in some instances inorganic salts (**Figure 2.1c**) (**Equation 2.1**) [14].

$$\textbf{Organic pollutants} \xrightarrow{hv} \textbf{intermediates} \rightarrow \textbf{CO}_2 \textbf{ and H}_2\textbf{O} \qquad \textbf{(Eq. 2.1)}$$
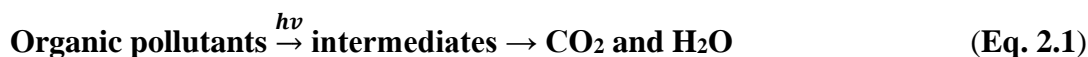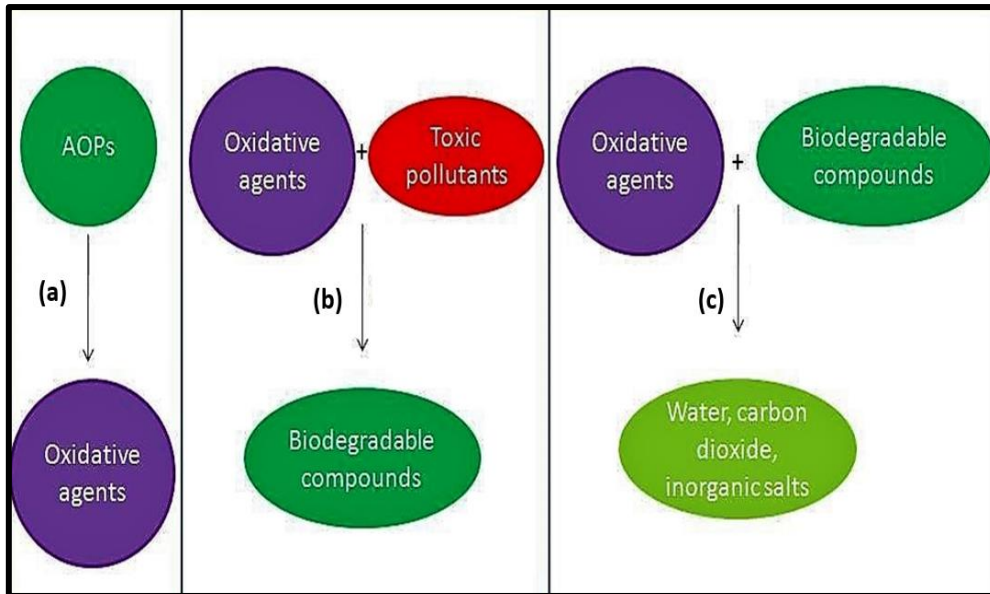
Figure 2.1:   Pictorial representation of AOPs principles [14].

Fogler [15] further illustrated that the overall reaction (**Equation 2.1**) can be explained using the following independent steps as shown in **Figure 2.2**:

i.   mass transfer of the organic pollutants in liquid phase (A) to the surface of the photocatalyst.

ii.   adsorption of pollutants or microorganisms onto the photon activated surface of the photocatalyst.

iii. photocatalysis reaction is initiated from phase (A to B)

- photons get absorbed by photocatalyst
- electrons (e^-) and holes (h^+) are generated
- transfer of photo-generated e^- and h^+ to the catalyst surface which induces the reaction

iv.   desorption of the intermediates from the surface of the photocatalyst (B).

v.   mass transfer of the intermediates from the interface into the bulk fluid (B).
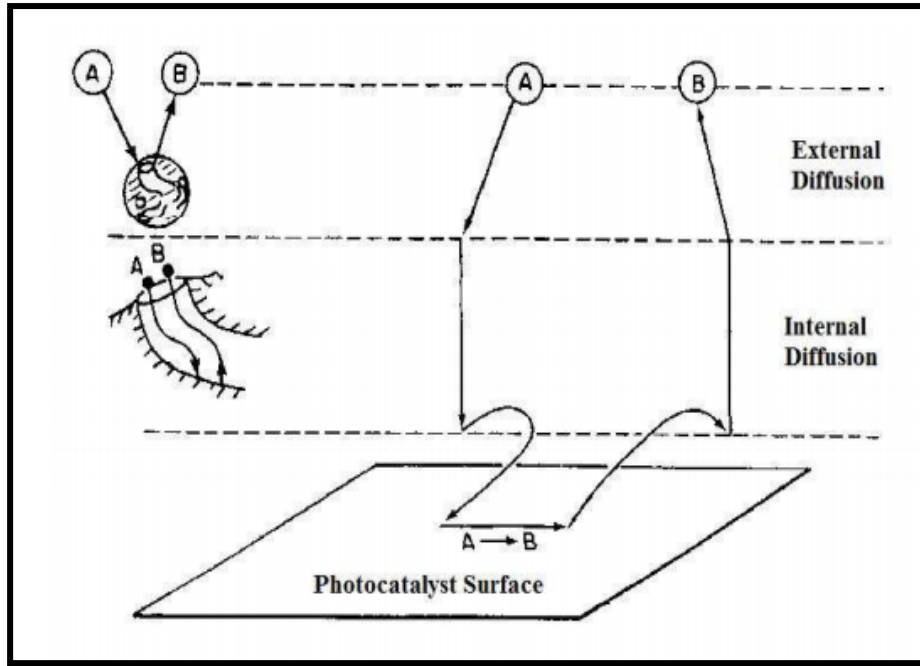
Figure 2.2:   Schematic illustration of a photocatalysis process [16].

During step (iii), a photon with energy greater than the bandgap activates the photocatalyst. When electrons (e^-) are promoted from the valence band (VB) to the conduction band (CB), charge carriers are created and electrons (e^-) and holes (h^+) are separated (**Equation 2.2**).

Photocatalyst + hv → photocatalyst (e^- + h^+)   (**Eq. 2.2**)
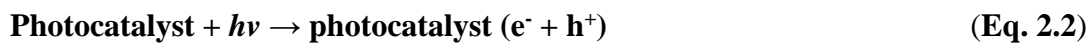
The generated e^-/h^+ pairs will partake in a few reactions (oxidation or reduction) at the photocatalyst surface with the adsorbed organic pollutant or microorganism (**Equation 2.3 - 2.6**) resulting in the decomposition of (R) (an organic pollutant or microorganism) [17].

e^- + O_2 → $O^{•2-}$ (**Eq. 2.3**)

h^+ + •OH → •OH_2   (**Eq. 2.4**)

R-H + •OH →$R^•$ + H_2O   (photodegradation due to •OH)   (**Eq. 2.5**)

R+ h^+ → $R^{+•}$ → final product   (photodegradation due to h^+)   (**Eq. 2.6**)
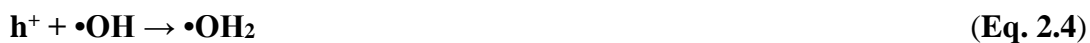
When $O^{\bullet 2-}$ gets protonated, $HO_2\bullet$ is formed which subsequently forms H_2O_2 (**Equation 2.7-2.9**). The generated species enhances the reaction rates and prevents recombination of electrons [17].

$$O^{\bullet 2-} + H^+ \rightarrow HOO\bullet \qquad \textbf{(Eq.2.7)}$$

$$HOO\bullet + e^- \rightarrow HOO^- \qquad \textbf{(Eq.2.8)}$$

$$HOO^- + H^+ \rightarrow H_2O_2 \qquad \textbf{(Eq.2.9)}$$

2.5   Photo-induced disinfection

Several photocatalysts have been reported in microorganism inactivation applications [18, 19]. To date bacteria such as *S. aureus*, *S. typhi*, *E. coli*, *P. aeruginosa* and others have been inactivated using photo-induced disinfection. During the inactivation process, the surface interaction between the photocatalyst and the microorganism is paramount for effective inactivation rate. The interaction is necessary and allows the generated photo-induced reactive oxygen species (ROS) to attack the cell wall of the microorganism. The general antimicrobial inactivation mechanism process is illustrated in **Figure 2.3** and typically; (i) the photo-induced ROS initially attack the lipopolysaccharide layer, (ii) followed by an attack on a particular site on peptidoglycan layer (iii) then the peroxidation and oxidation of proteins in the cell occurs which cause the cytoplasm to leak out of the bacterial cells and ultimately results in cell death [20].
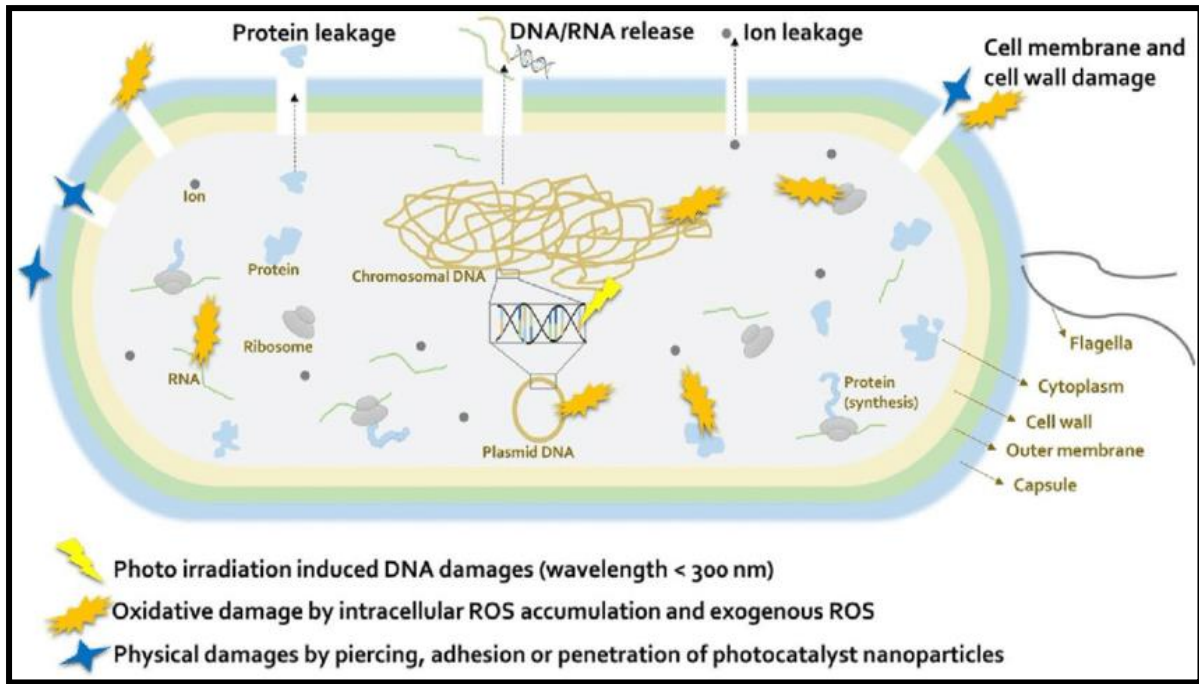
Figure 2.3: An illustration of the photo-induced bacterial inactivation mechanism [20].

2.6   Photocatalysis

In this study, photocatalysis was chosen and employed as a potential technology of treating water polluted with EPs as well as in the disinfection of microorganisms. The premise of the choice was informed by the following reasons: (i) the ability to obliterate all organic pollutants without pollution transfer into another phase, (ii) can be utilized and applied in water disinfection, (iii) cost-effectiveness, reusability, and the recyclability of the photocatalysts and (iv) the utilization of relatively low energy UV-A light. In some instances, sunlight may even be utilized to activate the photocatalyst [21].

2.6.1   Parameters affecting photocatalysis

2.6.1.1 Effect of pH

The role of pH is significant in photocatalysis and is also influential on the oxidation potential, ionization state, surface charge, photocatalyst agglomeration and the adsorption ability of the organic pollutants [22]. Isoelectric point (PZC) is the pH at which the photocatalyst surface charge is neutral. At low pH values (pH < PZC) the functional moieties on the photocatalyst

becomes protonated and favours electrostatic interaction with negatively charged organic pollutants [23]. The rates of adsorption are enhanced at lower pH values. Conversely, at higher pH values (pH > PZC) the photocatalyst surface becomes negatively charged and as a result the anionic compounds are repulsed, while at neutral pH (pH = PZC) photocatalyst aggregation is induced and minimal adsorption of both negatively and positively charged compounds is expected.

2.6.1.2 Effect of temperature

Typically, photocatalytic reactions take place at ambient temperature. However, during the photocatalytic reaction some energy may be released, and this results in an increase in the overall temperature of the reaction. A steady increase in temperature increases the photocatalytic rate. Studies have reported the maximum temperature for photocatalytic reaction to be $\leq 80\ ^{\circ}\text{C}$ [24]. Temperatures beyond 80 $^{\circ}$C are unfavourable to the exothermic adsorption of organic pollutants. Besides reducing the photocatalytic rates, temperatures $\geq 80\,^{\circ}\text{C}$ also promote electron recombination or result in decomposition of thermally unstable pollutants. Conversely, at temperatures < 20 $^{\circ}$C there is an increase in apparent activation energy, and this is unfavourable for photocatalysis [25].

2.6.1.3 Effect of organic pollutant concentration

The concentration of organic pollutants in water influences the photocatalytic rate, since at higher initial organic pollutant concentrations; (i) fewer photons are able to reach the photocatalyst surface and this increases the irradiation time needed to fully mineralise organic pollutants, (ii) the generation of reactive radicals is significantly reduced as a consequence of the active sites of the photocatalyst being saturated by the organic pollutants and none available for photocatalysis [26]. The saturation of active sites by pollutants may sometimes lead to photocatalyst deactivation [27].

2.6.1.4 Effect of photocatalyst loading

Generally, the rate of photocatalysis increases as the photocatalyst load is also increased. This phenomenon is ascribed to a higher number of reactive radicals being generated at higher photocatalyst dose [28]. Studies have shown however, that beyond the optimal catalyst loading,

the photocatalysis rate starts to decrease. The decrease is ascribed to light scattering principle; as the opacity of the solution increases, the light scattering also increases. This is coupled with diminishing light penetration, meaning fewer photocatalyst active sites will be activated [29].

2.6.1.5 Effects of irradiation intensity

The rate of photocatalysis is directly proportional the irradiation intensities, and as the intensity of the irradiation increases, the probability of exciting the photocatalyst increases due to higher photon flux. However, at intensities in the range 0-20 mW/cm^2, charge carrier separation and recombination are in competition with each other, and this negatively affects the generation of reactive radicals [30]. However, at higher irradiation intensities the rate of photocatalysis is independent of the light source.

2.6.1.6 Effects of photocatalyst doping

Dopants are incorporated to the photocatalyst either interstitially or substitutionally. In the interstitial incorporation; the radius of the dopant should be smaller than lattice of the photocatalyst. While in substitutional incorporation, the newly introduced dopant typically substitutes the ion or lattice oxide [31].The main purpose of introducing dopants into a photocatalyst is to induce a bathochromic shift which enhances the photocatalytic efficiency by: (i) altering the bandgap or introducing intra-band gap states as a means to diminish elctron-hole recombination, (ii) increasing the visible light absorption, (iii) the generation of O_2-deficient sites and (iv) producing more active sites that allow the adsorption of organic pollutants. The addition of additional energy levels, the narrowing of bandgaps, and the presence of oxygen vacancies promote photon adsorption in the visible region, hence increasing the rate of photocatalytic reactions [32].

2.6.1.7 Effects of oxidants

Oxidants are irreversible electron acceptors (i.e H_2O_2, $Na_2S_2O_8$, $KBrO_3$, $K_2S_2O_8$, HNO_3) that are often introduced to improve the photooxidation reaction. They achieve this by diminishing the electron-hole recombination or generating sufficient reactive oxygen species for oxidative reactions [33]. In addition to delaying the recombination rate, these oxidants are also responsible for generating intermediate radicals that improve the oxidation rate as well as the

overall photooxidation reaction rate. The commonly used oxidant in AOPs is H_2O_2, the use of H_2O_2 is known to improve the organic pollutant degradation because of the formation of $•OH$ and O_2 radicals as demonstrated in **Equations 2.10**-**2.12** [34]:

$$H_2O_2 + •O_2^- \rightarrow •OH + OH^- + O_2 \qquad \textbf{(Eq. 2.10)}$$

$$H_2O_2 + hv \rightarrow 2•OH \qquad \textbf{(Eq.2.11)}$$

$$H_2O_2 + eCB^- \rightarrow HO• + HO^- \qquad \textbf{(Eq.2.12)}$$

Recently, other oxidants such as $Na_2S_2O_8$ and $K_2S_2O_8$ were reported to offer competitive advantages compared to H_2O_2 due to their easy handling and non-toxicity. For the purpose of this study, the oxidant employed needed to also exhibit excellent disinfection properties. For that reason, peracetic acid (PAA) was chosen as a preferred oxidant and will be delved into in further depth in the subsequent section. In comparison to H_2O_2, PAA has a higher oxidation potential, is less mutagenic, has better bacteriostatic properties, and requires less contact time than H_2O_2 [35].

2.7   Peracetic acid

PAA ($CH_3C(O)OOH$) is a colourless liquid and a strong oxidizing agent, characterized by a strong and pungent odour **(Figure 2.4)**. PAA is formed by reacting acetic acid ($CH_3C(O)OH$) with hydrogen peroxide (H_2O_2) using sulfuric acid (H_2SO_4) as a catalyst (**Equation 2.13**) [36]:

$$CH_3C(O)OH + H_2O_2 \xrightarrow{\text{H2SO4}} CH_3C(O)OOH + H_2O \qquad \textbf{(Eq. 2.13)}$$
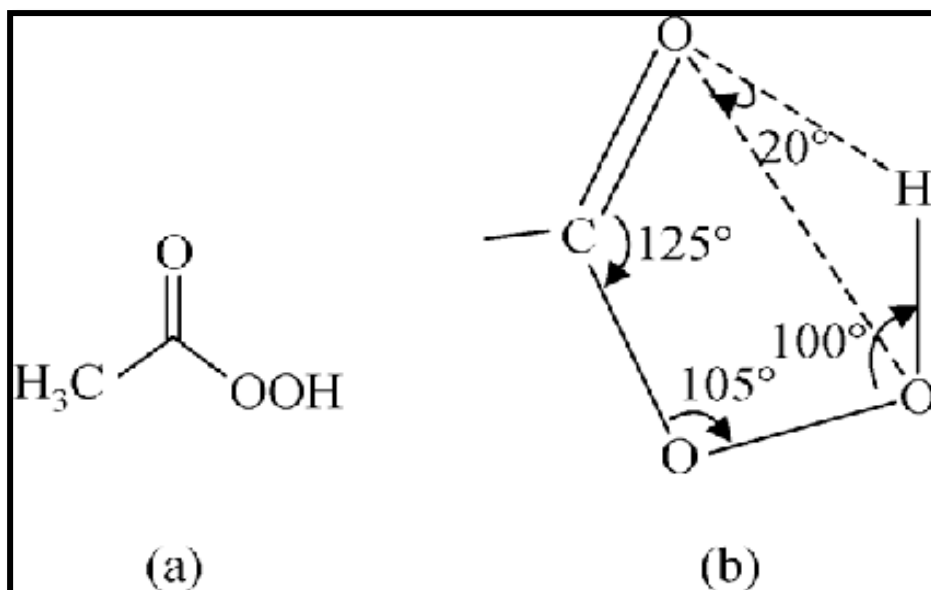
Figure 2.4: Chemical structure of peracetic acid (a) chemical bonds and (b) intramolecular hydrogen bond structures [35].

2.7.1   Peracetic acid as an oxidant

During AOPs the most important step is the *in-situ* generation of the reactive radical species (i.e $SO_4^{\bullet-}$, $\bullet OH$ or $\bullet O_2^-$) [36]. In comparison to chlorine, ozone, chlorine dioxide and other regularly used oxidants and disinfectants, $\bullet OH$ has higher oxidation potential (~2.72 V) (**Table 2.2**) [37]. The efficiency, however, of $\bullet OH$-based AOPs is often affected by $\bullet OH$ radical scavengers typically found in complex water matrices. Examples of such radicals include natural organic matter (NOM) and carbonate or bicarbonate anions [38]. To mitigate this, new radical species with higher selectivity have been proposed. In this regard, PAA was investigated as a potential oxidant in this study.

Table 2.2: **Oxidation potentials of the different oxidants applied in AOPs.**

Oxidant	Oxidation potential (V)
Hydroxyl radical	2.72
Sulfate radical	2.5 - 3.1
Ozone	2.1
Persulfate	2.0
Peracetic acid	1.96
Peroxymonosulfate	1.8
H_2O_2	1.8
Potassium permanganate	1.7
Chlorine dioxide	1.5
Chlorine	1.4

2.7.2 **Peracetic acid as a disinfectant**

PAA combines the advantages of being both an oxidant and a disinfectant, thus postures great potential of substituting chlorination disinfection in WWT. Unlike chlorine, PAA is not affected by pH and it has enhanced sterilisation capabilities and reduced generation of toxic disinfection by-products (DBPs) in treated effluent. Furthermore, PAA can easily be retrofitted in existing treatment plants. PAA also exhibits excellent efficacy in inactivating fungi, viruses, and bacterial spores [39]. The major strategy of employing PAA in place of chlorine is based on the following favourable features of PAA: (i) the lower toxicity compared

to chlorine (ii) the high oxidation potential (iii) microbial activity that is comparable to chlorine, (iv) the formation of little to no toxic DBPs and finally (v) it being an economically viable and a feasible method [40].

Several studies were conducted to examine the DBPs formed during PAA disinfection [41-43]. The results from these studies confirmed that none of the DBPs formed were either chlorinated or brominated phenols. While the formation of some aldehydes was observed, the studies went on to demonstrate that PAA was able to further oxidise the aldehydes into carboxylic acids which were later oxidised to form carbon dioxide. The studies also confirmed that the aldehydes formed were within the permissible concentrations. Mutagenicity and genotoxicity tests were further conducted, and the results gave an indication that no mutagenic DBPs were formed during PAA disinfection [41, 42]. The aforementioned data makes PAA a great substitute for chlorination in water treatment.

2.7.3 Activation of peracetic acid

PAA has been recently applied in the degradation of organic pollutants as well as in the inactivation of microorganisms [43-45]. In these studies, to generate the reactive radicals from PAA that are required to degrade organic pollutants, there is need for activation either by applying external energy or employing catalysts (metal oxides or carbon-based). **Table 2.3** summarizes recent literature on some of the catalysts used to activate PAA. It is important to activate PAA for generation of free radicals because the radicals produced by activated PAA differ significantly from those produced by direct oxidation of PAA. As a result, activated PAA has a higher removal efficiency of organic pollutants compared to PAA alone and this is born from the formation of other radical species such as acetyloxyl $CH_3C(O)O^{\bullet}$ and acetylperoxyl $CH_3C(O)OO^{\bullet}$.

2.7.4 GQDs as catalysts for peracetic acid activation

The activation of PAA to generate ROS for organic pollutant removal has primarily depended on transition metals and metal oxides as catalysts. PAA has also been activated using external energy such as UV irradiation [46-48]. The aforementioned methods are unfortunately limited

due to several factors; in the case of UV, the high cost associated with the method and the potential health hazards of UV radiation pose some challenges. Metal oxides and transition metals suffer from leaching which results in secondary contamination, poor reusability of the catalyst, toxicity of metal catalyst and catalyst deactivation [48]. To mitigate these limitations; cost-effective, green, and metal-free catalysts are recommended. The high cost of traditional metal catalysts has resulted in their replacement by carbon-based materials [48].

Data from **Table 2.3** shows that only activated carbon filters (ACFs) have been used as carbon-based materials to accelerate the activation of PAA in the removal of organic pollutants [49]. In this work, metal-free GQDs were employed and reported for the first time as alternative catalysts for activation of PAA. GQDs were selected specifically because they are stable and have better activity and regeneration capabilities than metal oxide or metal catalysts. They are also cost-effective as well as environmentally benign with no possibility of leaching which often results in secondary contamination.

Table Error! No text of specified style in document.**.1: List of PAA activators, applications, and the highlights of the studies.**

PAA activator		Applications	Highlights	Ref.
Radiation	UV (254 nm)	Degrading 4-chlorophenol	98% of 4-chlorophenol was degraded	[50]
		Degradation of clofibric acid (CA), naproxen (NAP), diclofenac (DCF), ibuprofen (IBP), bezafibrate (BZF), ketoprofen (KEP) and carbamazepine (CBZ),	All the pharmaceuticals were photo degraded by UV/PAA compared to when using PAA alone.	[51]
	Solar light	Degradation of degrade chloramphenicol (CAP).	14-32% of CAP was degraded after 120 min simulation by solar/PAA UV-C/PAA. Process was more efficient for degradation of CAP ($t_{1/2}$ was 20 mins when using 415 mg CAP/L)	[52]
		Inactivating antibiotic resistant (AR) *E. coli*		

			Low PAA doses were used to inactivate *E. coli*. LOD achieved at $Q_{UV} = 0.3$ kJ L^{-1} with 0.2 mg PAA L^{-1} 99.8% and 99.7% of *E. coli* and	[53]
		Inactivation of *E. coli* and *Enterococci*	*Enterococci* were inactivated when using a PAA dose of 12 mg·L^{-1}.	[54]
	Ultrasound (US)	Degradation of phenol	70% of phenol was removed within the first 60 mins using the US-induced oxidation. Only 40% of the phenol was removed in the absence of US.	[55]
Metal catalyst	Cobalt	Degrading sulfamethoxazole (SMX) furosemide, trichorophenol, and naproxen (NAP)	89.4% of SMX was removed after 15 mins of treatment.	[50]
		Degrading CBZ, NAP, and bisphenol-A (BPA)	Removal efficiency was as follows: between 55.0 -100% for BPA, 24.4-98.5% for NAP and 33.0-87.7% for CBZ.	[56]

Iron	Degrading BPA, of methylene blue (MB) and NAP, BPA.	89.4%, 98.2% and 87.7% removal efficiency for MB, NAP and BPA respectively.	[52]
Iron-modified zeolite	Degrading aqueous SMX	100% removal within 50 mins.	[57]
Iron oxide-pillared montmorillonite (Fe_2O_3-montmorillonite)	Degrading dichlorophenol (DCP)	70% of DCP was removed after 3.5 hours	[58]
Manganese	Degrading phenol	70% of phenol was removed during the first 60 mins	[57]
Manganese Ag^+/Cu^{2+}	Disinfecting helminth egg, *V. cholerae,* fecal coliforms *Salmonella sp, P. aeruginosa* and Shigella	Optimal ratios and times for Ag:Cu:PAA were: 1.2:12.0:90.0 mg L^{-1} at 60 mins in the removal of microorganisms in WW	[58]

| Carbon-based | Activated carbon fibers (ACFs) | Removal of Reactive Brilliant Red X-3B (dye) | Using ACFs alone the degradation rates were 53.85%, 53.54%, 53.31%, 51.56%, and 48.47% at pH values of 3, 5, 7, 9, and 11, respectively and increased to 97.6%, 98.7%, 98.9%, 97.7%, and 98.4% after the addition of PAA at the same pH values | [52] |

2.8   Graphene oxide quantum dots (GQDs)

GQDs are carbon-based zero-dimensional (0D) oxygen-rich materials with a graphitic plane with typical thicknesses of 2 nm and lateral dimensions of 10 nm [59].

2.8.1   Structural properties

The carbons in GQDs are structured into six-atom rings and stacked in a honeycomb-like crystal lattice. GQDs with sp^2 hybridized properties are the result of this arrangement. Electrons in the π--orbitals are also delocalized because of the arrangement [60]. The GQDs are endowed with exceptional optical and electrical capabilities as a result of this phenomena. The kind of edges found in GQDs determines the shape of the GQDs. In GQDs, there are two types of edges: (a) zig-zag; and (b) armchair edges (**Figure 2.5a** and **b**). While zig-zag edges (also known as carbene-like edges) contain two unshared valence electrons on every carbon atom at the edge, armchair edges have three carbon atoms bonded together, and this type of edge mimics carbyne molecules [61]. When two identical edges (zig-zag and zig-zag, or armchair and armchair) are present, corners are usually produced at 120°. However, 90° corners will be formed when different edges come together (a zig- zag and armchair come together). The presence of the same type of edges, as well as the formation of six 120° angles, will form hexagonal-shaped GQDs. The presence of both zig-zag and armchair edges that form four 90° angles characterizes rectangular-shaped GQDs (**Figure 2.5c**). In cases where the corners are not properly developed, oval and round-shaped GQDs will be formed.
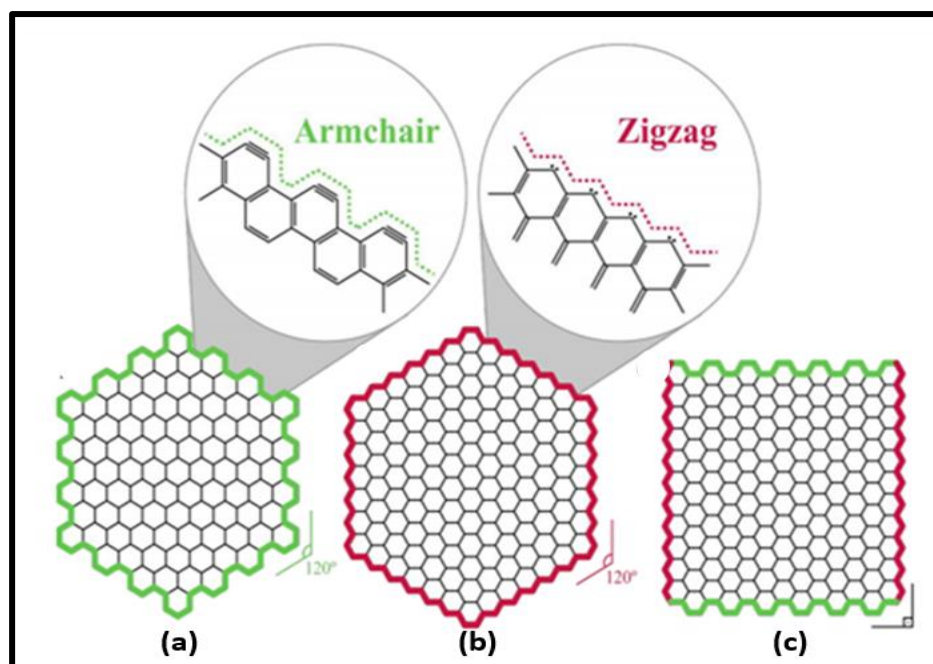
Figure 2.5: Different type of edges found in GQDs; (a) armchair edge, (b) zig-zag edge and (c) hybrid armchair and zig-zag [61].

Due of the π-π^* of the phenyl rings and the C=C bonds, GQDs can photon-harvest in the shorter-wavelength region efficiently. They also absorb a lot of light in the near ultraviolet (NIR) range (260-320 nm). GQDs are characterized by tails that extend into the visible range and show shoulder peaks in the range 270-390 nm, which is attributed to the π-π^* transition of the C=O bonds. The oxygen group functionality on the GQDs' surface is also responsible for a signature peak at 290-320 nm [62].

2.8.2 Photoluminescence (PL) and fluorescence properties

The emission wavelength and intensity of GQDs are clearly excitation dependent, which means that when the PL maximum redshifts, the excitation increases as well. This behavior is related to the quantum confinement effect of the conjugated π--domains, the surface state in GQDs, and the combined influence of both elements [63]. Due to their multilayer surface and excellent crystallinity, GQDs have a high PL quantum yield (QY). They also show configurable PL properties that may be modified to fine-tune them.

2.8.3 Electrochemiluminescence and electrochemical properties

The main distinction between electrochemiluminescence (ECL) and photoluminescence (PL) is that ECL distinguishes itself by surface states, whereas PL focuses on the core state. GQDs are known to have ECL properties with a steady ECL and onset potential near 0 V. This is due to the high sp^2 hybridization, which speeds up electron transmission. According to the suggested ECL mechanism, GQDs (R*) in their excited form are generated by the obliteration of the -ve charged (R•-) and +ve charged (R•+) species by electron transfer. As a result, an ECL signal is created because of relaxation to the ground state. The interaction between doped heteroatoms and functional groups determines the electrochemical characteristics of GQDs [64]. When there are oxygenated groups near the basal plane, the electron transfer arising from the disruption of the conductive sp^2-carbon arrangement is affected. The edge sites found in GQDs, as well as their vast surface area, allow for effective high-speed electron transmission.

2.9 Synthesis of GQDs

GQDs can be obtained using either a stepwise organic synthetic technique or a one-step top-down or bottom-up synthetic route (**Figure 2.6**). The choice of precursor materials and synthesis technique influences several aspects of the GQDs i.e surface features, size, form, and opto-electrical properties.

2.9.1 Top-down approach

Cleaving bulk graphene-like precursor materials into quantum sizes is typical of the top-down synthetic method [65, 66]. To produce GQDs, the precursors are treated to various physical, chemical, and electrochemical treatments under precise reaction conditions. Exfoliation, acidic oxidation, hydrothermal and solvothermal processes, surface-catalysed breakdown reaction, and controlled chemical oxidation are examples of top-down processes reported in the literature [67, 68].

The lack of precise control over size distribution and shape of the GQDs, which are all crucial variables for designing and fabricating of GQDs, is the main disadvantage of the top-down synthetic approach. Furthermore, this method employs harsh experimental conditions that are not suitable for large-scale production, such as strong acidic media, high voltage, strong oxidizing agents, or excessively extended reaction durations. GQDs have recently been exfoliated using less severe non-acidic oxidants such as ozone and H_2O_2 [69].

2.9.2 Bottom-up approach

This synthesis strategy entails using sequential chemical reactions to convert smaller organic molecules like citric acid into GQDs. Direct pyrolysis (carbonisation) or hydrothermal treatments are then used to obtain the GQDs. This method, in contrast to the top-down approach, is scalable, cost-effective and provides excellent control over morphology, form, surface condition, and sizes, as well as fewer defects [70].
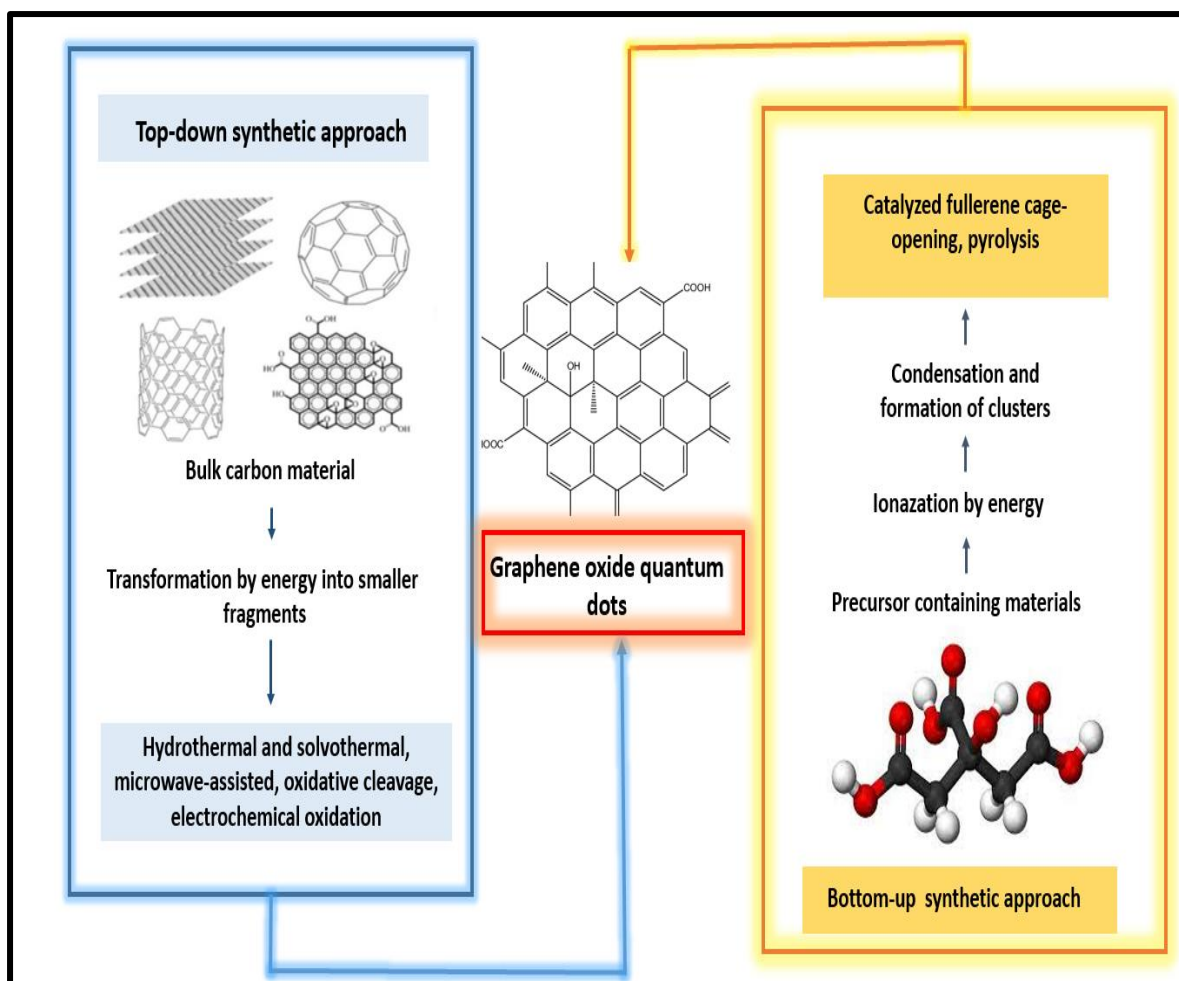
Figure 2.6: Illustration of the different synthetic techniques used in the synthesis of GQDs.

The GQDs employed in this study were synthesized *via* pyrolysis of citric acid. This method of synthesis has several advantages, including the use of green and low-cost materials, the lack of complex post-synthesis processes, the lack of strong acids or bases, simplicity, and the fact that it produces no harmful gases [71]. The GQDs synthesis and purification processes employed in this thesis are described in detail in (**Chapter 3**).

2.10   Modification and functionalization of GQDs

An *in-situ* one-pot functionalisation of GQDs, doping, or surface modification can improve several features of GQDs [72]. Pristine GQDs have limited applications, thus they must be modulated to improve their properties.

2.10.1   Doping of GQDs

GQDs have a honeycomb-like structure that permits various heteroatoms to penetrate the carbon lattice (**Figure 2.7**). B, P, Ag, N, S, and Cl are some of the heteroatoms that have been doped into GQDs [73]. As a result of the number of electrons in its VB and having a size comparable to that of carbon, nitrogen has been employed more than any other heteroatom. Co-doping with more than one heteroatom has been documented in several publications [74]. Charge transfer between GQDs and the functional groups is responsible for the change in PL characteristics of these GQDs. Surface or edge effects come from the introduction of distinct functional groups, resulting in band gap and electronic density perturbation, as well as a change in the overall dipole moment [72]. The overall dipole moment is influenced by a few factors, including the functional groups, the position of the connected functional group, and the shape. Surface modification improves the optical characteristics of GQDs both theoretically and empirically by lowering the impact of non-radiative emissions during excitation [75]. The creation of new types of surface states is credited with the improvement in PL characteristics caused by doping. N, S, or S/N doping (where N or S atoms are injected into the graphitic core) is very effective at generating new surface states [76]. These newly created surface states will contain emissive traps, resulting in a larger recombination yield.
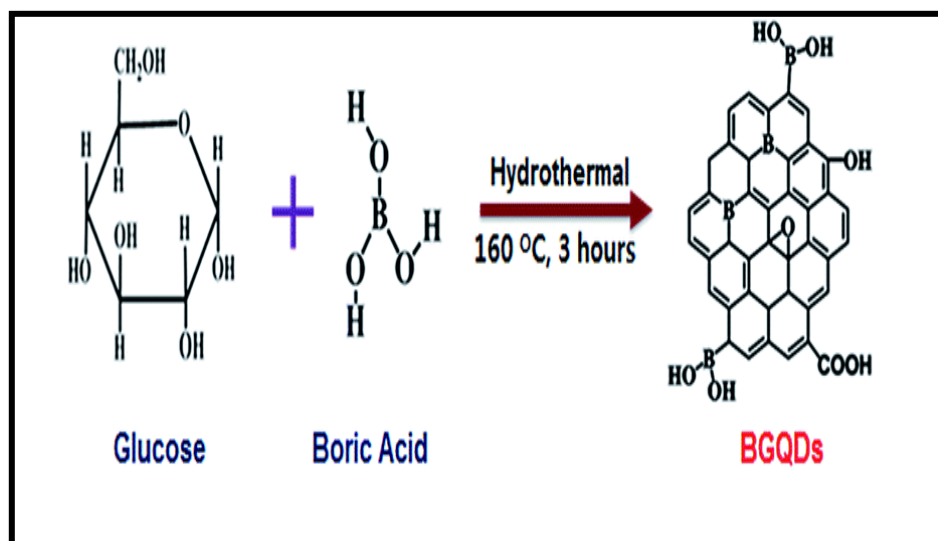
Figure 2.7:   Modification of GQDs surface *via* doping [77].

2.10.2 Surface modification of GQDs

With surface modification/functionalization; a variety of inorganic and organic compounds have been used (**Figure 2.8**). To offer GQDs tunable photoluminescence characteristics, primary amines have been doped on the edges [78]. The presence of an extra interband within the energy gap due to the $-NH_2$ groups is responsible for the PL change. The interband is a result of the hybridization of the p-orbitals of the C-N atoms on GQDs. The red-shifted absorbance of functionalised GQDs is caused by charge transfer between the GQDs and the functional groups and changes in pH as a result of protonation and deprotonation. Adding amino and thiol groups to the GQDs' surface allows them to be further conjugated to a variety of molecules [79, 80].
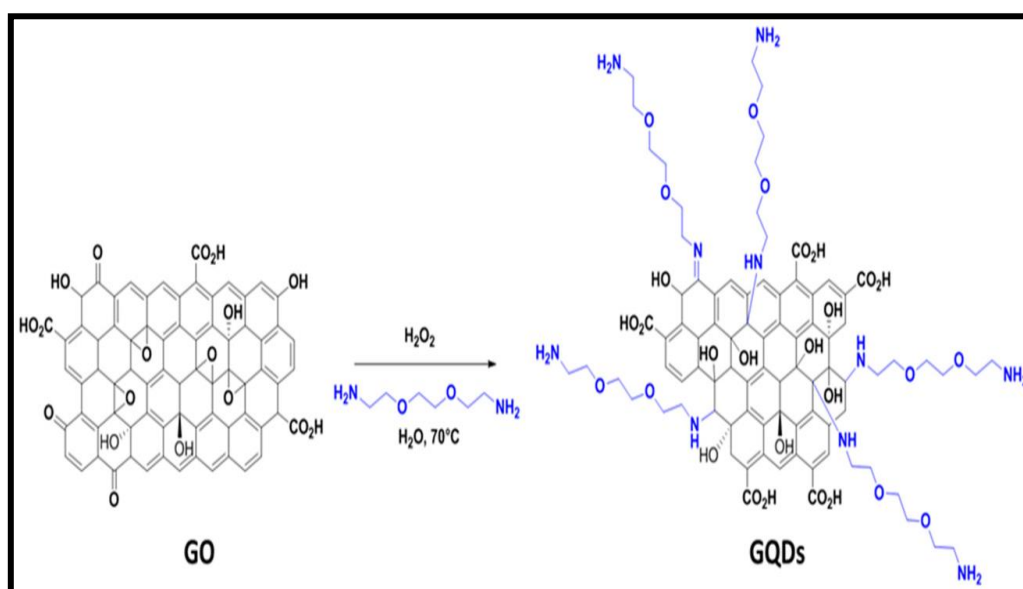
Figure 2.8: Surface modification of GQDs *via* surface modification [81].

2.10.3 Conjugation of GQDs

Another way for modifying the properties of GQDs is to conjugate them to other functionalities after they have been synthesized (**Figure 2.9**). The -COOH and -OH groups on the GQDs' surface enables the covalent attachment to a variety of biomolecules and nanoparticles, owing to the π-π interactions emerging from the planar structure comprised of delocalized electrons, additional π-conjugated aromatic compounds can also be coupled to GQDs [82, 83]. Controlled post-synthesis functionalization of GQDs with appropriate biomolecules, tailored

nanoparticles, and macrocyclic chemicals has resulted in improved photophysical and chemical characteristics. ZnO nanoparticles were conjugated to the GQDs in this study to effect and increase the photocatalytic and disinfection characteristics of the GQDs. This will be described in greater depth in the following section.
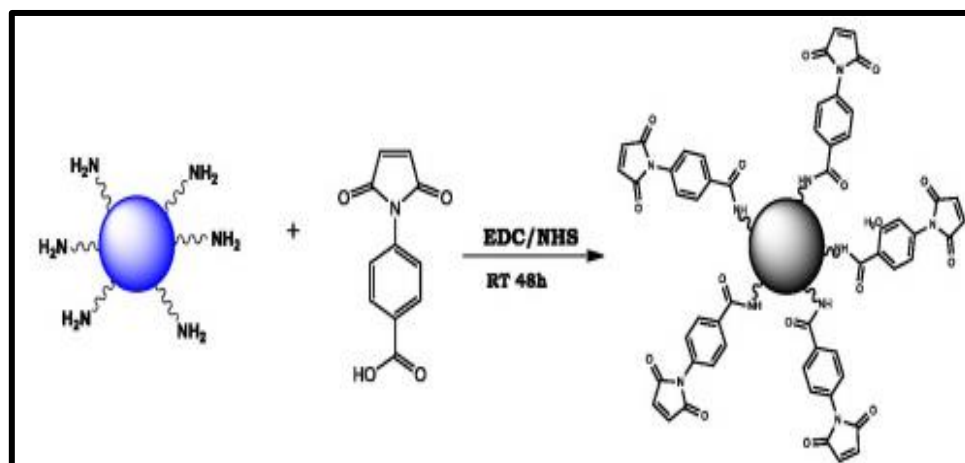
Figure 2.9: Surface modification of GQDs *via* conjugation [84].

2.11 Conjugation of GQDs with other photocatalysts

As previously mentioned, GQDs features can be modulated and modified through conjugation to form heterojunctions. In this study, GQDs were conjugated to ZnO to enhance the photocatalytic activity and disinfection properties. Furthermore, recent studies have demonstrated that ZnO is preferable to TiO_2 and outperforms it significantly [85]. While ZnO has many advantages, it also has certain disadvantages, such as a low utilization of visible light as a result of its wide bandgap, which promotes photo-excited carrier charge recombination.

Herein, the purpose of the modification was to:

i. Overcome the challenges of ZnO as a photocatalyst while combining the advantages of GQDs by designing a nanocomposite with superior photocatalytic performance through a simple yet effective method.

ii. Exploit the electrical properties of GQDs, by allowing the GQDs to act as reservoirs for the photogenerated electrons, thus increasing the lifetime of the electrons.

iii.   Exploit the ability of GQDs to absorb light in the UV or visible region where it can act as a photosensitizer for the generated electrons, and in turn increase the number of available photoelectrons that will partake in the photoreactions.

iv.   Take advantage of the $\pi \rightarrow \pi*$ transition in GQDs that allow more harvesting of sunlight photons as well as increasing the surface area of the nanocomposite.

v.   Increase the absorbability of organic pollutants onto the surface of the photocatalyst, owing to the similarity in the sp^2 - bonded structure of carbon network in the GQDs and in the organic pollutants as well as the high specific surface area of the GQDs.

2.12   Zinc oxide

ZnO is an n-type, binary semiconducting material characterized by a wide and direct bandgap ($\sim$3.3 eV), a large exciton binding energy (60 meV) and hexagonal wurtzite structure (**Figure 2.10**). A number of morphologies and size ranges have been reported for ZnO, with each shape exhibiting unique physico-chemical, optical, structural and photocatalytic capabilities [86]. These differently shaped nanoparticles are prepared by various methods as summarized in **Table 2.4**.
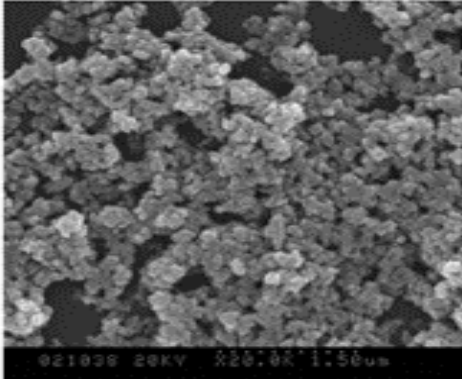
The attractive properties of ZnO for photocatalysis applications include [87]:

i.   emission and absorption bands in UV and visible light spectrum.

ii.   high electron mobility (approximately 300 cm^2 V^{-2} s^{-1} for the bulk ZnO and 1000 cm^2 $V\ s^{-1}$ for ZnO), which enhances the electrons transfer capabilities.

iii.   high redox potential responsible for various reduction and oxidation reactions during the photocatalysis process, and the large bandgap that provides an excellent driving force to trigger the redox reaction under UV irradiation.
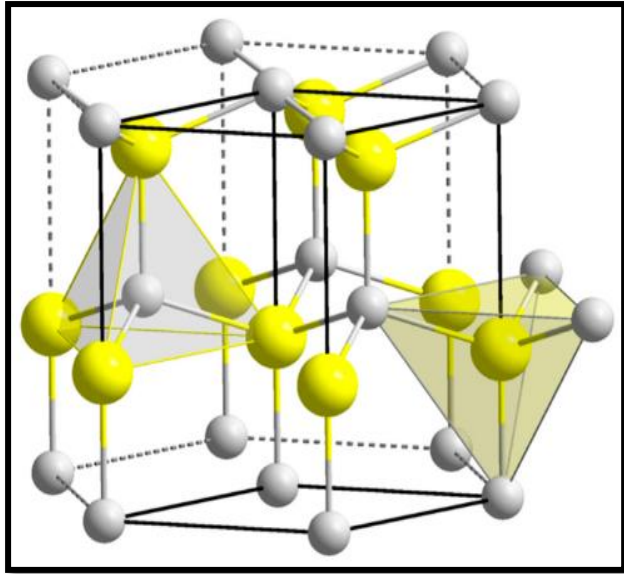
Figure 2.10: Wurtzite structure of ZnO [88].

Table 2.4: Synthesis methods of ZnO, precursors used, synthesis conditions and the morphology of the ZnO.

Synthesis method	Precursor	Synthesis conditions	Shape of ZnO	TEM/SEM image of ZnO	Ref.
Co-precipitation	Zinc acetate dihydrate $(Zn(CH_3COO)_2 \cdot H_2O)$ and ammonium carbonate $(NH_4)_2CO_3$	The precursors (5g) were dissolved, and the solutions were dosed into a strongly mixed aqueous PEG solution first, followed by 3 hours of calcination at 450°C. glycol) first, calcination at 450 °C for 3 hours	Spheres		[89]

Microwave decomposition	Zinc acetate dihydrate $(Zn(CH_3COO)_2 \cdot H_2O)$	5.5 g of the precursor was dissolved in 50 mL of water, then 16 g of NaOH was gradually added. Thereafter $Zn(OH)_4{}^-$ solution and 2 mL of 1-butyl-3-methylimidazolium bis(trifluoromethylsulfonyl)imide ionic liquid [bmim][NTf2] was added. The suspension placed in a microwave oven (2.45 GHz, 850 W) The white precipitate was collected by centrifugation.	Spheres		[90]
Hydrothermal	Zinc acetate dihydrate $(Zn(CH_3COO)_2 \cdot H_2O)$	6 g of the precursor was dissolved in 50 mL of water, and 0.25 M of polyvinylpyrolidone (PVP) (purity 95%) was added to the reaction flask at room temperature, followed by 50 mM of sodium hydroxide (NaOH) poured dropwise into the reaction flask under continuous stirring. The solution was autoclaved for 3 hours at 70 ° C. The obtained white powders were centrifuged and dried.	Flakes		[91]
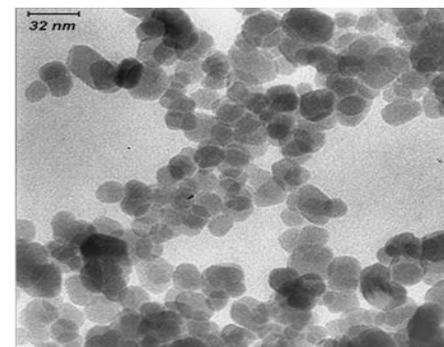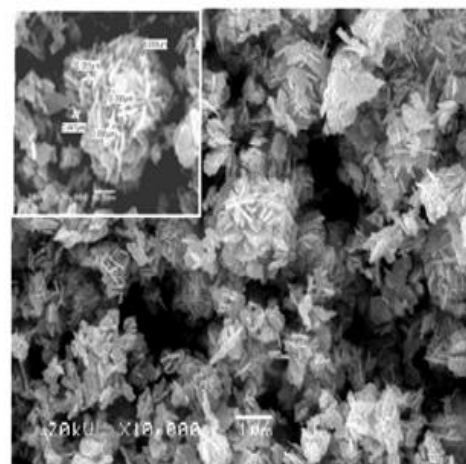
Wet chemical route	Zinc acetate dihydrate $(Zn(CH_3COO)_2 \cdot H_2O$	0.2 M of the precursor zinc was dispersed in water (100 mL) and stirred. 0.1 M of tri-n-propylamine (TPA) was added dropwise to the resultant solution until white solution was formed, indicating the formation of zinc oxide. The white precipitate was washed and dried.	Nano-flowers		[92]
Microwave hydrothermal	Zinc nitrate $(Zn(NnO_3)_2.6H_2O)$	0.02 mol/L of the precursor was suspended in solution made up of (10 mL water and 40 mL absolute ethyl alcohol (C_2H_5OH)). To which 0.075 mol of triethanolamine (TEA, was added. The resultant solution was treated by ultrasonic processing for 10 mins and transferred into an autoclave and heated to 180 °C for 15 mins in a microwave (600 W). The resultants white	Hexagonal prismatic rods		[93]
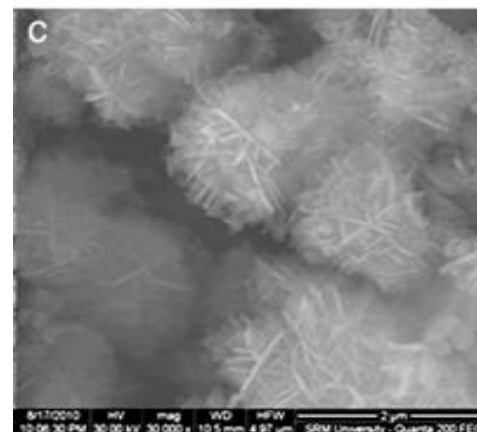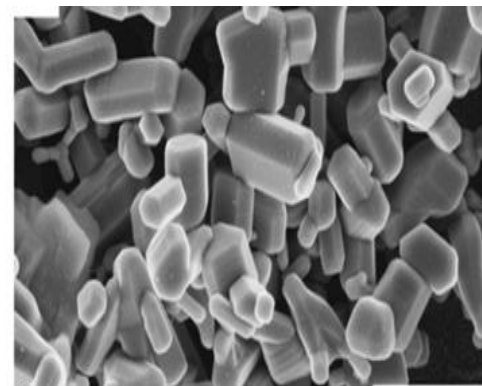
precipitate was filtered and
washed with deionized water and
ethanol 3 times and then dried.

2.13 Photocatalyst immobilisation and support

The greatest challenge in applying photocatalysts on a large scale in water pollution remediation is the difficulty in separating, recovering, and reusing the photocatalyst. To mitigate this challenge, there is a need to immobilise powder photocatalysts on a support. **Figure 2.11** shows an illustration of the two main schemes in which a photocatalytic membrane reactor (PMR) can be configured; (a) photocatalysts immobilised in/on the membrane and (b) photocatalysts suspended [94]. When the photocatalysts are in a slurry system they can achieve higher photocatalytic rates as a result of the higher exposed active surface area of the photocatalysts. The limitations of this method include the difficulty in fully recovering the photocatalyst after use. If the photocatalysts are not completely removed after treating the water, they could get discharged in the environment and posture genotoxicity and cytotoxicity in the environment. Furthermore, suspended photocatalysts also contribute to membrane degeneration, reduced flux, and increased fouling in suspended PMR [95]. With immobolised photocatalysts, the photocatalytic rate is admittedly slightly lower than that of suspended photocatalysts. However, the membrane immobilised photocatalysts enhances some features of the membrane such as: (i) the hydrophilicity (ii) self-cleaning properties (iii) increased degradation of organic pollutants (iv) the reduction of the sludge produced, (v) the reduced use of chemicals as well the physical properties such as porosity and mechanical strength [96].

2.13.1 Ideal properties of photocatalyst support material

Photocatalyst supports may be selected from a plethora of available materials; however, it is necessary for the selected material to exhibit certain characteristics [97].

The photocatalyst supporting material should:
  i.   provide a large surface area
  ii.   permanently and strongly immobilise the photocatalyst
  iii. be resistant to the degadation by the strong oxidative radicals that are generated during the photodegradation process

iv.   efficiently absorb organic pollutants on the surface to allow efficient photodegradation process

v.   should not affect photocatalyst performance after immobilisation

vi.   after the immobilisation process, the final photocatalyst should have a high surface area.
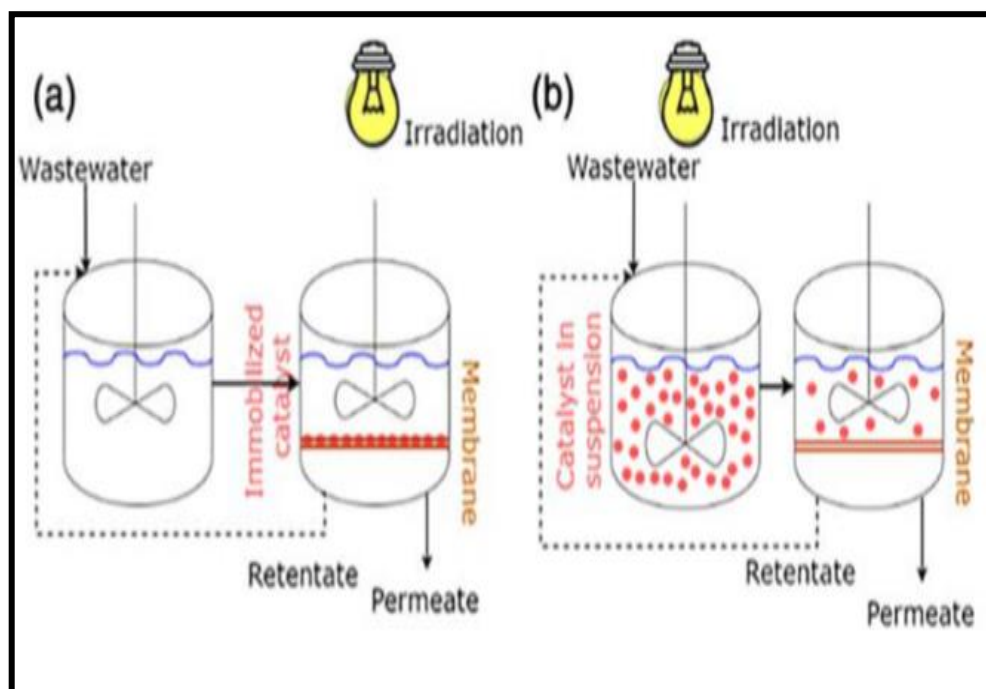
Figure 2.11:   Schematic illustration of the two configurations of a PMR (a) photocatalysts immobilised in/on the membrane and (b) photocatalysts suspended in the reactor [98].

2.13.2 **Photocatalytic membranes**

In this study, the photocatalysts were immobilised in a polymeric membrane. The utilization of photocatalytic membranes was targeted because it enables the photocatalytic process to occur on the membrane's surface and allows the discharge of treated water into the environment without the release of any photocatalysts in the effluent. The choice to use polymeric membrane was based on the favorable attributes of membrane processes: (i) wide spectrum removal ability in single step, (ii) low energy consumption, (iii) reduced use of

chemicals (iv) great selectivity, (v) exceptional performance, (vi) robustness and additionally there is no transfer of pollutants from one phase to another [99].

There are several possible ways in which photocatalysts can be immobilised in/on a membrane [100]. **Figure 2.12** depicts the three different physical immobilisation techniques; (a) surface coating, (b) surface grafting and (c) blending. With surface coating, the coating materials (photocatalysts in this case) adsorb on the membrane surface either through hydrogen bonding, crosslinking, electrostatic, or Van der Waals interactions. The limitation associated with surface coating is that over time there is possibility of leaching. Surface grafting on the other hand, immobilises functional group moieties on the membrane surface *via* covalent linkage. This method is proven to be superior to surface coating. The blending approach incorporates the photocatalysts in the membrane through electrospinning or phase inversion. Typically, in the blending approach the polymer solution is converted into solid membrane films or sheets. This approach is the most common owing to the versatility, cost effectiveness and simplicity of the procedure [101]. Hence, in this study the blending approach was used to immobilise the photocatalyst.
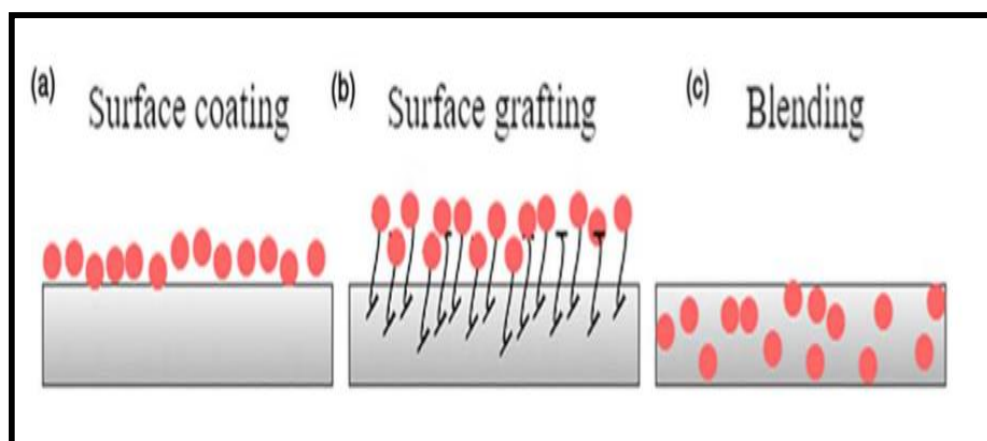
Figure 2.12:   Schematic depiction of the three different physical methods of immobilising photocatalysts in/on polymeric membranes [102].

The performance of membranes can however be hindered by fouling, a phenomenon that occurs when contaminants build up on a membrane's surface blocking the pores of the membrane as shown in **Figure 2.13**. Due to the increased pressure required to overcome biofilm resistance, this resultant layer lowers water flux, reduces membrane lifespan and

performance, and increases energy consumption. To overcome this drawback, membranes with the ability to degrade organic pollutants and remove the fouling layer have been sought [103]. The combination of membrane processes and AOPs has been proposed as an alternative solution to mitigate membrane fouling. Unlike conventional membranes, photocatalytic membranes offer: (i) higher efficiency by improving hydrophilicity (ii) high performance (iii) reduced fouling and (iv) increases the lifetime of membrane.
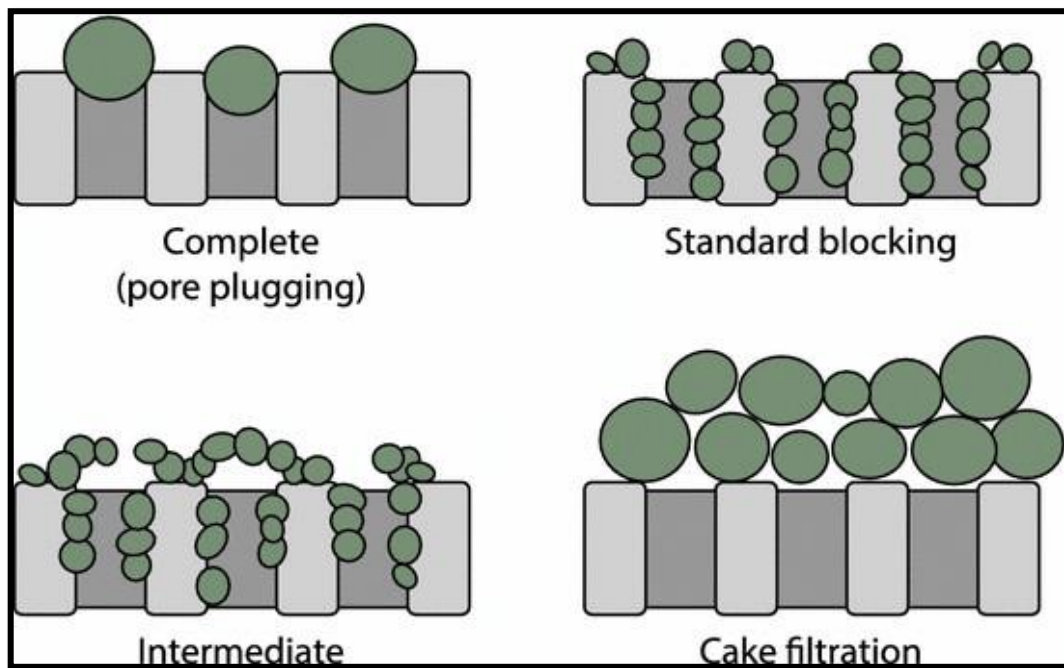
Figure 2.13: Schematic illustration of the different types of membrane fouling mechanisms [104].

2.14   Electrospun nanofibrous membranes (ENMs)

Electrospinning is a method of producing continuous nanofibers in a non-woven form from polymer solutions using a high voltage electric field. The diameter of the fibres varies from 80 nms to several hundred nanometres. It differs from standard membrane production processes in that it produces a relatively uniform pore size distribution, resulting in high pore interconnectivity, large specific surface area, and low density [105]. Furthermore, the properties of nanofibers can be modified to the desired levels by adjusting and manipulating electrospinning parameters such as choice of material as well as the post-processing treatment [105]. **Figure 2.14** shows an illustration of a typical the electrospinning set-up.
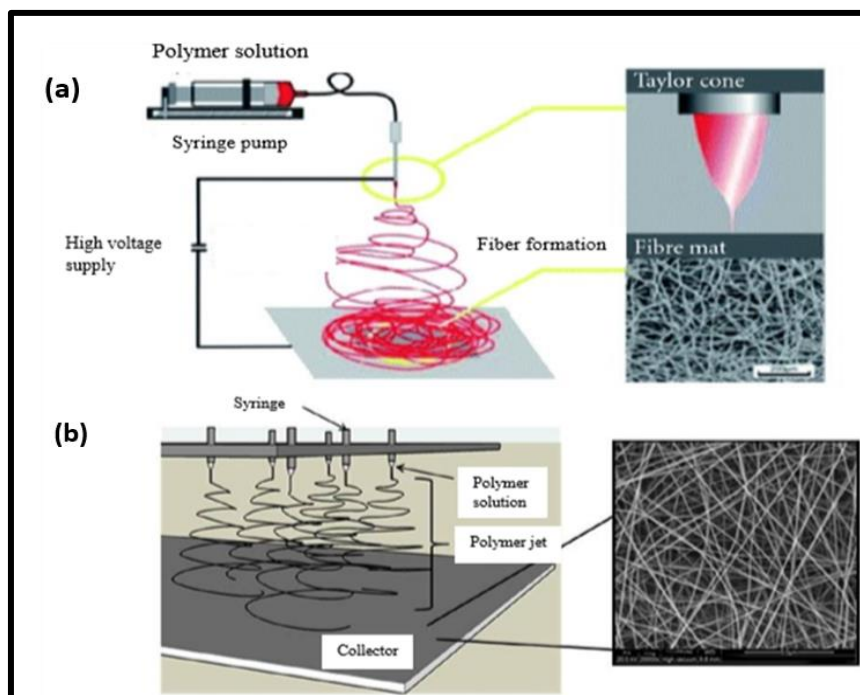
Figure 2.14: Illustration showing (a) mononozzle and (b) multinozzle electrospinning setups [106].

The electrospinning process is affected by a number of variables such as:

i. process parameters i.e the distance between capillary tip and collection screen, flow rate, the ambient temperature, applied voltage as well as the humidity.

ii. nature of solvent

iii. nature of polymer; polymer length and its distribution

iv. properties of polymer solutions such as the concentration, surface tension, conductivity and viscosity.

2.15   Assessment of degradation by-products' toxicity

Ideally, the photodegradation process should completely mineralise the organic pollutants to CO_2 and H_2O. However, several studies have shown that dyes, pharmaceuticals and their degradation by-products can be mutagenic and genotoxic [107,108]. The mutagenicity and

genotoxicity of these degradation by-products will as a result affect the DNA and interfere with the reproductive systems of organisms in the environment [109]. It is therefore essential to assess the quality of the treated water before discharging into the environment by carrying out ecotoxicity studies. The purpose of the ecotoxicity studies is to predict or determine the effect of the degradation by-products on the environment. Ecotoxicity studies are preferred over chemical analysis since they are able to assess complex mixtures and are not only limited to known, target organic pollutants [110].

The Comet and Ames assays have been used to determine the mutagenicity. The Ames assay (**Figure 2.15)** can be used to detect whether the degradation by-products formed during the photodegradation process are able to chemically induce the gene mutation of the histidine strains of *Salmonella typhimurium.* The TA 98 and TA 100 strains are very sensitive to frame shift mutations and GC pair substitutions. Typically, the culture is incubated in growth medium in the presence of histidine at 80˚C overnight. The agar plate is filled with exposure medium that lacks histidine, and the degradation by-products are also inoculated [111, 112]. This is done to simulate the metabolic activation of target organisms, to determine the effect should they ingest the degradation by-products through their livers, S9-fraction of rat liver extract can be added to the culture medium [113]. After incubation the indicator medium is added, and the culture results can be read after 48 hours of incubation. Reverent cells are purple and the non-reverent are depicted as yellow (**Figure 2.15**). The sensitivity of the assay can also be improved by using different strains. The YG7108 strain responds to DNA damages as a result of alkylating agents and was developed in 1995 by Yamada et al. [114] and has also been applied in the detection of mutagenicity of wastewater.
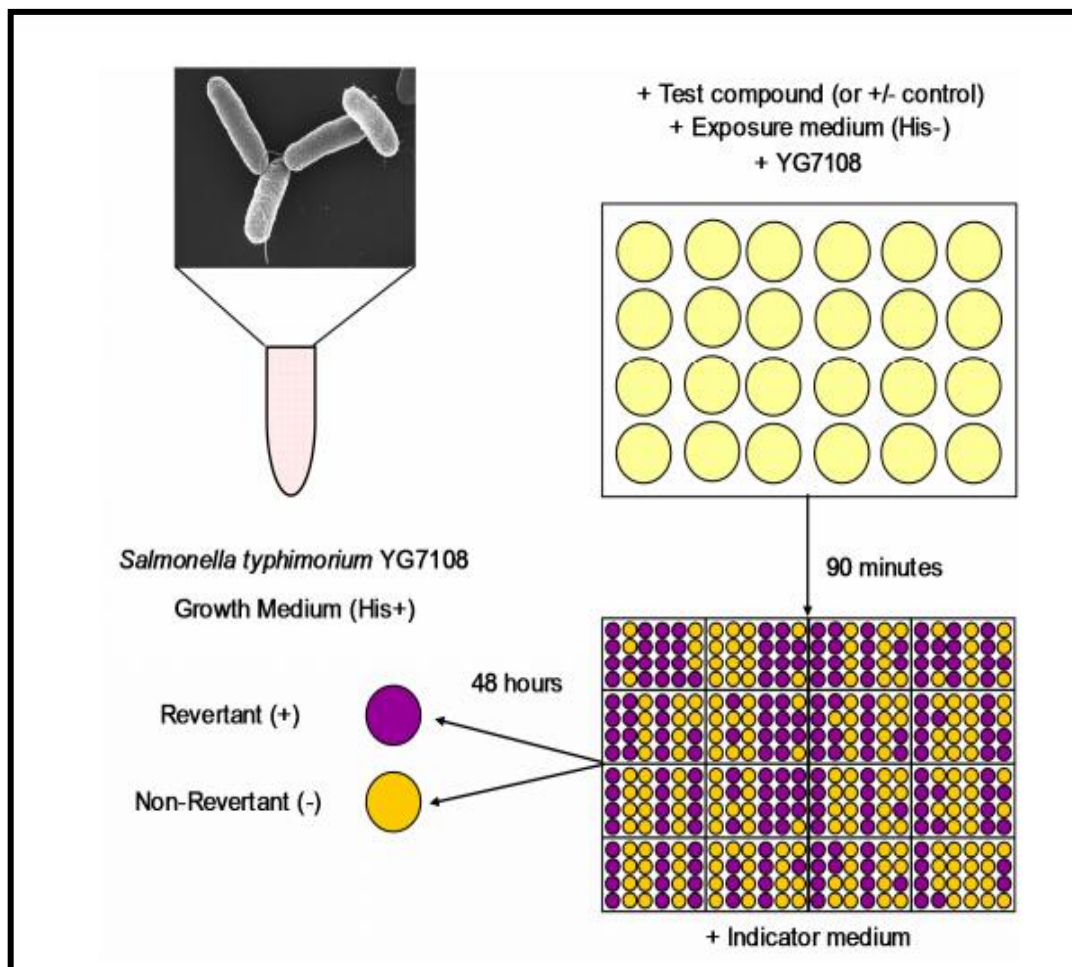
Figure 2.15: Schematic illustration of Ames used to detect the mutagenicity of wastewater using YG7108 strain [114].

2.16   Brief overview of relevant past studies

2.16.1   Removal of emerging pollutants using GQDs-based nanocomposites

A GQDs/Mn-N-TiO$_2$/g-C$_3$N$_4$ (GQDs/TCN) nanocomposite was employed in a simultaneous photodegradation of an organic contaminant and photocatalytic production of H$_2$ from water splitting [115]. Surprisingly, this nanocomposite was capable of degrading organic pollutants in wastewater while also generating new energy. The elimination of organic substances such as p-nitrophenol, ciprofloxacin, and diethyl phthalate was examined and

after 2 hours of reaction time, the maximum photodegradation efficiency rate of p-nitrophenol was 89% and H_2 generation rate was 0.87 mmol $L^{-1}g^{-1}$. In another study, N-GQDs anchored on nanocubic TiO_2 were able to breakdown bisphenol A (BPA), a synthetic hormone disruptive chemical, according to Lim et al. [116]. Adding 0.5 wt% of the N-GQDs, enhanced degradation of 1.85 times that of pure TiO_2 was reached in 30 mins. Surprisingly, as the weight % of N-GQDs increased from 0.5 to 2.5, a drop in the quantity of active radicals produced was decreased as a result [117]. The presence of optimum amount of N-GQDs, were responsible for the suppression of e^-/h^+ recombination which resulted in enhanced photo-efficiency [118].

The N-GQDs-$BiVO_4$/g-C_3N_4 Z-scheme heterojunction was also used to breakdown antibiotics (tetracycline (TC), oxytetracycline (OT), and ciprofloxacin), with 91.5% of tetracycline degraded in 30 mins. N-GQDs were ascribed with the high quantum yields and reaction rates because they expedited effective charge separation and showed strong oxidation and reduction abilities, facilitating the breakdown of organic contaminants [119]. Deng et al. [120] developed a new Ag/N-GQDs/ g-C_3N_4 system by combining the local surface plasmon resonance (LSPR) effect of Ag nanoparticles (NPs), the up-conversion properties of N-GQDs, as well as the ability of g-C_3N_4 to respond to visible light in the degradation of the antibiotic drug tetracycline (TC). Both N-GQDs and Ag NPs played important roles in the photocatalytic activity of the hybrid. Combining the up-conversion capabilities of N-GQDs with the LSPR effect of Ag NPs improved the light transfer and absorption capacity of Ag/N-GQDs/ g-C_3N_4, resulting in increased photogenerated charges and subsequent suppression of charge recombination. The synergistic effects between the g-C_3N_4, N-GQDs, and Ag NPs, resulted in enhanced visible light absorption, conversion, and improved impacts of solar light utilisation.

Hao et al. [121] devised a co-assembly approach to allow ultra-small GQDs to be incorporated into a mesoporous Bi_2MoO_6 photocatalyst (M-BM) to generate a GQDs-BM hybrid. Under simulated sunshine irradiation, a GQDs-BM hybrid was employed to eliminate BPA, ciprofloxacin (CIP), methylene blue, phenol, TC, and RhB. The incorporation of GQDs improved light-harvesting performance in the UV to near-infrared region (NIR), which is advantageous for the formation of active e^- and h^+ on Bi_2MoO_6. Furthermore, the GQDs acted as electron traps, which resulted in reduced surface carrier

charge recombination. When bare M-BM were employed, only 42% of RhB was degraded within 30 mins, while when GQDs were added, 90% was degraded. In the case of BPA, adding GQDs enhanced the degradation efficiency by approximately 2.3 times higher compared to the bare M-BM. Similarly, Lei et al. [122] used GQDs/AgVO$_3$ heterojunction nanoribbons to study the degradation of ibuprofen (IBP) which was reported to have stronger photoactivity than pure AgVO$_3$ nanoribbons. A 3 wt% GQDs/AgVO$_3$ composite photodegraded more than 90% of IBP in less than 120 mins which was roughly 5 times that of pure AgVO$_3$ nanoribbons. The TOC reduction of IBP was greater than 80%. The effective transport of electrons in the conduction band of AgVO$_3$ nanoribbons to the GQDs and the enhanced interfacial contact between the AgVO$_3$ nanoribbons and GQDs, were credited with the improved photocatalytic activity of the 3 wt % GQD/AgVO$_3$. After four cycles, the composite was found to be photostable with an IBP degradation rate of 98%.

2.16.2 GQDs in polymer composites

2.16.2.1 Dye rejection

GQDs were employed as hydrophilic nanofillers to improve polyvinyl chloride (PVC)-based membranes; the membranes were fabricated *via* phase-inversion. Filtration experiments using the Reactive Blue 19 dye (RB-19) indicate that membranes with different GQDs loadings (0.05-2 wt %) had a rejection rate of greater than 95%. The GQDs with a 2 wt% loading had the greatest rejection percentage of 97.6% [123]. Work conducted by Bi et al. [124], showed that adding GQDs *via* in-situ interfacial polymerization using trimesoyl chloride (TMC) resulted in membranes with pore diameters ranging from 1.2-1.72 nm and rejection rates of 92.9 to 98.8% for Alcian blue and Congo red, respectively. When electrospun GQDs polymer sheets were employed to photodegrade RhB, 97% of the solution was degraded in 210 mins. The broad optical response range under white light was responsible for the high photodegradation rate. A thin film nanocomposite (TFN) created by an interfacial polymerization technique had a rejection rate of 99.8% and 97.6% for Congo red and methylene blue (MB), respectively. TFN was generated by reacting GQDs with tannic acid (TA) produced by an interfacial polymerisation process [125].

A physically bonded layer of GQDs atop the TFN polyamide nanofiltration (NF) membrane was used to separate MB and methyl oxalate. The addition of GQDs to the surface changed the surface properties, resulting in improved attributes such surface roughness, surface hydrophilicity, and electronegativity. Regarding NF membranes, the negatively charged selective layer allowed the positively charged MB solution to absorb on the membrane surface, resulting in a lower constant flow dye rejection, images of the membranes were obtained (**Figure 2.16c** and **d**), and the NF was fouled by MB; fouling was greatly reduced when the GQDs were introduced. However, there was no substantial methyl orange adsorption on the NF surfaces, indicating that the GQDs coating can be deployed in antifouling applications.

MB and methyl orange (MO) dyes were separated using a physically bonded coating of GQDs on the TFN polyamide nanofiltration (NF) membrane [126]. The addition of GQDs to the surface improved attributes of the membrane such surface roughness, surface hydrophilicity, and electronegativity. **Figure 2.16** shows that when a GQDs-coated membrane was utilized, the constant water flux of methylene blue solution reduced from 83.3 LMH to 75.4 LMH; similarly, the dye rejection decreased from 75.4% to 71.0% (**Figure 2.16b**). In the methyl orange solution, however, there was an increase in water flux from 106.8 to 124.4 LMH, which was accompanied by a corresponding increase in dye rejection from 89.2 to 97.0% (**Figure 2.16a**). These findings were attributed to changes in electrostatic attraction. The positively charged MB solution absorbed on the membrane surface due to the negatively charged selective layer on NF membranes, resulting in a lower constant flow.
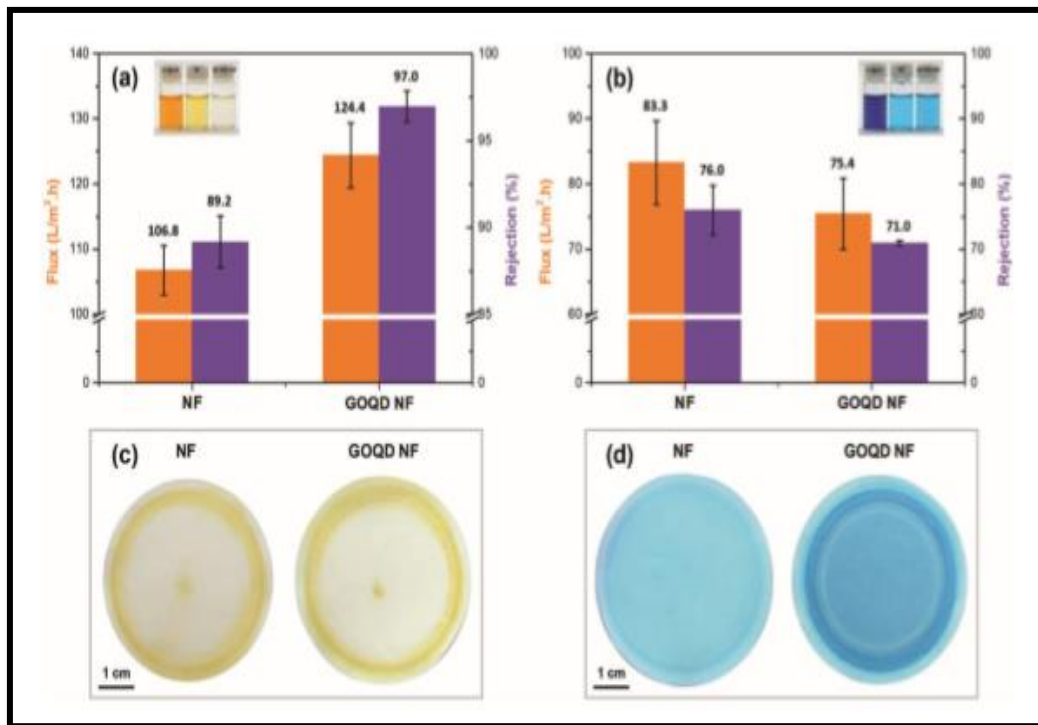
Figure 2.16: Water flux and dye rejection performance of the fabricated membranes. Images of the fabricated membranes after testing in (c) MO and (d) MB dyes. Inserts of panels (a) and (b) show images of feed solutions and filtrates [126].

2.16.2.2 Antifouling and antimicrobial properties

Fouling in pressure-driven membranes is the most significant constraint associated with membrane processes [127]. Previously, GQDs have been introduced to polymers to reduce fouling caused by pathogen growth on the surface of a membrane. GQDs have outstanding antibacterial characteristics, which arise from their capacity to physically penetrate bacterial cells and create oxidative stress. The addition of GQDs improves the dispersibility, charge transfer, and other features that are significant in the production of ROS [128]. Zeng et al. [129] employed *E. coli*-contaminated feedwater in a filtering trial to show that GQDs covalently connected to amino functionalised polyvinylidene flouride (PVDF) resulted in considerable inactivation of *E. coli* and *S. aureus* cells when compared to 1D single walled carbon nanotubes (SWCNTs) and 2D GO sheets. The zones of inhibition (ZOI) were in the range 9 - 40 mm, with the maximum ZOI corresponding to the maximum loading of GQDs (10 wt %), confirming their biocidal activity. PVDF NF membranes implanted with GQDs

rejected > 98% of bovine serum albumin (BSA) protein [130]. In another study with *E. coli*, silver phosphate loaded GQDs (GOQD/AP) were used in the fabrication of a TFN as nanofillers to result in TFN with antibacterial characteristics. The resulting TFN-GOQD/AP inactivated the *E. coli* both in the light and in the dark (**Figure 2.17**) [131].
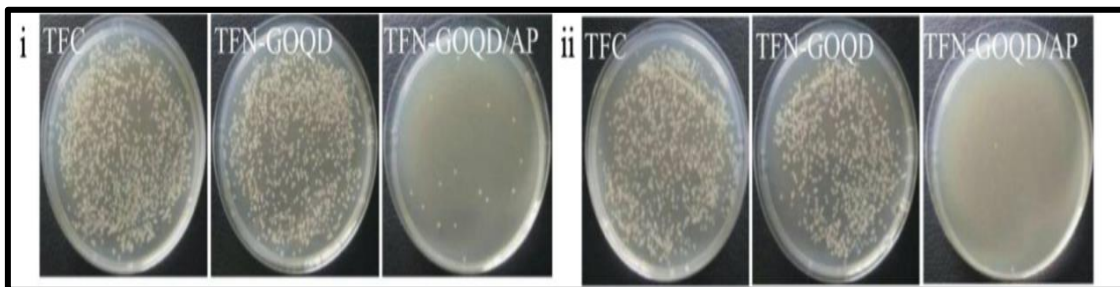
Figure 2.17: *E. coli* colonies after exposure TFC and GOQD and TFN-GOQD/AP50 (i) in the dark and (ii) in the light [131].

Even though there has been relatively little study on GQDs embedded in membranes, some researchers have investigated the antibacterial properties of GQDs and GQD nanocomposite. The antibacterial activity of ZnO/GQDs generated by the hydrothermal technique was improved against *E. coli* [132]. Bacterial colonies were drastically reduced after exposure to UV, according to micrographs of the *E. coli* colonies (**Figure 2.18a-f**). The ZnO/GQDs composite inactivated 100% of the *E. coli* colonies after 5 mins of irradiation.
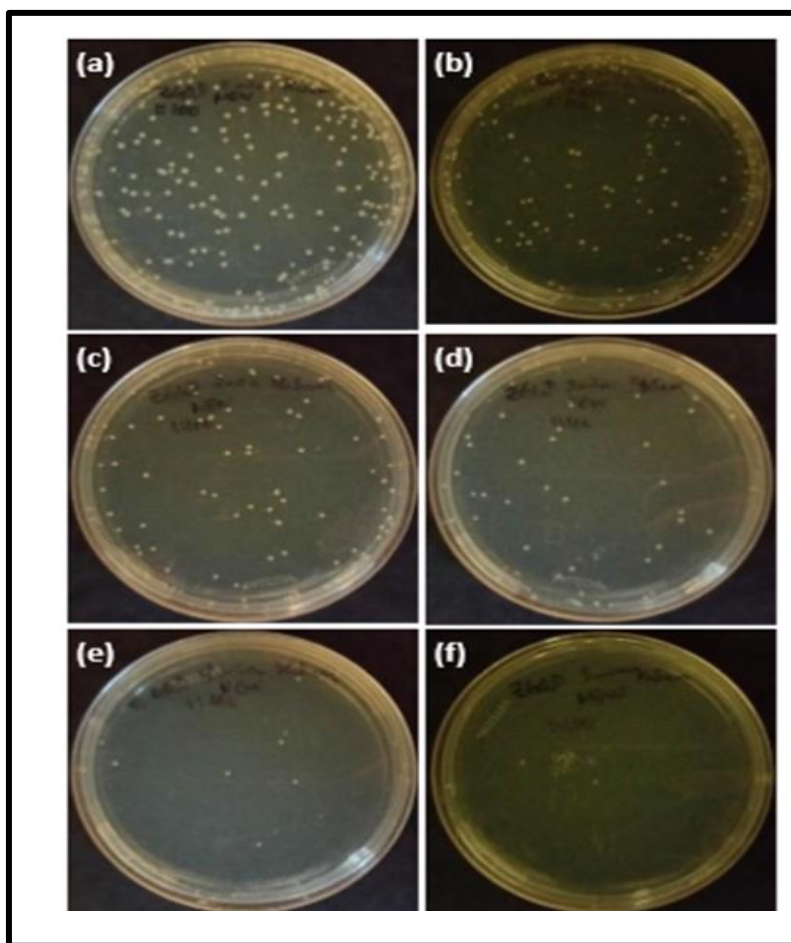
Figure 2.18: Images of *E. coli* colonies cultured after treatment with ZnO/GQDs at time: (a) 0 min, (b) 1 min, (c) 2 mins, (d) 3 mins, (e) 4 mins, and (f) 5 mins [132].

Zhang et al. [133] attached AgNPs to GQDs and employed the resulting hybrid (GQDs-AgNPs) in photodynamic treatment and bacterial photodynamic therapy and tested against *S. aureus* and *E. coli*. The GQDs-AgNPs greatly enhanced the ROS production of pristine GQDs and improved the stability of AgNPs. **Figure 2.19** shows the morphological alterations in *E. coli* and *S. aureus* before and after being treated with GQDs-AgNPs and 450 nm light irradiation.
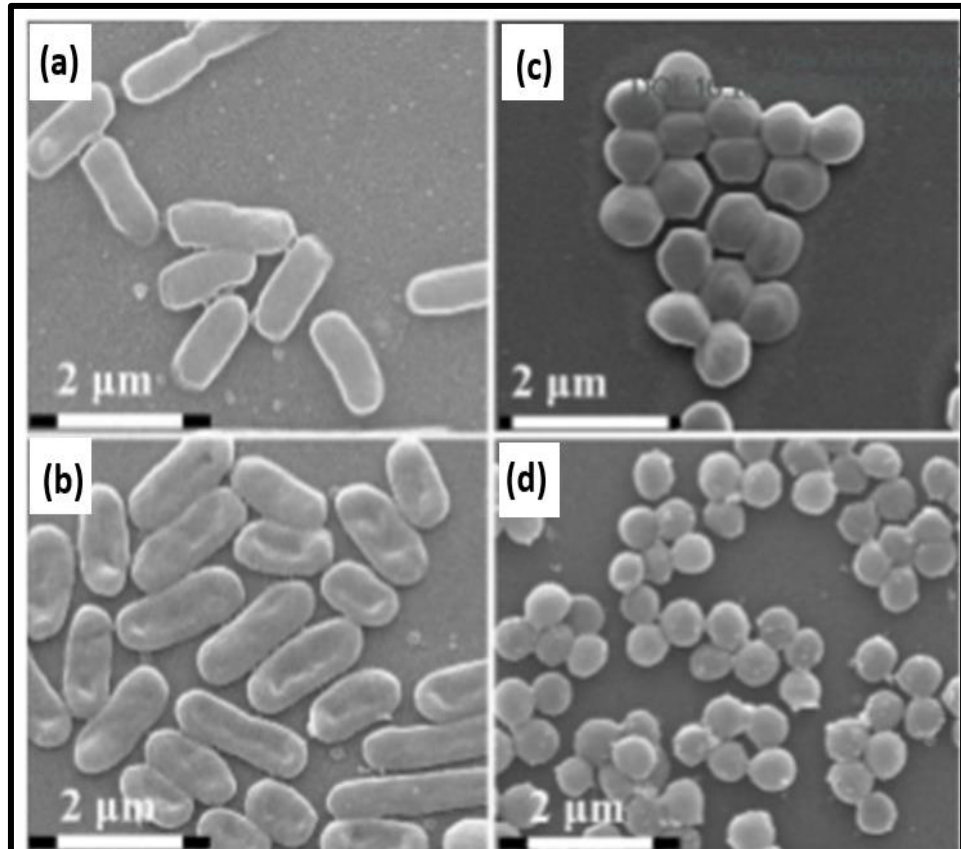
Figure 2.19: SEM micrographs of *E. coli* (a, b) and *S. aureus* (c, d) before (a, c) and after (b, d) treatment with GQDs-AgNPs [133].

The untreated bacterial cells (**Figure 2.19a** and **c**) had intact cell walls and a smooth surface. After being subjected to GQDs-AgNPs (1.0 mg/mL) and light for 10 mins before incubation, the cell wall of *E. coli* appeared crumpled and eventually collapsed (**Figure 2.19b**). Similarly, due to the collapsed cellular wall structure, the treated *S. aureus* developed a rough surface with cytoplasmic leaking of contents. The synergistic impact between the toxic nature of Ag^+ in AgNPs and the improved photodynamic and photothermal antibacterial properties of GQDs-AgNPs, resulted in enhanced antimicrobial effects [134].

2.17   Conclusion

This literature survey presented GQDs as a potential photocatalyst for tackling emerging pollutants in water. The deployment GQDs in AOPs has been reported for successful degradation of dyes, pesticides, and pharmaceuticals into less harmful compounds. The impact of this in a real wastewater treatment is that less sludge is formed and there are minimal environmental effects from the products of the AOPs. Additional processes, such as membrane filtering, may be required in some circumstances to improve the quality of the water obtained using AOPs. Studies on the toxicity and mutagenic potential of the generated photodegradation by-products is still very limited and this thesis seeks to tap into that knowledge gap.

References

1. Chen K. Ohman, C. Metcalfe M.G. Ikonomou P.L. Amatya, J. Wilson, *Water Qual. Res. J. Can*. 41 (4) (2006) 351.

2. Gogoi A, Mazumder, P. Tyagi, V.K. Chaminda, T.G.G, Kyoungjin, Kumar, M. *Sustain. Dev.* 6 (2018)169.

3. Vasilachi C, Mihaela Asiminicesei, F. Daniela Gavrilescu. *Water* 13 (2021) 181.

4. Hlavinek P, Zizlavska, M., Ed.; Springer International Publishing AG: Cham, Switzerland (2018) 231.

5. Wang X.W, Sun G.Z, Li N, Chen P., *Chem. Soc. Rev* 45 (2016) 2239.

6. Zheng X.T, Ananthanarayanan A, Luo K.Q, Chen P, *Small* 11 (2015) 1620.

7. Yan Y, Gong J, Chen J, Zeng Z, Huang W, Pu K, Liu J, Chen P, *Adv. Mater*. 31 (2019) 1.

8. Facure M. H. M, Schenider R, Mercante L.A, Correa D.S, *Environ. Sci. Nano*. 7 (2020) 3710

9. Benitez-Martinez S, Valcarcel M, *Sensor. Actuator B. Chem.* 197 (2014) 350.

10. Xing W, Ngo, H.H, Kim, S.H, Guo, W.S, Hagare P. *Biores. Tech*. 99(18) (2008) 8674.

11. Yang X. Shang, C Huang J.C *Water Res.* 39(19) (2005)4755.

12. Ternes T.A, Stüber, J, Herrmann, N, McDowell, D, Ried, A., Kampmann, M, Teiser, B, *Water Res.,* 37(8) (2003) 976.

13. Tebbutt T.H.Y, Proceedings of the Institution of Civil Engineers-Water Maritime and Energy, 112(1) (1995) 39.

14. Gadupudi C.K, Rice, L, Xiao, L, Kantamaneni, K, *Sci. Rep* 3(1) (2014)11.

15. Miklos D.B, Remy, C, Jekel, M, Linden, K.G, Drewes J.E, Hübner, *Water Res.* 139 (2018) 118.

16. Tsydenova O, Batoev V, Batoeva, A. Inter. *J. Environ. Res. Public Health*. 12(8) (2015) 9542.

17. Fogler H.S. (1999) Elements of Chemical Reaction Engineering. Prentice Hall of India, New Delhi.

18. Chong M.N, Jin B Chow C.W, Saint C, *Water Res.*, 44(10) (2010).

19. Cooper A.T, D. Y. Goswami, S. S. Block, *J. Adv. Oxi. Tech*. 3(2) (1998)151.

20. Armon R, N. Laot N. Narkis I. Neeman. *J. Adv. Oxi. Tech,* 3(1998)145.

21. Hussein-Al-Ali S. H, El Zowalaty M. E, Hussein M. Z, Geilich B. M, Webster T. *J. Int. J. Nanomed.* 9(2014)3801.

22. Xiao M, Wang, Z, Lyu, M, Luo, B, Wang, S, Liu, G, Cheng, H.M, Wang, L. *Adv. Mater.* 31(38) (2019)1801369.

23. Valencia A.M, Caldas M, *J. Phys. Rev*, 96 (2017) 125431.

24. Li L, Wu G, Yang G, Peng J, Zhao J, Zhu J, *Nanoscale* 5 (2013) 4015.

25. Zhu C, Yang S, Wang G, Mo R, He P, Sun J, *J. Mater. Chem*. C. 3 (2015) 8810.

26. Shen J, Zhu J, Yang X, Zong J, Zhang J, Li C, *New. J. Chem*. 36 (2012) 97.

27. Pouretedal A. Norozi M. H. Keshavarz A. Semnani, *J. Haz. Mater.* 162(2-3)(2009) 674.

28. Saleh T.A, Gondal. M, Drmosh Q, Z. H. Yamani, AL-yamani A, *Chem. Eng. J.* 166(1) (2011) 407.

29. Shifu C, Z. Wei, L., Huaye, Y. Xiaoling, *Chem. Eng. J*, 155(1-2)(2009)466.

30. Cao Y. Yu, P. Zhang, L. Zhang, *Sep. Purif. Techn.* 104(2013) 256.

31. Tian C. Li, F. Gu, H. Jiang, Y. Hu, J. Zhang, *Chem. Eng. J.* 151(1–3) (2009)220.

32. Huang C. Xu Z. Wu Y. Huang, J. Lin J. Wu, *Dyes Pigments*, 77(2) (2008)327.

33. Sobana K. Selvam M. Swaminathan, *Sep. Purif. Techn.* 62(3) (2008)648.

34. Bounoure F, Fiquet H, Arnaud, P, American *J. Health System Pharm.* 63(5) (2006)451.

35. Kitis M, *Environ. Internat*. 30(1) (2004)47.

36. Coyle E.E, Ormsbee L.E, Brion G.M, *Water Environ. Res*. 86(8) (2014)687

37. Ma J, Yang, Y, Jiang X, Xie, Z, Li X, Chen C, Chen H, *Chemosphere,* 190(2018) 296.

38. Rossi S, Antonelli M, Mezzanotte V, Nurizzo C, *Water Environ. Res*. 79(4) (2007)341.

39. Kitis M, *Environ. Internat.* 30(1) (2004)47.

40. Xie X, Li, X, Chen, C.*J. Appl. Bacteriol*.54 (1983)417

41. Monarca D, Feretti I, Zerbini C, Zani A, Alberti S.D. Richardson, IWA world conference, Berlin, Germany (2001)

42. Monarca S.D, Richardson D, Feretti M, Grottolo A.D, Thruston C. *Environ. Toxicol. Chem*. 21 (2002)309.

43. Gehr D, Cochrane M, French Proc. of the U.S. Water Environment Federation Disinfection Conference (2002).

44. Colgan S, Gehr R, *Water Environ. Technol.* 13 (2001)29.

45. Stampi G, De Luca F, Zanetti, *J. Appl. Microbiol.*91 (2001)833.

46. Cai M, Sun P, Zhang, L, Huang C.H, *Environ. Sci. Technol*. 51(2017)14217.

47. Wu W, Tian D, Liu T, Chen J, Huang T, Zhou X, Zhang Y, *Chem. Eng. J.* 394 (2020)124938.

48. Sharma S, Mukhopadhyay M, Murthy Z.V.P, 2014. *Clean. Soil. Air. Water* 42 (2014) 276.

49. Hollman J, Dominic J. A, Achari G, *Chemosphere* 248 (2020)125911.

50. Rizzo L, Lofrano G, Gago, C, Bredneva T, Iannece P, Pazos M, Krasnogorskaya N Carotenuto M, *J. Clean. Prod.* 205(2018) 67.

51. Cai M, Sun P, Zhang L, Huang C.H, *Environ. Sci. Technol*. 51(2017)14217.

52. Zhang T, Wang T, Mejia-Tickner B, Kissel J Xie, X, Huang C, *Environ. Sci. Tech.* 54(15) (2020)9652.

53. Balachandran S, Charamba L.V, Manoli K, Karaolia P, Caucci S, Fatta-Kassinos D, *Water Res*., 202(2021) 117403.

54. Li G. Wu G. Yang, J. Peng, J. Zhao, J.J. Zhu, *Nanoscale* 5 (10) (2013) 4015.

55. Kundu V.K. Pillai, *Multifunct. Mater*. (2020)169.

56. Ohta A. Bostwick T. Seyller K. Horn E. Rotenberg, *Science* 313 (5789) (2006) 951.

57. Lee H.Y. Kim H. Yoon J. Kim J.S. Suh, *Carbon* 106 (2016) 48.

58. Xie Z. Wang, W. Zhou, Y. Liu, L. Fan, Y. Li, X. Li, *Anal. Methods* 8 (20) (2016) 4001.

59. Luo G. Qi, K. Chen, M. Zou, L. Yuwen, X. Zhang, W. Huang, L. Wang, Adv. *Funct. Mater*. 26 (16) (2016) 2739.

60. Zheng A, Ananthanarayanan K.Q, Luo, P. Chen, *Small* 11 (14) (2015) 1620

61. Zhu S. Tang J. Zhang B. Yang, *Chem. Commun.* 48 (38) (2012) 4527.

62. Zhu J. Zhang S. Tang C. Qiao L. Wang H. Wang X. Liu B. Li Y, Li W, Yu, X. Wang, *Adv. Funct. Mater.* 22 (22) (2012) 4732.

63. Peng W, Gao B.K, Gupta Z, Liu R, Romero-Aburto L, Ge L, Song L, B. Alemany X, Zhan, G. Gao, S.A. Vithayathil, *Nano Lett.* 12 (2) (2012) 844.

64. Liu Q, J. Zhang, H. He, G. Huang, B. Xing, J. Jia, C. Zhang, *Nanomaterials* 8 (10) (2018) 844

65. Zhuo S, M. Shao, S.T. Lee, *ACS Nano* 6 (2) (2012) 1059.

66. Melo P.L. Ríos P. Povea C, Morales-Verdejo M.B. Camarada, *ACS omega* 3(7) (2018) 7278.

67. Gan Z H, Xu Y, Hao J, *Nanoscale* 8 (15) (2016) 7794.

68. Tian P, Tang L, Teng K, Lau S.P, *Mater. Today Chem.* 10 (2018) 221.

69. Mahalingam A, Manap A, Omar F.W, Low N.F, Afandi C.H. Chia N. Abd Rahim N, *Renew. Sust. Energ. Rev*. 144 (2021) 110999.

70. Sweetman M, Hickey S.M, D.A. Brooks, J.D. Hayball, S.E. Plush, *Adv. Funct. Mater.* 29 (14) (2019) 1808740.

71. Kim S, Hwang M.K, Kim D.Y, Shin D.H, Shin C.O, Kim S.B, Yang J. H, Park E, Hwang S.H, Choi G, *ACS Nano* 6 (9) (2012) 8203.

72. Liu B. Guo Z, Rao B, Zhang J.R, Gong J, *Nano Lett.* 13 (6) (2013) 2436.

73. Qu D, Zheng P, Du Y, Zhou L, Zhang D, Li H, Tan Z, Zhao Z, Xie Z, *Nanoscale* 5 (24) (2013) 12272.

74. Qian J. Ma X, Shan L, Shao J, Zhou J, Chen H, Feng H, *RSC Adv.* 3 (34) (2013) 14571.

75. Wang D, Chen J, Dai L, *Part. Part. Syst. Charact.* 32 (5) (2015) 515.

76. Zhang J, Intern. Conference Electronis and Optoelectronics (ICEOE), IEEE 3(2011)3

77. Zhang P, Ram M.K, Stefanakos E, Goswami D, *J. Nanomater.* (2012) 1.

78. Li B.P, Zhang J.X, Zhao Z.H, Ge X.K, Zhao L. Zou, *Appl. Surf. Sci*. 279 (2013) 367.

79. Rahimi A, Yazdani M, Ahmadirad M, *Mater. Res. Bull*. 98 (2018) 148.

80. Sarkar D, Tikku S, Thapar V, Srinivasa R.S, Khilar K.C, *Colloids. Surf. A: Physicochem Eng. Aspects* 381(1-3) (2011)123.

81. Das S, Srivastava V.C. *J. Nano. Res*. 35(2016)21.

82. Qin N, Xiang Q, Zhao H, Zhang J, Xu *J. Cryst. Eng. Comm.* 16(30) (2014)7062.

83. Schlur L, Calado J.R, Spitzer D, *Royal Soc. Open Sci.,* 5(8) (2018)180510.

84. Vinod R, Sajan P, Achary S.R, Tomas C.M, Munoz-Sanjosé, V, Bushiri M.J, *J. Phys. D: Appl. Physics* 45(42) (2012) 425103.

85. Shen T, Zhang P, Xu L, Zhang J, Liu Z, Chen, *Appl. Catal. B Environ*. 219 (2017)12.

86. Cheng G, Zeng D, Huang L, Cui P, Xu C, Zhang Y, Liu Y, *Chem. Eng. J.* 284 (2016) 582.

87. Nguyen T.P, Tran Q.B, Ly Q.V, Le D.T, Tran M.B, Ho T.T.T, Nguyen, X.C, Shokouhimehr M, Vo, D.V.N, Lam S.S., Do H.T, *Arabian J. Chem*. 13(11) (2020)8361-8371.

88. Esplugas S, D.M. Bila, L.G.T. Krause, M. Dezotti, *J. Hazard. Mater*. 149 (2007) 631.

89. Zakria H.S, Othman M.H.D, Kamaludin R, Kadir S.H.S.A, Kurniawan T.A, Jilani A, *RSC Advances* 11(12) (2021)6985.

90. Ursino R. Castro-Muñoz E, Drioli L, Gzara M. H, Albeirutty A, Figoli A, 8(2018)1.

91. Warsinger D, S. Chakraborty E. W, Tow M. H, Plumlee C, Bellona S, Loutatidou L, Karimi A. M. Mikelonis, A. Achilli A, Ghassemi L. P, Padhye S. A. Snyder, S. Curcio, C. D. Vecitis, H. A. Arafat, J. H. Lienhard, Prog. Polym. Sci, 81(2018) 209.

92. Huang Z, Y-Z Zhang, M. Kotaki, S. Ramakrishna, *Compos. Sci. Technol.* 63 (2003) 2223.

93. Bhardwaj N, Kundu S, *Biotechnol. Adv.*28 (3) (2010) 325.

94. Agarwal A, A. Greiner, J. H Wendorf, *Prog. Polym. Sci.* 38 (6) (2013) 963.

95. Zugle R, E. Antunes, S. Khene, T. Nyokong, *Polyhedron* 33 (2012) 74.

96. Vom Eyser C, Börgers A, Richard J, Dopp E, Janzen N, Bester K, Tuerk J, Water sci. tech. 68(9) (2013)1976.

97. Dirany A, Aaron S. E, Oturan N, Sires I, Oturan M. A, Aaron J. J. *Analy. Bioanalyt. Chem.* 400 (2009) 353.

98. Sanchez W, Egea E, 2018. Health and environmental risks associated with emerging pollutants and novel green processes.

99. National Research Council, 2014. A framework to guide selection of chemical alternatives. National Academies Press.

100. Mortelmans K, Zeiger E, *Mutagenesis*, 455(1-2) (2000)29.

101. Margolin B.H, Kim B.S, Risko, K.J, J. Americ. Stat. Assoc, 84(407) (1989) 651.

102. Iyer, W Szybalski, *Appl. Microbiol*. 6 (1958)23.

103. Yamada M, Espinosa-Aguirre J.J, Watanabe M, Matsui K, Sofuni T, Nohmi T, *Mutagenesis* 375(1) (1997)9.

104. Lim, K.H. Leong, L.C. Sim, A. Abd Aziz, P. Saravanan, *Environ. Sci. Pollut. Res.* 26 (4) (2019) 3455.

105. Shen Y, X. Yu, W. Lin, Y. Zhu, Y. Zhang, *Appl. Surf. Sci.* 399 (2017) 67.

106. Kamisaka H, T. Adachi, K. Yamashita, *J. Chem. Phys.* 123 (8) (2005) 084704.

107. Phophayu S, P. Pimpang, S. Wongrerkdee, S. Sujinnapram, S. Wongrerkdee, *J. Reinf. Plast. Compos*. 39 (3-4) (2020) 81.

108. Kamisaka H, T. Adachi, K. Yamashita, *J. Chem. Phys.* 123 (8) (2005) 084704.

109. Yan X, Qu, Q. Niu, C. Tian, C. Fan, B. Ye, *Anal. Methods* 8 (7) (2016) 1565.

110. Deng L, Tang, C. Feng, G. Zeng, J. Wang, Y. Lu, Y. Liu, J. Yu, S. Chen, Y. Zhou, *ACS Appl. Mater. Interfaces* 9 (49) (2017) 42816.

111. Hao Z, Jin, J. Xu, S. Min, G. Lu, *Superlattice. Microst.* 94 (2016) 237.

112. Lei J.J, Wang, L. Wang, X.Y. Yang, G. Xu, L. Tang, *J. Hazard. Mater.* 312 (2016) 298.

113. Lim K.H, Leong, L.C. Sim, A. Abd Aziz, P. Saravanan, *Environ. Sci. Pollut. Res.* 26 (4) (2019) 3455.

114. Jafari N, Derlon, P. Desmond M.C, van Loosdrecht, E. Morgenroth, C. Picioreanu, *Water Res.* 157 (2019) 335.

115. Ajmal I. Majeed R.N. Malik, H. Idriss, M.A. Nadeem, *RSC Adv.* 4 (2014) 37003.

116. Anwer H, A. Mahmood, J. Lee, K.H. Kim, J.W. Park, A.C. Yip, *Nano Res.* 12 (5) (2019) 955.

117. Ayodhya G. Veerabhadram, *Mater. Today Energy* 9 (2018) 83.

118. Mahmoodi N, M. Arami, *J. Photochem Photobiol. B Biol. 94* (1) (2009) 20.

119. Kamisaka H, T. Adachi, K. Yamashita, *J. Chem. Phys.* 123 (8) (2005) 084704.

120. Ardejani F.D, K. Badi N.Y, Limaee N.M, Mahmoodi M, Arami S.Z, Shafaei A. R, Mirhabibi, *Dyes Pigments* 73 (2) (2007) 178.

121. Pan D, J. Jiao Z, Li Y. Guo C, Feng Y, Liu L, Wang M, Wu M, *ACS Sustain. Chem. Eng.* 3 (10) (2015) 2405.

122. Chinnusamy S, R. Kaur A, Bokare F, Erogbogbo F, *MRS Communications* 8 (1) (2018) 137.

123. Bu X, S. Yang, Y. Bu, P. He, Y. Yang, G. Wang, H. Li, P. Wang, X. Wang, G. Ding, J. Yang, *Chemistry Select* 3 (1) (2018) 201.

124. Badiei A, E. Pourbashir, A.H. Mashhadzadeh M.T, Munir G, Mahmodi P, Zarrintaj P, *J. Water Process Engin.* 38 (2020) 101652.

125. Bi R, R. Zhang J, Shen Y.N, Liu M, He X, You Y, Su Z, Jiang Z, *J. Membr. Sci.* 572 (2019) 504.

126. Zhang L, L. Liu, J. Wang, M. Niu, C. Zhang S, Yu Y, Yang, *J. Nanopart. Res.* 22 (2020) 1.

127. Zhao R, Hu J, Li H, Zhu H, *Sci. China Mater.* 62 (8) (2019) 1177.

128. Zhao X, Wang L, Wu W, Wu Y, Zheng L, Lin S, Weng X, Lin X, *Colloids Surf. B: Biointerfaces* 179 (2019) 17.

129. Rojas-Andrade G. Chata D, Rouholiman J, Liu C, Saltikov S. Chen S, *Nanoscale* 9 (3) (2017) 994.

130. Zeng D, Yu Z, He J, Liu F.X, Xiao Y, Zhang R, Wang D, Bhattacharyya T.T. Y, Tan T, *Sci. Rep.* 6 (1) (2016) 1.

131. Vatanpour V, S.S.M. Khadem M, Masteri-Farahan N, Mosleh M.R, Ganjali A, Badiei E, Pourbashir A.H, Mashhadzadeh M.T, Munir G, Mahmodi P, Zarrintaj C, J. *Water Proc. Engineer.* 38 (2020) 101652.

132. Liu B, J. Xie, H. Ma X, Zhang Y, Pan J, Lv H. Ge, N. Ren, H. Su X, Xie, L. Huang, *Small* 13 (18) (2017) 1601001.

133. Zhang, L. Liu, J. Wang, M. Niu, C. Zhang, S. Yu, Y. Yang, *J. Nanopart. Res*. 22 (2020) 1.

134. Xiao, M, Wang, Z, Lyu, M, Luo, B, Wang, S, Liu, G, Cheng, H.M, Wang, L. *Adv. Mater.* 31(38) (2019)1801369.

135. Shen J, Chen W, G. Lv, Z. Yang, J. Yan, X. Liu, Z. Dai, *Int. J. Hydrog. Energy* 46 (1) (2021) 796

CHAPTER 3
EXPERIMENTAL METHODOLOGY

3.1   Introduction

This chapter presents a thorough overview of the experimental procedures followed to acquire data and fulfil the objectives of this study.

3.2   Chemicals and reagents

All solvents used in this work were of analytical grade and were used without further purification. Dimethylformamide (DMF)(C_3H_7NO), toluene (C_7H_8), ethanol (C_2H_5OH), hydrochloric acid (HCl), acetonitrile(C_2H_3N), N-Methylpyrrolidone (NMP)(C_5H_9NO), nitric acid (HNO_3), peracetic acid (PAA)($C_2H_4O_3$) and dimethyl sulfoxide (DMSO)(C_2H_6OS), disodium phosphate (Na_2HPO_4), potassium dihydrogen phosphate (KH_2PO_4), chloride salts, sodium hydroxide pellets(NaOH), methanol(CH_3OH), p-benzoquinone($C_6H_4O_2$), ethylenediaminetetraacetic acid disodium salt (EDTA-2Na)($C_{10}H_{16}N_2Na_2O_8^{+2}$) and ascorbic acid ($C_6H_8O_6$) were all purchased from Sigma-Aldrich®, South Africa. Silver nitrate ($AgNO_3$) was acquired from Merck®, South Africa. Unless indicated otherwise, all aqueous solutions used in this work were prepared using deionized water obtained from Elix integral-10 water purification system. Citric acid ($C_6H_8O_7$), silica gel for size exclusion chromatography, zinc acetate dehydrate ($Zn(CH_3COO)_2$), ammonium hydroxide (30% NH_3 in H_2O), 3-aminopropyl-triethoxysilane (APTES)($C_9H_{23}NO_3Si$), 1-ethyl-3-3-dimethylaminopropyl carbodiimide (EDC)($C_8H_{17}N_3$) and N-hydroxysuccinimide (NHS)($C_4H_5NO_3$) were acquired from Sigma-Aldrich®, South Africa. Gafone 3100P polyether sulfone (PES) (MW = 58,000 and density of 1.37 g/cm^3) was supplied by Solvay (Brussels, Belgium). Hollytex®-3329 non-woven polyester fabric exhibiting the following characteristics: air permeability 5.1 cfm, bulk porosity 49.57%, thickness 0.13 mm, water holding capacity 24.15 wt% and weight 96.5 g/m^2 was acquired from Kevin Filter Products Co. Farmingdale, New Jersey, USA. Mueller-Hinton (MH) agar and broth, nutrient agar (NA), physiological saline, iodonitrotetrazolium chloride (INT), *salmonella typhimurium* tester strains TA 98 and TA 100, nutrient broth, sodium thiosulphate ($Na_2S_2O_3$), 2,2 diphenyl-1-picrylhyrazyl (DPPH)($C_{18}H_{12}N_5O_6$) glutaraldehyde, ascorbic acid ($C_6H_8O_6$) and

catalase were purchased from Merck®, South Africa. LIVE/DEAD *Bac*light staining kit was purchased from Thermo-Fischer Scientific®, South Africa. The microbial strains tested in this work were all purchased from KWIK-STIK™ a product line of Microbiologics®, South Africa and are summarized in **Table 3.1**.

Table 3.1:   **Microbial strains used in the thesis**

Strain	ATTC number	Characteristics	Ref.
Escherichia coli (*E. coli*)	ATCC 25922	Gram-negative, non-spore forming bacteria that belongs to the *Enterobacteriaceae* family. Selected in this study because it is an indicator of fecal, sewage and animal waste contamination in water.	[1]
Staphylococcus aureus (*S. aureus*)	ATCC 25923	Gram-positive, non-endospore producing bacteria that belongs in the *Staphylococcaceae* family. Chosen for this study because of its known multidrug resistance and its prevalence in the environment.	[2]

Bacillus cereus (*B. cereus*)	ATCC 14579	Gram-positive, spore forming bacteria, belonging to the *Bacillaceae* family. Selected because of its prevalence in the environment and the spores and vegetative cells of *B. cereus are* expected to be found in water.	**[3]**
Pseudomonas aeruginosa (*P. aeruginosa*)	ATCC 27853	Gram-negative bacteria, belonging to the *Pseudomonadaceae* family. Selected due to its ubiquitous occurrence in the environment.	**[4]**

Selected model pollutants

In this study, two classes of model pollutants were studied: dyes and pharmaceuticals. For the dyes, Brilliant black, methyl orange and Rhodamine B were selected, and sulfasalazine were chosen as a model pharmaceutical.

3.3   Characterization of the synthesized GQDs and GQDs-based nanocomposites

3.3.1   Structural analysis of the synthesised nanomaterials

The structural analysis of the prepared nanomaterials was achieved using the following techniques:

- A Zeiss Libra 120 TEM operating at 80 Kv was used to obtain Transmission electron microscope (TEM) micrographs. Before the TEM analysis, GQDs were dispersed in ethanol and sonicated for 3 mins, the resulting solutions were drop-cast on a copper grid and evaporated at room temperature before analysis. The micrographs were processed used iTEM software and the sizes of the nanomaterials estimated using Image J software.

- A Bruker Alpha IR (100 FT-IR) with universal attenuated total reflectance (ATR) in the range 600 - 4500 cm^{-1} was used to obtain FT-IR spectra.

- The morphology of the nanomaterials was determined using both an FEI QUANTA 200 F Scanning Electron Microscope (FESEM) High-resolution Scanning Electron Microscope HR-(SEM) and JEOL STM- IT300 operating in the range of 15-20 kV. Before the SEM measurements, the samples were fixed on a conductive carbon tape and coated with gold (5 nm) using a sputter coater (Balzers Union SCD 030). For the cross-sectional analysis of the fabricated membranes; the membrane samples were immersed in liquid nitrogen for 30 seconds, the liquid nitrogen was used to splinter the membranes before mounting them on the aluminum stubs. All the membrane samples were mounted on the aluminum stubs that were held in place using double-sided tape and subsequently sputtered with gold (5 nm) coating before imaging.

- Confocal Raman spectrometer (514 nm laser) (XploRA™ Plus HORIBA Scientific, France SAS) was used to collect Raman spectral data. To minimise local heating by the laser employed, the power was set at 0.4 mW.

- The elemental composition of the synthesized nanomaterials was verified using energy dispersive X-ray spectroscopy (EDX) using an INCA PENTA FET coupled to VAGA TESCAN at a20 kV accelerating voltage.

- The particle size distribution analysis was carried out using dynamic light scattering (DLS) on a Malvern Zetasizer nanoseries, Nano-ZS90, all samples were dispersed in

distilled water by agitating for 10 mins prior analysis.

- Atomic force microscope (AFM) Alpha300 (Germany) was used to study the surface topography of the synthesised nanomaterials.

- X-ray diffraction (XRD) patterns were collected using a Bruker D8 Discover equipped with a Lynx Eye detector, using Cu-Ka radiation (= 1.5405 A°, nickel filter). The data were collected in the range from 20 = 10° to 100°, scanning at 1° min⁻¹, filter time-constant of 2.5 s per step and a slit width of 6.0 mm. Prior to analysis, the samples were placed on a silicon wafer slide. The X-ray diffraction data were processed using Eva (evaluation curve fitting) software. Debye-Scherrer equation **(Equation 3.1)** was used to determine the crystalline sizes of the nanomaterials.

$$\boldsymbol{d} = \frac{\mathbf{0.9}\,\boldsymbol{\lambda}}{\boldsymbol{\beta}\cos\boldsymbol{\theta}} \qquad\qquad \textbf{(Eq. 3.1)}$$

where d is the mean diameter of a quantum dot in nanometers (nm), λ the wavelength of the X-ray source (1.5405 Å), β the full width at half maximum of the diffraction peak, and θ the angular position of the peak.

- X-ray photoelectron spectroscopy (XPS) analysis was carried out using AXIS Ultra equipped with Al (monochromatic) anode and a charge neutralizer. The following operating parameters were used: the emission was 10 mA, the anode (HT) was 15 kV and the operating pressure below 5 x 10-9 Torr. A hybrid lens was used and resolution to acquire scans was at 160 eV pass energy in slot mode. The centre used for the scans was at 520 eV (width of 1205 eV) with steps at 1 eV and dwell time at 100 ms. The high-resolution scans were acquired using 80 eV pass energy in slot mode. The core level binding energies (BEs) were aligned with respect to the adventitious carbon C1s binding energy of 284.5 eV.

3.3.2 **Photo-physical characterization of the synthesized nanomaterials**

The photo-physical characteristics of the prepared nanomaterials were performed with the following techniques:

- The ground state electronic absorption of the nanomaterials was performed on a Lambda 650 S UV-Vis spectrophotometer in the range of 250-800 nm. **Equation 3.2** was used to calculate the band gap of the nanomaterials.

$$\textbf{Eg} = \frac{\textbf{h c}}{\lambda} \qquad\qquad\qquad\qquad\qquad \textbf{(Eq.3.2)}$$

where Eg is the band gap in eV, h is planks constant (6.626×10^{-34} J.s^{-1}), c is the speed of light (3.00×108 ms^{-1}) and λ is the wavelength in nm.

- The emission spectra were obtained using fluorescence excitation emission matrix (FEEM), GQDs were dispersed in deionized water before analysis.

- Horiba Fluorolog 3 FL3 fitted with xenon lamp was used to obtain the photolumiscence spectra, the GQDs and GQDs-based nanocomposites were dispersed in deionized water before analysis.

- The thermal properties of the materials and the stability of nanomaterials were determined using Thermo-gravimetric analysis (TGA) was performed using a Thermogravimetric analyser (TGA) 5500 Discovery series (TA instruments). The analysis was carried out under N$_2$ flow rate of 120 cm^{-3}/min^{-1}. The samples were weighed and thereafter heated from 50 to 800 $^{\circ}$C at a rate of 10 $^{\circ}$C /min^{-1}.

3.3.3 Electrospun membrane fabrication and characterization

The nanofibrous membranes were fabricated using a NE-8000 High pressure syringe pump (KF Technology) electrospinning set-up as illustrated in **Figure 3.1**.

Figure 3.1: NE-8000 High pressure syringe pump (KF Technology) electrospinning set-up.

The optimized conditions for steady-state electrospinning for fabricating the membranes used in this study are detailed in **Table 3.2**.

Table 3.2: **Optimal electrospinning conditions for the fabricated membranes in this study.**

PES (wt%)	GQDs loading (wt%)	Solvent [NMP] (wt%)	Tip-to-collector Distance (cm)	Flow rate (μL/min^{-1})	Voltage (kV)
	5	69			
26	7.5	66.5	18	333	20
	10	64			

- The wettability of the fabricated membrane was quantified using contact angle goniometer (DSA30 Krűss GmbH, Hamburg, Germany). A drop of deionized water was placed on different parts of the surface of the membrane using a micro-syringe at the room temperature and the recorded average values were reported as the final contact angle values.

- Dead end cells were used to measure pure water flux and rejection rates of the membranes.

- EZ-Fit Manifold attached to the Filtration vacuum pump/laboratory EZ-Stream™ Merck Millipore was used in filtration studies.

3.3.4 Antimicrobial studies

- The model microorganisms were incubated using Memmert incubator supplied by Lasec- SA.
- The absorbance of the bacteria was measured using SPECTROstar Nano.
- The microfuge used was an Eppendorf minispin.
- The live or dead bacterial cells were viewed under Zeiss Laser Scanning Microscope LSM 780.

3.3.5 Techniques used to measure the water quality parameters

- The pH was measured using pH 80+ DHS probe.
- The total organic carbon (TOC) was measured using Teledyne Tekmar TOC Fusion analyser (Ohio, USA).
- A multiparameter meter (YSI Professional Plus) was employed to measure the Total Dissolved Solids (TDS) and Electrical Conductivity (EC).
- The turbidity of the wastewater was analysed using the Orion TM AQUAfast AQ3010 Turbidity Meter.

3.3.6 Techniques used in photodegradation experiments

- For visible light experiments, a customised rectangular stainless-steel photoreactor equipped with LED lights (20 mW) placed around the circumference of the reactor (Glasschem) was employed in the initial stages of this study. The irradiation was measured using a Digital Lux meter and was found to be approximately 80 mW cm^{-2}.
- For photodegradation experiments using UV light, experiments were carried out using the custom-made Lelesil photoreactor manufactured by Lelesil Innovative systems (India) **(Figure 3.2)**.
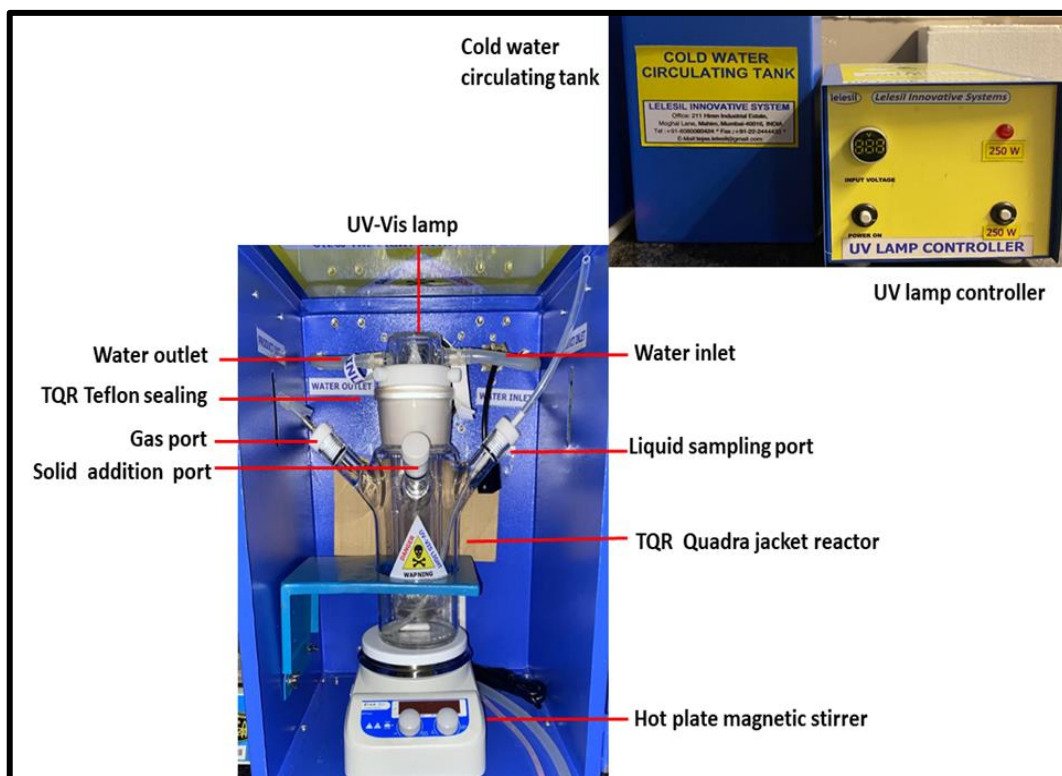
Figure 3.2:   Photoreactor used in the photodegradation of model pollutants.

During photodegradation experiments of pollutants, there is a possibility of various resultant degraded products. The degradation products were analysed using LC-Q-TOF-M Dionex Ultimate 3000 ultrahigh-performance liquid chromatography coupled to a Bruker Impact II Quadrupole time-of-flight (QTOF) tandem mass spectrometer (MS/MS). The analytes were separated on an Acquity BEH C18 column (2.1 x 100 mm, 1.7 µm) using an Agilent 1200 binary pump system.

3.3.7   LC-Q-TOF-MS analysis conditions

The mobile phase was made up of solvent A (water containing 40 mM ammonium acetate with 2.5% acetonitrile at pH 7.8 adjusted with ammonia solution 2.5%) and solvent B (acetonitrile). The gradient used was as follows: after injection; isocratic conditions (100%) mobile phase A for 0.1 mins then linear gradient to 95% mobile phase over 2 mins followed by a gradient up to 55% mobile phase A in 8 mins and isocratic conditions of 55% mobile phase A for a further 0.4 mins before returning at 100% in 0.1 mins followed by a reconditioning step at 100% mobile phase A for 5 mins. The flow rate was 0.40 mL min^{-1} at 50°C.

3.3.8   Detection conditions

MS tuning was conducted in negative electrospray ionisation (ESI) mode, and this was done by infusing the solution of each analyte separately (concentration = 10 µg mL^{-1}), flow rate of 10 µL min $^{-1}$ composed of solvent A and B (50: 50, v/v; 0.40 mL min $^{-1}$) using a T-connector. Quantitative analysis was performed using tandem MS in selected reaction monitoring (SRM) mode alternating two or three transition reactions for each compound with different dwell times.

3.3.9   Data processing software

Except in the case of photomicrographs obtained from TEM, AFM and SEM and unless otherwise stated, all other data presented in this study were plotted and processed using Origin®8 software.

3.4   Synthesis of GQDs and GQDs-based nanocomposites

3.4.1   Synthesis of GQDs

The GQDs utilized in this study were obtained using a simple single-step process of citric acid pyrolysis previously reported by Dong et al. [5] with minor modifications (**Figure 3.3**). In a flask, 5 g of citric acid was heated for 30 mins at 240°C. The mixture was allowed to melt until it changed color from colorless to light yellow, then dark orange. Deionized water was used to dissolve the melted solution. To get pure GQDs, the resultant solution was purified using silica gel chromatography with 0.01 M NaOH as the developing phase (**Appendix A1**).
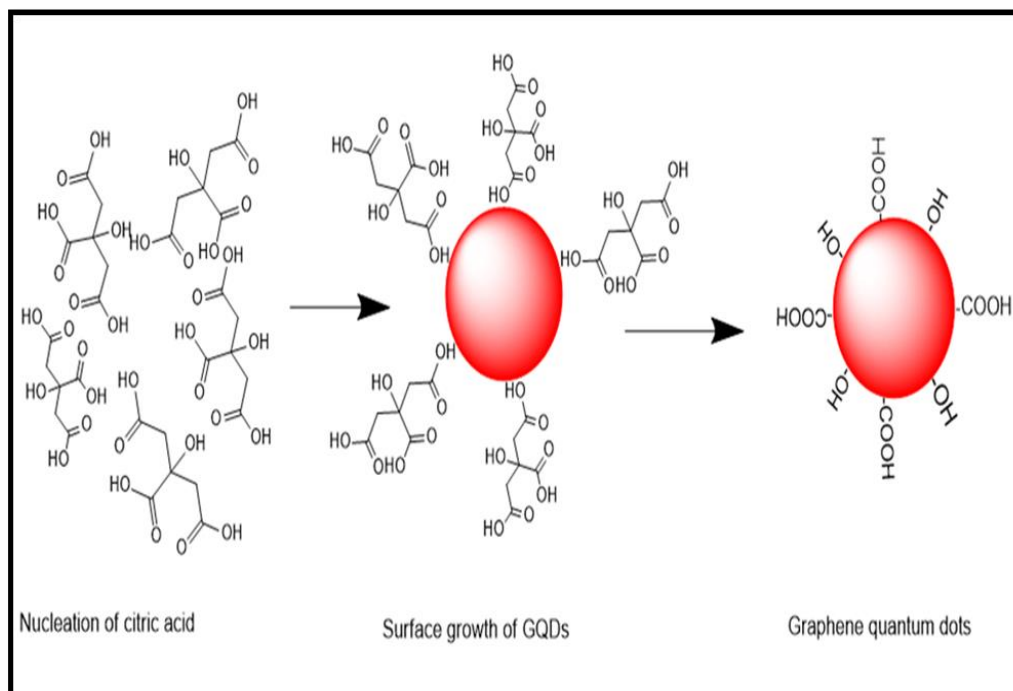
Figure 3.3:   Schematic illustration of GQDs synthesized using citric acid pyrolysis.

3.4.2   **Synthesis of ZnO nanoparticles**

3.4.2.1   ZnO rods (ZnO-R)

With some modifications, ZnO rods were synthesized using previously published protocols. [6]. Zinc acetate (2.195 g) was dissolved in distilled water (200 mL). The clear solution was continuously stirred for 30 mins prior to the addition of sodium hydroxide (1 M; 50 mL) to adjust the pH. A white precipitate was formed while the sample was heated to $90^{\circ}C$ under continous stirring for 1 hour.

3.4.2.2   ZnO flakes (ZnO-F)

In the case of ZnO flakes, a previously reported method was adopted [7]. Zinc acetate (2.195 g) was also dissolved in distilled water (200 mL) and the resulting clear solution stirred continuously for 30 mins. Ammonium hydroxide (30-33%) was used to adjust the pH, increasing the temperature to $90^{\circ}C$ (under continuous stirring for 1 hour) resulted in white precipitate forming.

In both synthesis methods, the resulting solutions were sonicated for 1 hour and left overnight for complete gelation and hydrolysis. The resultant ZnO nanoparticles were rinsed with water and EtOH, centrifuged and kept in an oven at 80°C overnight to dry.

3.5   Amino functionalization of ZnO nanoparticles

The functionalization of the synthesized ZnO nanoparticles was accomplished as per the published approach [8], with minor changes that are briefly explained. Anhydrous EtOH and toluene were used to wash samples 10 g of the ZnO nanoparticles. The washed ZnO nanoparticles were subsequently added to a mixture of DMF (12 mL) and toluene (8 mL) and mixed thoroughly. After suspending the mixture in an ultrasonic bath for 10 mins, APTES (1 mL) was added drop by drop with a syringe. The resulting mixture was stirred at room temperature for 24 hours under argon gas flow, centrifuged and rinsed with copious volumes of EtOH, and the amino functionalized ZnO nanoparticles were produced.

3.6   Conjugation of GQDs to ZnO nanoparticles

GQDs were covalently bonded to the resultant amino functionalized ZnO NPs. Tshangana et al. [8] presented an EDC/NHS coupling chemistry approach for conjugating amino functionalized ZnO nanoparticles to GQDs. The –COOH- groups of GQDs were activated in this method by dissolving GQDs (10 mg) in weak NaOH (10 mL) and subsequently adding EDC (2 mL, 1.2 mM). Under argon gas flow, the mixtures were stirred for 48 hours (room temperature). Amino functionalized ZnO nanoparticles (5 mg) were suspended in NHS (2 mL, 1 mM) before being introduced to activate GQDs.

To facilitate the linking of the GQDs to the ZnO nanoparticles, the solution was stirred for further 12 hours under argon gas flow at room temperature. With dropwise addition of EtOH, the products were precipitated and rinsed with copious volumes of EtOH (**Figure 3.4**). To remove GQDs that did not adhere to the ZnO nanoparticles, size exclusion chromatography (eluting solvent; pH 9) was used. Throughout the thesis, the conjugates of amino functionalized ZnO nanoparticles conjugated to GQD are represented as *ZnO-R-GQDs and ZnO-F-GQDs* for the rods and flakes nanohybrids respectively.
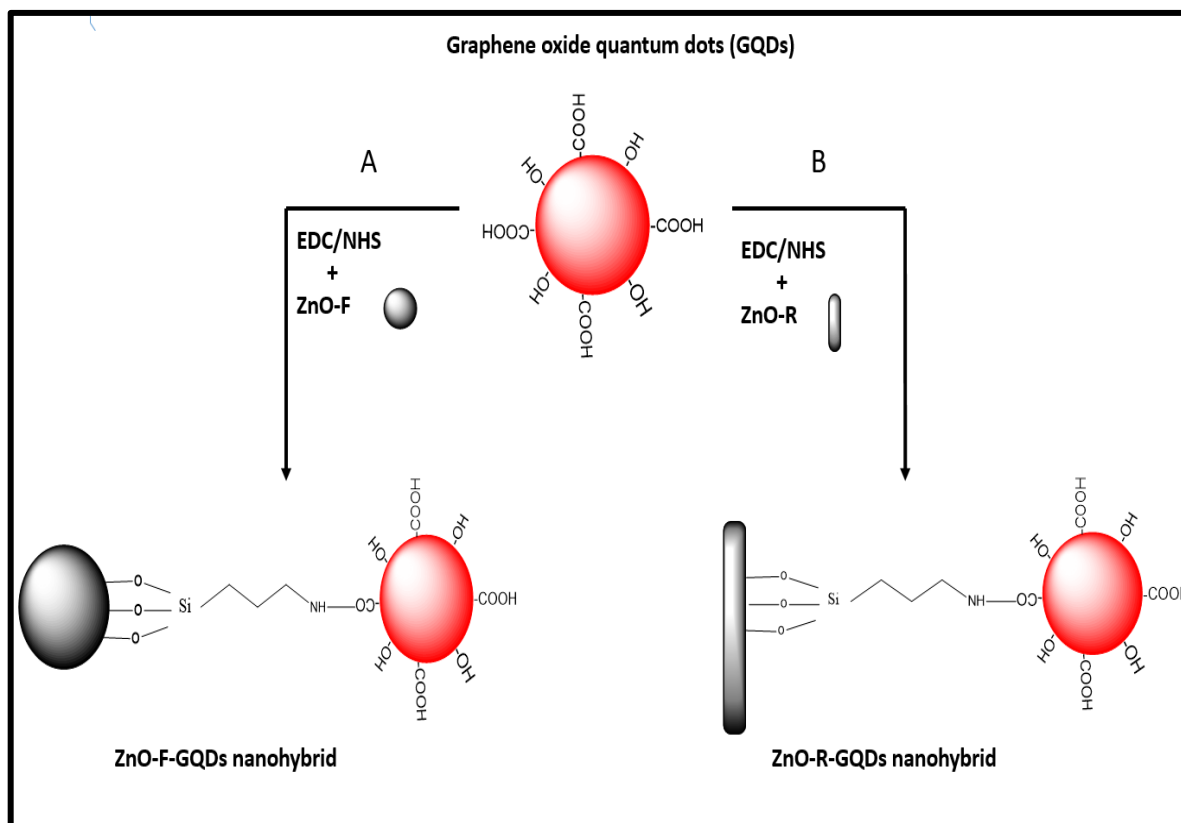
Figure 3.4: Schematic illustration of the covalent linkage of the GQDs to (a) ZnO-F and (b) ZnO-R.

3.7 Photodegradation experiments for dye degradation

Two sets of experiments were conducted, namely: a) the use of BB as a model organic pollutant. To this end, 1 mg of GQDs were added to the BB dye (50 mL); and b) wastewater sample collected from a treatment plant that was spiked with 10 ppm of the BB dye and 1 mg of GQDs added to 50 mL solution (15 mL BB dye solution + 35 mL wastewater). The degradation was carried out using white LED strips (20 mW) which were mounted around the inner walls of a customized reactor. The set-up was complete with a magnetic stirrer and beaker. Furthermore, the entire set-up was covered with an aluminium foil to shield it from external light. Prior to irradiation, the solutions (mixtures of GQDs and synthetic water; GQDs and spiked wastewater) were stirred in the dark for 30 mins, after which the LED lights were switched on. Aliquots of the solutions (3 mL) were over the course of 180 mins extracted using a disposable syringe at 30 mins intervals. The aliquots were filtered using a 0.45 µm PVDF syringe filter. The absorbance of the filtrate was measured to track changes in the BB dye concentrations.

3.7.1 Conjugates of ZnO/GQDs as photocatalysts

Similarly, to the GQDs photocatalytic experiments, to investigate ZnO/GQDs nanohybrids as photocatalysts; ZnO/GQDs nanohybrids (1 mg) were added to the of the organic pollutant model dye (BB) (10 ppm, 50 mL). The solutions were stirred in the dark for 30 mins to allow adsorption and desorption equilibrium after which the LED lights were switched on. The absorbance of the solutions was measured at 30 mins intervals. The photolysis studies were carried out as described above without adding the photocatalysts.

3.7.2 Photodegradation using PAA and GQDs

In the first experiment (a) 0.05 g /L of GQDs were added to the BB dye (95 mL, 10 ppm) which was inoculated with 5 mL of *E. coli* (IBRC-M11018; ATCC 25922). Prior to conducting the photocatalytic experiments, the solutions (mixtures of GQDs and BB dye solutions inoculated with *E. coli*) were mixed by stirring for 30 mins in the dark, before the LED lights were turned on. The reaction was initiated and timed as soon as different concentration of PAA (0.5, 1.0 and 1.5 mM) were added into the solution. In the subsequent experiments (b) and (c), 0.10 g/ L and 0.1.5 g/ L of GQDs were added respectively with the other conditions maintained the same. Aliquots of the solution (4 mL) were sampled using a disposable syringe at 30 mins intervals (for a total of 150 mins) and immediately injected into a 1.0 mL phosphate buffer solution (0.20 mol L^{-1}, pH 8) to quench the reaction. Thereafter, the aliquots were filtered using a 0.45 µm PVDF filter and analysed within 24 hours. Variations in the concentrations of the BB dye under illumination were assessed by measuring the absorbance of the filtrate using the UV-Vis spectrophotometer.

3.8 Photodegradation experiments of pharmaceuticals (SSZ)

3.8.1 Photodegradation using PAA and GQDs

The experiments for the degradation of SSZ were conducted using a custom-made photoreactor from Lelesil Innovative systems (India) at room temperature (**Figure 3.2**). To investigate the effect of initial SSZ concentrations on the photodegradation process; three different concentrations of SSZ were used (200, 300 and 500 µM). The pH of each of the SSZ solutions were maintained at pH 5 by adding (1:1) of 1 M HCl/NaOH. A series of experiments were

carried out with real wastewater samples collected at a wastewater treatment plant and with synthetic water. Both real wastewater and synthetic water samples were spiked with SSZ (10 ppm) to ensure detection with analytical instruments. For the photodegradation experiments, 0.15 mL of GQDs were added to the SSZ solutions (10 ppm). Prior to conducting the photodegradation experiments the solutions (mixture of GQDs and SSZ) were mixed by stirring for 30 mins in the dark, before turning the UV light on. The reaction was initiated and timed as soon as the PAA at different concentrations (0.5, 1.0 and 1.5 mM) were added. Aliquots of the solution (4 mL) were sampled using a disposable syringe at different time intervals (0, 30, 60, 90, 120 and 150 mins) and were immediately injected into 1.0 mL phosphate buffer solution (0.20 mol L^{-1}, pH 8) to quench the reaction. The aliquots were further filtered using a 0.45 µm PVDF syringe filter. Variations in the concentrations of the pharmaceuticals under illumination were measured using UV.

The percentage degradation of all model pollutants used in this study were calculated using the following **Equation 3.3**.

Degradation efficiency $\% = \frac{C_i - C_t}{C_i}$ **x 100** (Eq. 3.3)

where C_i and C_t represent the initial concentration of the model pollutant at times 0 and t, respectively.

3.9   Kinetic studies

Kinetic rate constants (k) and half-live $t_{\frac{1}{2}}$ were calculated using the integrated Langmuir-Hinshelwood (L-H) model using **Equation 3.4**.

$$\ln\left(\frac{C_t}{C_i}\right) = -k_1 t$$ (Eq. 3.4)

where t is the irradiation time and k_1 is the apparent rate constant of the photodegradation. When $\ln\left(\frac{C_t}{C_i}\right)$ is plotted versus irradiation time, a straight line is obtained, and the slope of the straight-line yields k_1, the apparent rate constant. The determination of coefficient (R^2) values was used to determine goodness of model fitness.

The half lifetimes were calculated using **Equation 3.5**.

$$t_{\frac{1}{2}} = \frac{0.693}{k'}$$
(Eq.3.5)

3.9.1 Radical scavenging experiments

To investigate reactive species generated in the photodegradation process, scavenging experiments were conducted. The same experimental procedures as previously described were carried out with the introduction of different radical scavengers at the beginning of the experiments. The radical scavengers used in the experiments had the same concentration of 60 mM. Silver nitrate, ethylenediaminetetraacetic acid disodium (EDTA-2Na), methanol and benzoquinone were used as scavengers for electrons (e^-), holes (h^+), hydroxyl radicals ($\bullet OH$) and superoxide ($\bullet O_2^-$) respectively [10]. Thereafter, the aliquots were filtered using a 0.45 µm PVDF filter and analysed using UV-Vis spectrophotometer.

3.9.2 Photocatalytic reusability experiments

Reusability experiments were carried out to determine the stability and recyclability of the GQDs photocatalyst. This is key parameter for practical applications. The reused GQDs (from the first cycle) were separated, recovered by centrifugation and dried in an oven and tested under the same experimental conditions as described above for subsequent cycles.

3.10 Toxicity studies

3.10.1 Ames assay

The toxicity studies were conducted to ensure that the resultants photodegradation by-products were not harmful. The mutagenic and genotoxicity potential of the reaction by-products formed during the SSZ degradation were evaluated using a *Salmonella typhirium* microsome assay as described by Mortelmans and Zeiger [11]. In the Ames assay, two *Salmonella typhirium* tester strains TA 98 and TA 100 without metabolic activation were used. The bacterial strains (100 µL) were incubated in Oxoid No.2 broth (20 mL) at 37 °C on a rotary shaker for 12 hours. The cultured *Salmonella typhirium* tester strains (100 µL) were added to 100 µL of the aliquots

collected at 0, 30, 60, 90, 120 and 150 mins with 500 µL of phosphate buffer and top agar (2 mL) made up of biotin histidine (0.5 mM). This top agar mixture was added to cover the surface of agar plate and incubated for 2 days at 37 °C (**Figure 3.5**). The positive and negative controls in the work were 2-nitroflurene for the TA 98 and nitrofurantoin for TA 100, respectively
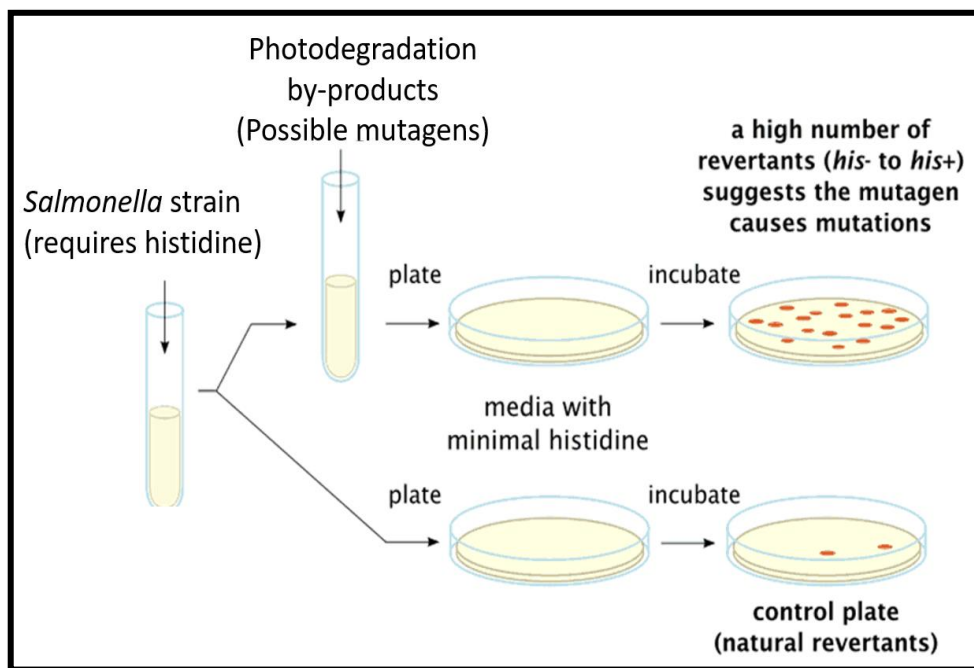
Figure 3.5:   Pictorial representation of the Ames assay principle.

3.11   Antimicrobial studies

3.11.1   Antimicrobial activity of the ZnO-F-GQDs and ZnO-R-GQDs nanohybrids

The effects of ZnO-F-GQDs and ZnO-R-GQDs on the selected bacterial strains were evaluated using the Kirby-Baüer method as previously described by Vijayakumar et al. [12]. A single colony of each of the selected bacterial strains was inoculated using Mueller-Hinton broth. Following this, each of the bacterial strains were cultured for 24 hours at 37 °C with light shaking until mid-log phase (OD$_{600}$ = 0.6). On Mueller-Hinton agar plates, the antibacterial efficacy of the four samples (ZnO-R, ZnO-F, ZnO-R-GQDs, or ZnO-F-GQDs) (4 mg/mL) was evaluated against bacterial suspensions (grown in bacterial lawn) with turbidity corresponding to 0.5 MacFarland standard. Blank sterile discs were positioned on the inoculated plate's surface, then 20 µL of the four samples were added, and the plates subsequently incubated for 24 hours at

37°C. Zones of inhibition (distance from disc circumference in mm) were measured for each disc in areas where bacterial growth was not seen. To ensure reproducibility, the experiments were repeated three times, with the average values presented. Before plating on a NA plate from the broth culture, 1 mL of each bacterial strain was diluted 50 times in sterile deionized water. The plates were then incubated at 37°C for 24 hours to allow for bacterial growth before counting the colonies.

Antimicrobial activity of GQDs-PES-electrospun nanofibrous membranes (ENMs)

Mueller-Hinton agar was used to cultivate the bacteria, which was prepared as per manufacturer's instructions. The strains were grown to mid-log phase ($OD_{600} = 0.6$) at 37°C with mild shaking for 24 hours after being inoculated into new Mueller-Hinton broth. The disc diffusion method was used to investigate the antibacterial activity of GQDs-PES ENMs, as described by Nthunya et al. [13]. On Mueller Hinton agar plates, bacterial lawns were grown from bacterial suspensions with turbidity comparable to 0.5 MacFarland standard. The GQDs-PES ENMs was soaked in NA for 10 mins after being cut into the same size discs (dimensions 0.5 cm x 0.5 cm) with a paper puncher (**Appendix A2**). After that, the wet GQD-PES ENMs discs were positioned on the surface of the inoculated plates and incubated for 24 hours at 37°C. For each bacterial strain, the experiment was repeated three times. The minimum inhibitory concentrations (MIC) of the bacterial strains were determined using the broth micro-dilution assay, which was modified slightly from Eloff's method [14]. The MIC is the lowest concentration of GQDs-PES ENMs needed to inhibit bacteria from growing. Grinding the GQDs-PES ENMs and suspending them in water resulted in ENM suspensions. The GQDs-PES ENMs solutions were serially diluted at varied dilution factors of 2, 4, 8, 16, and 32 times their starting concentrations. Each of the three bacterial cultures was added (50 μL) to each well. After that, the 96-well plates were incubated at 37°C overnight. Bacterial viability was demonstrated by adding freshly prepared iodo-nitro-tetrazolium chloride (INT); 40 mL of 0.2 mg/mL of INT was added to each well and incubated for 30 mins at the same temperature. The presence of viable bacterial cells was indicated by the colour turning purple in the wells.

3.11.2 **Antimicrobial activity of GQDs-PAA**

The antimicrobial efficiency of the GQDs/PAA system was evaluated against *S. aureus* (ATCC 25923). The experiments were conducted using the serial dilution protocol as reported by Elisha

et al. [15]. Stock solutions of the GQDs, PAA and GQDs/PAA (1 mL) were used to serially dilute 96-well plates containing an overnight culture of *S. aureus*. The plates were incubated overnight at 37°C stained with iodo-nitro-tetrazolium chloride (INT), all experiments were performed in triplicates.

3.11.3 Antimicrobial activity of GQDs-PAA in raw municipal wastewater

The experiments were conducted as described for the photodegradation of the pharmaceutical except that raw municipal wastewater was used instead of cultured bacteria. Further difference is that after quenching the PAA, 20 µL of the aliquots collected at different time intervals 0, 30, 60, 90, 120 and 150 secs were plated on NA plates, incubated at 37°C and the number of colonies were counted. The procedure for antimicrobial activity was adopted from Flores et al. [16]. Bacterial culture was grown in a nutrient broth and the bacterial inoculums incubated at 37°C for 24 hours. The solution was prepared from culture that had reached the beginning of the stationary phase of growth and was diluted to 1/100 using physiological saline. The prepared *E. coli* culture was added to the solution (at varying PAA concentrations and GQDs loadings). After 30 mins intervals the samples were collected and immediately mixed with 200 µL of sodium thiosulphate and 500 µL catalase to prevent PAA from further reaction. 20 µL of the solution was plated using spread-plating technique and incubated at 37°C for 24 hours. The initial concentrations of *E. coli* were always around 10^5 CFU mL^{-1} (colony forming units) at t = 0. In this study the estimate number of viable bacteria were obtained using colony-forming unit (CFU) values that were calculated using **Equation 3.6**:

$$\mathbf{CFU\ (mL)} = \frac{\textbf{Volume plated x dilution factor}}{\textbf{Total colonies}}$$

(Eq. 3.6)

3.11.4 SEM characterization of microbes

Bacterial cells in the logarithmic phase were treated with PAA, GQDs and GQDs/PAA and irradiated for a total of 10 mins. Bacteria were collected at 1 min intervals and centrifuged at 5000 rpm for 3 mins and washed with sterile saline three times. The bacteria were fixed with glutaraldehyde overnight at 4°C and dehydrated with increasing treatment of 50%, 70%, 85%, 90% and 100% EtOH for 10 mins each and gold sputter coated and observed by SEM.

3.11.5 **Cell viability**

The viability of *E. coli* and *S. aureus* cells were examined using LIVE/DEAD Baclight staining kit. The kit consists of dyes SYTO® 9 and propidium iodide that are used as a function of the membrane integrity of the cell. *E. coli* or *S. aureus* cells with membrane cells that are compromised and are considered to be dead or dying will stain red while the healthy and live *E. coli* or *S. aureus* cells (with intact cell membranes) will stain green. The viability experiments were carried out as per manufacturer's guidelines. Equal amount of SYTO® 9 and propidium iodide (50 µL) were mixed in a microfuge tube. From this mixture 3 µL was added to the *E. coli* or *S. aureus* suspension treated with GQDs/PAA. The microfuge tubes were incubated for 30 mins in the dark at room temperature. After this 5 µL of the stained *E. coli* or *S. aureus* cells was pipetted onto a microscope slide and covered with a coverslip and the cells were imaged using a Zeiss Laser Scanning Microscope LSM 780.

3.12 Membrane fabrication, characterization, and performance indicators

3.12.1 **Fabrication of PES/GQDs mixed matrix membranes (MMM)**

The PES/GQDs membranes were prepared *via* phase inversion method. Pristine membranes (M0) were prepared without the incorporation of GQDs. M1 is for the GQDs incorporated membrane, 5 wt% (*w/w*) concentration of GQDs as nanofillers in the PES matrix (**Appendix A3**). The membrane casting solutions were obtained by dissolving PES powder (20 wt%) and corresponding 5 wt% (*w/w*) of GQDs in NMP solvent which was vigorously mixed using a mechanical stirrer overnight at room temperature. Before casting, the homogenous polymer solution was kept overnight to eliminate bubbles before casting. Prior to casting, the surface of the non-woven fabric was wetted with NMP solvent.

Subsequently, the polymer solution was spread thin on the non-woven fabric supported on a glass substrate using a casting knife (air gap set at 150 µm). Thereafter, the membranes were submerged in a coagulation bath filled with deionized water for 15 mins at room temperature. The exchange between the solvent (NMP) and non-solvent (deionized water) resulted in the precipitation of the polymeric membrane off the glass. The resultant membranes were kept in deionized water (which was changed regularly to prevent the growth of bacteria) and dried before use. The composition of the membranes utilized in this work is shown in **Table 3.3**.

Table 3.3: **Composition of the fabricated pristine and PES/GQDs membranes**

Membrane	PES (wt %)	GQDs loading (wt %)	NMP
M0	20	0	80
M1	20	5	75

3.12.2   Surface charge and hydrophilicity

Sessile drop observation was used to determine the PES/GQDs membranes' surface contact angle both with and without the GQDs. Contact angle (CA) tests were conducted to measure the hydrophilicity. A drop of deionized water was deposited on the surface of the membrane using a micro-syringe at room temperature. The recorded average values were reported as the final contact angle values.

3.12.3   Zeta potential

The zeta potential (ζ) of the fabricated membrane surfaces was measured using Anton Paar SurPASS Electrokinetic (Graz, Austria) analyzer. Membranes were mounted symmetrically opposite each other on sample holders, which were held in place with double-sided tape. To accurately measure the streaming potential, the membranes' surface was flushed with electrolyte solution. All measurements were carried at 300 mBar with potassium chloride solution (10 mM) as electrolyte at a pH range of 6-9. The zeta potentials (ζ) were determined using the Helmholtz-Smoluchowski equation **(Equation 3.7)**.

$$\zeta = \frac{\Delta V.\eta\delta}{\Delta P.\varepsilon} \qquad\qquad \textbf{(Eq. 3.7)}$$

where ΔV is the measured streaming potential (V), η is the electrolyte viscosity (Pa.s), δ is the electrolyte conductivity (S/m), ΔP is the applied pressure (Pa), and ε is the permittivity of water.

3.12.4 **Porosity**

The porosity of the membrane was determined using the gravimetric method. The membranes were cut and measured. Before weighing, excess water droplets were removed by dabbing with a paper towel and the membranes were incubated overnight at $45^{\circ}C$. The membranes were weighed again the following day. Several samples were weighed to obtain an average value. The total porosity of each of the membranes was calculated using (ε %) of the membranes were determined using **Equation 3.8**.

$$\varepsilon\,(\%) \ = \frac{W_w - W_d}{P_{w\,A\,\delta}} \qquad\qquad \textbf{(Eq. 3.8)}$$

where ε is the porosity of membrane, W_w is the weight (g) of the wet membrane, W_d is the weight (g) of the dry membrane, ρ_w is the density of pure water (g/cm^3), A is the membrane area (cm^2) and δ is the thickness of membrane (cm).

3.12.5 **Permeation and water retention tests**

Permeation tests experiments were conducted using a cell fixed in dead-end mode (**Figure 3.6**). The membranes were cut into circles with a surface area of 3.73 cm^2 and the membranes were loaded as depicted in **Figure 3.6**. DI water was used as the feed solution and the external pressure was varied from 1- 6 bar, for a minute long at each applied pressure. The net water flow was obtained from correlating information of the membrane surface area, volume of effluent and the time taken using **Equation 3.9.**

$$J_W = \frac{V}{A\,x\,T} \qquad\qquad \textbf{(Eq. 3.9)}$$

where V is the volume of permeate (L), A is the effective membrane area (m^2) and T is the permeation time (h).
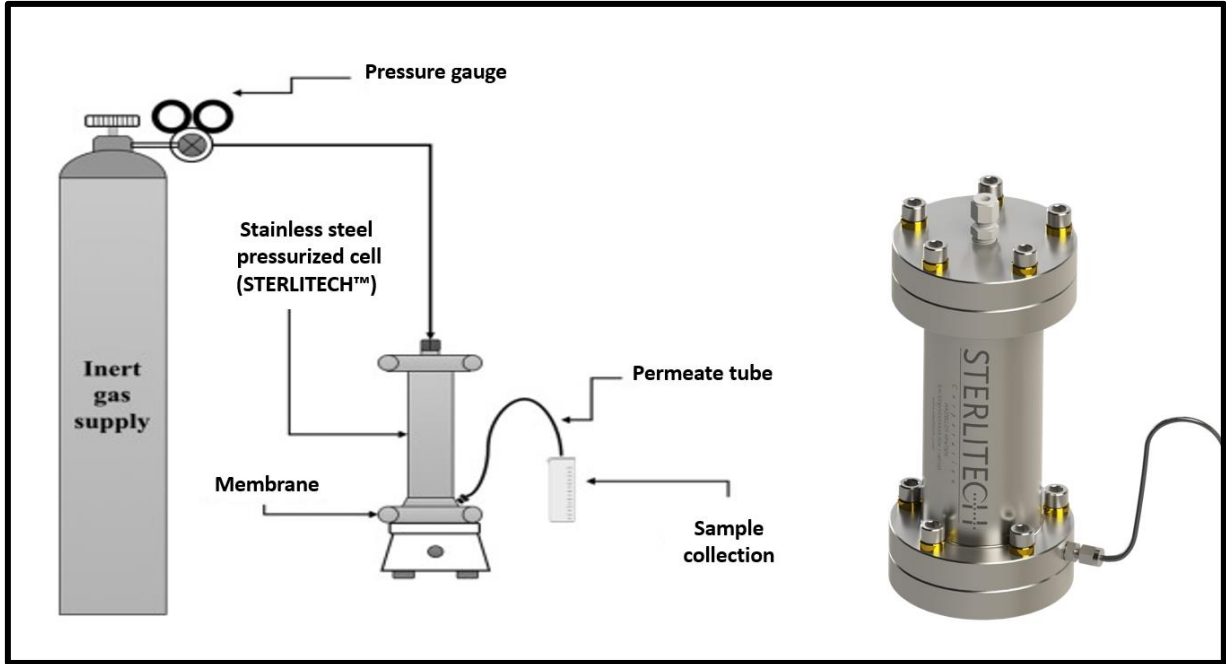
Figure 3.6:   Dead-end cell used in this study.

Water retention capabilities tests of the synthesized membranes were carried out by soaking 0.1 g of the membrane in DI water for a period of 24 hours. The weight of the wet membrane was calculated. The membranes were then dried in the oven for 10 hours and the weight of the dry membrane was calculated. Based on these calculations the water retention capabilities were obtained using **Equation 3.10.**

$$\textbf{Water retention capacity} = \frac{\textbf{wet weight} - \textbf{dry weight}}{\textbf{wet weight}} \textbf{ x 100} \qquad \textbf{(Eq. 3.10)}$$

3.12.6   Rejection studies

Rejection capabilities tests of the membranes were performed using the synthesized membrane samples and 0.01 M of different salt solutions made up of Na_2SO_4, NaCl and $MgSO_4$ salts. The operational pressure in these experiments was 6 bar. Membrane solute rejection R (%) was determined using **Equation 3.11**.

$$\textbf{R (\%)} = \left(1 - \frac{C_p}{C_f}\right) \textbf{x 100} \qquad \textbf{(Eq. 3.11)}$$

where C_p and C_f are solute concentrations in the permeate and feed solution.

3.12.7 Dye removal tests

M0 and M1 membranes were employed for the investigation of dye removal using dye solutions of methyl orange (MO) and Rhodamine B (RhB) (15 ppm). The operational pressure in the experiments was 6 bar. For each membrane, the test time was 60 secs. UV-vis spectroscopy measurements were performed in the determination of the concentration of the dye that permeated through the membranes M0 and M1.

3.12.8 Antibacterial testing of PES/GQDs membranes against *E. coli*

E. coli (ATCC 25922) was used to determine the antibacterial efficacy of the PES/GQDs using a shake flask method as well as colony counting method. The *E. coli* cells were cultured overnight 37 $^{\circ}$C in nutrient broth. To assess the antibacterial activity, the PES/GQDs membrane (area of 2.5 cm × 2.5 cm) was immersed into flask containing 20 mL of sterile 0.9% saline which was sonicated for 20 mins. The flask was inoculated with 500 μL of bacterial suspension of *E. coli* ($1\text{-}5 \times 10^7$ CFU/mL). After inoculation the flasks were incubated for 2.5 hours at 37 $^{\circ}$C on a rotary shaker to allow the continuous stirring. The bacterial suspension (1 mL) was drawn at time 0 and after 2.5 hours and spread on NA plates using the spread plating technique. Subsequently, the plates were incubated overnight at 37 $^{\circ}$C and the number of colonies enumerated. The reduction in the number of viable *E. coli* cells was calculated using the following **Equation 3.12**.

$$\% \text{ reduction} \frac{\text{no.of colonies at } T_0 - \text{no.of colonies } T_t}{\text{no.of colonies at } T_0} \text{ x } 100 \qquad \textbf{(Eq.3.12)}$$

where T_0 is time at 0 hours and T_t is time at t hour.

After the shake flask method, the PES/GQDs membranes were rinsed once with saline and the bacteria on the membrane surface was visualized using FESEM.

3.12.9   **Antibacterial testing of real wastewater effluent**

After being subjected to real wastewater effluent, the bacterial content of the fabricated PES/GQDs and the commercial membrane (Film Tec™NF270) (used for comparative purposes), was evaluated by incubating the membranes after use for 24 hours at 37 $^\circ$C in LB to obtain total bacterial count.

3.13   **Sampling site and sample collection**

3.13.1   **Wastewater sampling site**

The wastewater effluent samples were obtained from a WWTP in South Africa. Wastewater in the WWTPs goes through different treatment stages including a primary clarifier, an aeration tank, a secondary clarifier and finally a disinfection unit where bacteria are removed. For the purpose of this study three sampling points were selected: namely before the primary clarifier, after secondary clarifier and after the disinfection. Keeping this in mind, the schematic representation of the WWTP showing the selected sampling points (denoted as **sampling point (1), (2)** and **(3)**) is depicted in **Figure 3.7**.

3.13.2   **Sample collection**

Clean 1 litre glass bottles were used for collecting the samples. The sampling bottles were completely rinsed with tap water after being cleaned with detergent. Thereafter, the sampling bottles were soaked at room temperature and for 24 hours in aqua regia (1:3 vol by volume (v/v) ratio of HNO_3: HCl) and rinsed before use. The sample bottles were filled to the brim with wastewater with no head space to reduce any possible contamination that may occur as a result of the trapped air. Upon arrival at the laboratory, the water samples were stored at 4 °C in a refrigerator.
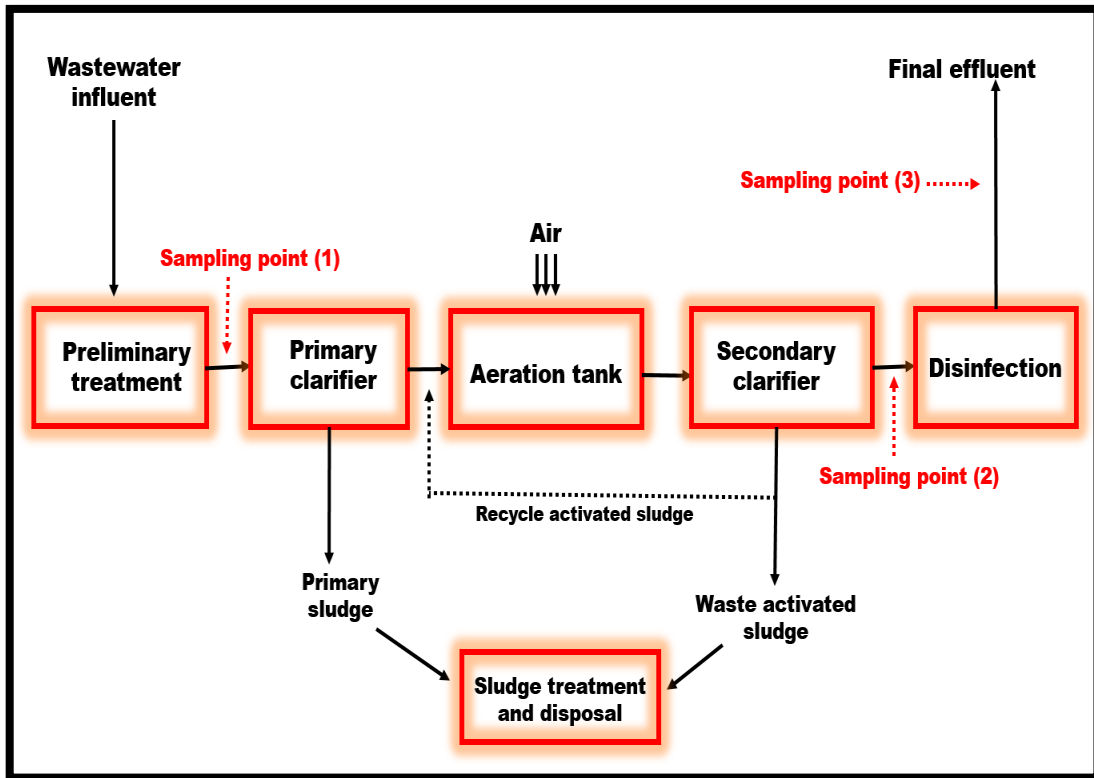
Figure 3.7: Schematic illustration of the WWTP including the sampling points.

3.13.3 **Change in wastewater quality**

The quality of the wastewater samples was assessed at the different sampling points by measuring the following parameters: electrical conductivity (EC), total organic carbon (TOC), total dissolved solids (TDS), pH and the turbidity. A multiparameter meter (YSI Professional Plus) was used to measure the pH, TDS and EC. Orion TM AQUAfast AQ3010 Turbidity Meter was used to analyze the turbidity, while the TOC was measured using a Teledyne Tekmar TOC Fusion.

The removal rate of the water quality parameters was calculated using **Equation 3.13**.

$$R = \frac{1-C_P}{C_f} \text{ x } 100 \text{ %} \tag{Eq. 3.13}$$

where C_p is the treated water quality parameter and C_f is the feed water quality parameter.

References

1. Kaper J. B, Nataro, J. P, Mobley, H. L, *Nature Rev. Microbiol.* 2(2) (2004) 123.

2. Mainous A. G., Hueston, W. J., Everett, C. J, Diaz, V. A, *The Annals Fam. Med*, 4(2) (2006) 132.

3. Bottone E. J, *Clin. Microbiol. Rev.* 23(2) (2010) 382.

4. Klockgether J, Tümmler, *Research* (2007) 6.

5. Dong Y, Shoa J, Chen C, Li H, Wang R, Chi Y, Chen G, *Carbon* 50(2020)4738.

6. Rani S., Suri, P., Shishodia, P. K, Mehra, R. M. *Sol. Energy. Mater. Sol. Cells*, 92(12) (2008)1639.

7. Zhao B, Chen, H. *Mater. Lett*. 61(27) (2007) 4890.

8. Tshangana Nyokong, T, *Spectrochimica Acta Part A: Mol. Biomol. Spectro*. 151 (2015) 397.

9. Kumar K. V., Porkodi, K., Rocha, F, *Catal. Commun*. 9(1) (2008)82.

10. Chu Y. M, Bach, Q. V. *Appl. Nanosci*. (2020)1.

11. Mortelmans K., Zeiger, E. *Mutagenesis*, 455(1-2) (2000) 29.

12. Vijayakumar S., Krishnakumar, C., Arulmozhi, P., Mahadevan, S, Parameswari, N *Microbial. Pathogen*. 116 (2018) 44.

13. Nthunya L. N., Masheane, M. L., Malinga, S. P., Barnard, T. G., Nxumalo, E. N., Mamba, B. B.,Mhlanga, S. D. *RSC Advances*, 6(98)(2016)95936.

14. Eloff J. N. *Planta Medica*, 64(08) (1998)711.

15. Elisha I. L., Botha, F. S., McGaw, L. J, Eloff, J. N. (2017). BMC *Comp. Altern. Med.* 17(1), 1.

16. Flores M. J., Lescano, M. R., Brandi, R. J., Cassano, A. E, Labas, M. D. *Water Sci. Technol.* 69(2)(2007) 3.

CHAPTER 4

SYNTHESIS AND CHARACTERIZATION OF GRAPHENE OXIDE QUANTUM DOTS

4.1   Introduction

GQDs are the backbone of this study and were synthesized, characterised, and applied in all the experiments throughout this study (unless otherwise stated). To avoid repetition in successive chapters of the thesis, this chapter focusses on the synthesis and characterisation of GQDs. The current chapter will be cross-referenced accordingly in subsequent chapters.

4.2   Synthesis of GQDs

The pristine GQDs employed in this thesis were produced *via* the pyrolysis of citric acid. Citric acid was deployed as a carbon precursor which subsequently aromatized and underwent pyrolysis. The incomplete carbonization of the citric acid results in GQDs, whereas if the citric acid is allowed to completely carbonize, the resultant material would be graphene oxide (GO) [1]. When citric acid is heated to its melting point, the hydronium ion formed after the decomposition of citric acid serves as a catalyst in the subsequent decomposition reaction stages. Aromatization and the synthesis of aromatic clusters are achieved through cycloaddition and aldol condensation. Burst nucleation occurs when the concentration of aromatic clusters reaches a crucial supersaturation point, resulting in the creation of GQDs, as reported by Naik et al. [2].

4.3   Characterization of GQDs

4.3.1   Identification of functional groups of GQDs using FT-IR spectroscopy

The chemical structure of the GQDs was ascertained by using FT-IR analysis (**Figure 4.1**). The spectrum corresponds with the structure of GQDs owing to the oxygenated functional moieties on their surfaces i.e epoxy, hydroxyl and carbonyl groups. The spectrum of the GQDs is characterized by a broad peak appearing between 3100 cm^{-1}-3600 cm^{-1}, which is ascribed to the O-H stretching vibrations. A stretching vibration of C-H is evidenced by the

peak appearing at 2962 cm^{-1} and stretching vibration of the C-O appearing in the range of 1273 cm^{-1}. The vibration of C-O suggests that the GQDs contain some incompletely carbonized citric acid [3]. The peaks at 1710 cm^{-1} and 1621 cm^{-1} correspond to the stretching vibrations of the C=O of carboxylic and/or carbonyl group. The CH$_2$ rocking vibration at 823 cm^{-1} is ascribed to the precursor and at times it may be very weak as a result of the drastic decrease in H concentration during formation of GQDs [4]. The FT-IR spectrum presented in this work is consistent with previously reported work [5, 6].
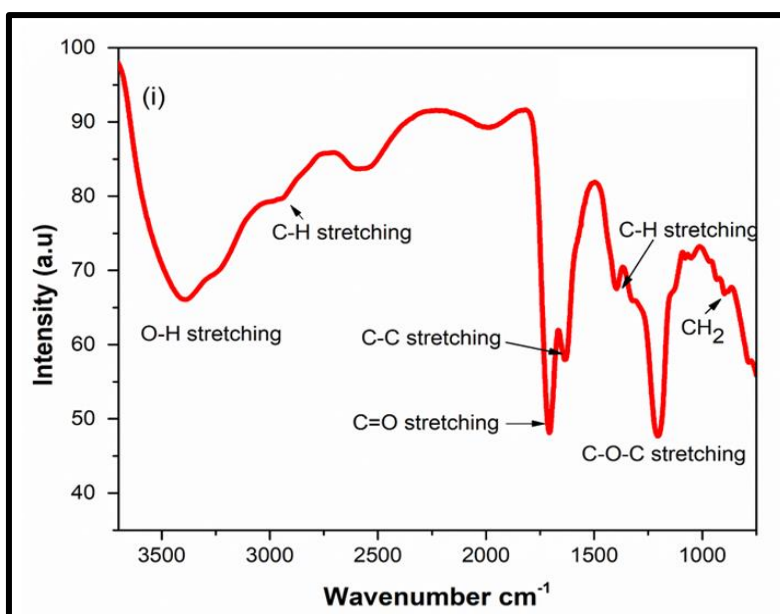
Figure 4.1:   FT-IR spectrum of the as-synthesized GQDs.

4.3.2   **Elemental analysis of GQDs using Energy dispersive X-ray spectroscopy (EDX)**

EDX was employed to qualitatively determine the chemical elemental composition of the GQDs as described in **Chapter 3**. As shown in **Figure 4.2**, the results of the synthesized GQDs indicate that GQDs are mainly composed of C and O. The results were consistent with the expected elemental composition of GQDs and the EDX spectrum data corresponds to structure of GQDs.
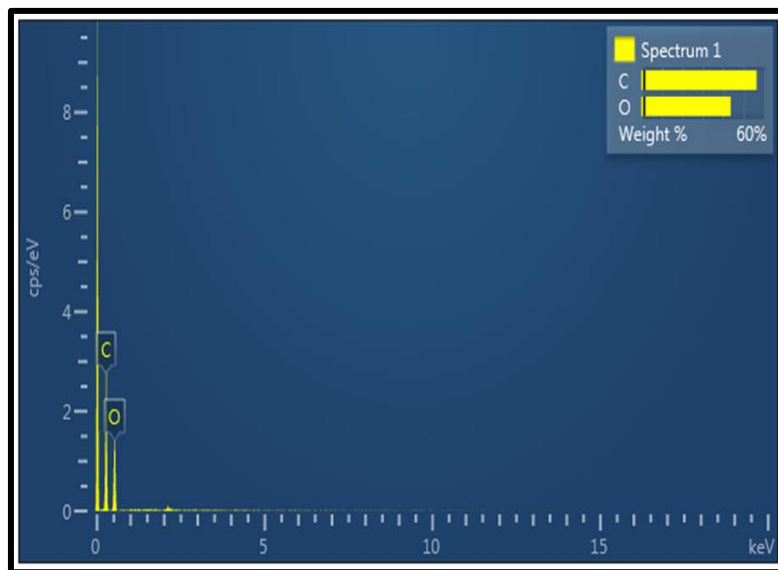
Figure 4.2: EDX spectrum showing the chemical elemental composition of the synthesized GQDs.

4.3.3 Crystalline phases analysis of GQDs using X-ray diffraction (XRD) analysis

The crystallinity of the GQDs as described in **Chapter 3** was assessed using XRD. The XRD pattern of the GQDs is shown in **Figure 4.3**. A prominent peak observed at $2\theta = 27$, is ascribed to (002) Bragg's reflection and an interlaying spacing of 0.36 nm [7, 8]. The noticeable peak indicates that the carbonization of citric acid produced GQDs with a more compact interlayer spacing than pristine graphene. In agreement with previously reported findings [9, 10], the synthesized GQDs were structurally similar to graphite. The slight humps around 35 and 48 degrees in the XRD spectra are as a result of the amorphous nature of the GQDs. The average crystallite sizes of the GQDs as discussed in **Chapter 3** and literature were measured using the Debye-Scherrer equation [11]. The sizes of the GQDs were found to be 3.1 nm and the broadness of the XRD peak at 27° also reflects that the crystallite sizes are small.
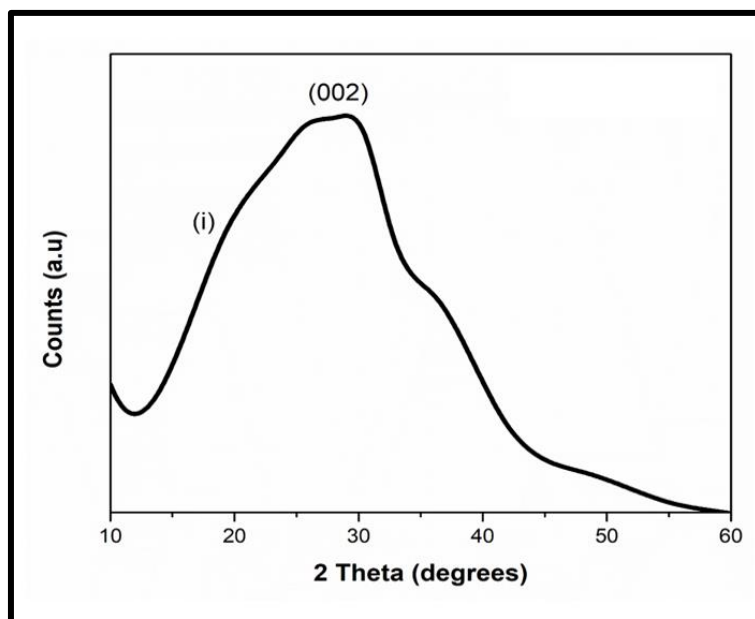
Figure 4.3:   XRD pattern of the as-synthesized GQDs.

4.3.4   Determination of crystallinity, chemical structure, and phase of GQDs with Raman spectroscopy analysis

The Raman spectrum of the GQDs shows two significant peaks (**Figure 4.4**) at 1362 cm^{-1} and 1611 cm^{-1} that resemble the disordered "D" band and a graphic (crystalline) "G" band, respectively. The "D" and G bands are characteristic of the GQDs peaks [12]. The "D" band arises from the disorder present on the surface of GQDs. The surface states (i.e., sp^3 C-C, sp^3 C-O and sp^2 C=O) result in the broadening of "D" band. The "G" band on the other hand is a characteristic of carbon materials possessing the sp^2 C=C bonds. The "G" band is ascribed to stretching of sp^2 C=C bond and arises due to vibration of E_{2g} phonon at Γ-point [13, 14]. The extent of sp^2/sp^3 hybridization of the carbon atoms is expressed using the ratio of the intensity of the "D" and G bands (I_D/I_G ratio). An I_D/I_G value of 0.845 was obtained, which confirms the highly crystallized structures of the GQDs.
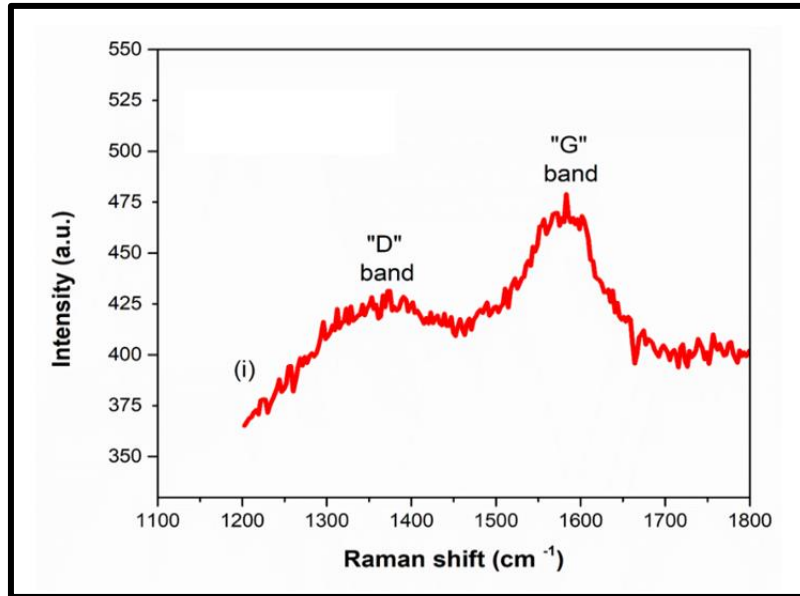
Figure 4.4: XRD pattern of the as-synthesized GQDs.

4.3.5 Morphology analysis and size measurement of GQDs using transmission electron microscopy (TEM) technique

The size and morphology of the GQDs were analysed using TEM as described in **Chapter 3**. The obtained TEM micrograph of the GQDs is depicted in **Figure 4.5a**. The micrograph shows that the GQDs were mostly spherical with no aggregation. The average particle sizes (**Figure 4.5b**) acquired from TEM were estimated using Image J software by plotting the particle size distribution histogram and the size was estimated to be 6.3 nm.
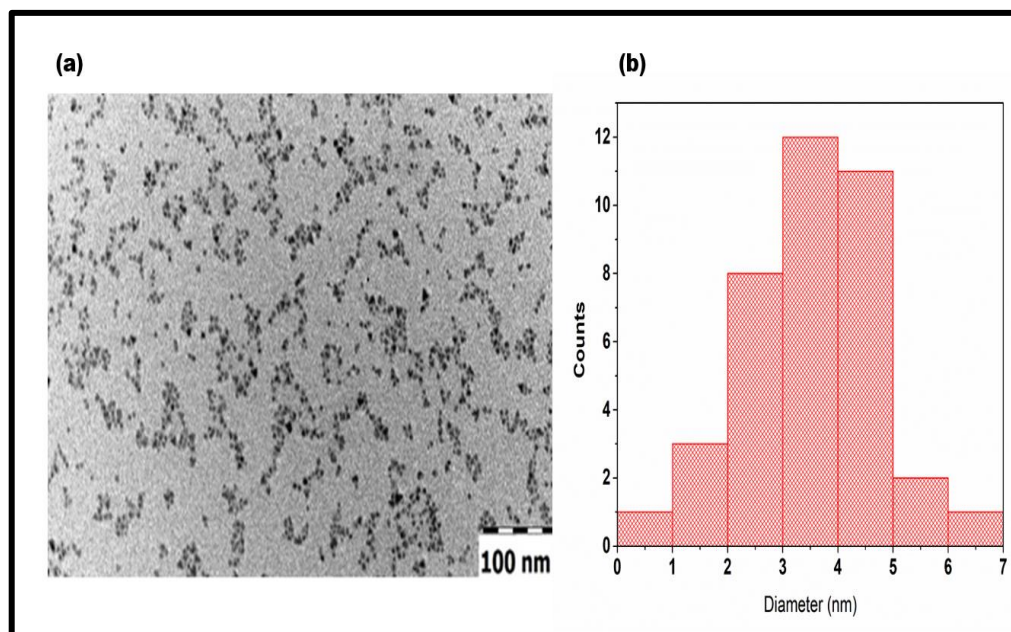
Figure 4.5:   (a) TEM micrograph of GQDs and (b) the particle size distribution histogram.

4.3.6   **Absorption and emission properties**

UV-vis and Fluorescence Excitation Emission Matrix (FEEM) techniques were used to measure the absorption and emission of GQDs respectively, as described in **Chapter 3**. **Figure 4.6** shows the absorption and emission spectra of the GQDs. An intense absorption peak in the UV region at 351 nm is ascribed to the $\pi \rightarrow \pi*$ transition of sp^2 C=C bonds. A shoulder peak in the visible region at 480 nm is ascribed to the n $\rightarrow \pi*$ transition of surface functional groups [15]. The emission peak at 480 nm at an optimal excitation wavelength of 390 nm indicates that the GQDs have fluorescence characteristics. The findings are consistent with prior findings on optical properties for GQDs [16].
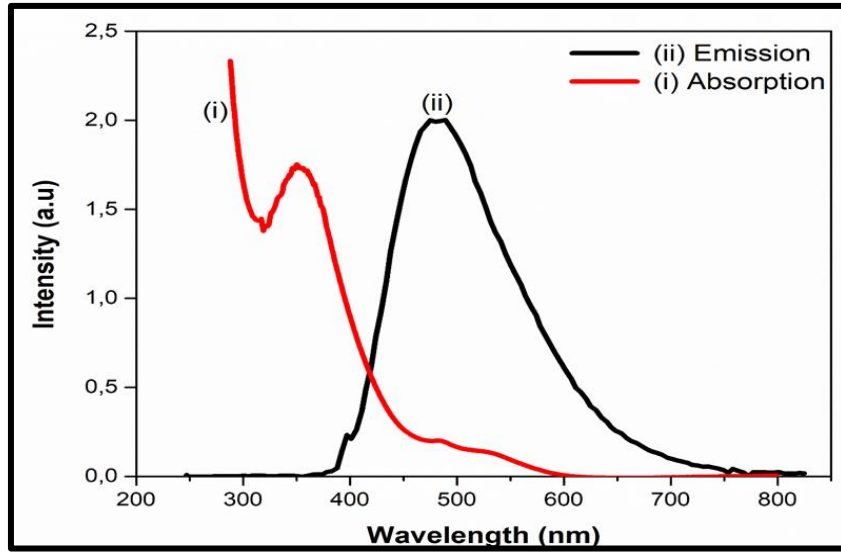
Figure 4.6: Optical properties showing (i) absorption and (ii) emission spectra of GQDs.

The topographic evaluation of the GQDs was verified by AFM. **Figure 4.7** shows a 2D view of the GQDs. The topographic height of the GQDs was found to be ~ 1.2 nm, inferring that the GQDs are composed of more than one layer of graphene, which is in accordance with values previously reported in literature [17].
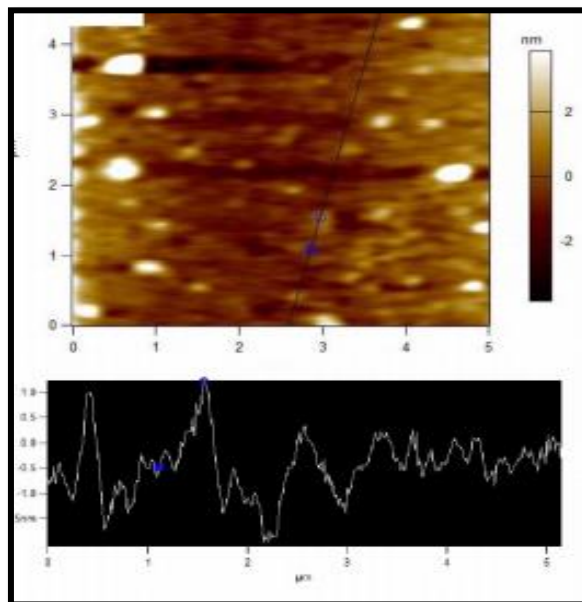
Figure 4.7: Surface topography of the pristine GQDs, insert shows the height profile.

4.3.7   **Zeta potential and dynamic light scattering (DLS) measurements**

The zeta potential measurements were used to evaluate the surface charge which will also give an indication of the stability of the synthesized GQDs in aqueous media. At pH 7 the pristine GQDs had high negative zeta charge of −2.34 mV. The negatively charged surface was as a result of the carboxyl and hydroxyl groups on the surface of the GQDs [18]. The sizes of the GQDs were further verified using DLS technique (**Figure 4.8**), from the data it was observed that the size of the pristine GQDs was < 10 nm which corresponds to the size distribution range obtained from the TEM results.
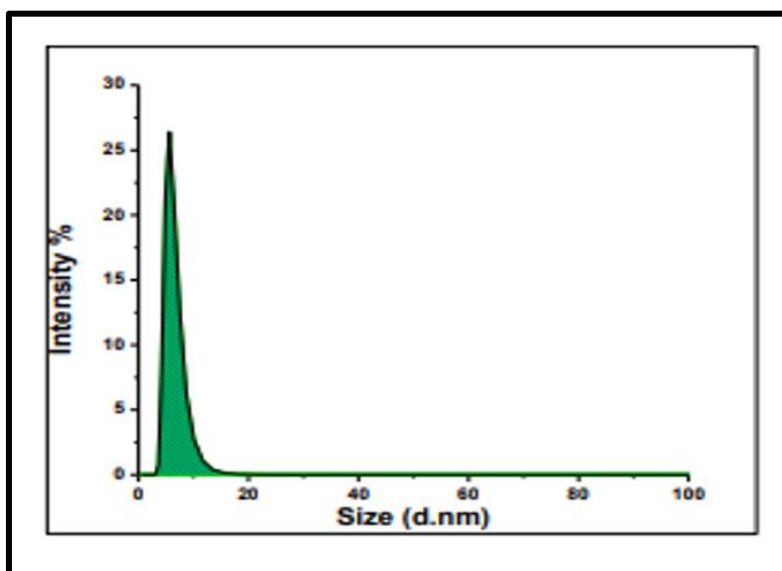
Figure 4.8:   DLS plot showing size of the synthesized GQDs.

4.3.8   **Thermogravimetric analysis**

The thermal properties of GQDs were studied using TGA. Even though in the applications specific for this study, significantly high temperatures were not required. It is satisfying to know that even at above $600\ ^{\circ}C$, only 10% weight loss percentage of the GQDs was observed (**Figure 4.9**). This signifies that the synthesized GQDs were stable and that even at high temperatures no graphene relaxation occurred which is often attributed for the weight loss percentage [19].
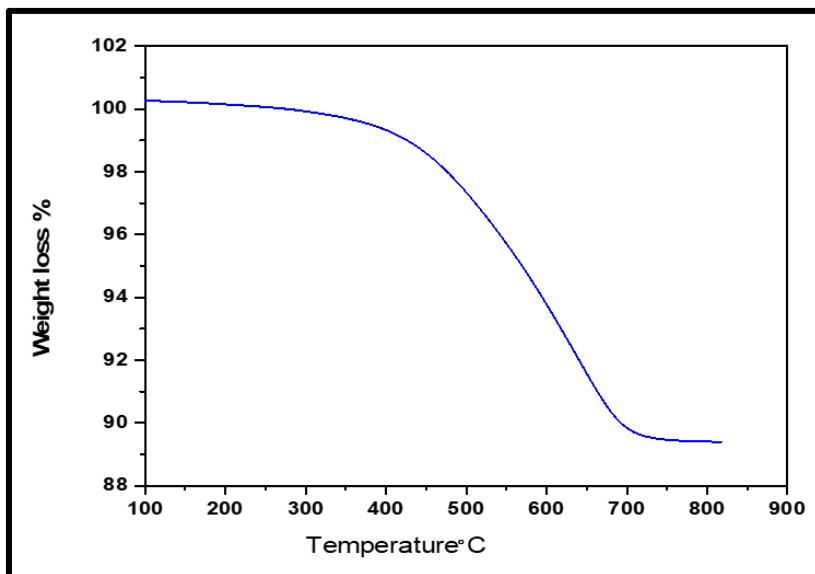
Figure 4.9:   TGA profile of the synthesized GQDs.

4.3.9   **X-ray photoelectron spectroscopy (XPS)**

The structural composition of the GQDs were further probed using XPS, for the full scan (presented in **Figure 4.10**) the signals for C1s, $O1_S$ and the Na auger peak were observed at 286.3, 531 and 495 eV respectively. The emergence of the Na auger peak at 495 eV was due to the NaOH that was used during the synthesis procedure.
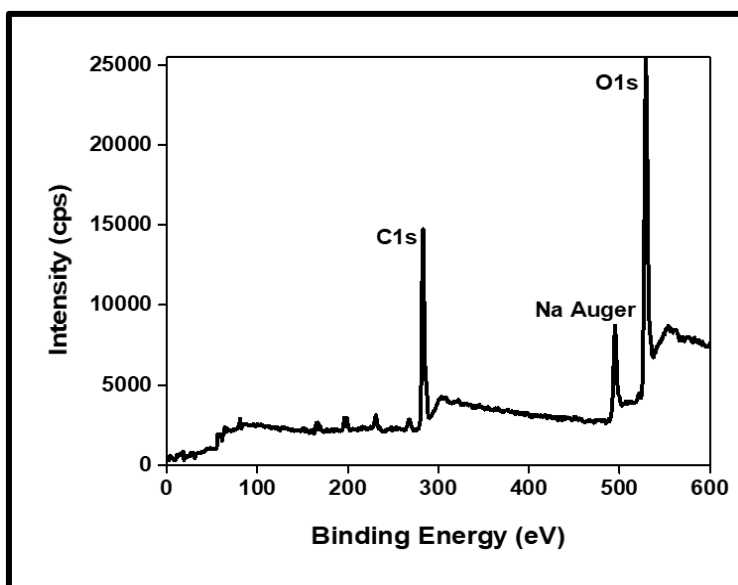
Figure 4.10:   XPS wide scan survey of the synthesized GQDs.

The C1s peak of the GQDs was further deconvoluted into three carbons species that are centred at 285.1, 287.5 and 288.4, these chemically distinct carbons are due to the sp^3 carbon (C-C, C-O), the sp^2 carbon (C=C) as well as the oxidized carbon (C=O) respectively (**Figure 4.11**).
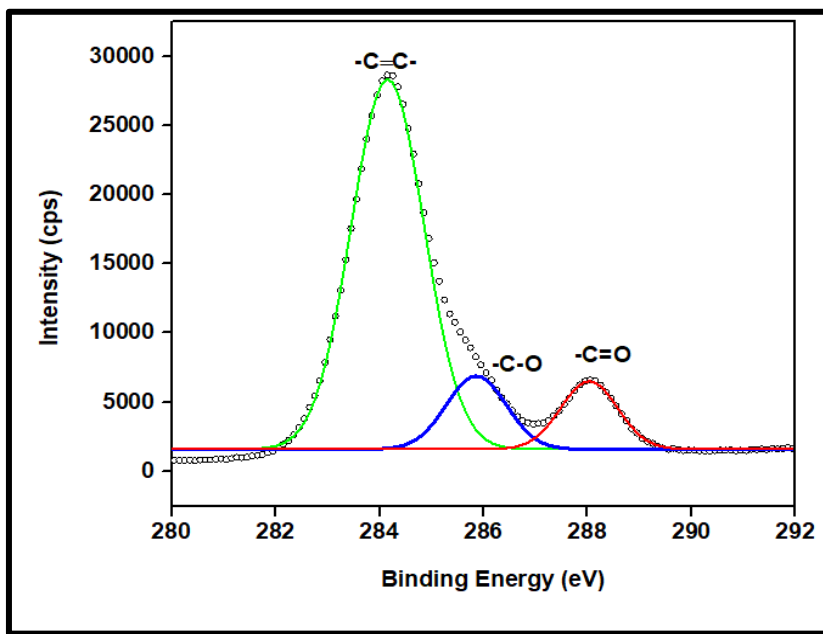
Figure 4.11: XPS spectra of the GQDs.

4.4   Conclusion

The synthesis and structural characterization of the GQDs were presented in this chapter. The results ascertained that pure GQDs were synthesized and were in line with the expected results. The morphology of the GQDs were spherical and monodispersed, the reported average size of the synthesized GQDs was 6.3 nm. The photophysical and photochemical properties of the GQDs were determined and the GQDs' stability was proven stable in a wide range of temperatures.

References

1. Dong Y., Shoa J., Chen C., Li H, Wang R., Chi Y., Chen G, *Carbon* 50(2012)4738.

2. Naik J.P, Sutradhar P, Saha M, *J. Nano. Chem.* 7(2017)85.

3. Zhu S., Zhang, J, Qiao, C, Tang, S, Li, Y., Yuan, W., Li, B., Tian, L., Liu, F., Hu, R., Gao, H *Chem. Comm.* 47(24) (2011) 6858.

4. Tang L., Ji R., Cao X., Lin J., Jiang H., Li X, Teng K., Luk C., Zeng S., Hao J., Lau S, *ACS Nano.* 6 (6) (2012) 5110.

5. Manna S, Bhattacharya S, Sengupta S, Das P, *J. Clean. Prod.* 203(2018) 83.

6. Štengl V, Bakardjieva S, Henych J, Lang K, Kormunda M, *Carbon* 63 (2013)537.

7. Zhang M, Bai, L, Shang, W, Xie, W, Ma, H, Fu, Y, Fang, D, Sun, H, Fan, L, Han, M, Liu *J. Mater. Chem.* 22(15) (2012) 7461.

8. Tetsuka H, R. Asahi, A. Nagoya *Adv. Mater.* 24(2012) 5333.

9. Hashemzadeh N, Hasanzadeh, M, Shadjou, N, Eivazi-Ziaei, J, Khoubnasabjafari, M, Jouyban, A. *J. Pharm. Anal.* 6(4) (2016)235.

10. Puvvada N, Kumar, B.P, Konar, S, Kalita, H, Mandal, M, Pathak, A, *Sci. Techn Adv. Mater.* 3 (4) (2012) 212.

11. Sapra S, Sarma, D.D, *Phys. Rev. B* 69(12) (2004)125304.

12. Chhabra V.A, Kaur, R, Rajesh, C, Deep, A. In 2018 Conference on Emerging Devices and Smart Systems (ICEDSS) (149-151). IEEE.

13. Sobon G, Sotor, J, Jagiello, Kozinski, R, Zdrojek, Holdynski, M, Paletko, P. Boguslawski, J. Lipinska, L. Abramski, K. M, *Opt. Express* 20 (2012) 19463.

14. Kudin K.N, Ozbas, B, Schniepp, H.C, Prud'Homme, R.K, Aksay, I.A, Car, R. (2008) *Nano letters* 8(1) (2008) 36.

15. Qu D, Zheng, M, Du, P, Zhou, Y, Zhang, L, Li, D, Tan, H, Zhao, Z, Xie, Z, Sun, Z (2013) *Nanoscale*, 5(24) (2013)12272.

16. Kumar D.K, Suazo-Davila, D, García-Torres, D, Cook, N.P, Ivaturi, A, Hsu, M.H, Martí, A.A, Cabrera, C.R, Chen, B, Bennett, N, Upadhyaya, H.M, *Electrochimica Acta,* 305(2019) 278.

17. Zhu X, Xiao X, Zuo X, Liang Y, *Nan J. Part. Syst. Charact.*31 (2014) 801.

18. Wu C, Wang C, Han T, Zhou X, Guo S, Zhang J, *Adv. Health. Mater.* 2(2013)1613.

19. Nurunnabi K. Zehedina, M. Nafiujjaman, L. Dong, L. Yong-kyu *ACS. Appl. Mater. Interfaces.* 5(2013) 8246.

20. Luo Z, Qi, G, Chen, K, Zou, M, Yuwen, L, Zhang, X, Huang, W, Wang, L (2016) *Adv. Funct. Mater*. 26(16 (2016) 2739.

21. Zheng K. Q. Ananthanarayanan, P. Luo, P. Chen P, *Small* 11(2015)1620.

CHAPTER 5

PHOTOCATALYTIC ACTIVITY OF GRAPHENE OXIDE QUANTUM DOTS IN THE PHOTODEGRADATION OF DYES IN REAL WASTEWATER

5.1 Introduction

AOPs are increasingly being applied in environmental remediation [1]. The issue however is; the focus of majority of the work documented on the use of AOPs in wastewater treatment has been on the degradation and reduction of the toxicity of organic dyes using model solutions [2-4]. While these studies have demonstrated the efficiency of the photocatalysts, the effect of parameters like pH values, the actual composition of the water, ion concentration, competing ions and the presence of organic and inorganic substances are rarely taken into account. The results obtained when using either distilled or demineralized water matrices are therefore not reflective of the photodegradation efficiency of the photocatalysts [5, 6]. In most instances, the results obtained when using either distilled or demineralized water matrices are rather too optimistic and do not paint an accurate picture of what would occur in real water [7]. It is anticipated that the performance of the photocatalyst will differ significantly when tested in real water compared to when the photocatalyst is evaluated in model solutions in the laboratory. Keeping this in mind, this chapter investigates the photocatalytic activity of GQDs in the discoloration and photodegradation of real wastewater spiked with Brilliant black (BB) dye. The quantitative photocatalytic performance of the GQDs was addressed in terms of kinetics, effect of catalyst loading and different water matrices. Scavenging experiments were also carried out to understand the degradation process during photolysis/photocatalysis. A mechanistic pathway was proposed for the photodegradation of BB dye in synthetic water and real wastewater.

5.2 Experimental procedure

5.2.1 Preparation of GQDs

GQDs were prepared using the pyrolysis of citric acid as described in **Chapters 3** and **4**.

5.2.2 Sampling site and collection

An image of the effluent from the WWTP where the wastewater was sampled from depicted in **Appendix A1.** It is alleged that the specific WWTP is responsible for the pollution of the nearby river resulting in the displeasing colour as can be seen in the picture [8]. The sampling approach used to collect the wastewater is detailed in **Chapter 3**. For the purpose of this chapter, the selected sampling point was before the primary clarifier and water quality parameters of the primary effluent are summarized in **Table 5.1**.

Table 5.1:   **Water quality parameters of the collected wastewater.**

Properties	Values
pH	6.9 ± 0.250
Turbidity (NTU)	110 ± 3.26
TOC (mg C.L^{-1})	22.30 ± 0.032
Electrical conductivity (μS cm^{-1})	743 ± 5.31
DO	10.9 ± 0.054

5.2.3 Photocatalytic activity evaluation

The photocatalytic performance of the GQDs was evaluated by measuring the rate of degradation of the model organic pollutant and colourant (in synthetic water and real wastewater samples. The photodegradation procedure is described in **Chapter 3**.

5.2.4 Scavenging experiments

The reactive species generated in the photodegradation experiments were investigated by carrying radical scavenging experiments as described in **Chapter 3**.

5.3   Results and discussion

5.3.1   Characterization of the GQDs

Comprehensive characterization of the GQDs were carried out using FT-IR, Raman, AFM, TEM, XRD, XPS, TGA, EDX and PL techniques as described in **Chapter 4**.

5.3.2   **GQDs as a photocatalyst**

A great photocatalyst is measured by its ability to adsorb reactants while simultaneously absorbing photon energy. The band gap of the photocatalyst as well as the redox potential of the absorbates influence the transfer of the photoinduced electrons to the adsorbed reactants. GQDs meet this criterion and have the added benefit of being able to operate as electron donors or acceptors, which helps to regulate the photogenerated charge and improve the photocatalytic activity of GQDs and GQD-based nanocomposites [9]. The role of GQDs in facilitating the adsorption of organic contaminants is credited with improving the photocatalytic efficiency of GQD nanocomposites. GQDs also have a wide surface area, variable surface chemistry, and great carrier mobility [10], as well as basal planes that allow for increased contaminant adsorption. In the absence and presence of light, GQDs have the ability to scavenge and generate reaction oxygen species (ROS) [11]. In the literature, there have been numerous proposed photocatalytic degradation mechanisms of GQDs [12].

When the electrons in the VB of GQDs are photoexcited, the photogenerated holes and electrons migrate to the active sites on the GQDs, as shown in **Figure 5.1**. Due to GQDs' excellent electron acceptor and donor characteristics, several things can happen: (i) charge carriers can be directly transferred onto adsorbed pollutants, initiating the photodegradation process; (ii) charge carriers can react with water and dissolved oxygen to form hydroxyl and superoxide radicals, respectively; or (iii) GQDs can transfer energy transfer energy to $3O_2$ and generate singlet oxygen $1O_2$, acting as a photosensitizer [9,12].
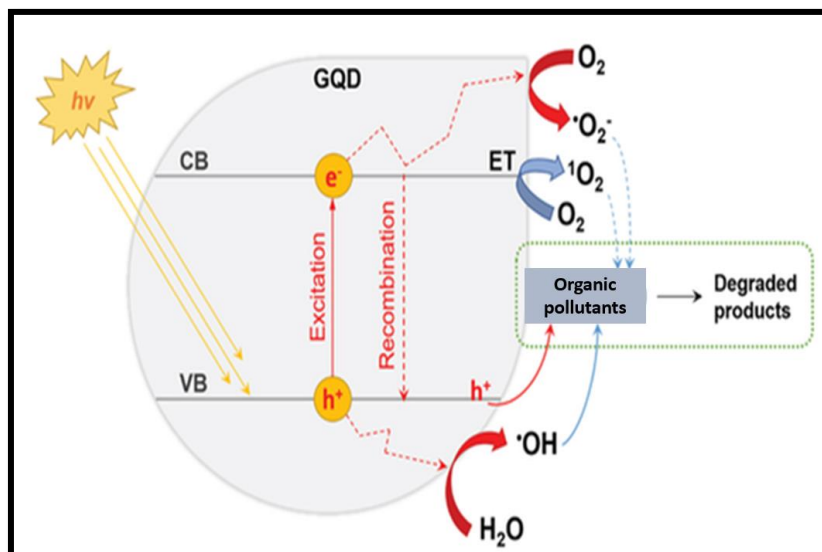
Figure 5.1: Proposed photodegradation mechanism of GQDs.

5.3.3 Photodegradation of Brilliant black dye

The photocatalytic efficiency of the fabricated GQDs was studied by evaluating the degradation of the BB pollutant dye in synthetic water and wastewater samples. The respective time dependent absorption spectra of degradation of the BB dye are presented in **Figure 5.2**. An incubation period of 30 mins in the dark was carried out prior to irradiating with light; this was done to allow the adsorption-desorption process between the dye molecules and the catalyst to reach equilibrium. After 180 mins of irradiation, significant degradation of the dye was observed for the dye in the synthetic (60% degradation) and wastewater (98% degradation) samples. In the control experiment (without the light), there was reduction in degradation percentage of 11%. The noticeable difference in the degradation percentage of the two samples is attributed to the pH; at low pH value of 4.1, the BB dye in the synthetic water sample contain non-dissociated carboxylic acids and epoxide groups [13]. In solution, the negatively charged surface of the GQDs (-23.47 mV) are the majority species, and the repulsive forces dominate resulting in the decreasing adsorption of the dye. For the wastewater sample spiked with the BB dye, the carboxylic acids and phenolic OH are ionized and the negatively charged surface of the GQDs attract the positively charged dye cations [14]. According to Ge et al. [15], GQDs can degrade up to 100% Rhodamine B (RhB) after 12 mins of irradiation. This is indicative of the higher

performance of GQDs under visible-light irradiation when compared with traditional catalysts.
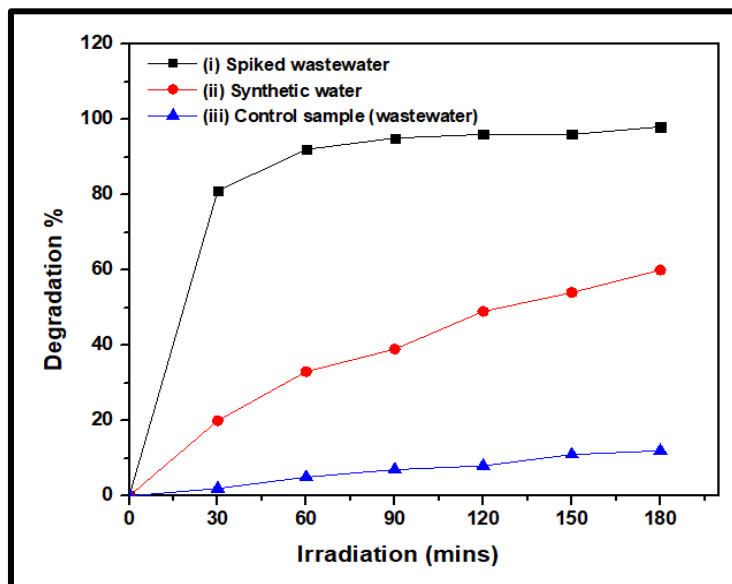
Figure 5.2:   Influence of different water matrices on the photocatalytic activity of GQDs in the degradation of BB dye in; (i) spiked wastewater (ii) synthetic water and (iii) the control experiments without BB dye.

Figure 5.3 shows the photographical images of the discoloration process after 180 mins of irradiation of the BB dye in both samples (i.e., BB dye in synthetic water and wastewater spiked with BB dye) when GQDs is used as a photocatalyst. In aqueous solution, the deep purple coloured BB dye (10 ppm) changed to a very light purple colour when 1 mg of GQDs were added at room temperature and under irradiation conditions (**Figure 5.3a**). The discoloration of the dye contaminated water indicate that chromophores present in the dye molecules are destroyed in the presence of GQDs. The destruction of the conjugated chromophore results from the breaking down of both the azo and aromatic groups, which are responsible for bonding the dye molecules [16, 17]. According to Xu et al. [18], the activity of the photocatalyst is enhanced when composites of oxidized nanoporous g-C_3N_4 (PCNO) are decorated with graphene oxide quantum dots (ox-GQDs). The features contributing to the enhancement of the photocatalyst include ameliorated light-harvesting ability, a higher charge-transfer efficiency, improved photooxidation capacity, as well as a large amount of reactive species owing to the upconversion properties, and strong electron capturing ability.

Moreover, GQDs are known to possess an excellent electron transfer ability, which is key in enhancing photocatalytic efficiency [19]. In addition, the high conductivity and strong electron capturing ability of ox-GQDs allow easier access to electrons and the electron diffusion process becomes much more effective, ultimately leading to an improvement in the charge transfer efficiency of the photocatalysts [20]. The discoloration can also be ascribed to low pH conditions because the H^+ ions are able to compete with the dye species resulting in a decreased in colour removal efficiency compared to when the wastewater sample were used (**Figure 5.3b**).
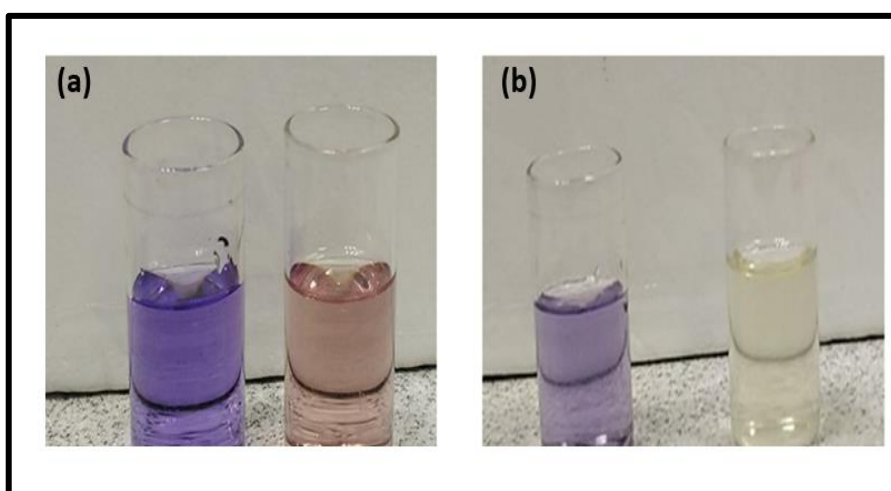
Figure 5.3:   Colour change of (a) synthetic water and (b) wastewater spiked with BB dye before and after addition of GQDs under visible light irradiation for 180 mins.

5.3.4   Kinetic studies

The degradation kinetics was studied using different light intensities to better understand the degradation behaviour of the BB dye molecules as depicted in **Figure 5.4**. Under different light intensities the photodegradation of the BB dye followed the pseudo-first order kinetics. The reaction kinetics of Brilliant Black degradation was studied, the results were fitted to a pseudo first order model and a plot based on the calculated $In\,(C_t/C_i)$ versus the irradiation time t was obtained from the linear form of **Equation 3.4**. The reaction rate was obtained using **Equation 3.4.** The half-life time ($t_{1/2}$) of the photocatalytic reactions were determined using **Equation 3.5**, both equations are described in **Chapter 3**.
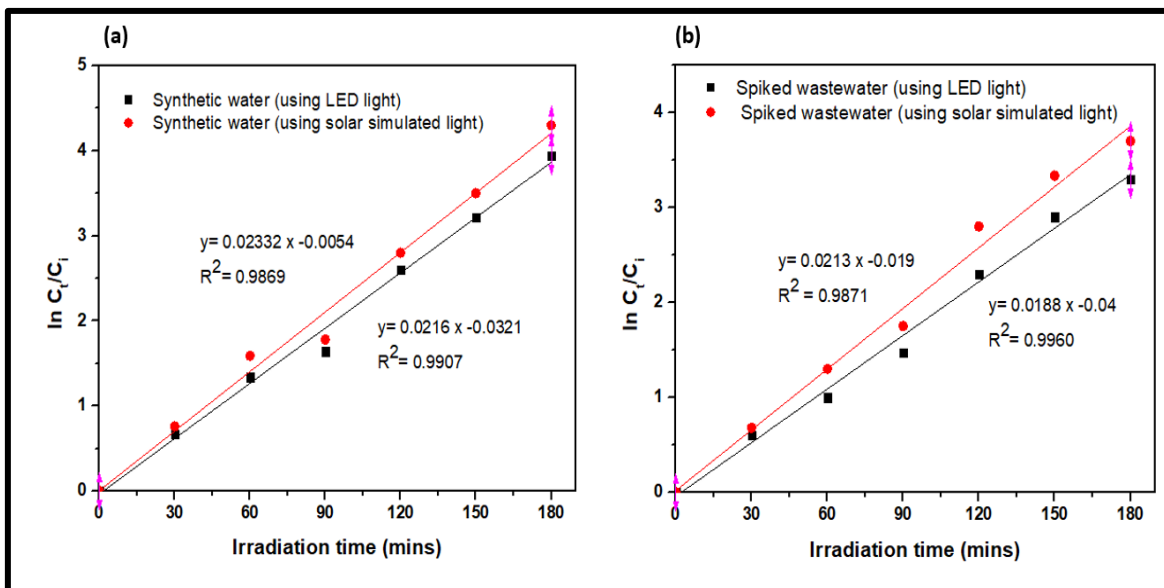
Figure 5.4:   Pseudo-first order kinetics of BB dyes degradation using different light intensities.

A reduced photocatalytic efficiency was expected in the wastewater sample owing to the complex composition of the wastewater. The obtained results proved otherwise; similar observations were made by Matamoros et al. [21]. The authors studied the effect of different water matrices (freshwater and river water) on the photodegradation of carbamazepine. The results obtained from the study showed an enhanced photodegradation of carbamazepine in river water. To explain this phenomenon, the authors ascribed the improved photodegradation efficiency of the carbamazepine to the high dissolved oxygen content (DOC) in the river water. Similarly, in this study we postulate the presence of natural organic matter (NOM) and the high DOC in the wastewater sample enhanced the BB dye degradation via indirect slow photodegradation during the photocatalytic processes. Hence explaining why, the wastewater sample had a higher photodegradation efficiency than the synthetic water sample.

Figure 5.5 shows the degradation efficiency of the GQDs as the initial concentration of the BB dye was varied. **Figure 5.4** demonstrates a similar trend, with the degradation percentage decreasing as the BB dye concentration increases in both samples. These findings show that the percentage of degradation is substantially influenced by the concentration of BB dye molecules in the solution. When the concentration of the BB dye molecules in solution was

increased, more BB dye molecules were adsorbed on the surface of the GQDs. An increase in the concentration of the BB dye means that the active sites of the GQDs become blocked thus reducing the efficiency of the photocatalyst. As the concentration of the BB dye increases, the number of photons reaching the surface of the GQDs decreases. Similar findings were reported by Rajabi et al. [22].
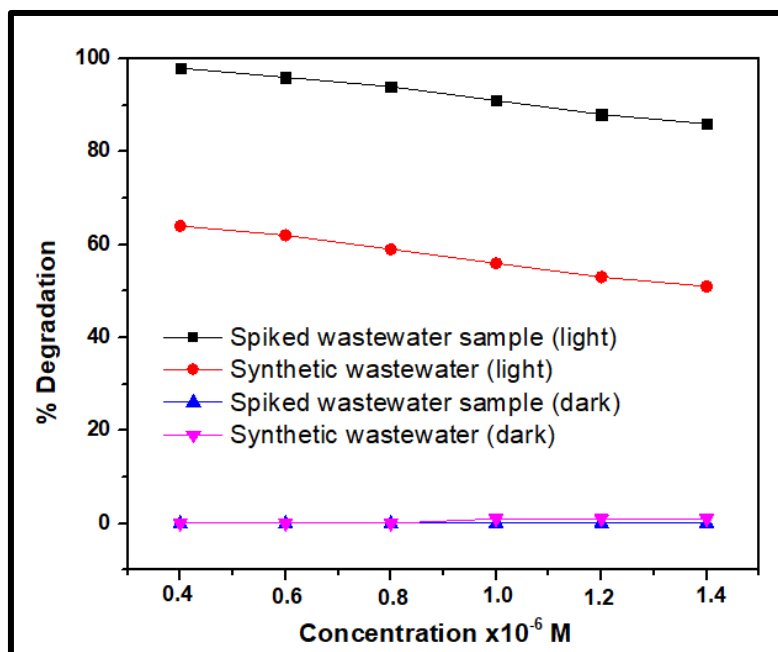
Figure 5.5:   The effect of initial BB dye concentrations on the degradation efficiencies of the GQDs under dark and light conditions.

Table 5.2 shows the kinetic data acquired by graphing the various concentrations of the BB dye against the irradiation period. Both the synthetic water and spiked wastewater samples were found to possess higher reaction rates (k) at lower BB concentrations, and as the concentrations increased the reaction rates (k) values decreased. The decrease in reaction rates (k) is expected because when the concentration of BB dye in the solution increases, photons entering the solution are intercepted, limiting BB dye photodegradation rates at higher concentrations [22]. The opposite is true for lower BB concentrations; a larger number of protons are absorbed. Furthermore, an increase in the reaction rate constant was found to result in faster dye decolorization, stronger catalytic activity, and shorter half-lives.

Table 5.2: Rate constant (k), half-life (t $_{1/2}$), maximum dye decolourization and R^2 values and of various initial concentrations of BB dye in synthetic water and spiked wastewater in the presence of GQDs.

BB Dye concentration (x 10^{-6} M)	k (x 10^{-3} min $^{-1}$)		Half life (min)		Maximum discoloration (%)		R^2 values	
	Synthetic Water	Spiked Waste water	Synthetic Water	Spiked Waste water	Synthetic water	Spiked Waste Water	Synthetic water	Spiked Waste water
0.40	0.0393	0.0427	17.63	14.84	64	98	0.8974	0.9314
0.60	0.0314	0.0418	22.07	16.58	62	95	0.9051	0.9089
0.80	0.0290	0.0371	23.09	18.68	59	93	0.9126	0.9866
1.00	0.0274	0.0315	25.29	22.00	56	91	0.8908	0.9329
1.20	0.0248	0.0309	27.94	22.43	53	88	0.9733	0.9779
1.40	0.0210	0.0261	33.00	26.55	50	85	0.8901	0.9398

To understand the mechanism of photodegradation further and to determine whether the degradation of the BB dye occurred as a result of the photocatalyst (GQDs) or light (self-photolysis), studies were conducted without GQDs. **Figure 5.5** shows that zero degradation of the dye was observed for the sample that was kept in the dark without irradiation. At the same time, 16% and 26% of the BB dye was degraded in the synthetic water and the spiked wastewater sample, respectively, thus providing evidence that self-photolysis forms part of the degradation mechanism. The data indicate that, without the self-photolysis reaction, photocatalytic activity accounts for approximately 76% of the degradation of BB dye in the real wastewater sample. Previously, researchers [23, 24] have attributed self-photolysis to the self-degradation of photoexcited dyes. However, as observed in **Figure 5.2**, the degradation of the BB dye is significantly enhanced by the addition of GQDs. It can be concluded that, while photosensitization degradation is one of the pathways in which degradation of the BB dye is achieved, the photodegradation mechanism is this research work is the dominant pathway. As can be seen from **Figure 5.6**, photocatalysis is the dominant mechanistic pathway responsible for the degradation of BB dye molecules. The data presented in **Figure 5.6** shows that adsorption is not the main mechanistic pathway followed in the degradation of BB dye in both the synthetic and real wastewater samples. It

is recommended that additional studies be conducted at the exit of the WWTP to determine the efficiency of this method.
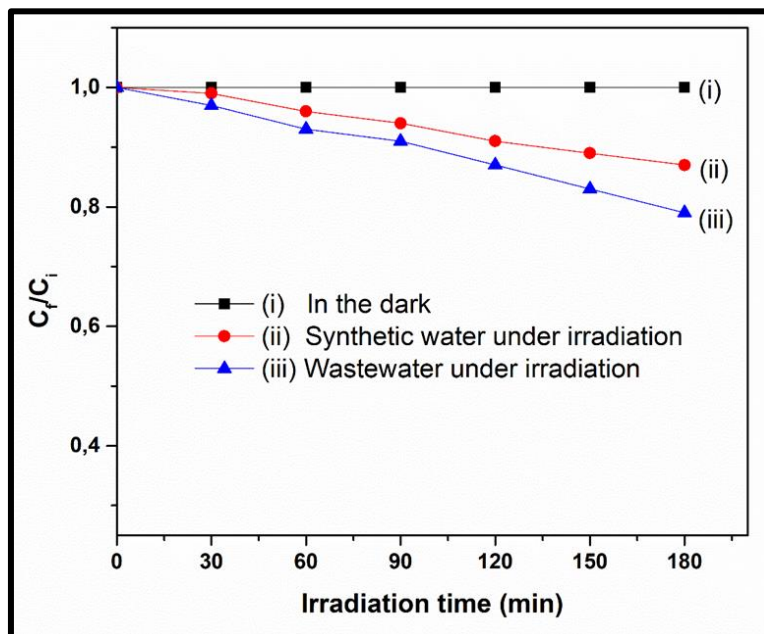
Figure 5.6:   Photolysis of BB dye (without GQDs) and under the LED light irradiation.

5.3.5   **Identifying radicals responsible for the photodegradation of BB dye**

Radical scavenging experiments were conducted to determine the contribution and influence of each radical responsible for the photodegradation of BB dye. Excess methanol, EDTA-2Na, p-benzoquinone and silver nitrate were employed as scavengers for •OH, h^+, •O_2^- and e^- respectively. **Figure 5.7** shows that h^+ (13%) and e^- (7%) contributed the least to the degradation of BB dye. Methanol on the other hand inhibited 82% of the •OH radicals making the •OH the greatest contributor, while p-benzoquinone inhibited 63% of the •O_2^-.
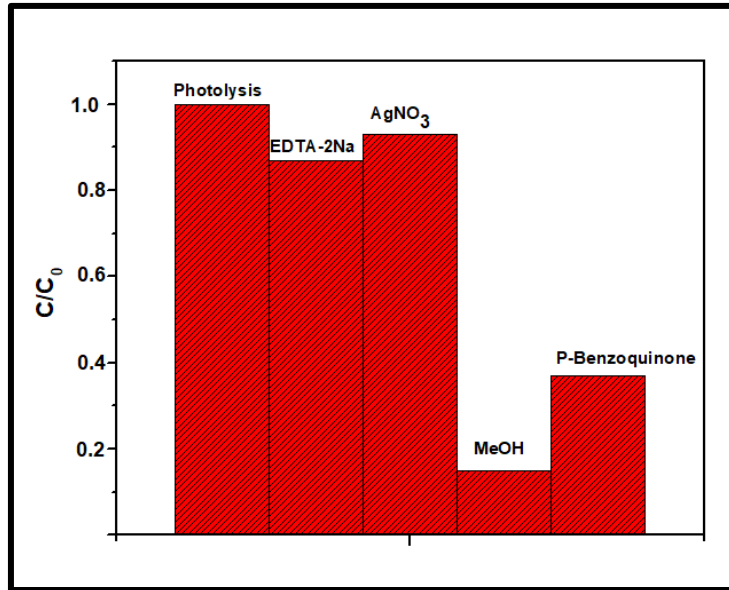
Figure 5.7:   Quenching experiments using radical scavengers, for comparative purposes experiments in the dark are also included.

5.3.6   Proposed mechanism for the degradation of BB dye

Based on the data from the quenching experiments on **Figure 5.8**, a proposed photocatalytic degradation pathway of BB dye by GQDs (**Figure 5.8a**). When both GQDs and the BB dye absorb sufficient light, the electrons in the VB of the GQDs gets excited, leaving a hole (h^+) and the migration of the electrons to the CB results in the generation of the electron-hole pair (**Equations 5.1-5.5**). The e^-/h^+ pair can be transferred to surfaces and interact with H_2O molecules, resulting in O_2 and •OH species, which are both highly reactive in the degradation of organic pollutants [25].

$$\text{GQDs} \rightarrow \text{GQDs}\ (e^-_{CB} + h^+_{VB}) \qquad\qquad \textbf{(Eq.5.1)}$$

$$\text{GQDs}\ (e^-_{CB}) + (O_2)_{ads} \rightarrow \text{GQDs} + (O_2^{-\bullet})_{ads} \qquad\qquad \textbf{(Eq. 5.2)}$$

$$(O_2^{\bullet-})_{ads} + H^+ \rightarrow HO_2^{\bullet} \qquad\qquad \textbf{(Eq. 5.3)}$$

$$2HO_2^{\bullet} \rightarrow H_2O_2 + O_2 \qquad\qquad \textbf{(Eq.5.4)}$$

$$H_2O_2 + e^- \rightarrow OH^- + OH^{\bullet} \qquad\qquad \textbf{(Eq.5.5)}$$
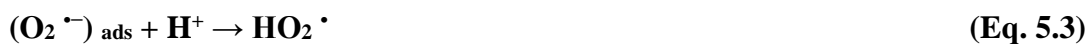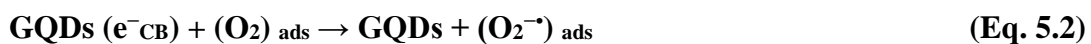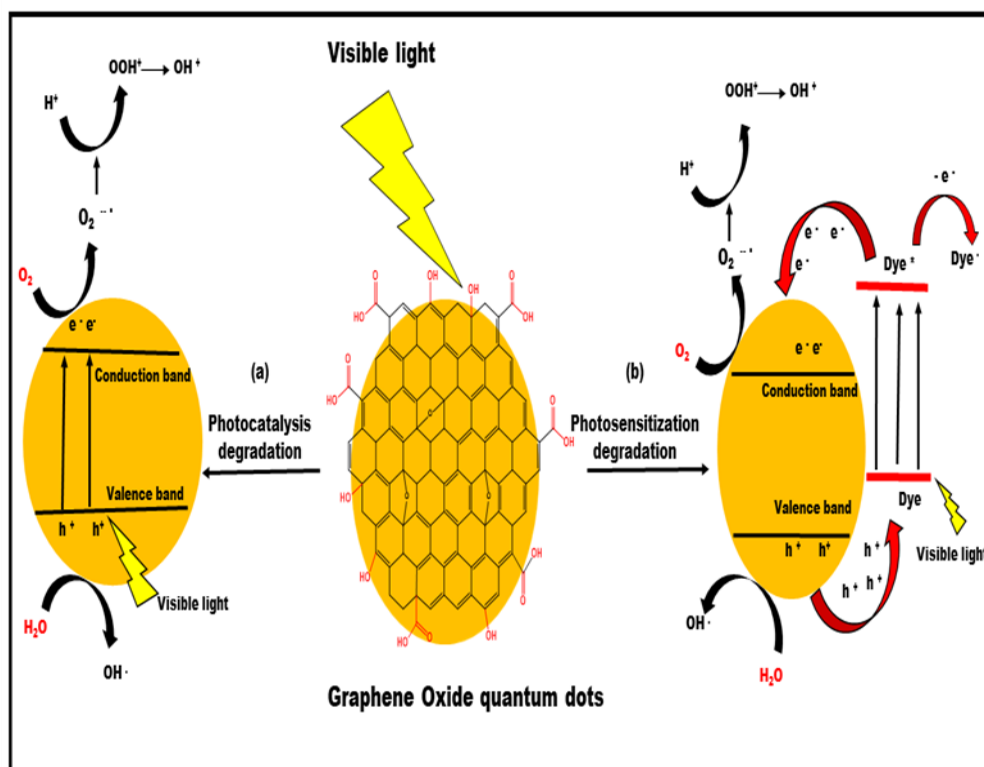
Figure 5.8:   Proposed mechanism of degradation of BB dye in synthetic water and real wastewater spiked with BB dye.

Additionally, the VB holes can directly oxidize the organic pollutant (BB dye) adsorbed on the surface of photocatalyst (GQDs) which can act as a barrier against the recombination of e^-/h^+ pair in order to stay reactive for longer times [25]. Alternatively, the VB holes can also indirectly mineralize the BB dye *via* hydroxyl radicals (•OH) generated when holes and water (H_2O) molecules react or are chemisorbed (OH^-) **Equations (5.6-5.8)**.

$GQDs\ (h^+_{VB}) + (H_2O)\ _{ads} \rightarrow GQDs + (HO^•)\ _{ads} + (H^+)\ _{ads}$ **(Eq.5.6)**

$GQDs\ (h^+_{VB}) + (HO^-)\ _{ads} \rightarrow GQDs + (HO^•)\ _{ads}$ **(Eq.5.7)**

$GQDs\ (h^+\ _{VB}) + Dye\ _{ads} \rightarrow GQDs + (Dye^{•+})\ _{ads}$ **(Eq.5.8)**
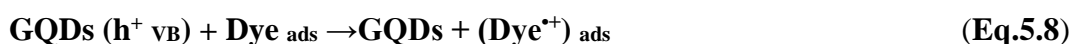
For the photosensitization degradative pathway (**Figure 5.8b**), the large surface area of GQDs [20] allows the efficient adsorption of BB dye molecules. When irradiated the electrons in the ground state of the dye gets excited, some of the excited electrons can be transferred to the CB of the GQDs. This allows the photoinduced active species (e.g., $•O_2^-$,

•OOH, •OH) to oxidize or degrade the organic pollutants absorbed on the surface of the GQDs as shown in **Equations 5.9- 5.11**.

Dye + hU(vis) → Dye*   **(Eq.5.9)**

Dye* + GQDs → Dye•+ + GQDs (e^-_{CB})   **(Eq. 5.10)**

GQDs (h^+_{VB}, •OH, •OOH or $O_2^{•-}$) + Dye → CO_2 + H_2O + small by-products   **(Eq.5.11)**
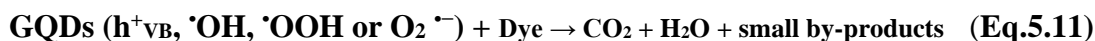
Although the proposed mechanism is not yet fully understood, we postulate that the degradation of the BB dye in both water matrices involves the irradiation of the dye molecules, and it proceeds *via* both photocatalytic and photosensitization degradation (**Figure 5.8** and **Equations (5.1-5.11)**).

5.3.7   **Photocatalyst reusability experiments**

Reusability studies were conducted to determine the stability and recyclability of the GQDs photocatalyst which is a key parameter for practical applications. The reused GQDs (from the first cycle) were separated, recovered by centrifugation, and dried in an oven and tested under the same experimental conditions as described in **Chapter 3**, for subsequent cycles. The photodegradation performances of the GQDs in both wastewater and synthetic water after 4 cycles is shown in **Figure 5.9**.
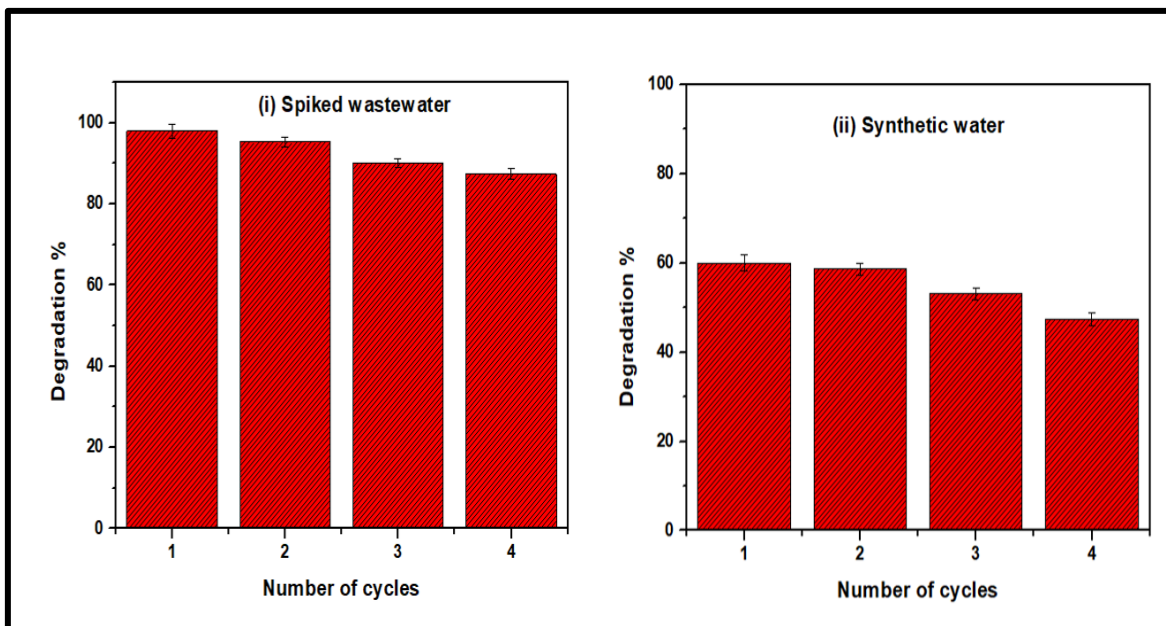
Figure 5.9: Reusability experiments of the GQDs in (i) spiked wastewater and (ii) synthetic water.

As the number of cycles increase, it was noted that the degradation rates of the GQDs decreased gradually from 98.0% of the first cycle to 85.9% after the fourth cycle. This trend is expected because as the GQDs photocatalyst is reused, the number of active sites inevitably gets reduced. It is encouraging to see that even after 4 cycles, the GQDs were still able to remove more than 85% of the dye. Even in the synthetic water samples the photodegradation reduced from 60% to 47%. The reusability performances of the GQDs suggests GQDs are stable and can therefore be applied in water treatment applications.

5.4   Conclusion

The GQDs photocatalysts were found to be efficient in the detoxification and discoloration of the BB dye from synthetic and the spiked real wastewater samples. While the anticipated results were that GQDs would perform better in synthetic water, it was interesting to observe an enhanced photocatalytic efficiency in wastewater. This was ascribed to the high dissolved oxygen content (DOC) in the wastewater sample and the presence of natural organic matter (NOM) which led to the enhanced the BB dye degradation *via* indirect slow photodegradation during the photocatalytic processes. Other key findings of the study included:

- The photocatalytic efficiency of GQDs was negatively impacted by increasing the initial concentration of the BB dye. The findings show that increasing the reaction rate constant led to faster dye discolouration, higher catalytic activity, and shorter half-lives.

- Under different light intensities, pseudo-first order model was a better fit for both the synthetic and spiked real wastewater samples. Coefficient of correlation (R^2) of 0.991 and 0.996 was obtained for the synthetic and real wastewater using LED light, respectively. While 0.9907 and 0.9871 were recorded for the synthetic and real wastewater respectively when using simulated solar light.

- Quenching experiments showed that e^-, h^+, $\bullet O_2^-$ and $\bullet OH$ radicals all contributed to the degradation of BB dye, however 82% of the photodegradation was as a result of the contribution of the $\bullet OH$ radicals. The photodegradation mechanism was therefore postulated to be a combination of both photocatalytic degradation and photosensitization of the dye, with the photocatalytic degradation being the more dominant mechanistic pathway.

The upscaling of this study is envisaged to efficiently detoxify and discolour toxic dyes from WWTPs. This would significantly reduce sludge formation and as a result the treatment process would be accelerated.

References

1. Putri L.K, Tana L.L, Onga W.J, Changc W.S. Chang, Chai S.P, *App Mater Today*. 4(2016) 9.

2. Tsai C.G, Tseng W.J, *Ceram Int*. 46(2020)14529.

3. Topkaya E, Konyar M, Yatmaz H.C, Öztürk K, *J. Colloid. Interface. Sci*. 430(2014)6.

4. Muleja A.A, and Mamba B.B, *J. Environ. Chem. Eng* 4(2018)4850.

5. Talwara S, Sangala V.K, Verma A, *J. Photo. Photobio. A: Chemistry* 353(2018)263.

6. Jalloulia N, Pastrana-Martínezb L.M, Ribeirob A.R, Moreirab F.F, Fariab J.L, Hentatia O, Silvab A.M.T, Ksibia M, *Chem. Eng. J* (2018)976.

7. Vela N, Calín M, Yáñez-Gascón M.J, Garrido I, Pérez-Lucas G, Fenoll J, Navarro S (2018) *J. Photochem. Photobiol. Chem* (2018) 271.

8. Valappil M.O, Pillai V.K, Alwarappan S, Appl. Mater. Today 9(2017) 350.

9. Dong Y, Shoa J, Chen C, Li H, Wang R, Chi Y, Chen, *Carbon* 50(2012) 4738.

10. Tshangana C.S, Muleja A.A, Nxumalo E.N, Mhlanga S.D *Environ. Sci. Pollut. Res* 27 (2020)26845

11. Sapra S, Sarma D.D, *Pramana* 65(2005)565.

12. Loh K.P, Bao Q, Eda G, Chhowalla M, *Nat. Chem.* 2(2010)015.

13. Konkena B, Vasudeva S, *J. Phys. Chem. Lett.* 3(2012) 867.

14. Xu J, Huang J, Wang Z, Zhu Y, *Chinese. J. Catal.* 41(2020) 474.

15. Ge J, Lan M , Liu W , Jia Q, Guo L, Zhou B, Meng X, Niu G, Wang P, *Sci. China. Mater.* 59(1) (2016)12-19.

16. Xiong J, Li X, Huang J, Gao X, Chen Z, Liu J, Li H, Kang B, Yao W, Zhu Y, *Appl. Catal. B. Environ* 266(2020)118602.

17. Zhang S, Sui L, Dong H, He W, Dong L, Yu, *ACS. Appl. Mater. Interfaces* 10 (2018) 12983.

18. Wang H, Xie C, Zhang, Cai S, Yang Z, Gui Y, *J. Hazard. Mater.* 141(2007) 645.

19. Rajabi H.R, Farsi M, *J. Mol. Catal. A. Chem.* 399 (2015) 53.

20. Shao M, Han J, Wei M, Evans D.G, Duan X, *Chem. Eng. J.* 168(2) (2011) 519.

21. Xiang X, Xie L, Li Z, Li F, *Chem. Eng. J.* 221(2013)222.

22. Rahimi, K, Yazdani, A, Ahmadirad, M, Mater. Res. Bull. 98(2018) 148.

23. Wanga J, Guoa Y, Liu B, Xu B, *Ultrason. Sonochem*. 18(2011) 177.

24. Kim C.O, Hwang SW, Kim S, *Sci. Rep.* 4 (2012) 5603.

25. Roushani M, Mavaei M, Rajabi H.R, *J. Mol. Catal. A: Chem.* 409 (2015) 102.

CHAPTER 6

CONJUGATING ZnO NANOSTRUCTURES TO GRAPHENE OXIDE QUANTUM DOTS FOR ENHANCED PHOTOCATALYTIC AND ANTIMICROBIAL ACTIVITY

6.1   Introduction

Studies have shown that pristine GQDs have limited applications and may need to be modulated to improve their properties [1, 2]. The properties of the GQDs can be enhanced by doping, surface modification or conjugation [3]. This chapter reports on the conjugation of ZnO nanostructures to GQDs and seeks to present an alternative method and low-cost "*dual nanohybrids*" in the treatment and disinfection of wastewater. The objectives of the study were to: overcome ZnO's two fundamental drawbacks as a photocatalyst that have been extensively discussed in the literature (i) the rapid rate of carrier charge recombination as well as (ii) the inability to capture a significant amount of sunlight due to its large band gaps [4,5]. Conjugating GQDs to ZnO aims to achieve this by: (i) delaying the carrier charge recombination owing to GQDs' ability to function as barriers, which allows them to stay active for extended periods, and (ii) allowing better sunlight harvesting as a result of the π–π* transition of GQDs in the visible region. The goal of this chapter using BB as a model dye was to: (a) understand how much the shape of the ZnO influences the overall photocatalytic features of its nanohybrid when conjugated to GQDs (b) to determine which between the flakes or rods nanohybrids has superior antibacterial action and to try to establish the inhibitory mechanism based on the structure of the ZnO nanostructures; and (c) to see if there's a link between photocatalytic and antibacterial activity, which would enable the resultant nanohybrids to function as "*dual nanohybrids*".

6.2 Experimental details

6.2.1 Amino functionalization of ZnO nanostructures

The ZnO flakes and rods as well as the GQDs used in this chapter were synthesized using previously published procedures [6-8], further details of the synthesis and functionalization of the ZnO nanostructures are detailed in **Chapter 3**.

6.2.2 Covalently linking amino functionalized ZnO nanostructures to GQDs

As demonstrated in **Scheme 3.2** in **Chapter 3**, the resulting ZnO nanoparticles (NPs) were covalently bonded to GQDs. EDC/NHS coupling chemistry was used to conjugate the amino functionalized ZnO nanostructures to GQDs, as explained in **Chapter 3**. The conjugates of the ZnO nanostructures conjugated to GQD are denoted as ***ZnO-R-GQDs*** and ***ZnO-F-GQDs*** throughout the entire thesis.

6.2.3 Photodegradation experiments

The photocatalytic and photolytic experiments were conducted as outlined in **Chapter 3**.

6.2.4 Antimicrobial studies

The effects of the ZnO-F-GQDs and ZnO-R-GQDs were tested against *B. cereus*, *E. coli*, *P. aeruginosa* and *S. aureus* and investigated using the Kirby Baüer method as outlined in **Chapter 3** of the thesis.

6.3 Results and discussion

6.3.1 Determination of morphology of ZnO nanostructures

The shape of the synthesized ZnO nanoparticles was confirmed by HR-SEM images (**Figure 6.1** and **6.2**), allowing us to investigate the impact of shape on photocatalytic and antibacterial capabilities. **Figure 6.1a** shows a cluster of spherical ZnO-Fs. The average diameters of the synthesized NPs were determined to be 23.5 nm determined using Image J

software. There were no noticeable changes in the shape of the ZnO-F-GQDs nanohybrid after conjugating GQDs to the ZnO-F (**Figure 6.1b**), but the size of the ZnO-F-GQDs increased to 68.57 nm, indicating a successful conjugation to between the GQDs and ZnO-F.
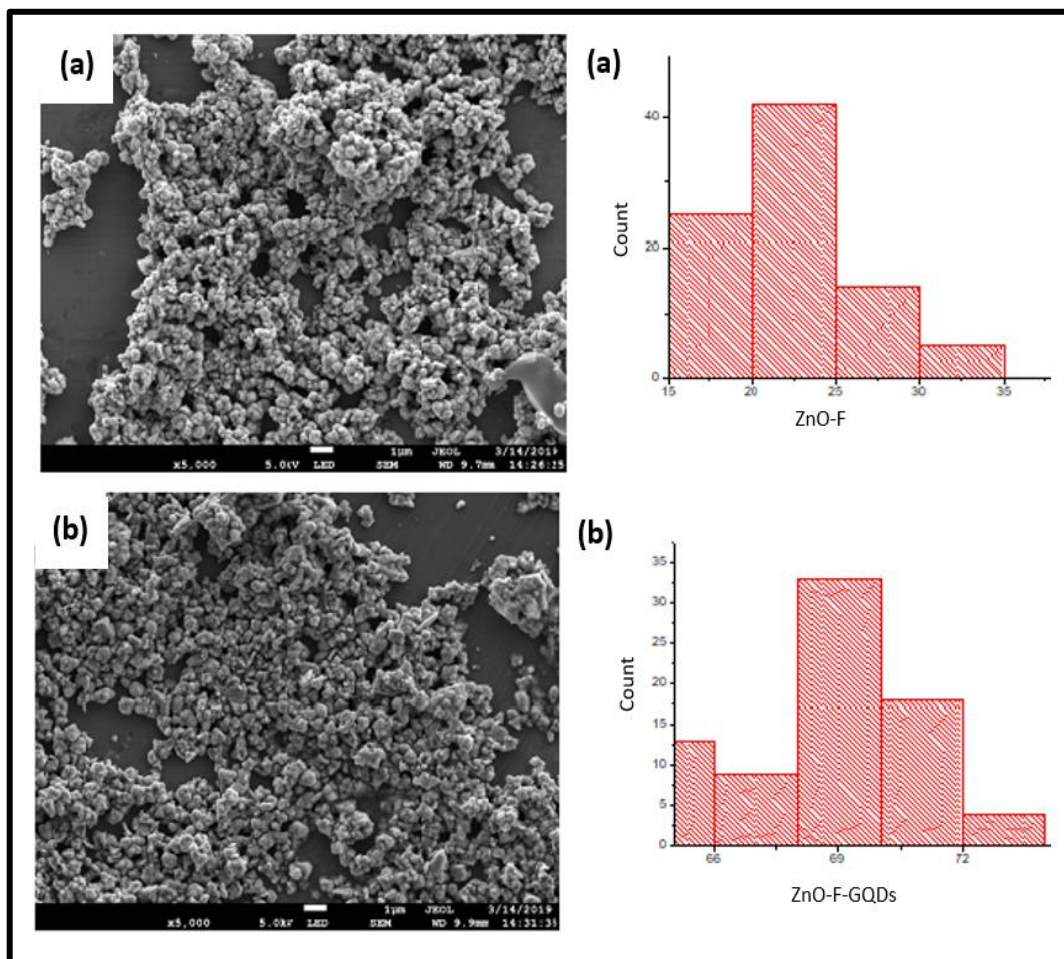
Figure 6.1:   SEM micrographs of (a) pristine ZnO-F and (b) ZnO-F-GQDs and corresponding size distribution.

Figure 6.2a shows rod-shaped ZnO-R with an average diameter of 53.75 nm, with the nanohybrids forming clusters with the addition of GQDs (**Figure 6.2b**). As a result, the diameters of individual ZnO-R-GQDs could not be calculated, thus the average diameter of the clusters was estimated to be 423.36 nm. Even though the nanohybrid aggregated, under higher magnification (insert on **Figure 6.2b**), it is evident that the pristine rod structure was maintained, which was important for our shape-dependent experiments. Linking the GQDs to the nanohybrids did not change the pristine shape of the ZnO-R.
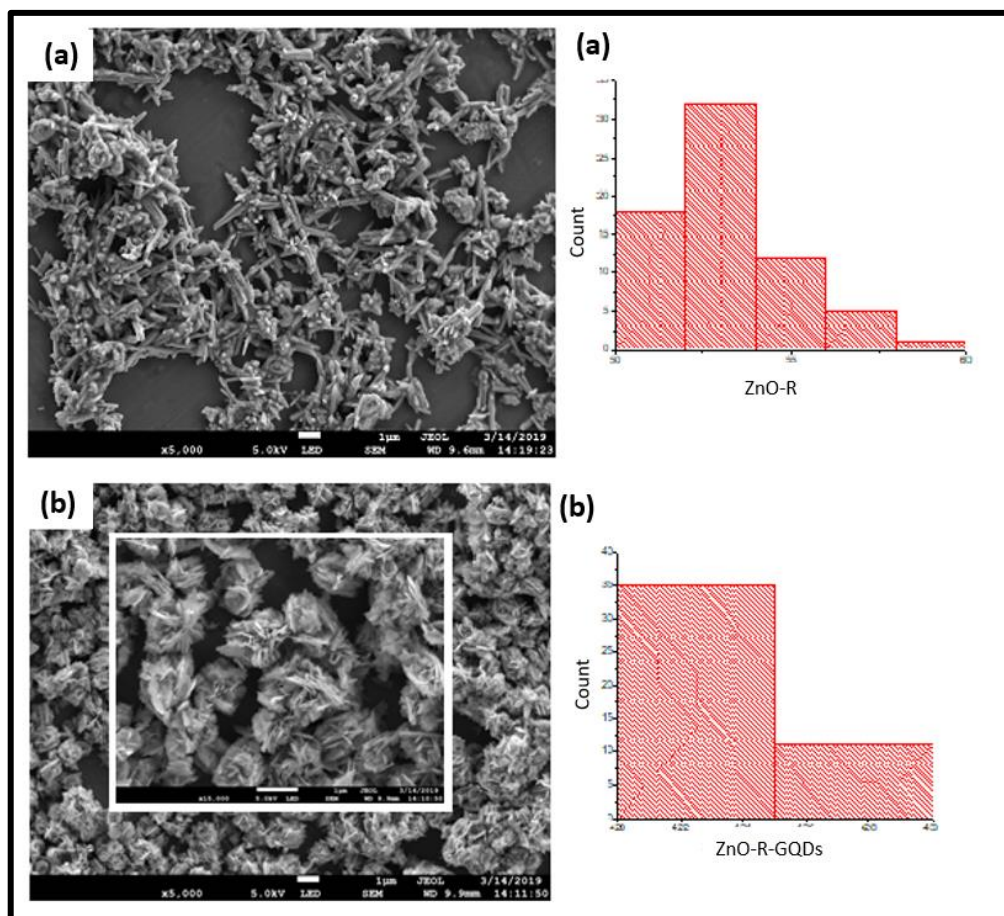
Figure 6.2:   SEM micrographs of (a) pristine ZnO-R and (b) ZnO-R-GQDs (insert) higher magnification of ZnO-R-GQDs and corresponding size distribution.

6.3.2   **Confirmation of successful linkage of the ZnO nanostrutures to the GQDs**

The covalent bond between ZnO-F or ZnO-R and GQDs was confirmed using FT-IR, as illustrated in **Figure 6.3a**. When the ZnO nanostructures were conjugated to GQDs (as shown in **Figure 6.3a** i and iii) the amide group (-NHCO-) peaks emerged, namely C=O at 1657 cm^{-1}, -NH- bend at 1566 cm^{-1}, and the -NH stretch about 3000 cm^{-1}, confirming the successful coupling of the ZnO nanostructures to the GQDs. The ZnO nanostructures (**Figure 6.3a**) (ii and iv) display the typical Si-O-Si peaks of 1034 cm^{-1} and 421 cm^{-1}, respectively, with a Zn-O stretching vibrational peak of 574 cm^{-1} that is indicative of wurtzite crystal structures. The symmetric and asymmetric C=O double bond vibrations as a result of the ionisation of carbonyl groups are attributed to two new peaks in ZnO-R at 1392 and 1579

cm^{-1} [9, 10]. Atmospheric moisture was responsible for the OH peak at 3450 cm^{-1} found in the ZnO nanostructures.
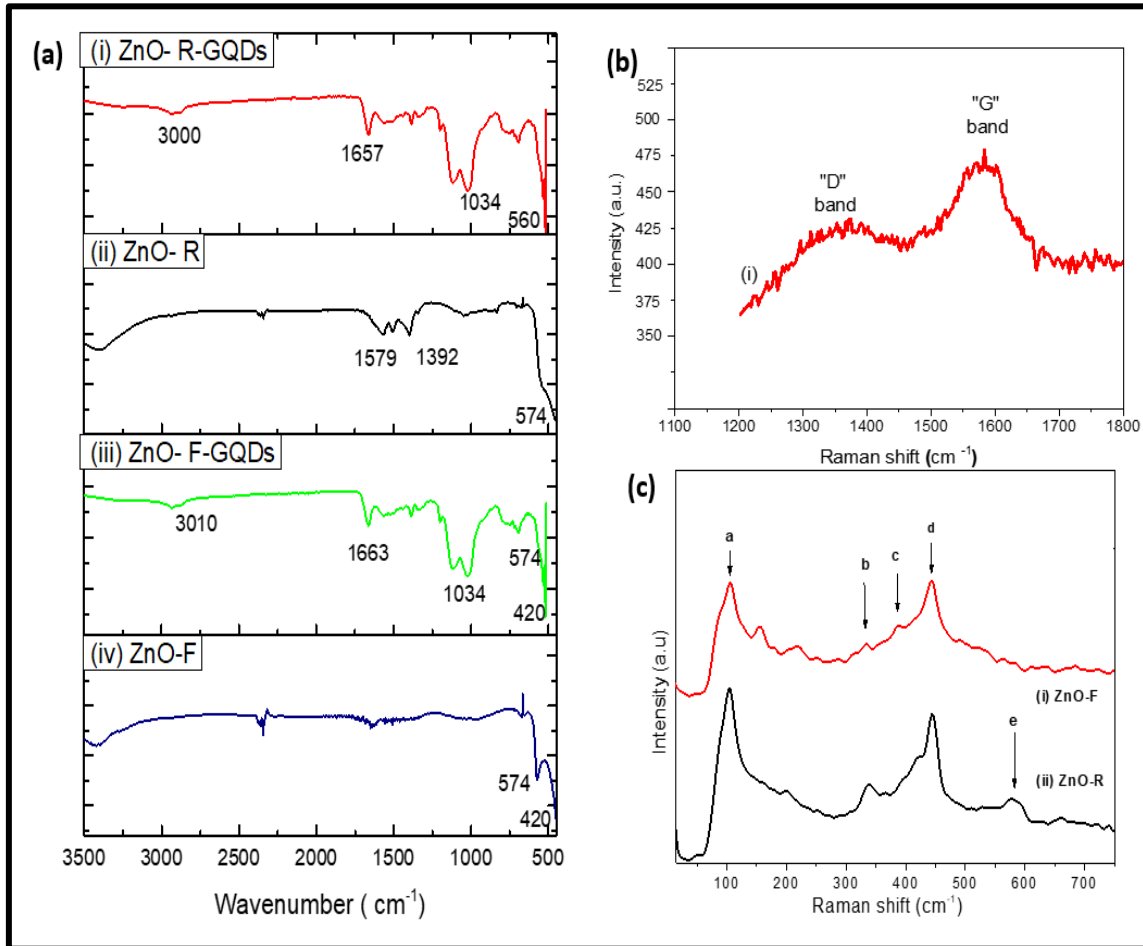
Figure 6.3: (a) FT-IR spectra of (i) ZnO-R-GQDs (ii) ZnO-R (iii) ZnO-F-GQDs (iv) ZnO-F and (b) Raman spectra of (i) GQDs and (c) Raman spectra of (i) ZnO-F and (ii) ZnO-R.

Figure 6.3b depicts the GQDs' unique Raman peaks, which include peaks at 1350 and 1600 cm^{-1} that correspond to the "D" and "G" bands respectively. **Figure 6.3c** shows the peaks labelled "a", "b", "c", "d", and "e" for the ZnO nanostructures, which is equivalent to E_2 (low) 103 cm^{-1}, $2E_2$ 332 cm^{-1}, A_1 (LO) 386 cm^{-1}, E_2 (high) 444 cm^{-1}, and A_1 (TO) 578 cm^{-1} overlapped with E_1 (LO) 592 cm^{-1}, respectively. The second order Raman spectrum from zone bound ZnO phonons was dubbed peak b ($2E_2$). There are five probable Raman modes for ZnO in a typical Raman spectrum: A_1 (TO), A_1 (LO), $2B_1$, E_1 (low), and E_2 (high) [9]. Due to $2B_1$ not being Raman active, it is frequently described as the "silent mode";

nevertheless, the spectrum does not always show all active modes. Only A_1 (LO) and E_2 are visible when incident light is normal to the ZnO surface (incident and dispersed polarization parallel). Only E_2 is detected in the case of perpendicular polarization. All of the modes can, however, be observed simultaneously [9-11].

6.3.3   **XRD analysis**

The crystalline structure of the ZnO nanostructures and GQDs was evaluated by XRD analysis (**Figure 6.4a** and **b**). The prepared ZnO nanostructures have XRD peaks that match those previously reported (hexagonal wurtzite with lattice constants of a = 3.26 Å and c = 5.21 Å) [12]. The absence of secondary phase and sharp diffraction peaks show that the ZnO NPs are pure. The XRD pattern of the GQDs, displayed a large peak at $2\theta = 24$ and correlates to previously synthesized GQDs [13]. The GQDs had an average crystallite size of 2.1 nm and 5.7 nm as well as 6.3 nm for ZnO-R and ZnO-F, respectively. The average crystallite diameters of the ZnO-R-GQDs and ZnO-F-GQDs conjugates were 16.6 nm and 17.4 nm, respectively. **Figure 6.4c** depicts the XRD patterns of the ZnO nanostructures preserved the typical ZnO peaks observed in **Figure 6.4a** with a little displacement of the major ZnO peak between 35- 38° to a lower degree. This is due to the inclusion of GQDs, which causes the lattice constants of ZnO to rise. A peak at 26.35°, attributable to the graphite (002) peak, appears demonstrating successful conjugation to the ZnO nanostructures, which is consistent with what Xu et al. found for ZnO-graphene nanomaterials [14].
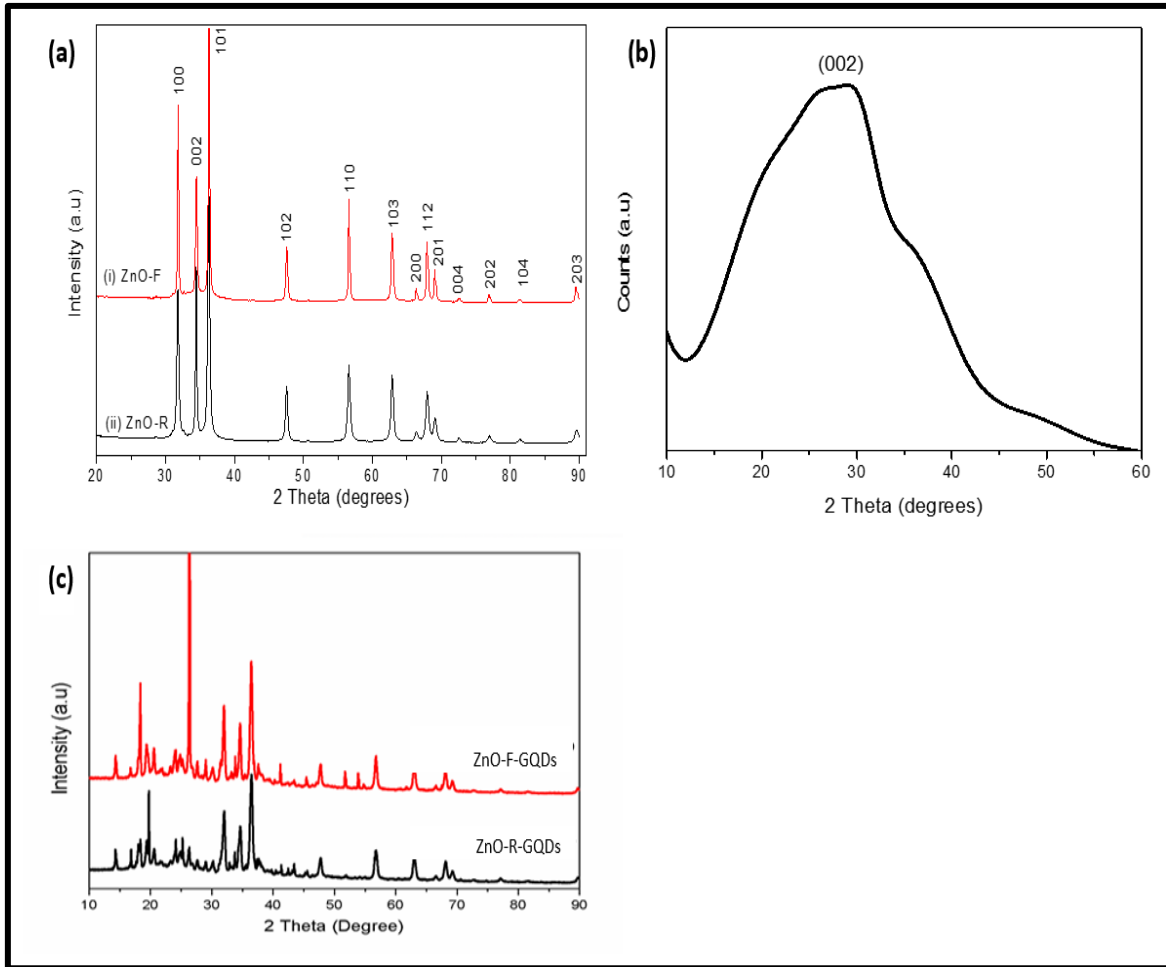
Figure 6.4: (a) XRD of (i) ZnO-R-GQDs (ii) ZnO-R (iii) ZnO-F-GQDs (iv)ZnO-F and (b) XRD of (i) GQDs and (c) XRD of (i) ZnO-F and (ii) ZnO-R.

6.3.4 Optical properties

Optical spectrophotometry was used to investigate the optical characteristics of the nanomaterials, as illustrated in **Figure 6.5**. **Figure 6.5a** shows that the reflectance of the ZnO nanostructures is around 400 nm, which conforms to a previous report [15]. A distinct optical absorption in the UV area is seen for GQDs (**Figure 6.5b**), with a tail extending in the visible range at 351 nm, which is ascribed to π–π* transition of aromatic C=C bonds [16]. When excited at 390 nm, the GQDs emit a narrow, distinct emission with a full width at half maximum (FWHM) of 480 nm. **Equation 3.2** in **Chapter 3** was used to determine the band gaps of the ZnO nanostructures.

135

Tauc's Plot (**Figure 6.5c**) was obtained by plotting $(\alpha h v)^{1/2}$ vs hv where α is the relative reflectance and $hv = hc/\lambda$ was utilized to extrapolate the band gaps. The band gaps of the ZnO nanostructures showed a marginal difference of about 0.2 eV (**Table 6.1**).
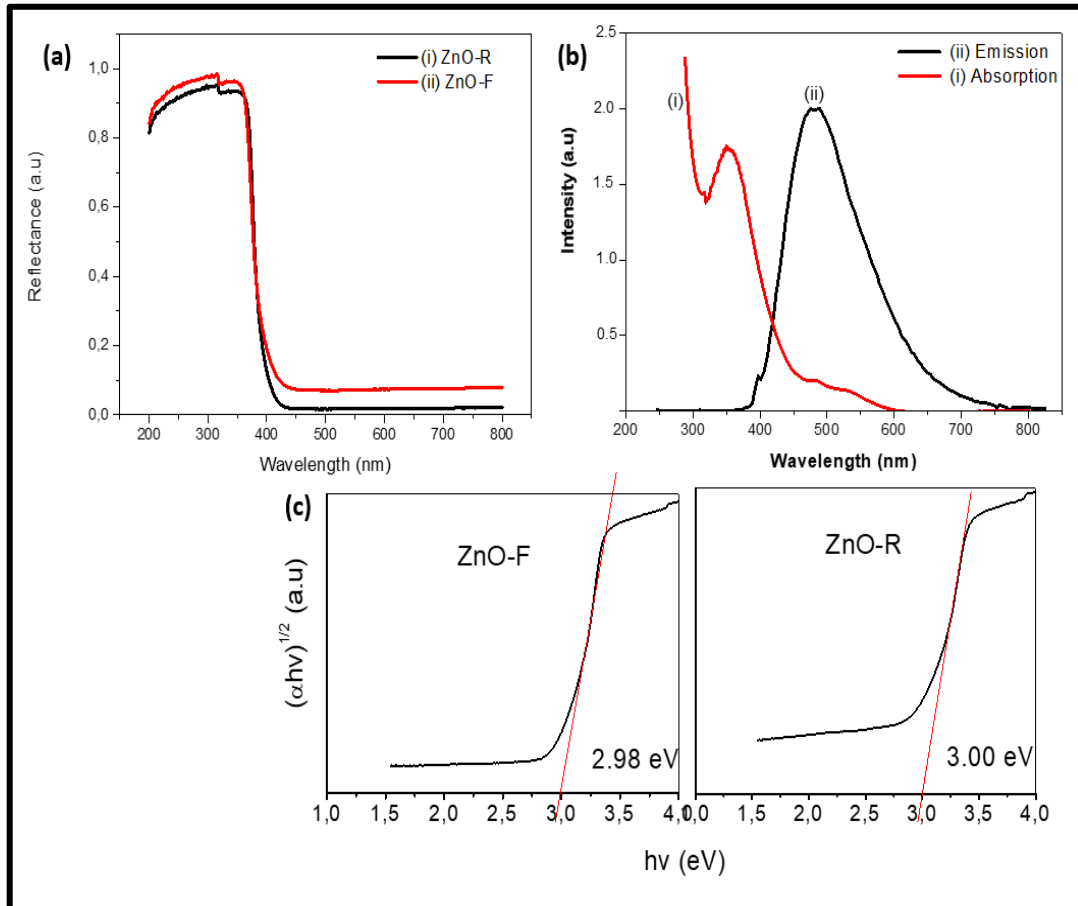
Figure 6.5:   UV-Vis spectra (i) ZnO-R and (ii) ZnO-F, (b) (i) emission and (ii) absorption of GQDs and (c) Tauc's plot of (i) ZnO-F and (ii) ZnO-R.

Table 6.1:   **Band gaps of the ZnO nanostructures.**

Material	Wavelength (nm)	Band gap (eV)	Band gap (eV) Tauc's Plot
ZnO-F	402	3.08	2.98
ZnO-R	402	3.08	3.00

The calculated bandgaps of the ZnO nanostructures were expected to have band gaps in the range of the pristine ZnO (~3.4 eV). However, bandgaps of 3.0 eV were obtained in this investigation for ZnO-F (2.98 eV) and ZnO-R (3.00 eV). The oxygen atoms in this experiment acted as impurities or defects, resulting in a smaller bang gap. The principle of band gap reduction is based on the presence of impurities in semiconductor crystal structures [17]. UV absorption was used to confirm that the ZnO nanostructures were successfully linked to GQDs (**Figure 6.6a**). The spectra of ZnO nanostructures and GQDs (**Figure 6.5a** and **b**) typically do not exhibit two peaks, however two distinct peaks pertaining to ZnO and GQDs were found in the nanohybrids. After adding GQDs, there was a considerable blue shift in the reflectance of the nanohybrids, which was attributable to the dominance of the quantum confinement effect. The appearance of a peak at 396 nm in the ZnO-R-GQDs indicated the existence of GQDs, while the peak ascribed to the ZnO was visible at 419 nm. The peak associated with GQDs in the ZnO-R-GQDs was now seen at 403 nm, whereas the ZnO peak remained at 419 nm.

Equation 3.2 in **Chapter 3** was used to determine the bandgap energies of the nanohybrids. The n value was set at ½, because ZnO has a direct transition between its valence and conduction bands [18]. For the ZnO-F-GQDs and ZnO-R-GQDs, the predicted bandgaps decreased from 2.98 eV to 2.61 eV and from 3.00 eV to 2.79 eV, respectively. The nanohybrids were able to harvest solar light since the bandgap was reduced, and covalently linking GQDs to ZnO nanostructures improved the photocatalytic potential, making them suitable photocatalysts. In comparison to the ZnO-F-GQDs nanohybrid, the ZnO-F-GQDs nanohybrid showed a higher decrease in bandgap after conjugating to GQDs, rendering it a better photocatalyst candidate.
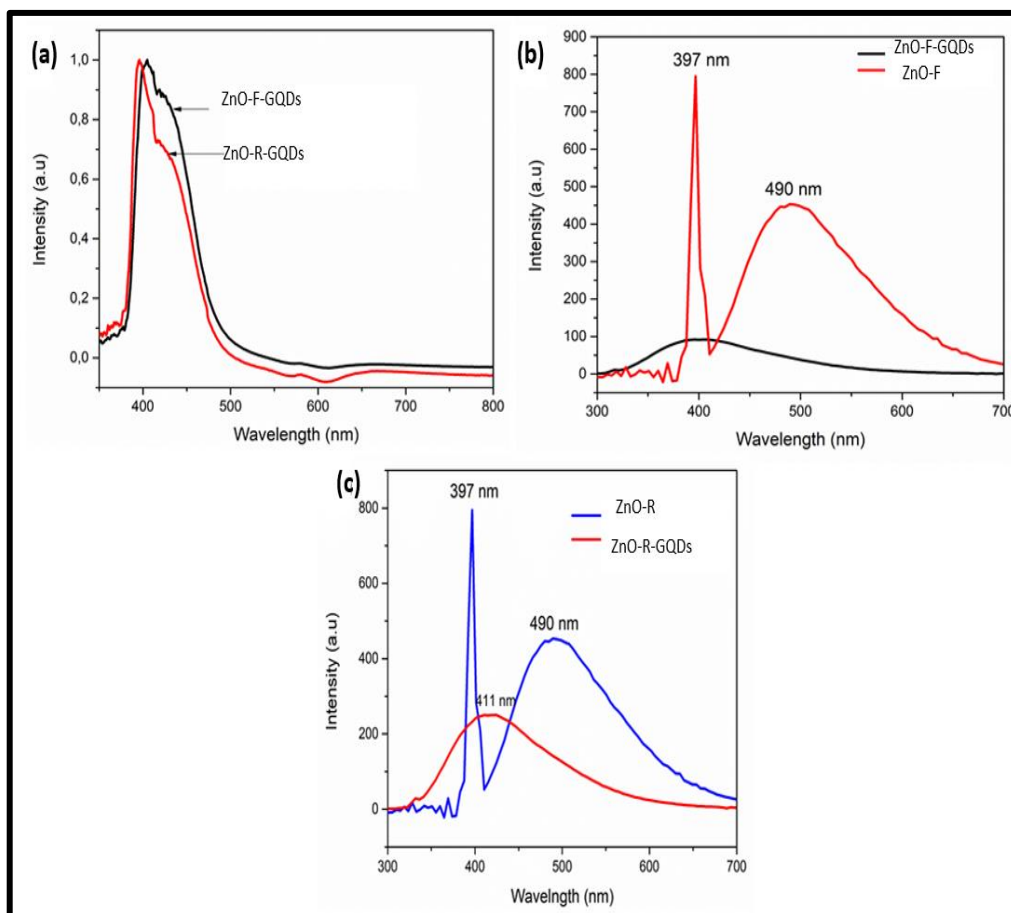
Figure 6.6: (a) UV spectra of (i) ZnO-F-GQDs and (ii) ZnO-R-GQDs (b) PL spectra of ZnO-R and ZnO-R-GQDs and (c) PL spectra of ZnO-F and ZnO-F-GQDs.

6.3.5 Photodegradation results

The photodegradation rate is greatly influenced by electron-hole pair recombination and the PL spectra can be used to determine the rate of recombination. The PL spectra of the ZnO nanostructures before incorporating and after incorporating GQDs were evaluated. All four samples were excited at 325 nm at equivalent concentrations (4 mg/mL). **Figure 6.6b** and **Figure 6.6c** shows an intense sharp narrow peak for the pristine ZnO-R at 397 nm and weaker and broader peaks for ZnO-R-GQDs in the range of 490 nm.

The recombination of free excitons generates the intense peaks in the UV area, while structural defects and singly ionized vacancies provide the larger peaks. When recombination of a photogenerated hole has a singly ionized charged state, this is usual [19, 20]. Both samples showed decreased PL after adding GQDs (**Figure 6.6b** and **c**), with the ZnO-F-GQDs nanohybrid having the largest reduction and loss of the broad band in the green region. The negligible reduction for the in the ZnO-R-GQDs was preceded by a peak broadening and shift to 411 nm. The aforementioned was ascribed the incorporation of GQDs, which increased quantum confinement.

The considerable reduction in PL after adding GQDs indicates a lower rate charge carrier recombination. The incorporation of the GQDs to the ZnO nanostructures allows the capture of photogenerated electrons, thus minimizing recombination with their hole counterparts, according to Akhavan et al. [21]. Non-trapped electron-hole pairs normally recombine; therefore these electrons or holes don't partake in photocatalytic reactions.

These findings corroborate those of the bandgap calculations and UV observations, which all point to the ZnO-F-GQDs nanohybrid being the superior photocatalyst. The better photocatalytic performance of the ZnO-F-GQDs is ascribed to an increased surface area of the nanohybrid, this allows better absorption of solar energy as evidenced by the greater absorption in the visible region as well as the considerable decrease in PL compared to the ZnO-R-GQDs. The effective surface area (the amount of target molecules adsorbing on the surface) is indicative of photocatalytic potential [22].

The contaminant molecules must typically be adsorbed onto the photocatalytic surface for the redox reactions to occur. Surface area and surface defects are critical in the photocatalytic activity of metal-oxide nanomaterials. The larger the effective surface area, the more target molecules will adsorb, resulting in improved photocatalytic activity. Our results contrast those of Manriquez et al. [23], who discovered that the photocatalytic activity of ZnO-R was somewhat higher than that of nanoparticles. Under UV light irradiation, ZnO nanoflowers were better at degrading 4-chlorophenol than ZnO nanorods was.

Absorbance spectra were used to determine the extent of BB dye degradation; intact BB dye absorbs at 573 nm. Degradation was defined as a loss of intensity and a shift in the BB peak position. The spectrum variations of BB dye when illuminated in the presence of nanohybrids are illustrated in **Figures 6.7a** and **b**. The absorbance of the BB dye peak decreased dramatically in the presence of ZnO-F-GQDs, as illustrated in **Figure 6.7a**. The absorption peak at 573 nm was noticeably diminished as time passed and a considerable red-shifting peak was also observed.

Decolorization was evidenced by a decrease in absorbance in the visible region due to deprotonation (cleavage of the N–N link), desulfonation, and desulfonation [24, 25]. The decolorization of the BB dye solution is linked to a decrease in peak absorbance (**Figure 6.7**) (insert). When the ZnO-R-GQDs was applied as a photocatalyst (**Figure 6.7b**), the BB peak gradually decreased with time, but not as drastically as the ZnO-F-GQDs, and the change in colour was likewise not as noticeable (**Figure 6.7b**) insert).
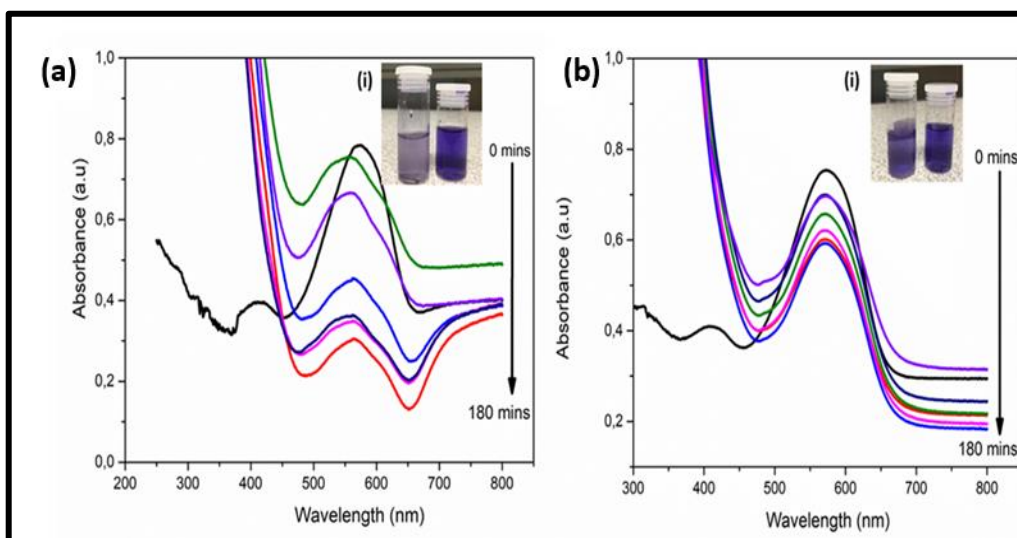
Figure 6.7:   Spectral changes observed during photodegradation of BB dye with (a) ZnO-F-GQDs and (i) BB dye solution using ZnO-F-GQDS (b) ZnO-R-GQDs and (i) Image of BB dye solution with ZnO-R-GQDs.

Experiments were conducted without the use of nanohybrids to determine whether the photodegradation was caused by the nanohybrids or by light. Without the photocatalysts, there was a slight reduction in the BB peak on photolysis as shown in **Figure 6.8a**, indicating that the nanohybrids were the main drivers for the degradation of the BB dye. Further photodegradation experiments were conducted without the GQDs using only the ZnO nanostructures and the changes in the BB peak were not as substantial. The function of GQDs in the nanohybrid was to enhance the formation of ROS and hence the improved photocatalytic efficiency. It should be noted that the ZnO-F (with and without GQDs) outperformed the ZnO-R.
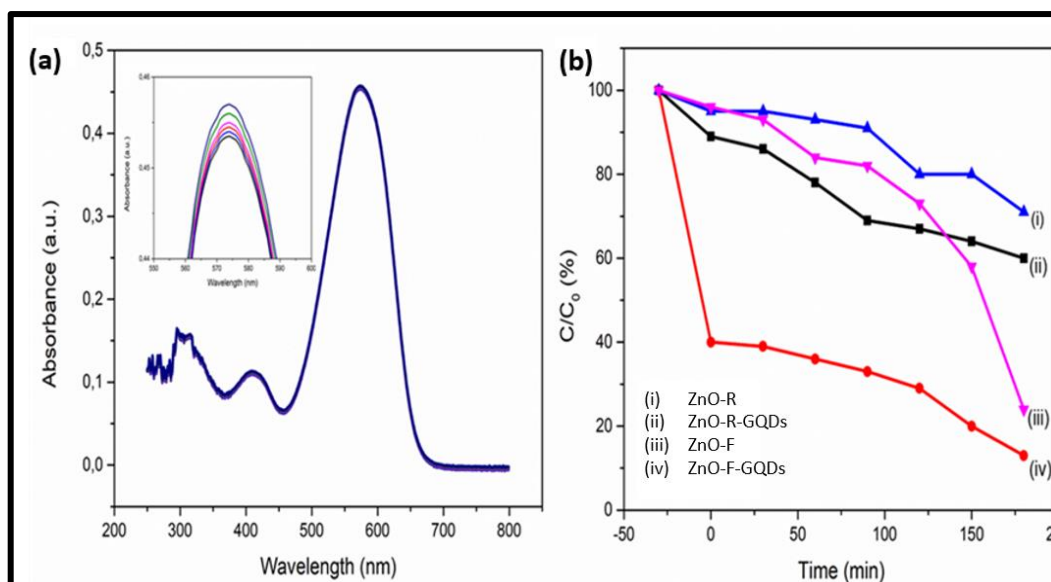
Figure 6.8:   (a) Spectral changes observed during photodegradation of BB dye in the absence of photocatalysts, (b) Photocatalytic degradation of BB dye by (i) ZnO-R (ii) ZnO-R-GQDs (iii) ZnO-F and (iv) ZnO-F-GQDs.

Plotting the different concentrations of the BB dye vs the irradiation time yielded the kinetic data presented in **Table 6.2.** When plotted **In** $= C_0/C$ vs time, the graphs were linear, indicating a pseudo-first order kinetics reaction. As the concentration of the BB dye was increased, the reaction rates (k_{obs}) decreased in the order ZnO-R < ZnO-R-GQDs < ZnO-F < ZnO-F-GQDs. The decrease in reaction rates was anticipated because as the BB dye concentration increases, the number of photons entering the solution will be intercepted, thus

lowering photodegradation rates of BB dye at higher concentrations [26]. At lower concentrations the opposite is true with a greater number of protons being absorbed, in addition a trend was established that; an increase in reaction rate also resulted in shorter half-lives.

Table 6.2: **Rate constant (*kobs*), and half-life (t $_{1/2}$) and R^2 values of various initial concentrations of BB dye.**

	K_{obs} (x 10^{-3} min $^{-1}$)				Half life (mins)				R^2 values			
	ZnO-R	ZnO-R-GQDs	ZnO-F	ZnO-F-GQDs	ZnO-R	ZnO-R-GQDs	ZnO-F	ZnO-F-GQDs	ZnO-R	ZnO-R-GQDs	ZnO-F	ZnO-F-GQDs
0.40	0.032	0.037	0.039	0.044	21.65	18.73	17.77	15.75	0.8926	0.9471	0.9007	0.9784
0.80	0.026	0.31	0.029	0.033	26.65	22.35	23.90	21.00	0.9004	0.9594	0.9431	0.9596
1.20	0.013	0.015	0.017	0.026	53.07	46.20	40.94	26.65	0.9216	0.9301	0.9567	0.9804
2.00	0.003	0.010	0.006	0.014	231.00	69.30	116.00	49.50	0.9351	0.9380	0.9612	0.9812

The largest *kobs* of all photocatalysts studied was ZnO-F-GQDs, which can be attributed to enhanced ROS production, which lead to better photocatalytic efficiency. In contrast, ZnO-R had the lowest photocatalytic activity. The half-lives of the nanohybrids were also estimated; half-life is the time it will take for half of the BB dye to decay, and the nanohybrids' half-lives were shorter and had faster reaction rates. According to the literature [27], the optimum model for describing pseudo-first-order Langmuir-Hinshelwood kinetics were observed to affect initial dye concentration on the photocatalytic transformation.

The linearity of the $\mathbf{In} = {}^{C_0}/_C$ vs time graphs for all samples indicated that they conformed to the pseudo-first-order Langmuir-Hinshelwood kinetics. The photocatalytic effectiveness of the ZnO-F-GQDs nanohybrid produced in the experiments is comparable to those that have been described in the literature by Ebrahimi et al. [27], who obtained roughly 2.8 times

higher photocatalytic performances employing ZnO NWs/GQDs. **Figure 6.8b** depicts a graph of the time variation of C/C_0 of BB dye degraded when using 1 mL of each of the samples. The negative values in the graph reflect the waiting period of 30 mins to allow adsorption and desporption to reach equilibrium. The photocatalytic activity of the ZnO-R was the least efficient, photodegrading only 19% of the BB dye after 180 mins. On the contrary, ZnO-F-GQDs recorded maximum photocatalytic activity amongst all the samples. As anticipated, the ZnO-F-GQDs degraded 80% of the BB dye in 180 mins and nearly entirely decolouring the solution, as shown in **Figure 6.7a**.

6.3.6   Radical scavenging results

To understand the contribution of each ROS, superoxide ($\bullet O_2^-$), hydroxyl ($\bullet OH$), electrons (e^-) or holes (h^+) in the photocatalytic process, scavenging experiments were carried out using radical scavengers using the better performing nanohybrid (ZnO-F-GQDs) . Excess methanol, EDTA-2Na, benzoquinone and silver nitrate were used as radical scavengers for $\bullet OH$, h^+, $\bullet O_2^-$ and e^- respectively. Data from **Figure 6.9** shows that the degradation of BB dye using ZnO-F-GQDs was not influenced by the addition of both EDTA-2Na and silver nitrate indicating that h^+ and e^- had no contribution in the degradation of BB dye. This is likely because the generated h^+ and e^- either recombined or were separated and transferred to surface of the particles. Based on these results in **Figure 6.9**, the chief contributor in the degradation of BB dye were $\bullet OH$ radicals, and this was marked by the noticeable decrease in the BB degradation after the addition of methanol. The degradation percentage reduced to 36% for ZnO-F-GQDs. While $\bullet O_2^-$ was responsible for 9% of the active species for ZnO-F-GQDs respectively.
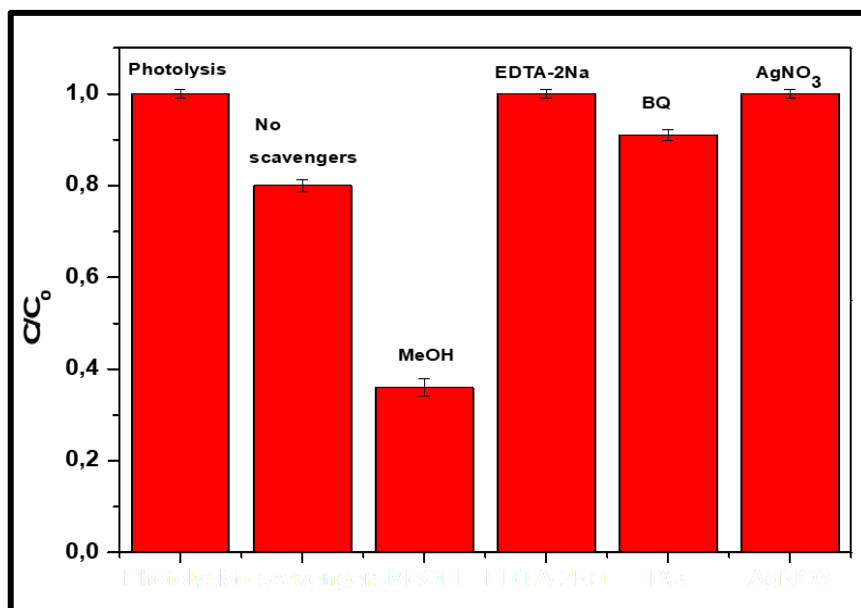
Figure 6.9: Quenching experiments of ZnO-F-GQDs nanohybrid using AgNO$_3$, Methanol, EDTA-2Na and benzoquinone (For comparison purposes experiments in the dark and in the light without scavengers are also included).

On the basis of the findings of the scavenging experiments, •OH and •O$_2^-$ were identified as radicals that contributed to the degradation of BB dye. The proposed underlying photodegradation mechanism radicals of the ZnO nanostructures in the degradation BB dye is presented in **Figure 6.1**. In previous work [28], the CB of GQDs was estimated to be around 3.0 to -3.5 eV which is more negative compared that of ZnO estimated at 4.19 eV. The increased interfacial contact between GQDs and ZnO in the hybrids will promote the transfer of photoexcited e$^-$ in the CB of the GQD to the CB of ZnO which is more negative. While the photoinduced h$^+$ will move from VB of ZnO to the VB of the GQDs and this will result in photoinduced e$^-$/ h$^+$. Owing to the CB potential of the ZnO being more positive (0.31 eV) than that of the GQDs, the transferred e$^-$ from the conduction band of the ZnO are unable to produce •O$_2^-$ [29].

In contrast, the transferred e$^-$ can produce H$_2$O$_2$ when H$^+$ ions are reacted with O$_2$ due to higher positive reduction potential of the O$_2$/H$_2$O$_2$ (0.695 eV). The •OH radicals were subsequently produced as the H$_2$O$_2$ molecules were degraded in the presence of photoinduced electrons [30]. The produced •OH radicals were the main drivers for the photodegradation of BB dye. In contrast, the photoinduced h$^+$ from the VB of the GQDs

were also able to directly photodegrade and mineralize the organic pollutants because they were unable to produce •OH radicals from OH^- and H_2O owing to the positive reduction potential of OH^- / •OH (2.38 eV) and H_2O / •OH. The proposed photocatalytic reaction mechanism is illustrated in **Equations 6.1- 6.6**.

$$GQDs - ZnO \xrightarrow{hv} GQDs - ZnO\ (h^+VB + e^-CB) \tag{Eq.6.1}$$

$$GQDs\ (e^-CB) \rightarrow ZnO\ (e^-CB) \tag{Eq.6.2}$$

$$ZnO\ (h^+VB) \rightarrow GQDs\ ((h^+VB) \tag{Eq.6.3}$$

$$ZnO\ (e^-CB) + H^+ + O_2 \rightarrow H_2O_2 \tag{Eq.6.4}$$

$$H_2O_2 + e^- + hv \rightarrow \bullet OH + OH^- \tag{Eq.6.5}$$

$$\bullet OH + h^+ + pollutants \rightarrow degradation\ products \tag{Eq.6.6}$$
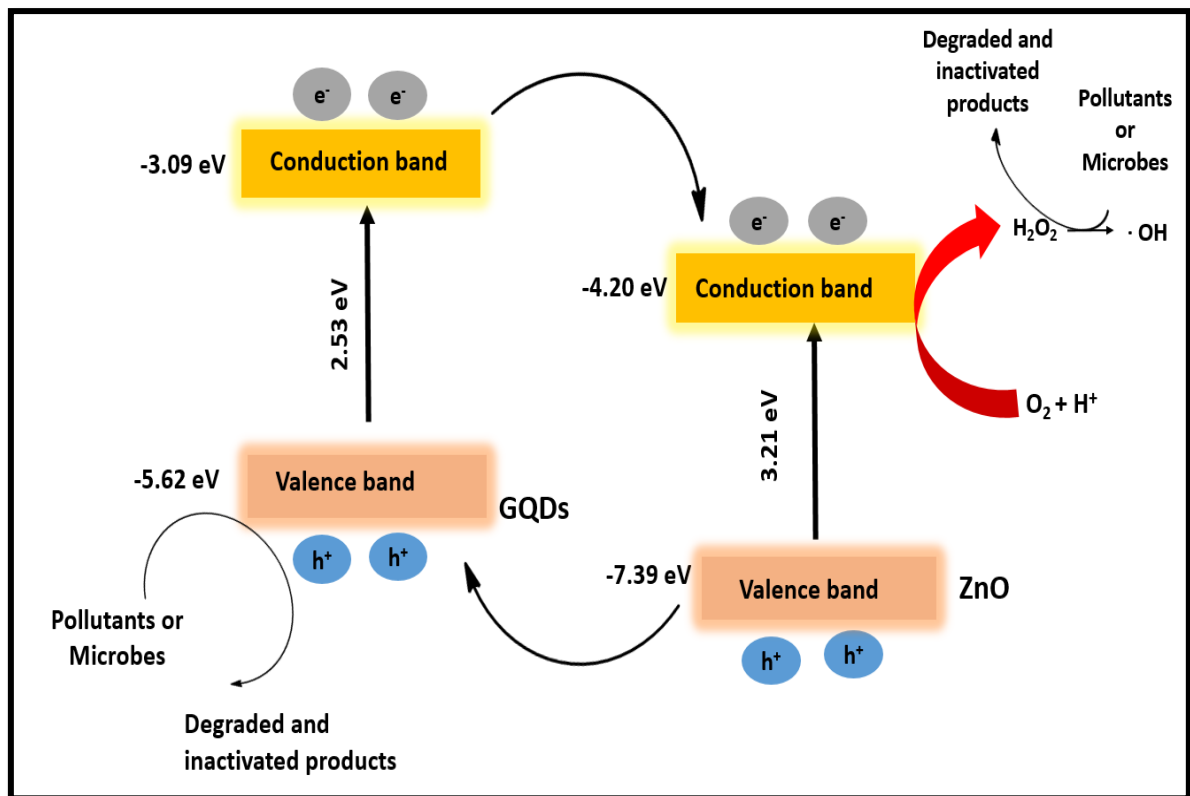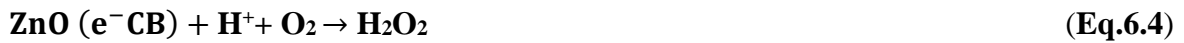
Figure 6.10: The proposed schematic illustration of the photodegradation of BB dye and inactivation of microbes using the nanohybrids.

6.3.7   **Reusability of photocatalysts**

For practical applications, it is critical to assess the stability and reusability of the nanohybrids. Recyclability and reusability tests were conducted using the recycled photocatalyst under similar experimental conditions. After the initial cycle, the nanohybrids were separated, dried in the oven briefly and applied in two subsequent cycles each time using fresh BB dye solution. The results shown in **Figure 6.11** depicts there was no significant change or decrease in the photocatalytic efficiency up to the third cycle of degradation (from 80% to 76%) for ZnO-F-GQDs and from 18% to 16% for ZnO-R-GQDs. Even though the ZnO-R-GQDs had a lower photocatalytic efficiency compared to ZnO-F-GQDs it is interesting to note there was no notable decrease in the photocatalytic efficiency. The obtained experimental results indicate that ZnO-F-GQDs (better performing photocatalyst) remains stable during the photodegradation experiments and can be reused and recycled is thus a suitable for practical applications.
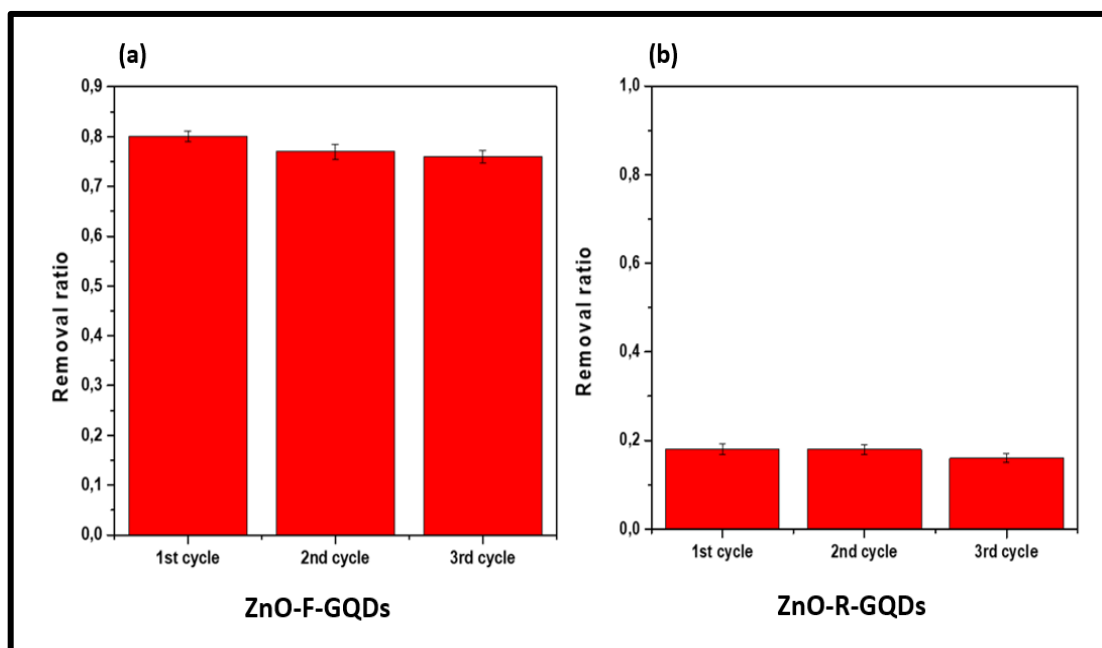
Figure 6.11:   Reusability results of (a) ZnO-R-GQDs and (b) ZnO-F-GQDs in the degradation of BB dye during three consecutive cycles.

6.3.8   **Antimicrobial activity**

If the nanohybrids synthesized have antibacterial activity, they could be employed as a "*dual-nanohybrids*" that exhibit both with photocatalytic and antimicrobial properties. The nanohybrids were tested against *E. coli* and *P. aeruginosa* (Gram-negative) and *S. aureus* and *B. cereus* (Gram-positive). The standard plate count, from which colony-forming unit (CFU) can be calculated, is a method used for quantifying bacterial populations. For the antibacterial studies (**Figure 6.12**), ZnO-R outperform ZnO-F, with the number of CFU for ZnO-R and the ZnO-F-GQDs nanohybrid being much lower. The general trend of the calculated efficiency was ZnO-R-GQDs < ZnO-R < ZnO-F-GQDs < ZnO-F and was more sensitive to the Gram-positive bacteria than the negative counterpart. When it comes to the internalization mechanism, shape plays a big role in the morphology of nanohybrids, which explains why the nanorods penetrate the bacteria's surface much more easily than the nanoflakes. This is also considering the ZnO-F-GQDs aggregated after being linked to the GQDs (**Figure 6.12**).

The antimicrobial performance of the ZnO-R or ZnO-R-GQDs can also be justified using active facets; normally, spherical NPs have (100) facets, but ZnO-R have (111) and (100); literature [31] has shown that nanoparticles with (111) have better antimicrobial efficiency. We anticipated the ZnO-F-GQDs to be significantly more efficient than ZnO-R since GQDs' function in the nanohybrid was to boost ROS production. However, this was not the case, indicating that shape is important. As a result, we hypothesize that inhibition occurs first through internalization (thus the preference for the rod-structure), which disrupts cellular function, and then through the generation of ROS. Gram-positive bacteria are more susceptible to nanohybrids than Gram-negative bacteria owing to structural differences in the cell walls of the bacterium.
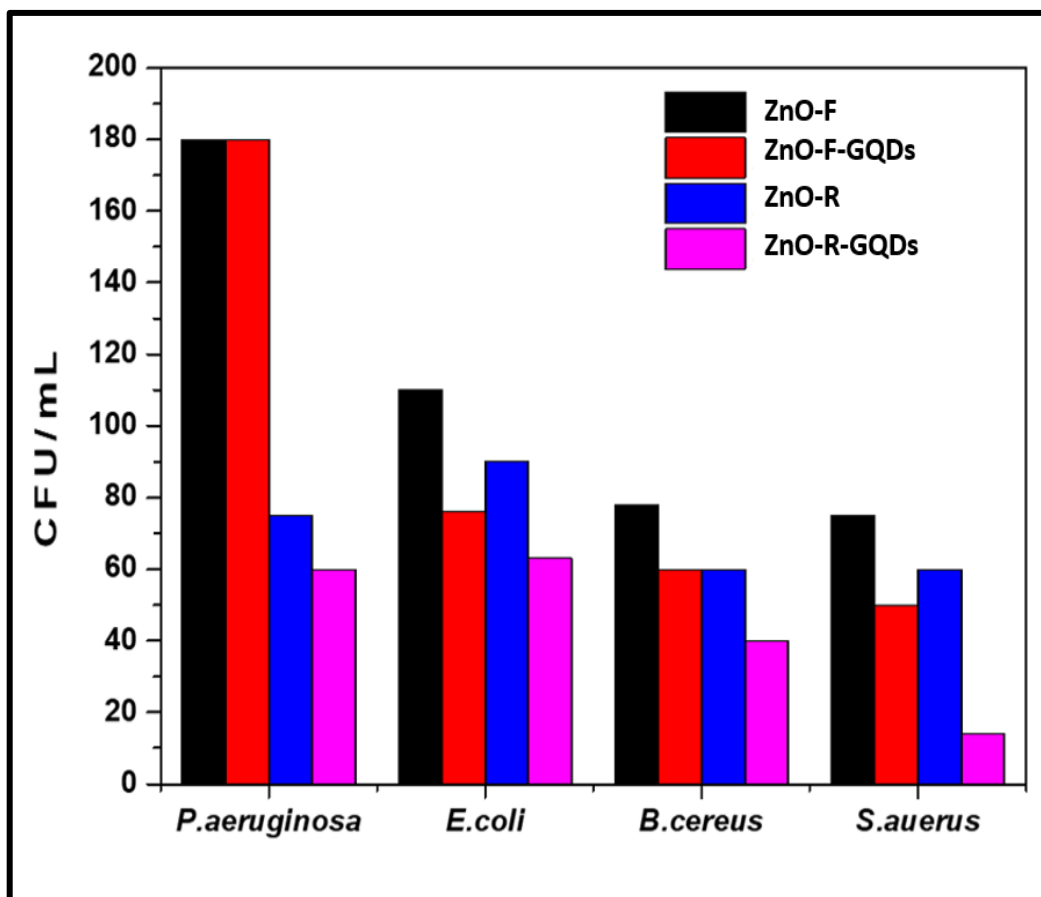
Figure 6.12: Calculated Colony-forming unit *E. coli, P. aeruginosa, B. cereus and S. aureus* when tested against ZnO-R, ZnO-R-GQDs, ZnO-F and ZnO-F-GQDs.

6.3.9 Disc diffusion method

Measurements of ZOI (**Figure 6.13**) yielded results were consistent with the CFU data, indicating that ZnO-R-GQDs had superior antibacterial activity. This is linked to the nanohybrids' shape and proposed antibacterial action, which allows for improved internalization of the nanohybrid. ZnO-R-GQDs had the largest inhibitory zone against *S. aureus* (40 mm), followed by ZnO-R-GQDs against *E. coli* (37 mm). ZnO-F, on the contrary, had a ZOI against *E. coli* of 11 mm. No inhibition was observed when ZnO-F and ZnO-F-GQDs were evaluated against *P. aeruginosa*, which was ascribed to the Gram-negative bacteria's cell morphology. Apart from the ZnO-F and ZnO-F-GQDs evaluated against *P. aeruginosa*, we found that adding GQDs to the nanohybrid increased its antibacterial properties.

The ZnO-R and ZnO-R-GQDs were able to penetrate further into the bacterial membrane due to their distinctive rod structure, causing irreparable damage to the respiratory enzymes and cytoplasmic contents, culminating in bacterial cell death [25].
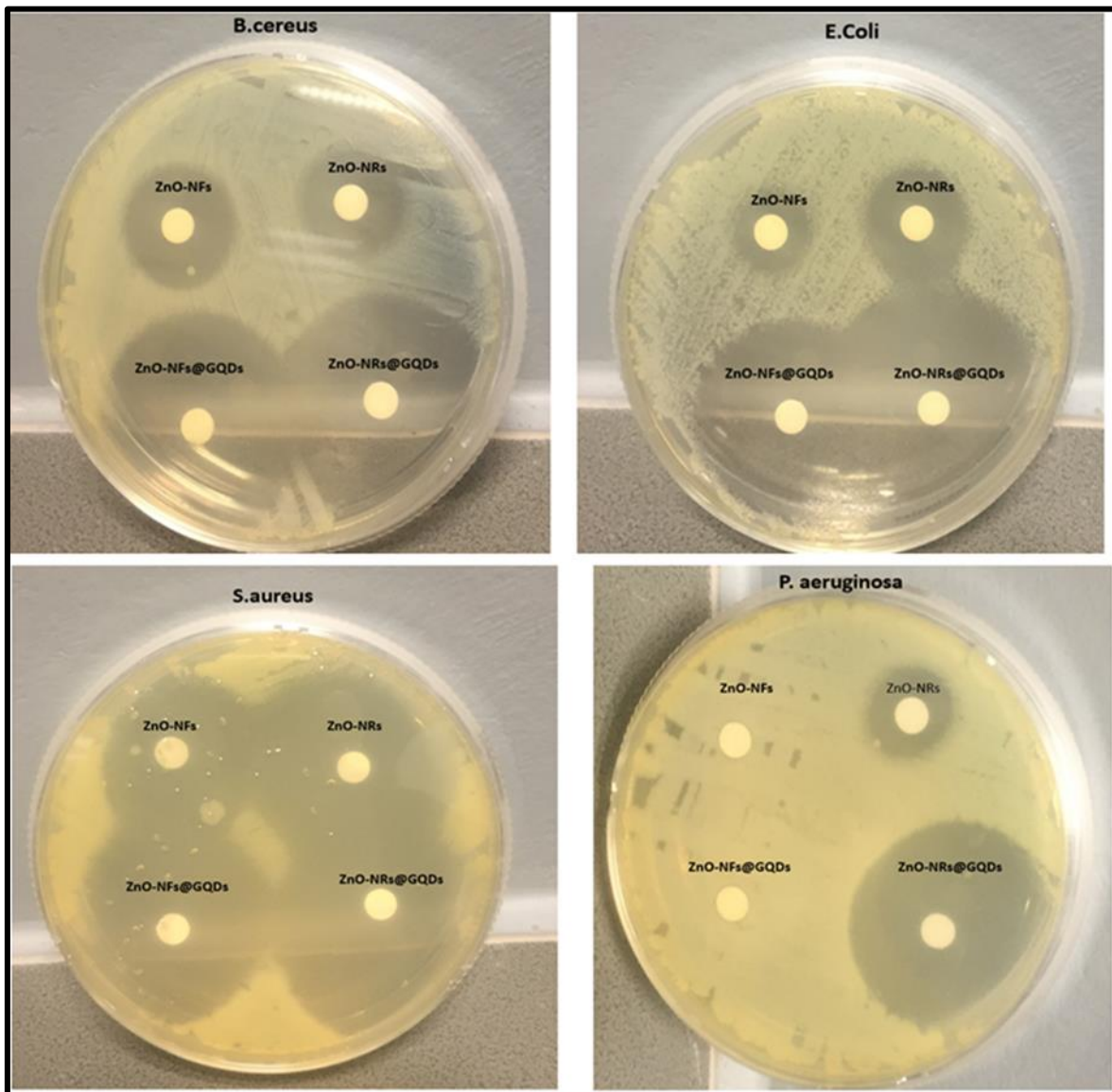
Figure 6.13: Inhibitory effect of the ZnO nanostructures and their nanohybrids on Mueller Hinton agar plates tested against *E. coli, P. aeruginosa B. cereus and S. aureus.*

6.3.10 **Antimicrobial mechanism**

The antimicrobial mechanism was postulated based on the better performing nanohybrid (ZnO-R-GQDs) (**Figure 6.14**). The inhibitory mechanism occurs in three molecular steps (i) Destruction cell wall/membrane, (ii) production of ROS and (iii) interaction with DNA/RNA to inhibit cell proliferation. For gram-negative bacteria, based on previous reports it is known that the outer membrane of gram-negative bacteria is typically made up of lipoteichoic acid which is composed mostly of a significant amount of polyphosphate anions [32]. This results in the outer membrane being negatively charged. This facilitates the electrostatic attraction between Zn^{2+} ions and the polyphosphate anion in outer membrane. The Zn^{2+} ions will diffuse through the outer membrane to reach the ribosome and mitochondria, the ZnO-R nanohybrids will diffuse with more ease compared to the ZnO-F nanohybrids.Inside the cytoplasm the activity of protein synthesis from the ribosome will be reduced and the activity of nicotinamide adenine dinucleotide hydrogen (NADH) in the mitochondria will also be prevented and thus killing the chromosomes. Alternatively, the interaction and direct attachment of GQDs to the phospholipid bilayer could result in the shrinkage of the cell membrane which leads to cell rupture and ultimately the discharge of cellular materials [33]. The accumulation of the nanohybrids either *via* diffusion of direct attachment on the surface of the cell will create membrane stress in the cell wall and cause cell membrane destruction as well as the leakage of the cytoplasma [34].
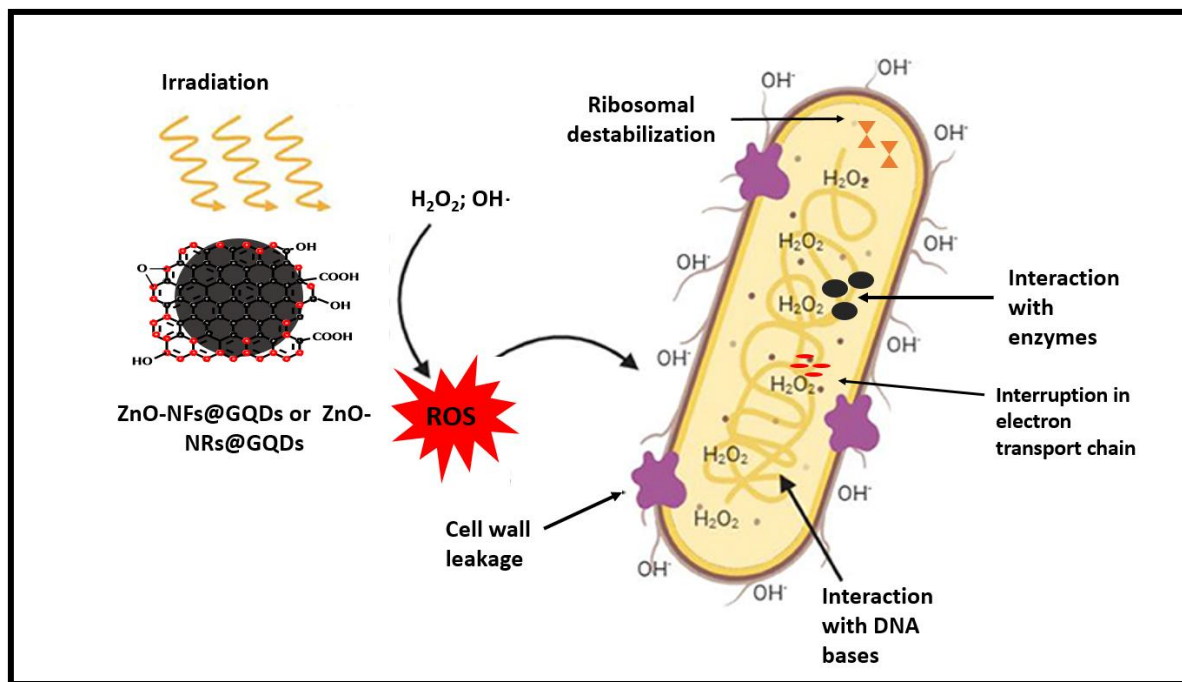
Figure 6.14: Representative illustration of the antimicrobial mechanism of ZnO-R-GQDs in the inactivation of microorganisms.

Furthermore, the release of Zn^{2+} and GQDs facilitates the formation of ROS which can occur on the inside and in some instances on the outside of the bacterial cells. In the case of GQDs, the high electron transfer facilitates the formation of excessive free radicals. In literature other radical such as per-hydroxyl anions OH^-, O^{2-} and triplet oxygen have been reported as some of the radicals responsible in the inactivation of microbes [32]. When ROS generated by the ZnO-R-GQDs nanohybrid accumulates in the bacterial cell it will hinder the replication and respiration, and will damage the lipids, mitochondria, ribosome as well as the chromosomes and will result in cell apoptosis. Both the Zn^{2+} ions and GQDs in the ZnO-R-GQDs nanohybrid will interact with nucleic acids and proteins and will hinder the cell replication and division as well as the adenosine triphosphate (ATP) production which cause cell death.

6.4   Conclusion

GQDs were successfully linked to the ZnO nanostructures and the influence of the shape of the ZnO NPs in the nanohybrids was studied, the key findings from this chapter were:

- The bandgap of the photocatalysts were reduced as a consequence of linking GQDs to the ZnO, as well as the rate of charge carrier recombination. The PL spectra of the nanohybrids significantly decreased as a result. The photocatalytic performance of ZnO-F-GQDs was higher compared to the ZnO-R counterpart, this enhanced photocatalytic performance was ascribed to the greater surface area of the ZnO-F, which allowed more solar energy to be absorbed.

- The incorporation of GQDs reduced the bandgap as follows; for ZnO-F-GQDs and ZnO-R-GQDs, the bandgap was reduced from 2.98 to 2.61 eV and 3.00-2.79 eV, respectively.

- Through the photolysis experiments, it was shown that adsorption was not the main mechanism responsible for the dye removal. The photocatalytic findings show that ZnO-F-GQDs (80%) outperformed ZnO-R-GQDs (18%) and the results were corroborated by optical data and PL tests.

- For the antimicrobial studies, ZnO-R-GQDs showed enhanced bacterial inhibition compared to ZnO-R-GQDs when tested against the four representative bacteria. The enhanced inhibition of the ZnO-R was directly linked to the shape of the rods. Based on the proposed antimicrobial mechanism, the nanohybrids initially get internalized by the bacterial cells before disrupting cellular function (thus the preference for hence the rod-shaped). The antimicrobial efficiency was in the order: ZnO-F < ZnO-F-GQDs < ZnO-R < ZnO-R-GQDs with superior efficiency being against *S. aureus*.

Finally, this chapter showed the choice of nanohybrid would be largely informed by the intended application. In photocatalytic experiments; a better option would be ZnO-F-GQDs, whereas for antimicrobial applications ZnO-R-GQDs would be better suited.

References

1. Ananthanarayanan A, Y. Wang, P. Routh, M.A. Sk, A. Than, M. Lin, J. Zhang, J. Chen, H. Sun, P. Chen, *Nanoscale* 7 (17) (2015) 8159.

2. Feng Q. Cao, M. Li, F. Liu, N. Tang, Y. Du, *Appl. Phys. Lett.* 102 (1) (2013) 013111.

3. Sweetman S.M. Hickey, D.A. Brooks, J.D. Hayball, S.E. Plush, *Adv. Funct. Mater*. 29 (14) (2019) 1808740.

4. Li B. P. Zhang, J. X. Zhao, Z. H. Ge, X. K. Zhao, L. Zou, *Appl. Surf. Sci*. 279 (2013)367.

5. Li L. Wang, J. Ge, J. Wang, Q. Li, W. Wan, B. Zhang, X. Liu, W. Xue, *RSC. Adv*. 6 (2016)106508.

6. Rani P. Suri, P. K. Shishodia, R. M. Mehra, *Sol. Energy Mater. Sol. Cells*. 92 (2008)1639.

7. Dong J. Shoa, C. Chen, H. Li, R. Wang, Y. Chi, G. Chen, *Carbon*. 50 (2012) 4738.

8. Jena R. Narayan, K. V.S. N Raju, *Prog. Org. Coat*. 89 (2005)82.

9. Vafaee M. S. Ghamsari, *Mater. Lett*. 61 (2007)3265.

10. Zhaochun H. Baibiao, Y. Yongqin, C. Deliang, *Mater. Sci. Eng. B*. 86(2001)109.

11. Huang M. Liu, Z. Li, Y. Zeng, S. Liu, *Mater. Sci. Eng. B*. 97(2003)111.

12. Manna S. Bhattacharya, S. Sengupta, P. Das, *J. Clean. Prod*. 203 (2018) 83.

13. Xu L.W. Zhang, H.Y. Cheng, Y.F. Zhu, *Mater Chem Phys*.132 (2012) 673.

14. Goh X. Xu, P. G McCormick, *Scr. Mater*. 78(2014)49.

15. Naik P. Sutradhar, M. Saha, *J. Nanostructure. Chem.* 7 (2017) 85.

16. Oba Y. Kumagai, *Appl. Phys. Express*. 11(6) (2018), 060101.

17. Ristić S. Musić, M. Ivanda, S. Popović, *J. Alloys.Compd*. 397(2005) 4.

18. Janotti C. G Van der Walle, *Rep. Prog. Phys*. 72 (2009)126501.

19. Xing Z. H. Xi, Z. Q. Xue, X. D. Zhang, J. H. Song, R. M. Wang, J. Xu, Y. Song, S. L. Zhang, D. P. Yu, *Appl. Phys. Lett*. 83 (2003)1689.

20. Djurišić Y. H. Leung, *Small*. 2 (2006)944.

21. Akhavan E. Ghaderi, K. Rahimi, J. *Mater. Chem.*22 (2012) 23260.

22. Vrinceanu R. M. Hlihor, A. Simion, L. Rusu, N. Barka, L. Favier, *Catalysts*. 9(9) (2019) 761.

23. Manriquez Ramirez J. A Wang, J. R. Gómez Romero, C. M. Reza San Germán, J. G. Hernandez Cortez A. Zuniga Moreno, M. Estrada Flores, *Sci. Res. Essays*. 2(10) (2014)469.

24. Abidin C.Z.A., Fahmi, M.R., Soon-An, O., Makhtar, S.N.N.M. and Rahmat, N.R., 2015. *Science Asia* 41 (2015) 49.

25. Nzaba S.K.M., Ntsendwana, B., Mamba, B.B. and Kuvarega, A.T. *Environ Sci. Pollut. Res.* 25 (2018) 15146.

26. Ebrahimi M. Samadi, S. Yousefzadeh, M. Soltani, A. Rahimi, T. Chou, L.C. Chen, K.-H. Chen, A.Z. Moshfegh, ACS Sustain. *Chem. Eng.* 5 (2016)367.

27. Pal Y. K. Tak, J. M. Song, *Appl. Environ. Microbiol.* 73(6) (2007) 1712.

28. Rahimi A, Yazdani M, Ahmadirad M, *Mater. Res. Bull.* 98 (2018) 148.

29. Zakria H.S, Othman M.H.D, Kamaludin R, Kadir S.H.S.A, Kurniawan T.A, Jilani A, *RSC Advances* 11(12) (2021)6985.

30. Jafari N, Derlon, P. Desmond M.C, van Loosdrecht, E. Morgenroth, C. Picioreanu, *Water Res.* 157 (2019) 335.

31. Ajmal I. Majeed R.N. Malik, H. Idriss, M.A. Nadeem, *RSC Adv.* 4 (2014) 37003.

32. Anwer H, A. Mahmood, J. Lee, K.H. Kim, J.W. Park, A.C. Yip, *Nano Res.* 12 (5) (2019) 955.

33. Ayodhya G. Veerabhadram, *Mater. Today Energy* 9 (2018) 83.

34. Rojas-Andrade G. Chata D, Rouholiman J, Liu C, Saltikov S. Chen S, *Nanoscale* 9 (3) (2017) 994.

CHAPTER 7

THE SYNERGISTIC EFFECT OF PERACETIC ACID ACTIVATED BY GRAPHENE OXIDE QUANTUM DOTS IN THE INACTIVATION OF E. COLI AND ORGANIC DYE REMOVAL

7.1   Introduction

This chapter presents the use of peracetic acid (PAA) an organic peroxide that is capable of producing highly reactive species as an oxidant. PAA has also been considered as a possible replacement for chlorine-based oxidants in the wastewater treatment largely because it does not generate toxic by-products such as haloacetics and trihalomethanes (THMs) during the disinfection process [1-3]. To date, transition metals, metal oxides and have been applied as catalysts in the activation of PAA [4-6]. The drawbacks of these activation methods include leaching, poor reusability of the catalyst, toxicity of metal catalyst and catalyst deactivation as well the high cost of using UV [7]. To overcome these limitations cost-effective, green and metal-free catalysts are recommended. The use of GQDs as metal-free catalyst in the activation of PAA for the degradation of organic dyes is reported for the first time in this chapter. Further this chapter exploits PAA's disinfection abilities in the inactivation of *E. coli.* The objectives of this chapter were to; (a) present the assessment of the performance of GQDs on PAA activation using a model Brilliant Black (BB) dye and the photodegradation kinetics therein (b) evaluate the inactivation of *E. coli* in the same BB dye mixture (c) study the effect of controlling PAA dosages and GQDs concentration and (d) explore the reactive radical species in PAA activation and examine the *E. coli* inactivation mechanism of PAA by GQDs.

7.2   Experimental details

7.2.1   Preparation of GQDs

GQDs as shown in **Scheme 3.1** in **Chapter 3** were synthesized as per the synthesis method detailed in **Chapters 3** and **4.**

7.2.2   Degradation of BB dye using GQDs/PAA

The photocatalytic degradation experiments of the dye was conducted as described in **Chapter 3**.

7.2.3   Identifying reactive species in photodegradation process

Scavenging experiments were carried out as outlined in **Chapter 3**.

7.2.4   Kinetic studies

Kinetic rate constants and half-lives were calculated using the integrated Langmuir-Hinshelwood (L-H) model as detailed in **Chapter 3**.

7.2.5   LC-Q-TOF-MS and detection conditions

LC-Q-TOF-MS analysis was carried out on an Acquity BEH C18 column (2.1 x 100 mm, 1.7 µm, employing an Agilent 1200 binary pump system. Details of the mobile phase, stationary phase as well as the detection conditions are specified in **Chapter 3**.

7.2.6   Bacterial inactivation

E. coli (ATCC 25922) was used as model bacteria. The experimental procedure employed was adopted from Flores et al. [8] and the exact details are outlined in **Chapter 3.**

7.2.7   Cell viability

The viability of *E. coli* cells was examined using LIVE/DEAD *Bac*light staining kit the principle of the staining kit and the experimental procedure are detailed in **Chapter 3**.

7.3   Results and discussion

7.3.1   Activation of PAA using GQDs

The activation of PAA was evaluated using BB dye as the model dye, **Figure 7.1a** shows that the degradation profile of BB dye in the presence of PAA (0.05 mM) alone was negligible, while about 30% decolourisation was observed in the presence of GQDs (0.05 g/L) alone. In the GQDs/ PAA system (using 0.05 g/L GQDs and 0.05 mM) almost 80% of the BB dye was degraded after 150 mins (**Figure 7.1b** and **c**). In its stable form, BB dye absorbs strongly at 573 nm, and any loss in peak intensity is considered as indication of degradation due to the breakdown of the colour-responsible chromophore. For the GQDs (0.05 g/ L) alone, the BB dye peak gradually decreased with a maximum discoloration of 2%, while in the GQDs/PAA system (using 0.05 g/L GQDs and 0.05 mM), enhanced degradation occurred in the first 30 mins and with further degradation of the dye up to 73%. This suggests that the naphthalene ring structure and azo bonds of the dye were oxidized by the PAA and that the PAA had a synergistic effect on the overall degradation of BB dye [9]. Other researchers further ascribed the decrease in peak intensity of the BB dye to the cleavage of the N-N bond (deprotonation) and ring opening (desulfonation) [10]. One can further postulate that PAA was largely responsible for generating the reactive species that were responsible for degrading the dye. A noteworthy observation was made at 240 nm; very little changes were observed in the intensity throughout the entire experiment giving evidence that the benzene structure was stable during the oxidation process.

The commercial PAA solution used in this work contained 4.5% *w/w* of H_2O_2. The contribution of H_2O_2 in the photodegradation of BB dye was evaluated (**Figure 7.1d**). The results showed that the degradation of BB dye in the presence of H_2O_2 (same concentration as in the commercial PAA solution) was negligible; meaning that the H_2O_2 in the PAA solution had minimal effect on the degradation. This further confirmed that PAA was better

activated by GQDs compared to H_2O_2 and this is attributed to the peroxide bond energy of the PAA which is reported to be lower (159 kJ mol^{-1}) than that of H_2O_2 (213 kJ mol^{-1}) [11]. The dissociation of the peroxide bond in PAA will easily generate reactive species than H_2O_2 [12].
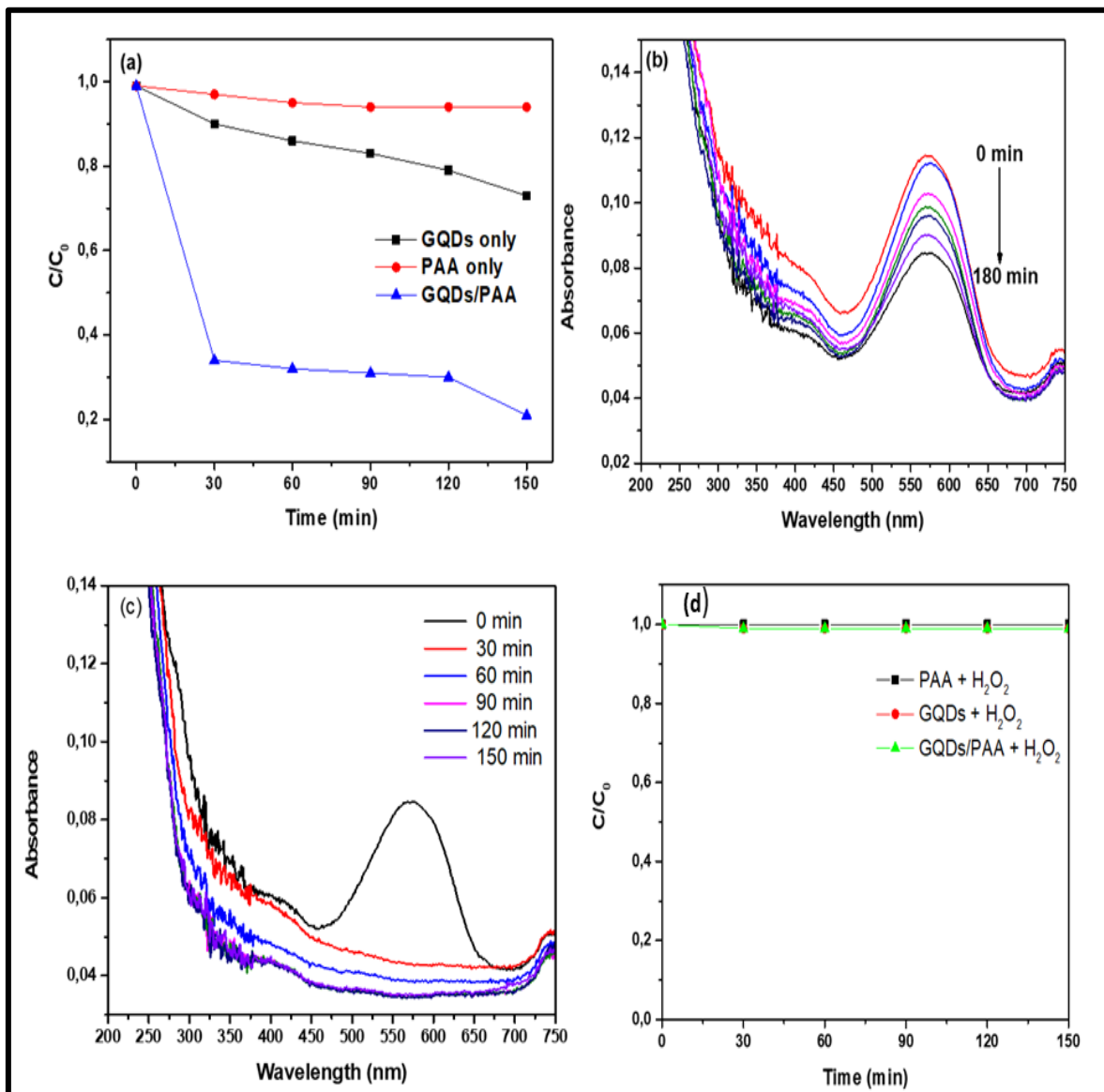
Figure 7.1: (a) Comparison of the degradation of BB dye using GQDs alone (0.05 g/L), PAA alone (0.05 mM) and GQDs/PAA system (0.05 g/L, 0.05 mM), degradation profile of BB dye using (b) GQDs and (c) GQDs/PAA system and (d) degradation of BB dye in the presence of H_2O_2.

Effect of GQDs loading

The effect of GQDs loading on the degradation of BB dye was evaluated by increasing the GQDs dosage and the results are presented in **Figure 7.2a**. In the absence of GQDs, very little of the dye was degraded (less than 3%). The minimal degradation was attributed to self-photolysis and previous work done by Shao et al. [13] and Xiang et al. [14] attributed this phenomenon to the self-degradation of photo-excited dyes. Upon increasing the GQD loading to 0.05 g/L the efficiency increased to 27%. A further increase in the loading to 0.10 and 0.15 g/L resulted in further enhancement of the degradation to 73% and 98% respectively. This trend can be best comprehended in terms of the availability of active sites present on GQDs which enhance their ability to generate ROS and effectively degrade the dye [15]. This also gives evidence that GQDs had significant impact in the GQDs/PAA system due to its activation of the PAA to produce radical species. Similarly, the influence of PAA concentration on the GQDs/PAA system in the degradation of the dye was investigated.

The concentration of GQDs (0.05 g/L) was kept constant in the system while varying the PAA concentration. In the absence of PAA, GQDs degraded 27% of the dye; this is due to known photocatalytic effects of GQDs. Increasing the PAA concentration resulted in an increase in the degradation of the dye. With a further increase of the PAA concentration; the anticipation was that this will significantly enhance the degradation efficiency even further, however from **Figure 7.2b** it was observed that the efficiency was only slightly enhanced. This can be explained in terms of the limited available reactive sites on GQDs to activate the PAA [16]. Alternatively, high loading of GQDs may have resulted in excessive reactive sites for PAA activation therefore quenching the reactive species generated from PAA activation [17].
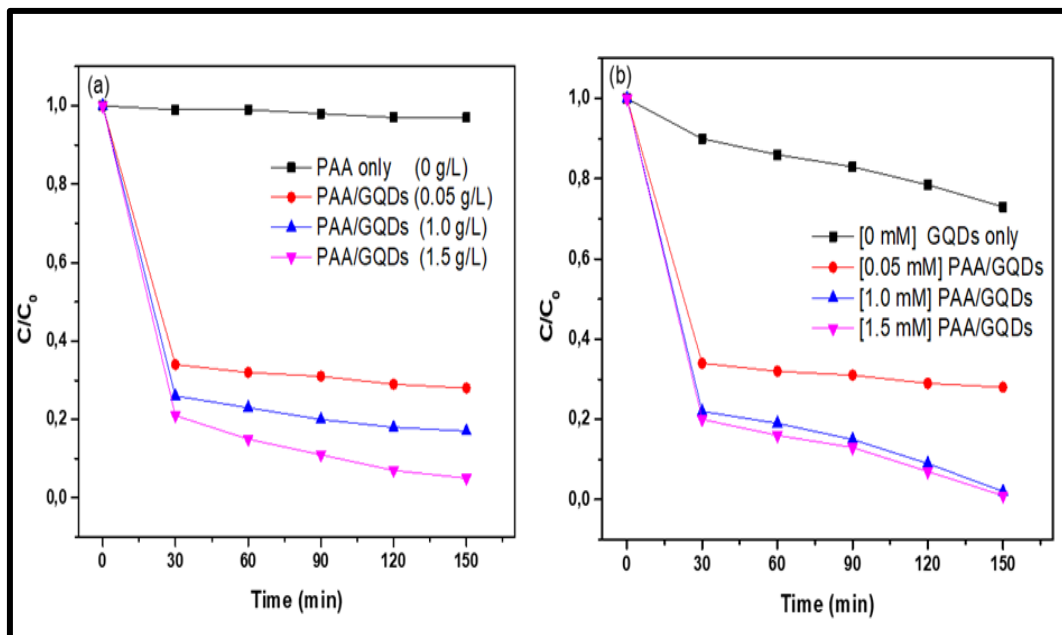
Figure 7.2: (a) Effect of GQDs loading in the GQDs/PAA system and (b) influence of the PAA concentration on the GQDs/PAA system in the degradation of BB dye.

7.3.2 Kinetic studies

To understand the photodegradation of the BB dye employing the PAA/GQDs system kinetic studies were carried out. The results were fitted to a pseudo-first order model and a linear plot was obtained by plotting $\mathbf{In} = {}^{C_0}/_C$ versus irradiation time. The kinetic data of the BB dye photodegradation are presented in **Figure 7.3**. A linear relationship was observed implying that all the reactions followed first-order kinetics. An increase in GQDs loading resulted in an increase in the rate constant which can be explained by availability of more active sites for the activation of PAA [18]. This indicated a synergistic effect of the PAA and GQDs during the reaction; such synergistic effect was possibly due to the activation of the PAA by GQDs.
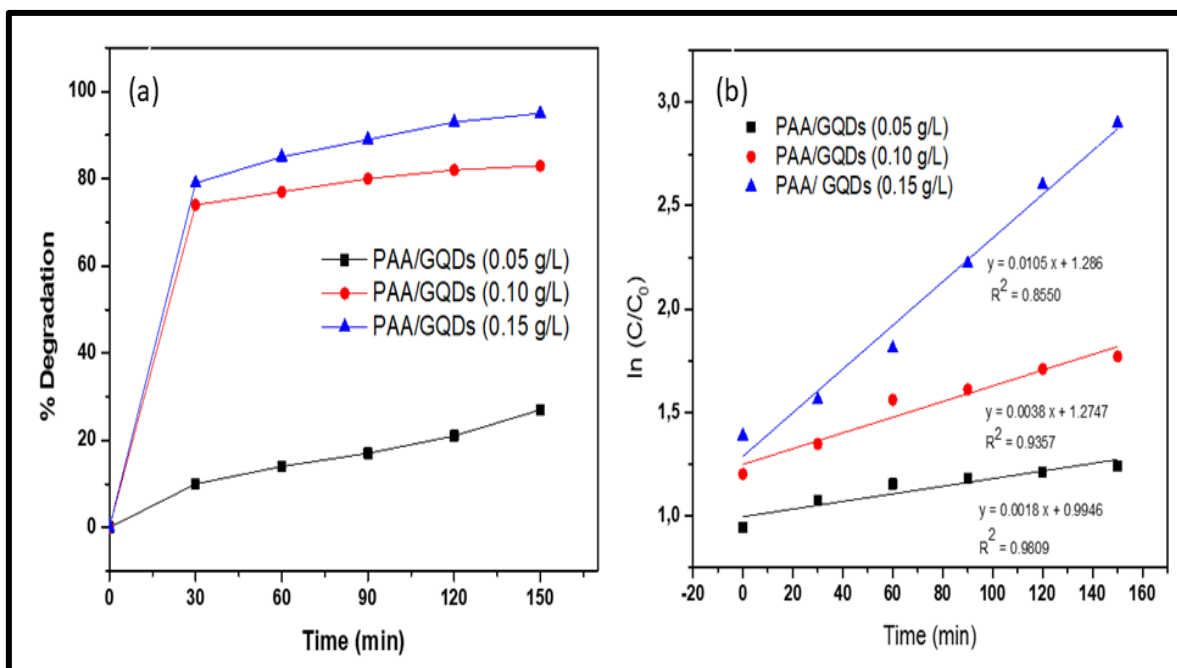
Figure 7.3: (a) Photodegradation efficiency and (b) Photodegradation kinetics of the PAA/GQDs system in the degradation of BB dye.

Kinetic data presented in **Table 7.1** show that an increase in the reaction rate was accompanied by a higher catalytic activity (faster decolorization) and shorter half-lives.

Table 7.1: **Kinetic parameters of the GQDs/PAA system.**

Sample	Photodegradation (%)	Rate constant (min $^{-1}$)	Half-life (mins)	R^2
PAA/GQDs (0.05 g/ L)	27	0.0018	6.42	0.9808
PAA/GQDs (0.10 g/L)	83	0.0038	3.03	0.9357
PAA/GQDs (0.15 g/L)	95	0.0105	1.1	0.8550

In previously reported work, Zhou et al. [19] conjectured that the removal of Reactive Brilliant Red X-3B (RR X-3B) using activated carbon filters ACFs/PAA system occurred through: adsorption and *in-situ* catalytic oxidation of the dye. In this present study, to rule out adsorption, photolysis experiments were carried out. From **Figure 7.4a** it is evident that the degradation of the dye was as a direct result of oxidation rather than through adsorption since the experiments carried out in the dark showed no degradation and thus validating the hypothesis.

7.3.3   Role of GQDs during the catalytic reaction

ACFs have an abundance of non-bonding free electrons [20, 21] in previous work done using ACFs to activate PAA; the speculation was that the free electrons were transferred to PAA to promote the generation of free radical species in the oxidation [22]. On the other hand, GQDs do not have free electrons as such it is proposed that the oxygen-rich surface of the GQDs accelerates its homolytic cleavage to generate radicals that result in the degradation of the dye.

7.3.4   Identifying active species

Typically, during the electron-hole pair photogeneration on the photocatalyst, various radical species can be formed. Such examples include the possibility of forming •OH due to the reaction of h^+ with H_2O as well as OH^-. Additionally, superoxide ion radicals ($•O_2^-$) can be formed in cases where free electrons (e^-) react with oxygen molecules. To determine which radicals were key in the photodegradation of BB dye in the PAA/GQDs system, quenching experiments were carried out by introducing radical scavengers to trap various radicals [23]. Should the photodegradation process occur due to the production of any of the radical species, the expectation is that the process should be moderate or completely hindered in the presence of the corresponding scavenger. To date, $CH_3•$, $CH_3O_2•$, •OH, CH_3C (=O) OO• have been recorded in literature as some of the radicals that exist when PAA is activated (**Equations 7.1-7.5**) [24]. **Equation 7.1** is the rate determining step in the homolysis of the oxygen-oxygen bond that is activated by GQDs. Of all the radicals produced HO•, $CH_3COO•$ are considered to be the most important in the degradation of contaminants. (**Equation 7.2**)

has a lower reaction rate compared to •OH and oxygen and as such is not as efficient [25, 26].

$$GQDs + CH_3C (=O) OOH \leftrightarrow GQDs + CH_3C (=O) O• + •OH \quad (Eq.7.1)$$

$$GQDs + CH_3C (=O) O• \rightarrow CH_3• + CO_2 \quad (Eq.7.2)$$

$$CH_3• + O_2 \rightarrow CH_3O_2 \quad (Eq. 7.3)$$

$$CH_3C (=O) OOH + •OH \rightarrow CH_3C (=O) OO• + H_2O \quad (Eq. 7.4)$$

$$CH_3C (O) OOH + CH_3C (=O) O• \rightarrow CH_3C (O) OO• + CH_3C (O) OH \quad (Eq. 7.5)$$
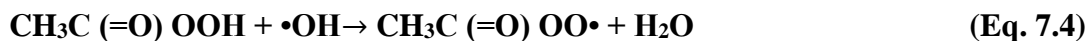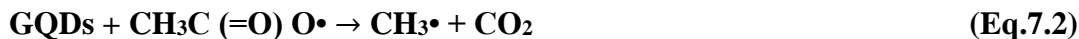
Reports have shown that other radical species may also contribute to the degradation of contaminants. Cai et al. [27] demonstrated the role of •OH in the degradation of ibuprofen and carbamazepine in UV/PAA system. This happens when the molecular oxygen near the interface of the GQDs/PAA is reduced to $•O_2^-$ which further reacts with H^+ to produce $HO•_2$. The $HO•_2$ will dissociate into H_2O_2. The H_2O_2 groups interact with the generated CB electrons to produce additional radicals.

$$(•O_2^-)_{ads} + H^+ \rightarrow HOO• \quad (Eq. 7.6)$$

$$2 HO_2^• \rightarrow H_2O_2 + O_2 \quad (Eq. 7.7)$$

$$H_2O_2 + e^- \rightarrow OH^- + •OH \quad (Eq. 7.8)$$

The effect of each radical scavenger on the BB photodegradation by the GQDs/PAA system is presented **Figure 7.4a**. The degradation of BB dye using the GQDs/PAA system without scavengers is also included in the figure for comparative purposes. As demonstrated in **Figure 7.4b**; the BB dye did not degrade under irradiation in the absence of the GQDs/PAA indicating that the dye is photostable and the photodegradation is as a direct result of the and not self-photolysis of the dye.

The addition of 0.1 mL $AgNO_3$ did not have a significant effect on the degradation efficiency inferring that the contribution of e^- in the BB decolourization was minimal and that the recombination of electron and holes was not restrained. Similarly, the addition of both p-benzoquinone and EDTA-2Na had no significant effect on the degradation efficiency. To the contrary, the addition of methanol reduced the degradation efficiency by almost 90% indicating that in the PAA/GQDs system, •OH radicals play a significant role. This is

ascribed to the abundant hydroxyl groups on the GQDs, and the hydroxyl radicals are formed from the homolytic cleavage upon irradiation. Rojas-Andrade et al. [28] looked at the main difference in hydroxyl formation between GQDs and reduced-GQDs and the results show that the composition of vinyl carbons and the expanded conjugation were responsible the hydroxyl radical formation. Additionally, peroxy radicals were key in the degradation of the BB dye as it has been demonstrated in literature [29], that in addition to scavenging •OH radicals, methanol can also react with peroxy radicals. From these results it can be concluded that peroxy radicals and hydroxyl radicals are primarily responsible for BB dye degradation. Other researchers reported similar findings; using ACFs/PAA, Zhou et al. [19] found that •OH and $CH_3C(=O)O•$ radicals were key in the degradation of Red X-3B, while Cai et al. [27] found that $CH_3C(=O)O•$ and $CH_3C(=O)OO•$) were responsible for the degradation of 2-napthoxyacetic and naproxen.
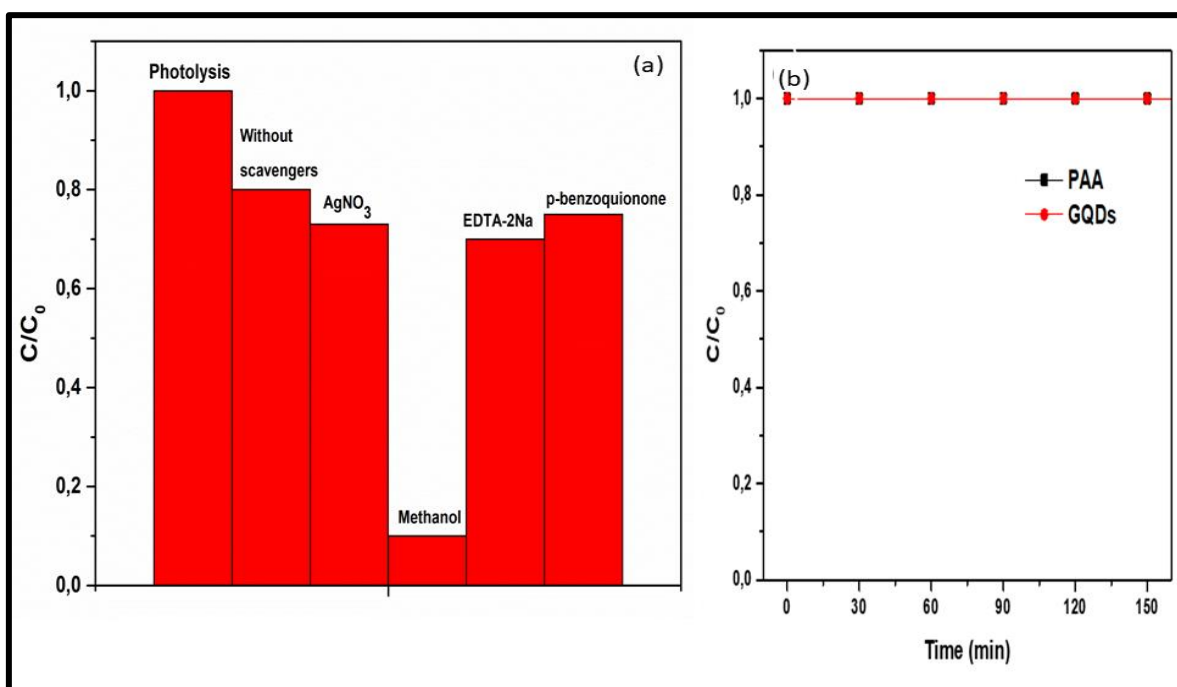
Figure 7.4: (a) Scavenger experimental results using $AgNO_3$, Methanol, EDTA-2Na and benzoquinone and (b) Photolysis experimental results using PAA and GQDs.

7.3.5 **Proposed photodegradation mechanism**

LC-MS analyses aided in elucidating the photodegradation pathway of BB dye using the GQDs/PAA. From the results presented in **Figure 7.5**, the proposed mechanism suggests that the •OH radicals of the GQDs/PAA system likely attacks the conjugated unsaturated (-N=N-) azo bonds localized between the two naphthalene rings in the BB dye molecule; this also is the primary cleavage (**Figure 7.5a**). The cleavage results in two aromatic naphthol compounds, which corresponds to the peaks labelled peak (a) and (b) in **Figure 7.6**. The corresponding *m/z* of the compounds labelled peak (a) and (b) are 407.04 and 365.11 respectively. The intermediate at peak (b) was further decomposed at the azo link (secondary cleavage) which is situated between the benzene ring and the naphthalene ring resulting in two aromatic compounds which also corresponded to peaks (c) (*m/z* = 173. 12) and (d) (*m/z* = 237.10) in **Figure 7.6a-d**.
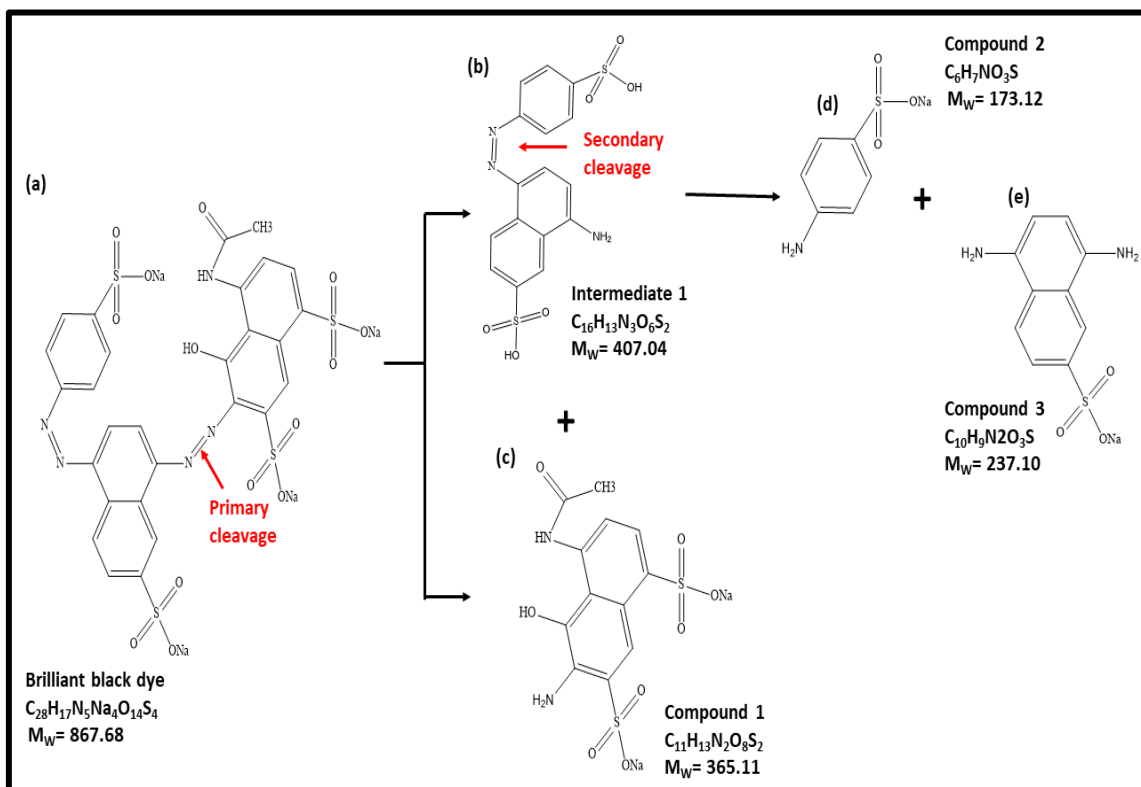
Figure 7.5: Proposed degradation pathway of BB dye using GQDs/PAA system.

Peak (A)

Peak (B)

166
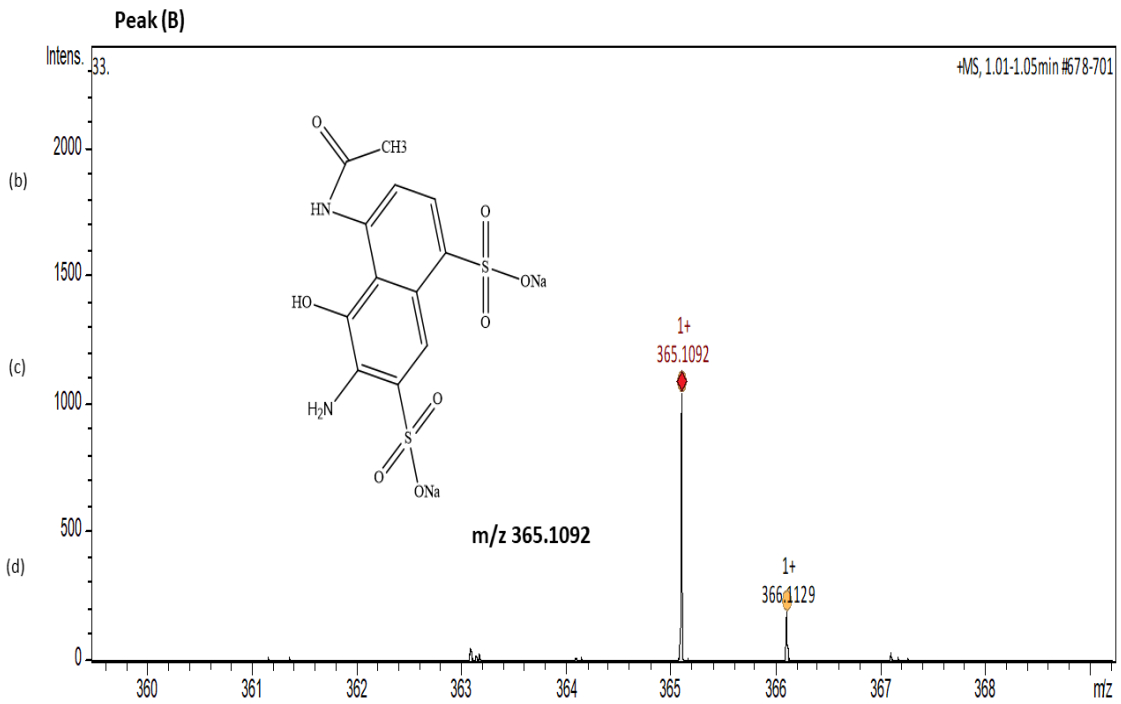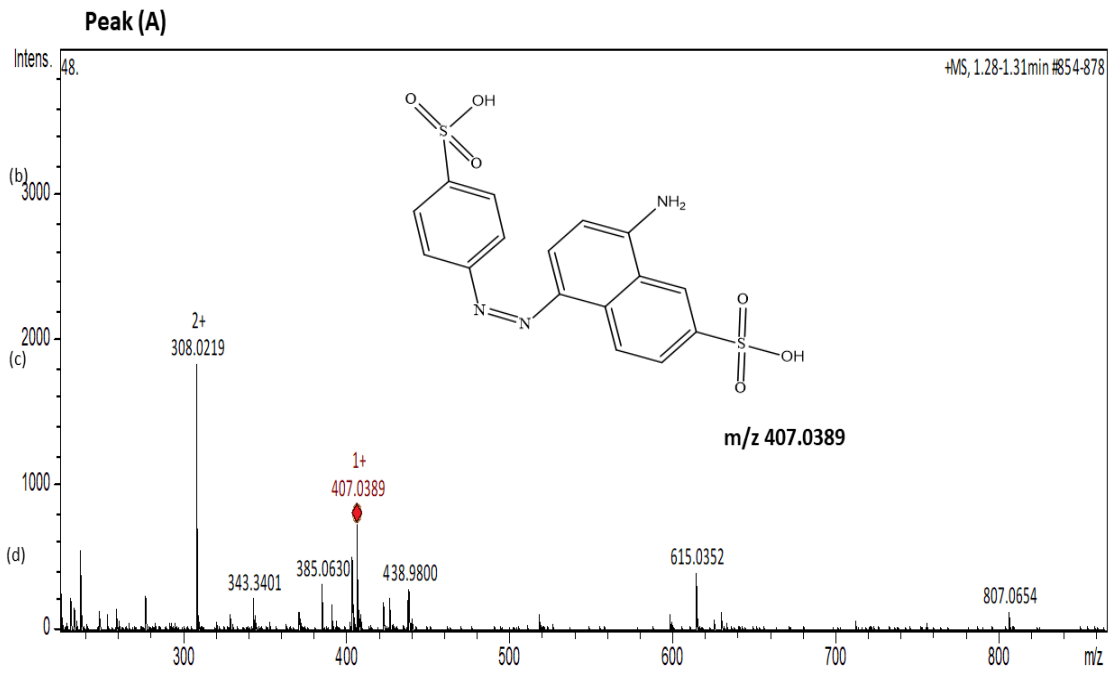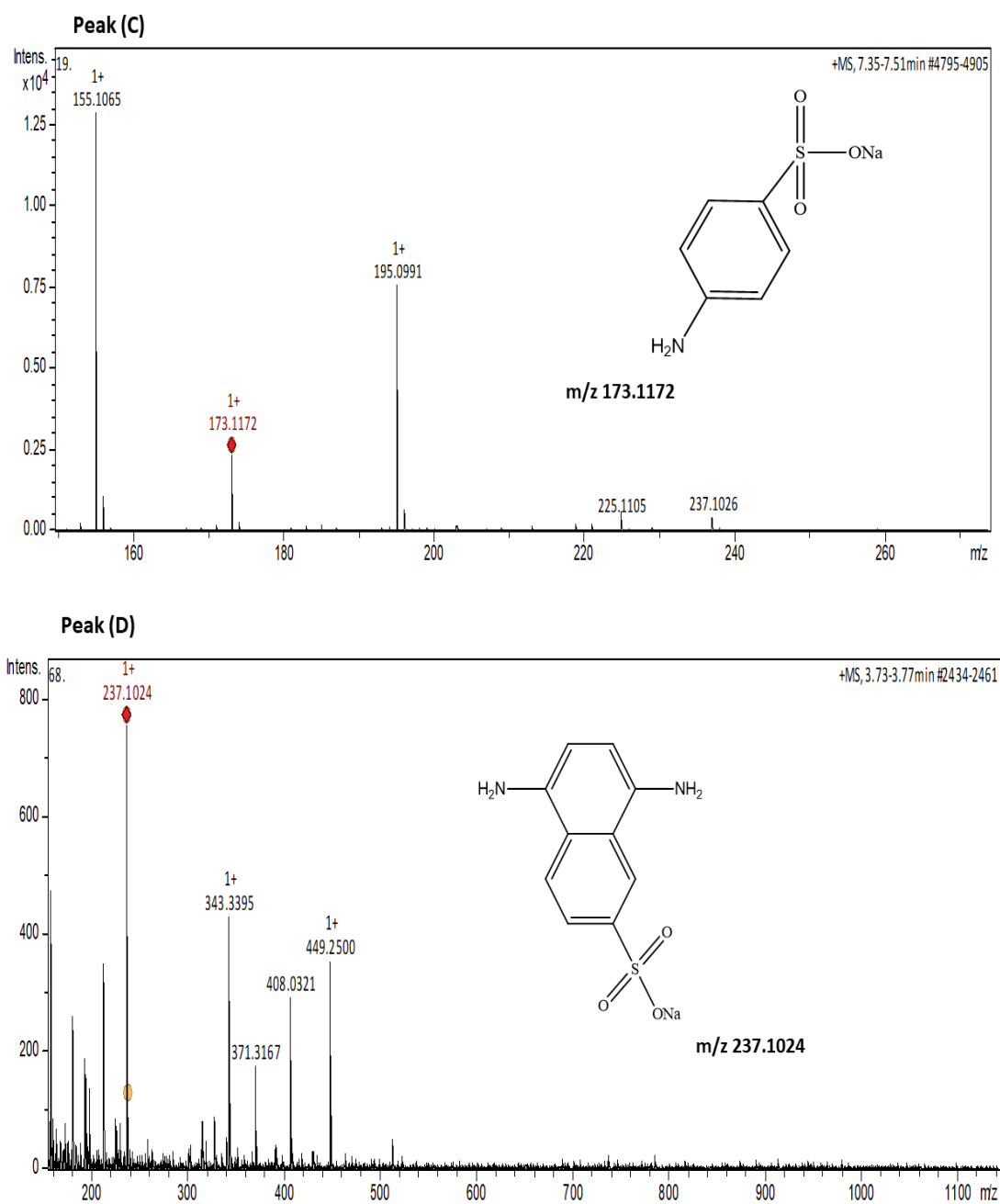
Figure 7.6:   HPLC-MS degradation products of BB dye after 150 mins irradiation time using GQDs/PAA system.

7.3.6   **Bacterial inactivation**

Antibacterial activity of GQDs/PAA system was evaluated against IBRC-M11018; ATCC 25922. The photo-irradiated *E. coli* was sampled at 30 mins intervals. From **Figure 7.7a** it was noted that GQDs alone were able to inactivate 48% of the *E. coli* after 150 mins while the introduction of PAA resulted in a complete inactivation of the *E. coli* alone and also in the GQDs/PAA system. Previous work demonstrated the efficiency of PAA in inactivating 99.9% *E.coli* in less than 5 mins [30]. To better understand the inactivation mechanism of bacteria by PAA and the GQDs/PAA system, the sampling time was reduced to 10 mins at 1 min intervals (**Figure 7.7b**). From these results it can be concluded that the addition of GQDs in the GQD/PAA system has an added advantage as 99.9% *E. coli* inactivation was achieved within 6-7 mins while for PAA alone it was achieved in 7-8 mins. The PAA/GQDs system was able to inactivate 99.9% of the *E.coli* in a shorter time period.
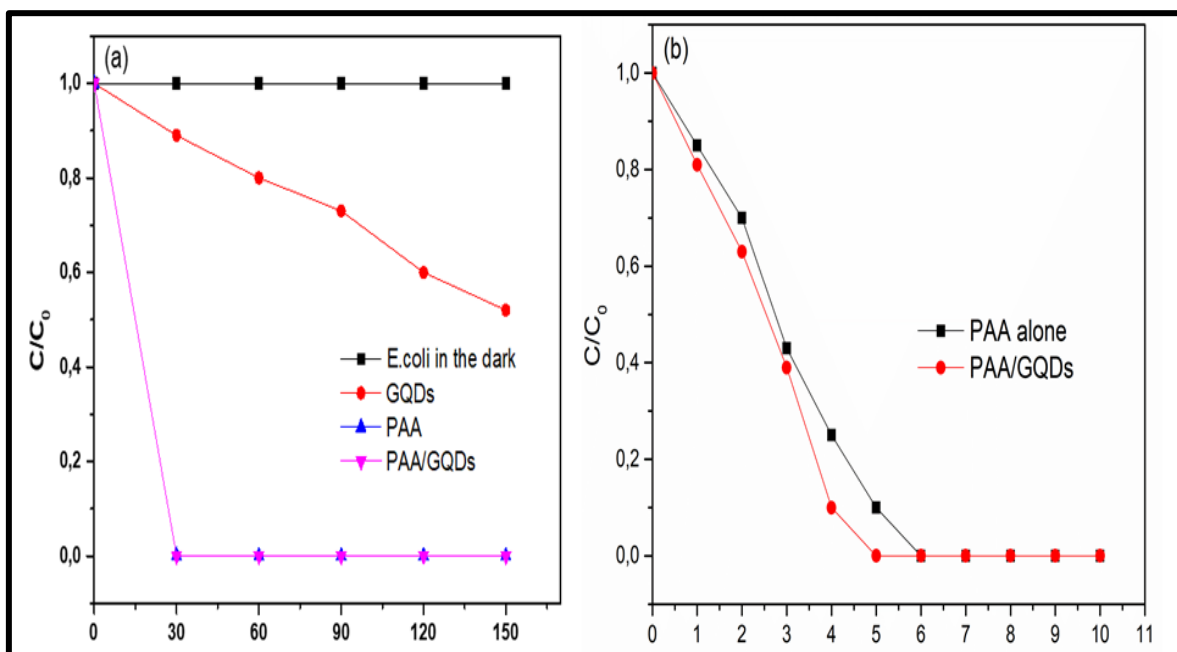
Figure 7.7:   (a) Inactivation of *E. coli* by GQDs, PAA and PAA/GQDs (b) Inactivation of *E. coli* in 10 mins in the presence of PAA and PAA/GQDs.

7.3.7   **Antibacterial mechanism**

Having demonstrated the antimicrobial activity of GQDs/PAA, the antibacterial mechanism was investigated. The morphological changes of *E. coli* exposed to GQDs/PAA were examined using SEM. The control (*E. coli* in the absence of GQDs/PAA) is presented in **Figure 7.8a**. After 4 mins (**Figure 7.8b**) the cell wall of the bacteria appeared shrunken, wrinkled and also ruptured. In comparison to the control, there was a significant change in morphology, suggesting a bacteriostatic effect. It is proposed that the bacterial inactivation occurred because of the synergy between GQDs and PAA. Initially the PAA will diffuse and permeate across the bacterial cell walls, weakening and impacting the outer membrane of the bacterial cells. The organic part of the PAA may aid in penetrating bacterial cells, as a result of the diffusion of the •OH radical being slower than its half-life [31]. The •OH radicals will react with carbohydrates, nucleic acids, amino acids and lipids and will inactivate the peroxidase enzyme [32].

Sequentially, the GQDs will interact with phospholipid bilayer resulting in the shrinkage of the cell wall [33]. The interaction of GQDs with the cell wall of *E. coli* can happen in one of two ways; (i) the large π-conjugated system of the GQDs can either attach on the wall of *E. coli* through electron transfer [34], (ii) due to the electrostatic interaction between the negatively charged cellular components and the positively charged GQDs [35]. Once inside the cell, the PAA will oxidize sulfhydryl and sulphur bonds in proteins and enzymes as well as disrupt the chemiosmotic functions of the cell. Furthermore, the peroxidase and catalase enzyme (a free radical quencher) will be inactivated by the PAA, while the photo-induced redox species and emissive excited states of the GQDs will lead to bactericidal functions.

The GQDs further transfer energy to the molecular oxygen which will give rise to singlet oxygen and subsequently forming species such as per-hydroxyl anions, superoxide singlet oxygen and hydroxide anions [36]. The production of these reactive species will induce oxidative stress and result in the leakage of cellular content. The bactericidal effect was fully confirmed by the lysis of cells which led to further changes in the morphology due to leakage of intracellular contents after 7 mins (**Figure 7.8c**). Further exposure to GQDs/PAA resulted in complete shrinkage of the cells after 10 mins of irradiation (**Figure 7.8d**). Zhang et al. [37] showed that *E. coli* treated with GQDs-AgNPs under 450 nm light irradiation (14.2 mW/cm^2) for 10 mins resulted in shrunken bacterial cells. Cells that were not exposed to

GQDs/PAA were intact and spaced out from each other (**Figure 7.8a**), while the cells treated with GQDs/PAA were aggregated with completely different morphology. Other authors previously observed that bacterial cells tend to aggregate when exposed to biocidal agents. Ulbin-Figlewicz et al. [38] reported similar observations for *E. coli*, while the phenomenon was also observed by Zhang et al. [37] in *E.coli* and *S. aureus*. Elsewhere, Tyagi and Malik [39] reported that when bacterial contents were leaked from the cells, they aggregated and appeared as sludge. Tang et al. [40] suggested that the aggregation was associated with oxidative stress and could also be a protection mechanism of the bacteria.
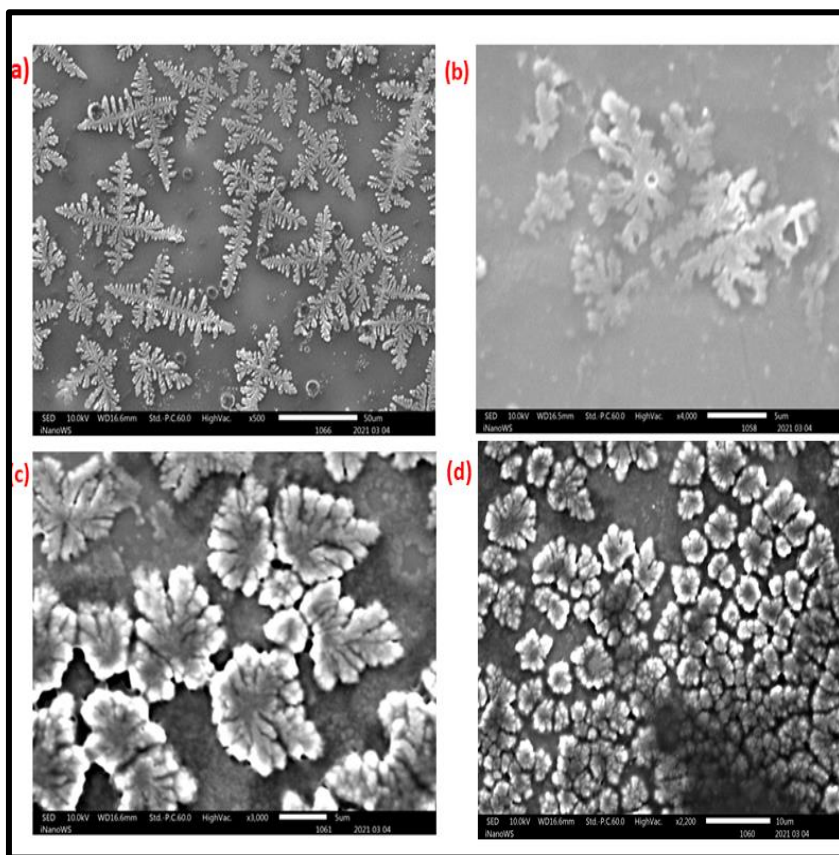
Figure 7.8: SEM micrographs of (a) *E. coli* cells in the absence of GQDs/PAA (control), (b) *E. coli* cells after being exposed to GQDs/PAA for 4 mins, (c) *E. coli* after being exposed to GQDs/PAA for 7 mins and (d) *E. coli* cells after being exposed to GQDs/PAA for 10 mins under irradiation.

7.3.8 Cell viability

The bactericidal effect of the GQDs/PAA was further verified using LIVE/DEAD *Bac*Light staining kit. From the photomicrographs presented in **Figure 7.9**, live healthy *E. coli* cells (negative control) prior to being treated with GQDs/PAA were stained green. After 3 mins exposure to GQDs/PAA, a mix of both green and red staining was observed indicating that some bacteria were beginning to die. The changes observed in the *E. coli* cell membrane integrity can be ascribed to the oxidation and degradation of proteins and enzymes due to exposure to GQDs/PAA [41]. At the 6 mins mark, there was complete inactivation of *E. coli* cells which was evidenced by the red staining. This observation gave evidence that GQDs/PAA were responsible for the loss of cell membrane integrity of *E. coli*. Similar findings were reported by Zhang et al. [37] who observed cell membrane disruption and cell inactivation when the bacterial cells were exposed to PAA.
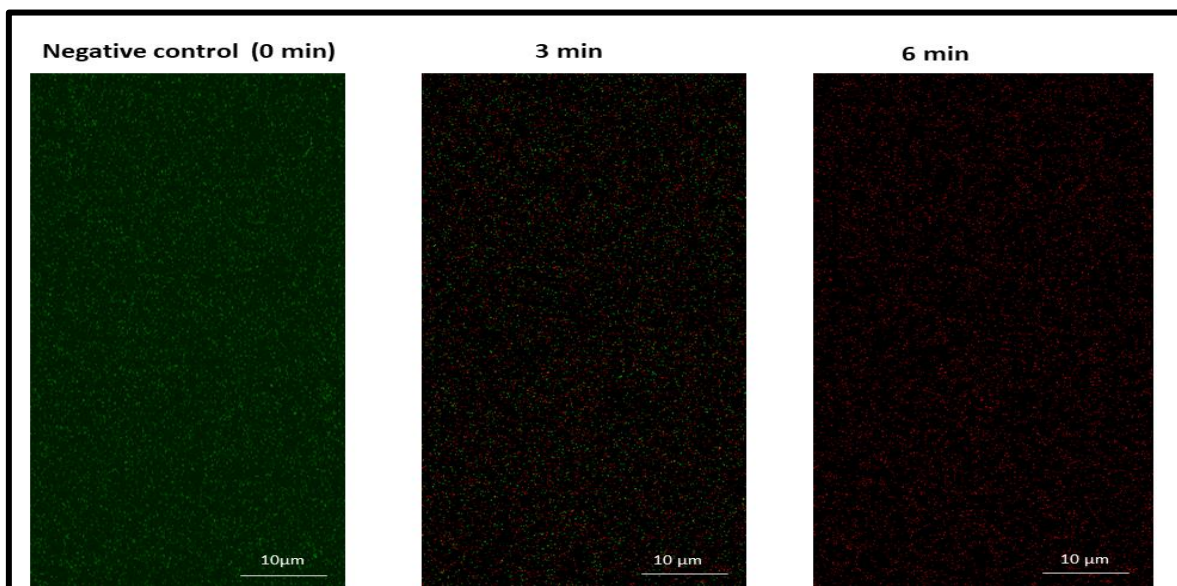
Figure 7.8: Photomicrographs of *E. coli* cells stained with LIVE/DEAD *Bac*light after treatment with GQDs/PAA at 0, 3 and 6 mins. Normal cells stained green, and the damaged cells were red. Magnification 1,000x bar = 10 µm.

7.3.9 Bacterial regrowth

The extent of cell damage could not be quantified by staining the *E. coli* cells. As such the *E. coli* regrowth potential was evaluated by mixing the disinfected cell suspensions in nutrient broth which was cultured overnight under ambient light at 37 $^{\circ}$C. **Figure 7.10** shows the microbial count after treating *E. coli* with GQDs, PAA and GQDs/PAA.
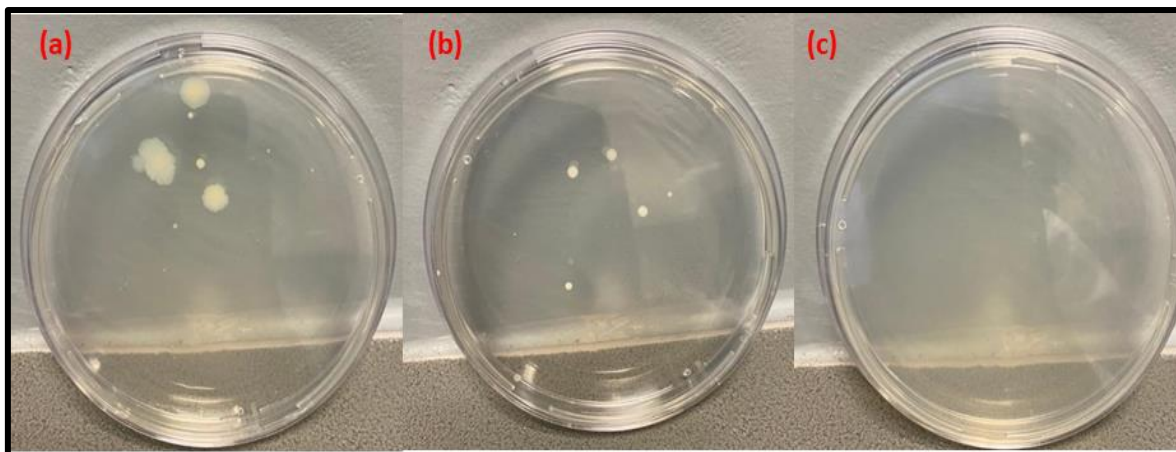
Figure 7.10: Assessing microbial re-growth of *E. coli* in the presence of: (a) GQDs, (b) PAA and (c) GQDs/PAA.

From these results it can be concluded that there was no appreciable growth that was observed after a 24-hour period even though the nutrient broth provided sufficient nutrients to allow the re-growth of the *E. coli*. The 3- and 5-mins colonies were formed after treating the bacterial cells with GQDs and PAA respectively, and the synergistic effect of GQDs/PAA resulted in no re-growth. It is evident that after subjecting *E. coli* to GQDs, PAA and GQDs/PAA, the cells were unable to repair the damage caused by GQDs/PAA. This suggests that the damage caused by GQDs/PAA was irreparable. From these results it can be concluded that GQDs/PAA is not just bacteriostatic, but it is also a bactericide. Other researchers have reported on the ability of PAA in preventing regrowth of *E. coli*, *P. aeruginosa* and *Bacillus* [42, 43].

7.4 Conclusion

GQDs effectively activated PAA and the resultant PAA/GQDs system could effectively degrade brilliant black dye and inactivate *E. coli*. Other significant findings from the chapter were:

- Increasing the GQDs loading in the system enhanced the photodegradation efficiency to 98% owing to the availability of abundant active sites provided by GQDs. In contrast increasing the PAA concentration only slightly enhanced efficiency as there were little active sites available.

- The role of the GQDs was established as a catalyst and quenching experiments confirmed that the degradation occurred through the generated radicals. Hydroxyl and peroxy radicals were the primary radical species responsible for BB photodegradation.

- Furthermore, the PAA/GQDs system was able to inactivate 99.9 % of *E. coli* within 7 mins and the antimicrobial mechanism was as a result of the synergistic effect of the GQDs and PAA in the GQDs/PAA system.

This work presents an opportunity to simultaneously degrade dyes and inactivate microorganisms and could be applied in tertiary treatment in urban wastewater treatment.

References

1. Formisano F, Fiorentino A, Rizzo L, Carotenuto M, Pucci L, Giugni M, Lofrano G, Process. *Saf. Environ. Protect.* 104 (2016) 178.

2. Schoeny R, Disinfection By-products, *Perspectives* (2010)33.

3. Ghani A, Dalvi I, Al-Rasheed R, Javeed M, *Desalination* (129) (2000) 261.

4. Sun H.Q, Kwan C, Suvorova, Ang H.M, Tadè M.O, Wang S.B, *Appl. Catal. B. Environ.* (154-155) (2014) 507.

5. Rokhina E.V, Makarova K, Golovina E.A, Van As H, Virkutyte, *Environ. Sci. Technol.* 44 (2010) 6815.

6. Popov E, Eloranta J, Hietapelto V, Vuorenpalo V.M, Aksela R, Jäkärä J, *Holzforschung* 59 (2005) 507.

7. Chen S, Cai M, Liu Y, Zhang L, Feng L, *Water. Res* 150 (2019) 153.

8. Flores M. J, Lescano M.R, Brandi R.J, Cassano A.E, Labas M.D. *Water. Sci. Tech* (2014) 358.

9. Wu W, Tian D, Liu T, Chen J, Huang T, Zhou X, Zhang Y, *Chem. Eng. J.* 394 (2020) 124938.

10. Nzaba S.K.M, Ntsendwana, Mamba B.B, Kuvarega A.T, *Environ. Chem. Eng.* 6 (2018) 15149.

11. Wang Z, Wang J, Xiong B, Bai F, Wang S, Wan Y, Zhang L, Xie P, Wiesner M.R, S, *Environ. Sci. Technol.* 54, (2020) 464.

12. Zhou X, Wu H, Zhang L, Liang B, Sun X, Chen B, *Molecules.* 25 (12) 2725.

13. Shao M, Han J, Wei M, Evans DG, Duan X, *Chem. Eng. J.* 168(2) (2011) 519.

14. Xiang X, Xie L, Li Z, Li F, *Chem. Eng. J.* 221 (2013) 222.

15. Karimi H, Rajabi H.R, Kavoshi L, *J. Photochem. Photobiol.A: Chemistry.* 397(2020)112534.

16. Chen J, Zhang L, Huang T, Li W, Wang Y, Wang Z, *J. Hazard. Mater.* 320 (2016) 571.

17. Wang L, Yao Y.Y, Zhang Z.H, Sun L.J, Lu W.Y, Chen W.X, Chen H.X, *J Chem. Eng* 251 (2014) 348.

18. Johnsen D.L, Zhang Z.Q, Emamipour, Yan Z.F and Rood M.J, *Carbon* 76 (2014) 435.

19. Zhou F, Chao L, Yao Y, Sun L, Pei K, Lu W, Chen W, Chem. Eng. J. 281 (2015) 953.

20. Wang L, Yao Y.Y, Zhang Z.H, Sun L.J, Lu W.Y, Chen W.X, Chen H.X, *J Chem. Eng* 251 (2014) 348.

21. Bokare A.D, Choi W.Y. *J. Hazard. Mater.* 275 (2014) 121.

22. Chen J, Zhang L, Huang T, Li W, Wang Y, Wang Z*, J. Hazard. Mater.* 320 (2016) 571.

23. Bach R.D, Ayala P.Y and Schlegel H.B, *J. Am. Chem. Soc.* 118 (1996) 12765.

24. Rokhina E.V, Makarova K, Golovina E.A, Van As H and Virkutyte, *Environ. Sci. Technol.* 44 (2010) 6815.

25. Rojas-Andrade M.D, Nguyen T.A, Mistler W.P, Armas J, Lu J.E, Roseman G, William, Hollingsworth R, Nichols F, Glenn L. Millhauser, Alexander Ayzner A, Saltikov C, Chen S, *Nanoscale Adv.* 2 (2020) 1074.

26. Koivunen J, Heinonen-Tanski H, *Water. Res*. 9 (2005) 1519.

27. Cai M, Sun P, Zhang, L, Huang C.H, *Environ. Sci. Technol.* 51(2017)14217.

28. Rojas-Andrade M.D, Nguyen T.A, Mistler W.P, Armas J, Lu J.E, Roseman G, William, Hollingsworth R, Nichols F, Glenn L. Millhauser, Alexander Ayzner A, Saltikov C, Chen S, *Nanoscale Adv.* 2 (2020) 1074.

29. Koivunen J, Heinonen-Tanski H, *Water. Res*. 9 (2005) 1519.

30. Tero Luukkonen, Simo O. Pehkonen (2017) *Environ. Sci. Techn.*, 47(1) (2017) 1.

31. Marjani, A, Golalipour, M.J, Gharravi, A.M, *Oman Med. J.* 25 (2010) 256.

32. Patra P, Roy S, Sarkar S, Mitra S, Pradhan S, Debnath N, Goswami A, *Appl. Nanosci*. 5 (2014) 857.

33. Kholikov K, Ilhom S, Sajjad M, Smith M.E, Monroe J.D, San O, Photodiagnosis *Photodyn. Ther.* 24 (2018) 7.

34. Rajendiran, Keerthiga, *Polymers*. 11(10) (2019).

35. Zhang Y, Zhang D, Liu A.H, *Polymers*. 11 (2019) 708.

36. Ulbin-Figlewicz. N, Jarmoluk A, Marycz, K, Ann. *Microbiol.* 65 (2015) 1537.

37. Tyagi AK, Malik A (2012) *Alternat Med.* (2012) 692625.

38. Tang Y. J, *Nano.Lett* 7(2007) 754.

39. Joux F, Lebaron P. *Microbes. Infect*. 2(12) (2000) 1523.

40. Zhang C, Brown P.J.B, Miles R.J, White T.A, Grant D.G, Stalla D. *Water Res* 2018 1.

41. Zhang, Chiqian, Brown, Pamela J.B, Miles, Randall J, White, Tommi A.; Grant, DeAna G.; Stalla, David; Hu, Zhiqiang, *Water Res* (2018) S0043135418308595.

42. Antonelli, M., Rossi, S, Mezzanotte, V. and Nurizzo, C, *Environ. Sci. Tech*. 40 (2006), 4771.

43. Tero Luukkonen, Simo O. Pehkonen, *Environ. Sci. Tech* (2017) 47 (2017) 1.

CHAPTER 8

THE SYNERGISTIC EFFECT OF PERACETIC ACID ACTIVATED BY GRAPHENE OXIDE QUANTUM DOTS IN THE INACTIVATION OF S. AUREUS AND REMOVAL OF SULFASALAZINE IN MUNICIPAL WASTEWATER

8.1   Introduction

Sulfasalazine (SSZ) is a drug prescribed for the treatment of inflammatory bowel disease and rheumatoid arthritis [1]. Concentrations of SSZ between 1.8 and 7.2 µM were shown to pose a great risk on microorganism resistance [2, 3]. Other researchers have attempted to photodegrade SSZ using AOPs, for instance; Fan et al. [4] used Fenton processes to degrade SSZ, while Ji et al. [5] achieved the degradation by UV and UV/peroxydisulfate process and recently Pelalak et al. [6] used ozone based AOPs in the degradation of SSZ. This chapter presents the degradation of SSZ in municipal wastewater using a synergistic effect between graphene oxide quantum dots and peracetic acid (GQDs/PAA). The objectives of the study were to; (a) evaluate the influence of reaction parameters such as initial concentrations of the oxidant (peracetic acid), drug (SSZ) and different water matrices, (b) identify the main reactive species responsible for the photodegradation process, study the kinetics of the photodegradation process as well as elucidate a photodegradation mechanism based on the results of the degradation products obtained on LC-Q-TOF-MS, (c) determine the genotoxic and mutagenic potential of the degradation products formed during the degradation of SSZ using the Ames test, (d) understand the bacterial inactivation mechanism by observing the morphological changes of the bacterial cell under SEM as well the cell viability studies

8.2   Experimental details

8.2.1   Photodegradation of sulfasalazine

The degradation of SSZ (**Figure 8.1**) was carried out at room temperature using a custom made photoreactor from Lelesil Innovative Systems, India.
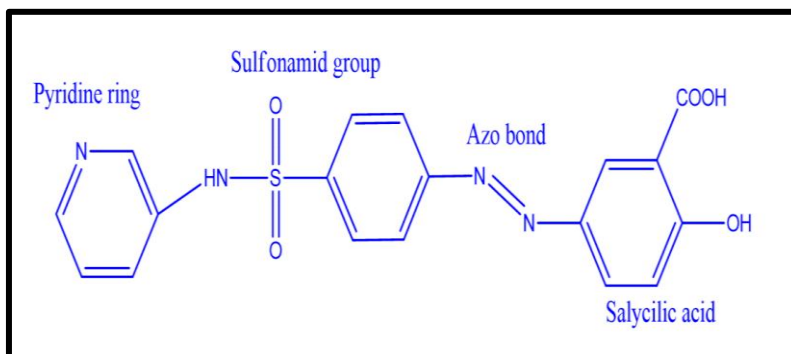
Figure 8.1:   Molecular structure of sulfasalazine ($C_{18}H_{14}N_{14}O_5S$).

8.2.2   Identifying reactive species in photodegradation process

The reactive species generated in the photodegradation of SSZ were investigated by carrying radical scavenging experiments and the experimental protocol as outlined in **Chapter 3**.

8.2.3   Determining mutagenic and genotoxicity potential of reaction by-products from SSZ photodegradation using Ames test.

The mutagenic and genotoxicity potential of the reaction by-products formed during the SSZ degradation were evaluated and the process is detailed in **Chapter 3**.

8.2.4   LC-QTOF-MS analysis and detection conditions

LC-QTOF-MS analysis was performed to identify the reaction-by products and the experimental procedure is outlined in **Chapter 3**.

8.2.5   Antimicrobial activity

The model microbe used in this work was *S. aureus* (ATCC 25923); the efficiency of the antimicrobial activity of the GQDs/PAA system was evaluated against *S. aureus*. The experiments were conducted as per the serial dilution method and is detailed in **Chapter 3**.

8.2.6   Antimicrobial activity in raw water

The experiments were similarly carried out as described for the photodegradation of SSZ as detailed in **Chapter 3**.

8.2.7   SEM characterization of *S. aureus*

The morphological changes of the *S. aureus* were observed using and SEM and is detailed in **Chapter 3**.

8.2.8   Cell viability using LIVE/DEAD Baclight staining kit

The viability of the *S. aureus* cells was determined using the LIVE/DEAD Baclight staining kit and the process is described in **Chapter 3**.

8.3   Results and discussion

8.3.1   Photodegradation of SSZ

8.3.1.1 Influence of PAA dosage on the photodegradation of SSZ

Oxidant dosage is an important parameter in establishing whether GQDs/PAA system is an economically viable method for degrading SSZ. The effect of PAA dosage on the photodegradation of SSZ was evaluated at pH 5 by varying the PAA concentration (0.05, 0.10 and 0.15 mM) while maintaining the GQDs concentration constant (0.05 g/L). When employing 0.05 mM of PAA in the GQDs/PAA system, 80% of the drug was degraded after 150 mins, while 99.0% and 99.8% of SZZ was degraded at 0.10 and 0.15 mM respectively (**Figure 8.2a**). Increasing the PAA concentration resulted in almost complete degradation of

the SSZ, and therefore the trend observed was dose dependent. There was also an increment in the k_{obs} value from 0.03612 to 0.03842 min^{-1} at higher PAA concentrations. Interestingly, while the k_{obs} value increased at higher PAA concentrations the growth rate remained almost the same which is a result of PAA scavenging effect on the •OH as well as the limited reactive sites on GQDs available to accelerate the PAA activation [7].

Another possibility is that the excessive PAA molecules can absorb more photons which in turn inhibit the photodegradation of SSZ or the high loading of GQDs could yield excessive reactive sites for PAA activation therefore quenching the reactive species generated from PAA activation [8]. Although literature on the degradation of SZZ using PAA or GQDs is not readily available, Cai et al. [9] investigated the UV/PAA on the degradation of seven pharmaceuticals and the obtained results showed no significant degradation of the pharmaceuticals when using 1 mg/L (13.1 µM) of PAA (pH 7). Moreso, increasing the PAA dosage to 1 g/L and adding 0.11 g/L H_2O_2 only eliminated 62.50% for naproxen and 29.70% for diclofenac and the removal rate for the other pharmaceuticals was less than 11.05%. The degradation efficiencies of the GQDs/PAA in this study were all above 80% indicating improved removal efficiencies.

8.3.1.2 Effect of initial SSZ concentration

The initial concentration of SSZ was varied (10-50 mg/L) while maintaining a constant concentration of GQDs/PAA (0.05 g/L: 0.10 mM) at pH 5. From **Figure 8.2b**, the lowest concentration of SSZ (10 mg/L) achieved the highest degradation efficiency of 100%, while the highest concentration of SSZ (50 mg/L) recorded the lowest removal efficiency of 20%. It was expected that as the initial concentration of SSZ was increased, the degradation efficiency would conversely decrease, as was observed. This is because as the concentration of the SSZ was increased, there was less available catalytic sites. Additionally, the decrease in the removal efficiency is also ascribed to less reactive species being available to degrade SSZ [10]. Gopinath and Krishna [11] observed the same phenomenon when the initial concentration of 2, 4 dichlorophenol was increased.

In contrast, in this study at lower SSZ concentrations (10 and 20 mg/L) the number of catalytic sites were not a hindrance, and the rate of degradation was proportional to substrate concentration as per apparent first-order kinetics.
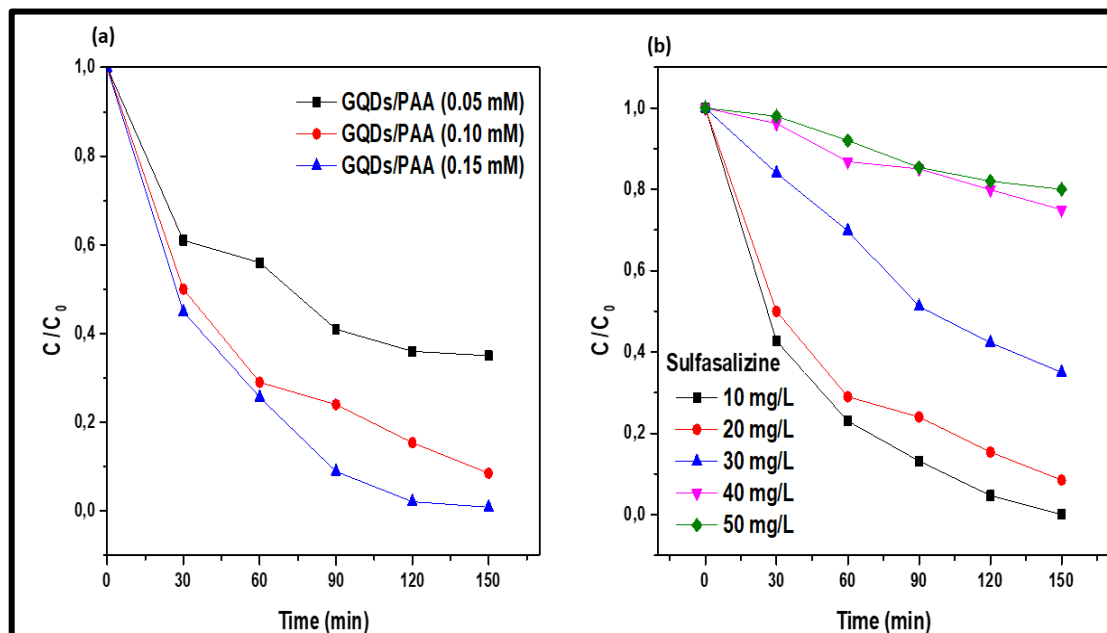
Figure 8.2: Influence of (a) PAA dosage (b) initial concentration of SSZ on the photodegradation process.

8.3.1.3 Effect of water matrix

Real wastewater (collected at two sampling points at a South African wastewater treatment plant) and synthetic water were used as target matrices. The SSZ degradation profile in both water matrices is presented in **Figure 8.3a**. In synthetic water using GQDs/PAA (0.05 g/L: 0.10 mM) the observed degradation efficiency was almost 100%, while 35% and 80% removal efficiency was recorded for wastewater collected at *sampling points 1* and *2* respectively. The lower degradation efficiency of SSZ in wastewater compared to synthetic water was expected and is largely ascribed to the complex nature of real water and selectivity issues. Numerous substances in real water (humic acid, bicarbonates, chlorides, and carbonates ions) have been reported to have the ability to scavenge radicals which in turn diminishes the degradation potential [12]. The difference in degradation efficiencies of SSZ at the two sampling points was due to the composition of the water. At *sampling point 1*; the raw wastewater will only have gone through preliminary treatment. The purpose of preliminary treatment is only to screen coarse and large materials, remove grit as well as to

prevent organic solids from settling [13]. It has been demonstrated that approximately 50% of the incoming biochemical oxygen demand (BOD), 70% of the total suspended solids (TSS) and some organic nitrogen, phosphorous and heavy metals are only removed after the primary clarifier [14].

Sampling before the primary clarifier (*sampling point 1*) means there will be a lot of competition on the photodegradation process with some ions in the wastewater. Luo et al. [15] showed that carbonate and bicarbonate ions can affect the degradation process as they tend to react with $\bullet OH$ and form $CO_3 \bullet^-$. In another instance humic acid was shown to also affect the degradation process by either acting as a scavenger or through the introduction of an inner filter effect arising from the large absorbance of humic acid [16]. Cl^- can also affect the degradation process as they interact with $\bullet OH$ and $SO_4 \bullet^-$ resulting in radicals that are less reactive such as $ClOH \bullet$, $^-Cl \bullet$ and $Cl_2 \bullet^-$ [16]. At *sampling point 2* (after secondary clarifier), the effluent from the primary clarifier will be treated using activated sludge to remove nitrogen, phosphorous, dissolved minerals as well as non-biodegradable organics [14], implying that the water matrix was less complex and that most ions were removed and were not able to scavenge the radicals hence the enhanced degradation efficiency of 81% compared to the 35% at *sampling point 1*. In addition to efficiently degrading SSZ, the synergy of disinfection capabilities of GQDs/PAA were investigated using *S. aureus* as a representative bacterium in real wastewater.
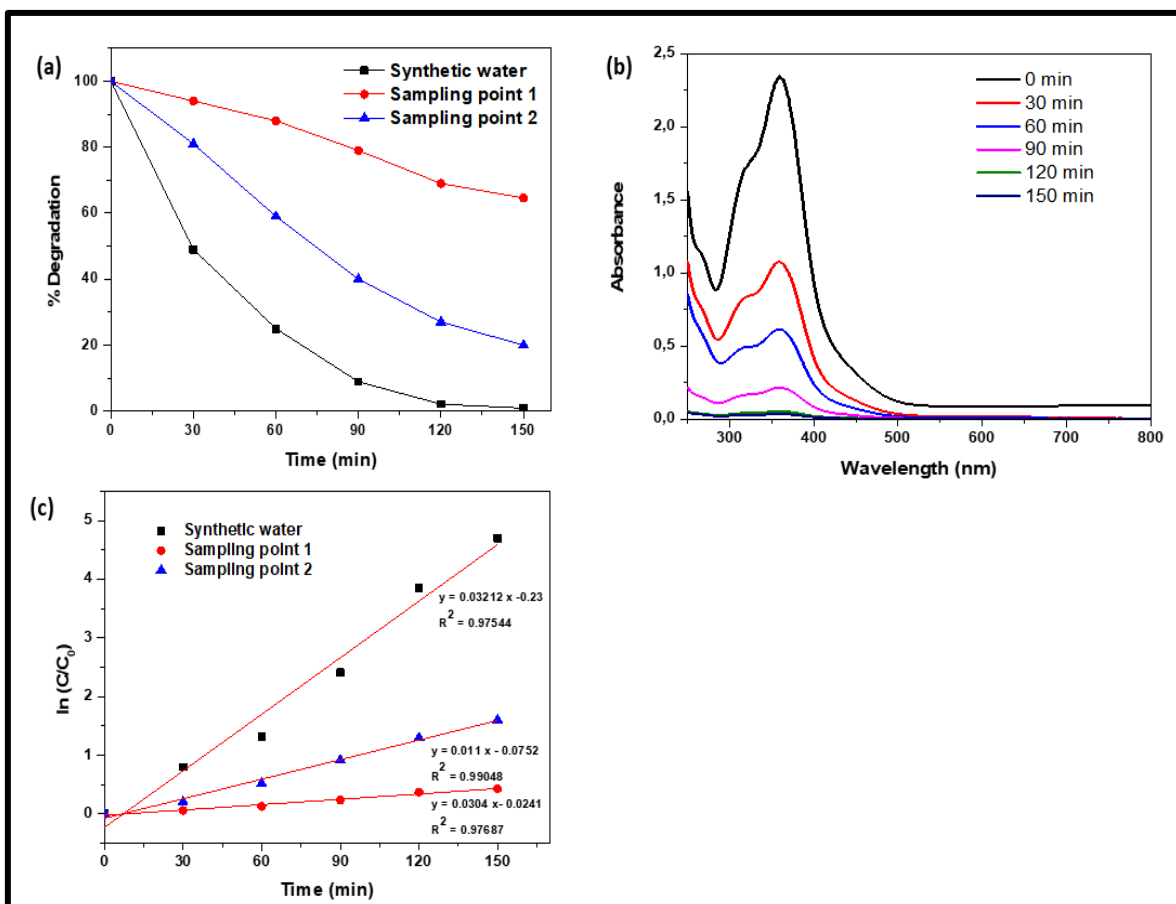
Figure 8.3: (a) Degradation profile of SSZ in different water matrices, (b) absorption spectra of SSZ and (c) Photodegradation kinetics of the PAA/GQDs system in the degradation of SSZ.

8.3.2 Photodegradation kinetics of SSZ

Changes in the absorption spectra of SZZ during the photodegradation are shown in **Figure 8.2b**. Over time, the SSZ peak decreased and eventually flattened out signalling complete degradation of SSZ. The results were fitted to a pseudo-first order model and a linear plot was obtained by plotting $\ln\left(\frac{C_0}{C}\right)$ versus irradiation time. The kinetic data of SSZ degradation in synthetic water and wastewater samples (*sampling point 1* and *2*) are presented in **Figure 8.3c**. The linear relationship observed between the $\ln\left(\frac{C_0}{C}\right)$ over time implied that first-order kinetics was followed in all samples. The synthetic water matrix had a higher rate constant (0.0321 min^{-1}) compared to the wastewater samples (0.0110 min^{-1} and 0.0304 min^{-1}) for *sampling point 1* and *2* respectively and this can be explained by the complexity of the water

182

matrix. Kinetic data for the degradation of SSZ is presented in **Table 8.1**. The degradation of SSZ in ultrapure water was higher and showed shorter half-lives.

Table 8.1: **Kinetic parameters of SSZ degradation using GQDs/PAA system.**

Water matrix	Photodegradation (%)	Rate constant (min^{-1})	Half-life (min)	R^2
Synthetic water	99.99	0.03212	21.57	0.97544
Wastewater *Sampling point 1*	80.02	0.03040	22.7	0.97687
Wastewater *Sampling point 2*	34.62	0.01100	63	0.99048

8.3.3 Identifying radicals responsible for the degradation of SSZ

The combination of GQDs and PAA degraded SSZ using a synergistic combination of different radicals to oxidize SSZ. The contribution of each radical was investigated by radical scavenging experiments, to identify the radicals responsible. Excess methanol, EDTA-2Na, benzoquinone and silver nitrate were deployed as scavengers for •OH, h$^+$, •O$_2^-$ and e$^-$ respectively. From **Figure 8.4**, it is evident that the degradation of SSZ was not affected by the addition of EDTA-2Na and silver nitrate suggesting that h$^+$ and e$^-$ had no active role in the degradation of SSZ, and this concurs with other previous studies [18]. However, •O$_2^-$ was responsible for less than 8% of the active species. Methanol inhibited 43.9% of the •OH radicals indicating that •OH contributed to the degradation of SSZ. The contribution of the •OH was attributed to the presence of GQDs in the GQDs/PAA system. In recent work by Cai et al. [19] the contribution of •OH in the degradation of two

pharmaceuticals using UV/PAA system was highlighted. The contribution of •OH occurs when the molecular oxygen near the interface of the GQDs/PAA is converted to superoxide anion radical ($•O_2^-$), and the resulting $•O_2^-$ will react with H^+ to form hydroperoxyl radical ($HO•_2$). The $HO•_2$ will react with trapped electrons to generate H_2O_2. These H_2O_2 groups will interact with the generated CB electrons to produce additional radicals while other radical such as $CH_3•$, $CH_3O_2•$, $CH_3C(=O)OO•$ and $CH_3C(=O)O•$ have been reported to also contribute to the degradation of organic compounds.
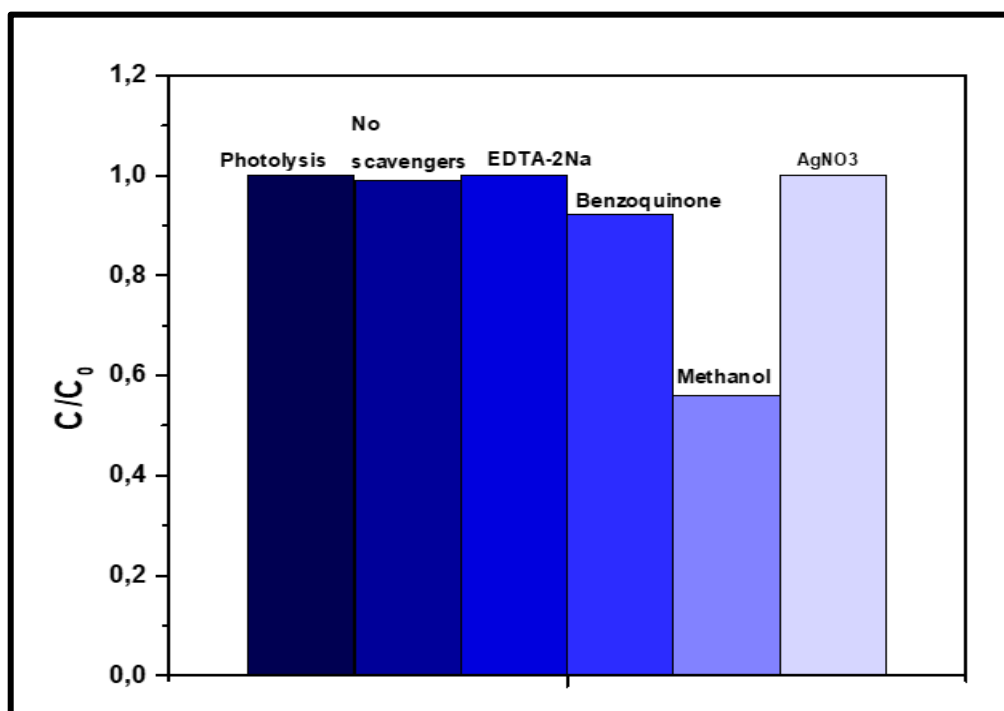
Figure 8.4:   Quenching experiments using AgNO₃, Methanol, EDTA-2Na and benzoquinone (For comparison purposes experiments in the dark and in the presence of light without scavengers are also included).

The proposed GQDs activated PAA radicals in the degradation SZZ are shown in **Equations 8.1-8.5**. The rate determining step and the homolysis of the oxygen-oxygen bond that is activated by GQDs is represented by **Equation 8.1**. $CH_3•$ and CH_3O_2 (**Equations 8.2** and **8.3**) have been ruled out as contributors because $CH_3•$ (k = 2.8- 4.1 x 10^9 M^{-1} s^{-1}) tends to quickly react with O_2 resulting in the formation of CH_3O_2. CH_3O_2 also has a significantly lower oxidation capacity [19], hence the degradation of SSZ is due to •OH, $CH_3C(=O)OO•$ and $CH_3C(=O)O•$ radicals.

$$GQDs + CH_3C(=O)OOH \leftrightarrow GQDs + CH_3C(=O)O\bullet + \bullet OH \qquad \text{(Eq. 8.1)}$$

$$GQDs + CH_3C(=O)O\bullet \rightarrow CH_3\bullet + CO_2 \qquad \text{(Eq.8.2)}$$

$$CH_3\bullet + O_2 \rightarrow CH_3O_2 \qquad \text{(Eq. 8.3)}$$

$$CH_3C(=O)OOH + \bullet OH \rightarrow CH3C(=O)OO\bullet + H_2O \qquad \text{(Eq. 8.4)}$$

$$CH_3C(O)OOH + CH_3C(=O)O\bullet \rightarrow CH_3C(O)OO\bullet + CH_3C(O)OH \quad \text{(Eq. 8.5)}$$
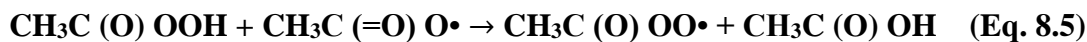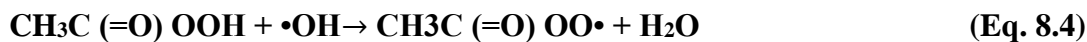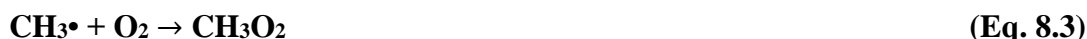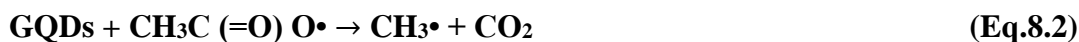
8.3.4 **Proposed degradation pathway**

The transformation and degradation pathway of SSZ with GQDs/PAA was evaluated using the degradation products obtained using LC-QTOF-MS. Molecular ion masses and MS fragmentation patterns were used to predict the molecular structure of the reaction intermediates. Typically, the chemical structure and functional moieties of SSZ allow it to be both oxidized and reduced during the photodegradation process. The oxidation process can occur as result of the –OH, -NH and –COOH of the SSZ attacking the OH, h^+ or $\bullet O_2^-$ radicals. Conversely, the –N=N- and –O=S=O bonds in SSZ facilitates its reduction [20]. From **Figure 8.5**, attack on the –N=N- bonds by $\bullet$OH and $CH_3C(=O)O\bullet$ results in SSZ forming two intermediates namely; 5-aminosalysylic acid (*m/z* 153.13) and sulfapyridine (*m/z* 249.0984) (**Figure 8.6a** and **b**). Other studies have documented that further attack of the 5-aminosalysylic acid by either $\bullet$OH or h^+ ought to result in the intermediates 1,3,4-triol-2-carboxilic-1,3 dibutene and acetaldehyde or into maleic acid and ethandiol amine [22], however that was not the case in the present study. Sulfapyridine was further attacked by the $CH_3C(=O)OO\bullet$ and the intermediate produced aniline (*m/z* 93.13) and (*m/z* 159.0581) (**Figure 8.6c**-**e**). This intermediate underwent desulfonation and was further broken into pyridine 2,3,5-triol (*m/z* 125.9860) and pyridine-3(4H)-one (*m/z* 95.9471) (**Figure 8.6**). Although no smaller molecular masses were picked up on the LC-QTOF-MS; the resultant intermediates are able to undergo ring-opening as a result of the reactive radicals ($CH_3C(=O)OO\bullet$) resulting in formation of lighter alcohols and acids which will eventually be completely mineralized into CO_2 and H_2O.
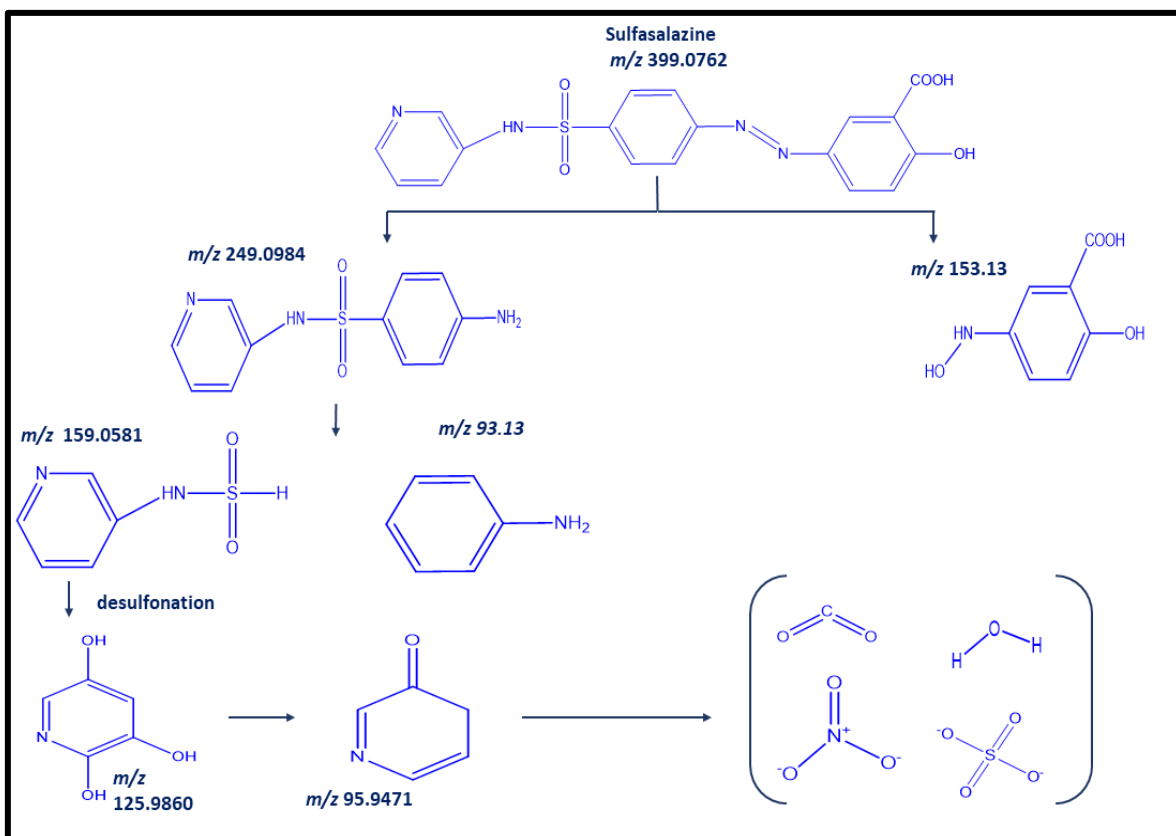
Figure 8.5: Proposed transformation and photodegradation pathway of SSZ using GQDs/PAA.
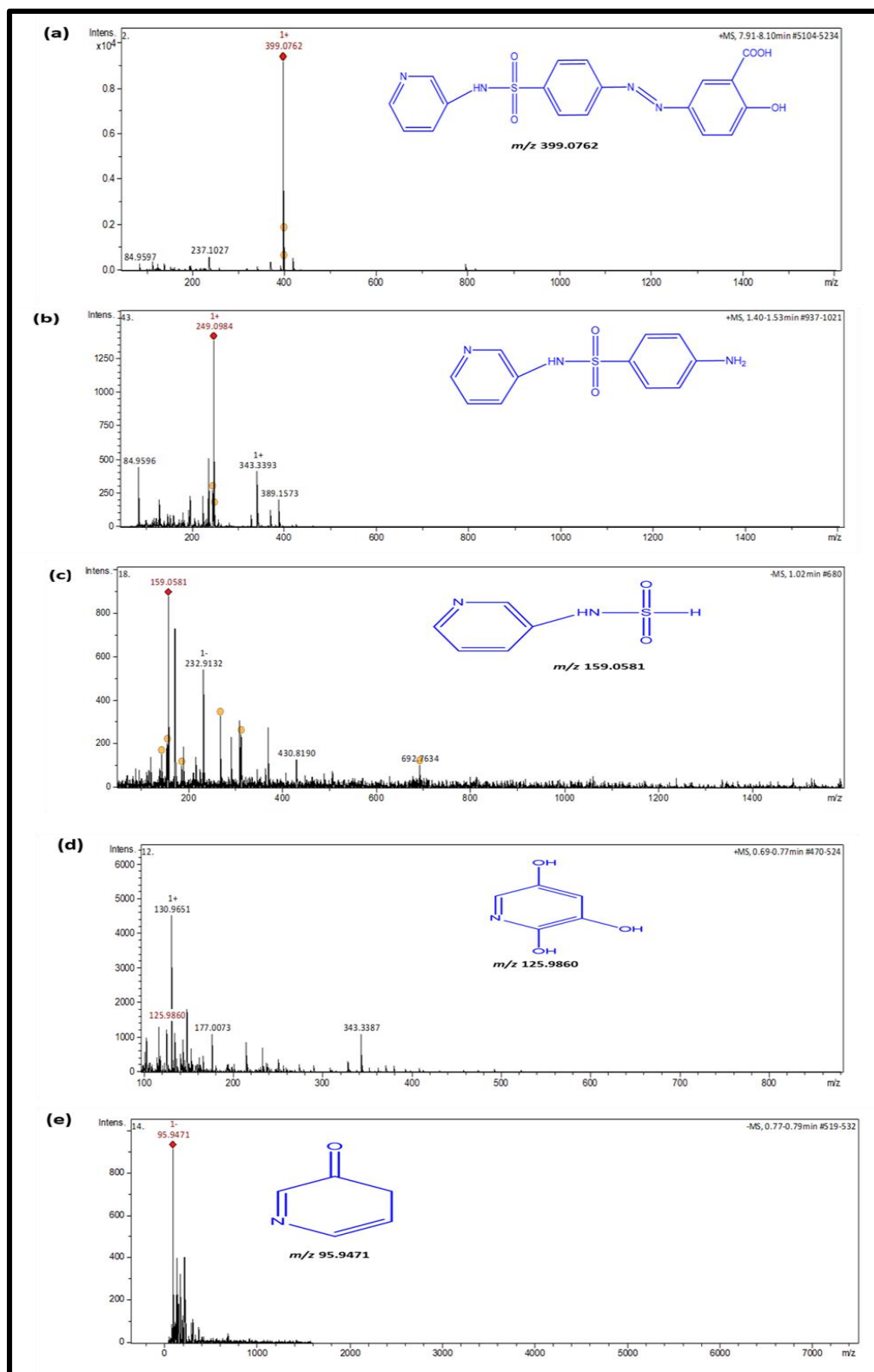
Figure 8.6: LC-QTOF-MS degradation by-products of SSZ after 150 mins irradiation time using GQDs/PAA, (a) shows the molecular structure of SZZ at 0 mins (b)-(e) degradation products obtained from 30 mins-150 mins.

8.3.5   Total organic carbon measurement

Even though there was an almost 100% degradation of SZZ, TOC analysis showed there was only 83.7% TOC eliminated when using 0.15 mM PAA (**Figure 8.7**). The incomplete TOC elimination as corroborated by LC-QTOF-MS results shown in **Figure 8.6** is attributed to the residual by-products that include aromatic ring structure of SSZ not being completely obliterated by the GQDs/PAA. Due to the inability of GQDs/PAA to completely destroy the aromatic ring of SZZ within the reaction time into smaller molecules with low molecular weight such as CO_2 and H_2O, however, the residual by-products are less toxic and appear in much lower concentrations than the parent pollutant. Additionally, PAA being an organic peroxide has previously been reported to partially contribute to the TOC in the reaction [8]. Elsewhere, a low degree of mineralization of SSZ was observed when using Fenton-like reactions, and in that case, the authors ascribed the 20% TOC elimination to the complexation of SSZ with Fe^{3+} [4]. As a result of SSZ not being completely mineralized, further tests to evaluate the mutagenic and genotoxicity potential of the reaction by-products formed during the degradation process were necessary.
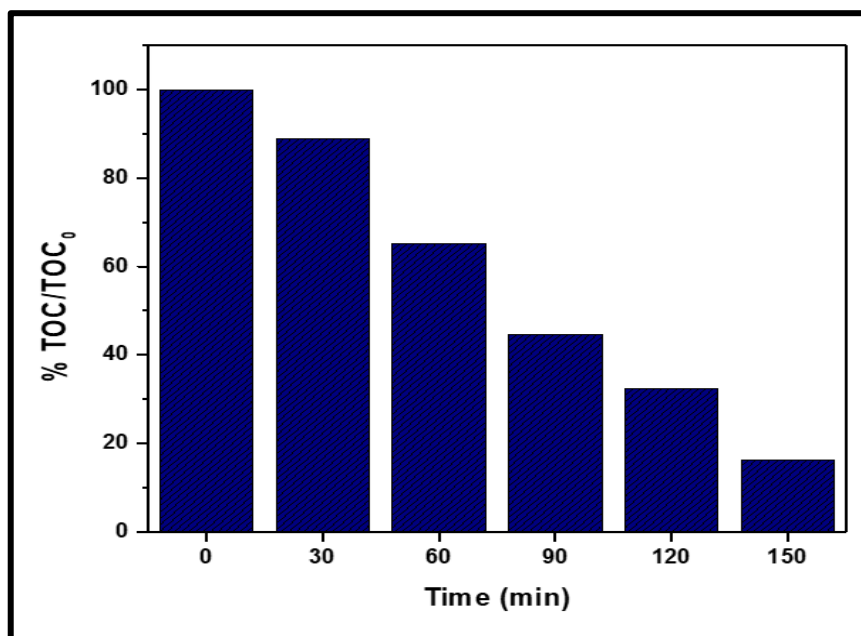
Figure 8.7:   TOC elimination of SSZ using GQDs/PAA.

8.3.6   **Genotoxicity and mutagenicity test using Ames assay**

The TOC results (**Figure 8.8**) indicated that some photodegradation intermediates remained even after SSZ was completely degraded and that complete mineralization was not achieved within the experimental time, which corroborated with a report by Fan et al. [4]. To verify whether the reaction intermediates formed during the photodegradation of SSZ were mutagenic; Ames assay was carried out. This assay, developed by Bruce Ames in 1970 [21] uses either *Salmonella* or *E. coli* bacterial strain to establish whether a specific chemical (in the case of this study the reaction by-products) are mutagenic. Typically, the bacterial strains used have a point mutation; (histidine in *Salmonella typhimurium*) and (tryptophan in *E. coli)* that will make it impossible for the bacterial strain to produce the corresponding amino acid. The point mutation results in the inability of the bacteria to produce corresponding amino acids and inhibit the growth of his- or trp- organisms unless histidine or tryptophan is supplied.

Culturing His-*Salmonella* in a medium containing the reaction by-products formed during the degradation of SSZ, may result in mutation on the histidine encoding gene, which will allow *Salmonella* to regain the ability to synthesize histidine. If the reaction by-products formed during the degradation of SSZ cause this reversion, the by-products will be considered as mutagens. The mutagenicity of the degradation by-products of SSZ will be proportional to the number of bacterial colonies counted on the test plate. Should there be many bacterial colonies on the test plate compared to the control, then the degradation by-products will be considered as mutagens. The assay made use of the aliquots collected at 30, 60, 90, 120 and 150 mins. The genotoxicity was expressed as the % of micronuclei per 10.000 nuclei and presented as the average per dose ± SD (**Table 8.2**).

Table 8.2:   **Mutagenicity of reaction-products in the photodegradation of SSZ using *Salmonella typhimurium* TA 98 and TA 100 tester strains.**

Reaction by-products/intermediates collected after	Number of colonies (mean ± SD)	
	TA 98	TA 100
0 min	16 ± 1	11 ± 1
30 mins	14 ± 3	17 ± 1
60 mins	11 ± 1	13 ± 2
90 mins	14 ± 2	56 ± 6
120 mins	16 ± 4	67 ± 8
150 mins	11 ± 1	12 ± 2
Positive control	652± 28	722 ± 21

Results presented in **Table 8.2** show that the reaction by-products are negative or weakly positive as per previous reports. The negative results give evidence that none of the reaction-by-products were toxic. This agrees with previous reports on PAA forming less toxic or no by-products at all when applied in the treatment of wastewater [22, 23]. Work reported by Monarca et al. [24] showed that no halogenated reaction by-products were formed after treating wastewater with PAA and mostly only carboxylic acids (which are not mutagenic) were reported, while weakly positive results were observed at 90 and 120 mins in the TA 100 strains, and were attributed to peroxy radicals, and hydroxyl radicals formed during the synergy of GQDs/PAA. Li et al. [25] Levin et al. [26] and Dillon et al. [27] reported that the presence of superoxide, singlet oxygen, and aldehydes gave positive results in the Ames assay. The reaction by-products from the SSZ degradation process did not induce any mutation in the two *Salmonella typhimurium* tester strains.

8.3.7   Antimicrobial activity of GQDs/PAA

8.3.7.1 Inactivation of representative bacteria *S. aureus*

The antimicrobial activity of the GQDs/PAA was evaluated on a representative bacterium, *S. aureus*. For comparative purposes the antimicrobial activity of PAA and GQDs was also

evaluated. Results demonstrated that under the same experimental conditions both PAA and GQDs were able to inactivate *S.aureus*, however, the addition of PAA significantly enhanced the antimicrobial activity (**Table 8.3**). The minimum inhibitory concentration (MIC) is the concentration needed to completely inhibit the growth of a microorganism. The lowest MIC was recorded for GQDs alone (45.1 µg/mL) and the highest recorded was for the GQDs/PAA (21.5 µg/mL). The improved antimicrobial activity of GQDs/PAA can be explained as follows: both GQDs and PAA have biocidal properties, the combined effect of GQDs/PAA results in complete cell destruction. The acetic acid of PAA is postulated to have reduced the intracellular pH as well as disrupted the chemiosmotic functions of the lipoprotein cytoplasmic membrane while the GQDs will inactivate bacteria because of direct contact as well as the oxidation of cellular components. Chang et al. [28] reported the MIC of *S.aureus* to be 0.33 mM when using 1 mM of PAA.

Table 8.3: **Minimum inhibitory concentration (µg/mL) of GQDs, PAA and GQDs/PAA.**

Materials	Minimum inhibitory concentration (µg/mL) of *S. aureus*
GQDs	45.1
PAA	32.8
GQDs/PAA	21.5

8.3.7.2 Bacterial inactivation mechanism of *S. aureus* and morphological observation by SEM

The mechanism of action of the GQDs/PAA against *S. aureus* was determined by morphological observation using SEM. The inactivation process was tracked by monitoring changes in morphology of the cell wall and the cell membrane of the cellular materials.

The SEM micrograph of the negative control (bacteria not exposed to GQDs/PAA) is shown in (**Figure 8.8a**); and from this micrograph an intact cell wall as well as the lining of the cellular material can be observed. The cell wall of the negative control is devoid of any artefacts and is relatively smooth. After 1 min of exposure to GQDs/PAA, the cell wall of the *S. aureus* started to disintegrate. It can be postulated that the PAA initially diffuses

through the cell wall of *S. aureus,* resulting in changes in the morphology of the cell wall. The cell wall looks visibly thinner and appears to erode at the surface and has a rougher edge, the same can be said about the cellular contents after 1 min (**Figure 8.8b**). After the diffusion of the PAA into the *S. aureus* cell wall, the GQDs will easily attach to the phospholipid lipid bilayer due to the electrostatic interactions resulting in further roughening of the cell wall and this is accompanied by an apparent deformation of the cellular material (**Figure 8.8c**). Once inside the cell, GQDs accumulate in the nucleus and the oxidative radicals will inhibit adenosine triphosphate (ATP), the replication of cells as well as cell respiration. Further exposure to GQDs/PAA (**Figure 8.8d** and **e**) resulted in the complete destruction of the cell-cortex and DNA compression. After 5 mins the *S. aureus* cells were completely destroyed and reduced to microscopic debris (**Figure 8.8f**). Based on the SEM micrographs it can be postulated that no regrowth of bacterial cells will occur due to the damage on the *S. aureus* being irreparable.
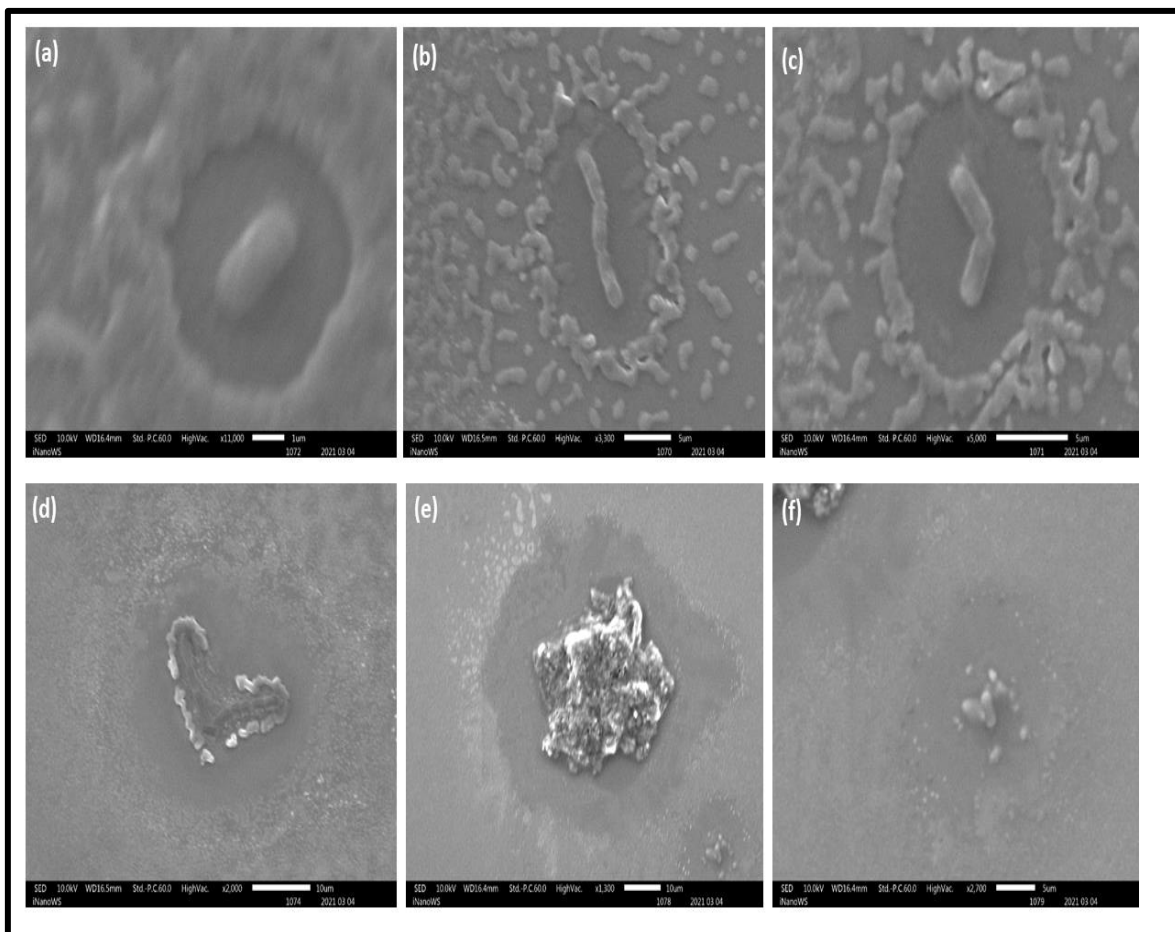
Figure 8.8: SEM micrographs of (a) *S. aureus* cells in the absence of GQDs/PAA (control), *S. aureus* cells after being exposed to GQDs/PAA for (b) 1 min, (c) 2 mins (d) 3 mins (e) 4 and (f) 5 mins under irradiation.

8.3.7.3 Cell viability

To further confirm the bactericidal effect of the GQDs/PAA combination on *S. aureus*, LIVE/DEAD *Bac*Light staining kit was used. Live healthy *S. aureus* cells (negative control) prior to being exposed to GQDs/PAA were stained green (**Figure 8.9**). After 1 min exposure to GQDs/PAA, both green and red staining was observed in the photomicrograph indicating that some *S. aureus* cells were beginning to die. The observed changes in the integrity of *S. aureus* cell membrane were due to the combined effect of GQDs/PAA in denaturing proteins and oxidizing enzymes which results in impaired intracellular cellular solute levels. After 3 mins a complete inactivation of *S. aureus* cells were stained red. These photomicrographs verified the role that GQDs/PAA plays in the loss of cell membrane integrity of *S. aureus*.

Using the same staining kit, results obtained by Costa et al. [29] reported that 2% and 0.25% of PAA were able to inactivate *S. aureus* after 30 mins contact time, while elsewhere Lee et al. [30] obtained a 100% inactivation of *S. aureus* on a biofilm after 60 seconds.
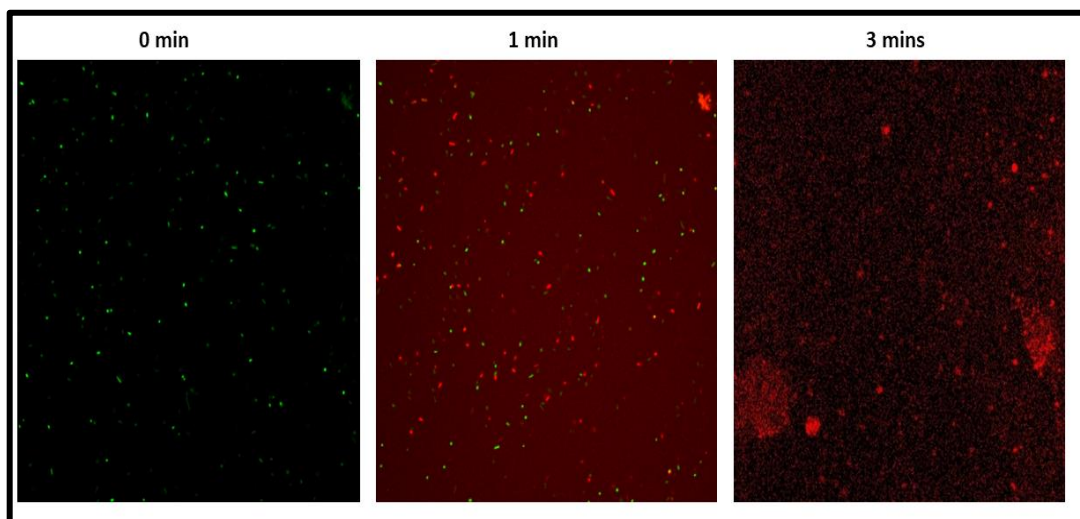
Figure 8.9:   Photomicrographs of *S. aureus* cells without GQDs/PAA and in the presence of GQDs/PAA after 1 and 3 mins.

8.3.7.4   Antimicrobial activity in real wastewater without spiking with model *S. aureus*

To examine the feasibility of the GQDs/PAA as a disinfectant, the disinfection ability was tested in raw water. The GQDs/PAA was added to WW samples under irradiation except using raw water and no addition of SSZ (only GQDs/PAA was used). At 30 seconds intervals the aliquots were collected and immediately mixed with 200 µL of sodium thiosulphate and 500 µL catalase to quench PAA from reacting further. 20 µl of the solution was plated using spread-plating technique and incubated at 37 °C for 24 hours.
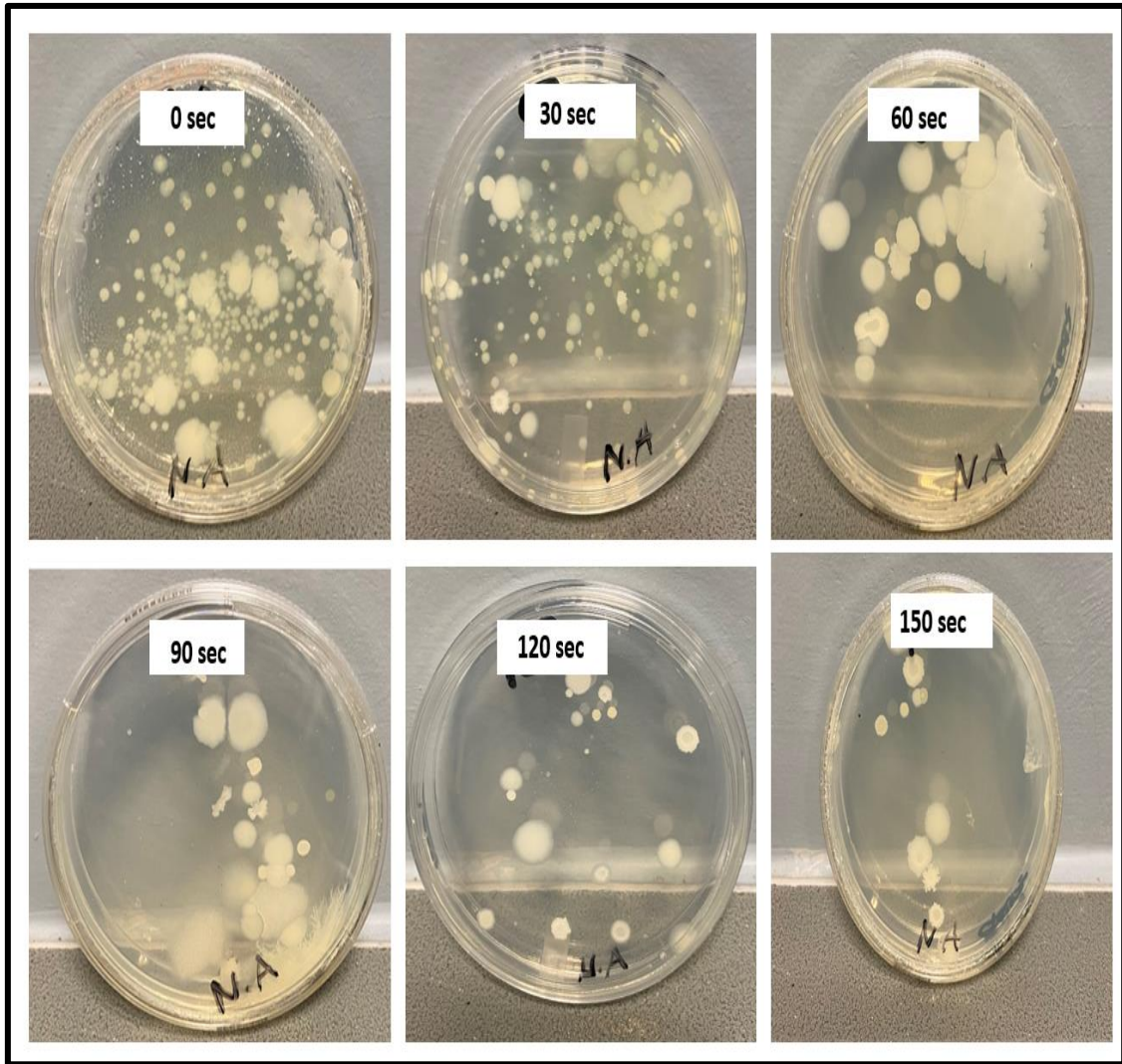
Figure 8.10: Bacterial colonies formed after treating raw wastewater with GQDs/PAA for 150 secs.

Figure 8.10 shows the microbial plate count, at time = 0 (before treatment with GQDs/PAA) and a significant number of colonies were observed on the plate. Increasing the exposure time to GQDs/PAA resulted in a reduced number of colonies on the plate. After 150 seconds, less than 10 colonies were present, indicating that the synergistic effect of the combination of GQDs and PAA was able to inactivate microbial species even in complex water matrices. Further studies need to be carried out to correctly identify the bacterial species that were not inactivated by GQDs/PAA. In an earlier study; Lefevre et al. [31] and Liberti et al. [32] cited that the limitation of PAA being used as a disinfectant was in its inability of inactivating viruses and protozoa at reasonable doses. More recently, Mezzanotte et al. [33] showed that

PAA efficacy was limited to other bacteria at lower doses. The recommendation from the study would be to vary the doses of PAA, the photocatalyst and even the contact time to yield better results.

8.4   Conclusion

A combination of graphene oxide quantum and peracetic acid (GQDs/PAA) was used to degrade SSZ in wastewater. Key findings include:

- The effect of PAA dosage on the photodegradation of SSZ was evaluated. The obtained results showed a dose-dependent trend wherein increasing the PAA concentration resulted in almost 100% photodegradation of the SSZ which was also accompanied by an increment in the k_{obs} value from 0.03612 to 0.03842 min^{-1} at higher PAA concentrations.

- Varying the initial concentration of SSZ (10-50 mg/L) while maintaining a constant concentration of GQDs/PAA (0.05 g/L: 0.10 mM) resulted in the lowest concentration of SSZ (10 mg/L) yielding the highest degradation efficiency of 100%, while the highest concentration of SSZ (50 mg/L) recorded the lowest removal efficiency of 20%.

- The main reactive radicals responsible for the degradation of SSZ in wastewater were identified as hydroxy (•OH) as well as peroxy radicals $CH_3C(=O)OO•$ and $CH_3C(=O)O•$.

- The genotoxic and mutagenic potential of the degradation products formed during the degradation of SSZ were confirmed to be non-mutagenic. GQDs/PAA was further evaluated as a potential disinfectant and *S. aureus* was completely inactivated. GQDs/PAA also eliminated more than 90% of bacteria present in raw wastewater.

This contribution presents an opportunity to simultaneously degrade pharmaceuticals and their active metabolites as well as inactivate microorganisms using GQDs/PAA. The results could potentially be applied in tertiary treatment of urban wastewater treatment systems.

References

1. Volin M.V, Campbell. P.L, Connors, M.A, Woodruff. D.C, Koch, A.E. *Exp. Mol. Pathol.* 73(2002) 84.

2. Neafsey K, Zeng. X, Lemley. A.T. *J. Agric. Food Chem.* 58(2010) 1068.

3. Kasprzyk-Hordern B, Dinsdale, R.M, Guwy. A.J. 2009. *Water Res*.43 (2009)363.

4. Fan X, Hao.H, Shen, X, Chen. F, Zhang, J. *J. Hazard. Mater*. 190(2011) 493.

5. Ji Y, Yang. Y, Zhou, L, Wang. L, Lu, J, Ferronato. C, Chovelon, *J. Water Res.* 133(2018) 299.

6. Pelalak R, Alizadeh. R, Ghareshabani. E, Heidari. Z. *Sci. Total Environ*. 734(2020) 139446.

7. Chen J, Zhang. L, Huang. T, Li.W, Wang. Y, Wang. Z*, J. Hazard. Mater*. 320 (2016)571.

8. Zhang L, Liu. Y, Fu. Y, *RSC Adv*. 10 (2020) 9907.

9. Cai A, Wang. Q, Chang. Y, Wang. X.J. *Alloys Compd.* 692(2017) 183.

10. Santhos. C, Malathi. A, Daneshvar. E, Kollu. P, Bhatnagar. A, *Sci. Rep.* 8(2018) 1.

11. Gopinath A, Krishna. K, *Photochem. Photobiol*. 95 (2019)1311.

12. Luo C, Ma, J, Jiang, J, Liu, Y, Song, Y, Yang, Y, Guan, Y, Wu, D, *Water Res*. 80 (2015) 99.

13. Kirk L.A, Tyler. C.R, Lye. C.M.Sumpter. J.P., *Environ. Toxicol. Chem*. 21 (2002) 972.

14. Sonune A., Ghate. R., *Desalination* 167(2004) 55.

15. Luo C., Ma. J., Jiang, J., Liu, Y., Song, Y., Yang, Y., Guan, Y, Wu, D., *Water Res.* 80(2005) 99.

16. Shi X.T., Liu. Y.Z., Tang, Y.Q., Feng, L, Zhang, L.Q., *Environ. Sci. Pollut. Res*. 25(2018) 672.

17. Wang Z., Wang. J., Xiong, B., Bai, F., Wang, S., Wan, Y., Zhang, L., Xie, P, Wiesner, M.R, *Environ. Sci. Technol.* 54(2019) 464.

18. Cai A., Wang. Q., Chang, Y, Wang, X., *J. Alloys Compd*. 692(2017) 183.

19. Omrania N., Nezamzadeh-Ejhieha. A, lizadehb, M., *Catalysts,* 17(2019) 24.

20. Ames B.N., McCann. J, Yamasaki, E., *Mutat. Res.* 31(1975) 567.

21. Monarca S., Richardso, S.D., Feretti, D., Grottolo, M., Thruston Jr, A.D., Zani, C., Navazio, G., Ragazzo, P., Zerbini, I, Alberti, A., *Environ. Toxicol. Chem*. 21(2012) 309.

22. Baldry M.G.C., *Crit. Rep. Appl. Chem*. 23(1988)91.

23. Monarca S., Feretti. D., Zerbini, I., Zani, C., Alberti, A., Richardson, S.D., Thruston Jr, A.D., Ragazzo, P, Guzzella, L., *Water Sci. Tech-W. Sup*. 2(2012) 199.

24. Li Y., Chen. D.H., Yan, J., Chen. Y., Mittelstaedt, R.A., Zhang, Y., Biris, A.S., Heflich, R.H. and Chen, T, *Mutat. Res. Genet. Toxicol*. 745(2012) 4.

25. Levin D.E., Hollstein. M., Christman. M.F., Schwiers, E.A, Ames, B.*Proceedings of the National Academy of Sciences*, 79(1982)7445.

26. Dillon D., Combes, R, Zeiger, E., *Mutagen*. 13(1998)19.

27. Chang W., Toghrol, F, Bentley, W.E., *Environ. Sci. Technol*. 40(2006)5124.

28. Costa S.A.D.S., Paula. O.F.P.D., Leão. M.V.P, Santos, S.S.F.D*., Braz. Oral Res*. 29(2015)1.

29. Lee S.H.I., Cappato. L.P., Corassin, C.H., Cruz, A.G, Oliveira, C.A.F., *J. Dairy Sci*. 99(2016) 2384.

30. Lefevre F., Audic. J.M, Ferrand, F, *Water Sci. Technol*. 25(1992)155.

31. Liberti L, Notarnicola, M., *Water Sci. Technol.* 40 (1999)235.

32. Mezzanotte V., Antonelli. M., Azzellino, A., Citterio, S, Nurizzo, C, *Water Sci. Tech-W. Sup*. 3(2003) 269.

CHAPTER 9

FABRICATION OF POLYETHERSULFONE ELECTROSPUN NANOFIBROUS MEMBRANES EMBEDDED WITH GRAPHENE OXIDE QUANTUM DOTS WITH ANTIMICROBIAL ACTIVITY AND ENHANCED FOULING RESISTANCE

9.1   Introduction

It is known that during wastewater treatment, slurry photocatalytic systems tend to result in secondary contamination. To mitigate this limitation, this chapter presents the development of novel electrospun nanofibrous membranes (ENMs) prepared by embedding GQDs into polyethersulfone (PES). The incorporation of GQDs bestows the membrane with biocidal properties, this is important because membranes are generally affected by bio-film formation. This occurs when pathogenic microbes grow on the membrane surface [1]. The presence of the biofilm will decrease the water flux as well as negatively affect the overall membrane performance, this results in increased energy consumption as a result of higher pressure being required to overcome the biofilm resistance [2]. The aims of this chapter were to: (a) optimize electrospinning parameters in the fabrication of GQDs-PES ENMs and (b) determine the fouling resistance of the resultant membranes by testing the antimicrobial activity the following bacterial strains : *E. coli*, *B. cereus* and *S.aureus*.

9.2 Experimental details

9.2.1 Preparation of GQDs-PES ENMs

The GQDs were embedded in the polymer as detailed in **Chapter 3**.

9.2.2 Fabrication of PES-GQDs ENMs

PES and GQDs polymer solutions were pumped using a KD Scientific Syringe Pump Series 100 the parameters are outlined in **Chapter 3**.

9.2.3 Characterization of GQDs and PES-GQDs ENMs

The fabricated materials were characterised by microscopy, spectroscopy and contact angle instruments as described in **Chapter 3**.

9.2.4 Antimicrobial activity

9.2.4.1 Selection of microbial strains

The antimicrobial activity of the GQDs-PES ENMs was evaluated against *E. coli* (ATCC 25922), *B. cereus* (ATCC 14579) and *S. aureus* (ATCC 25923).

9.2.4.2 Antibacterial activity

All the antimicrobial experiments were conducted as described in **Chapter 3**.

9.3 Results and discussion

9.3.1 Morphology and size distribution determination of ENMs

Several parameters can influence the electrospinning process, including the distance between the capillary tip, the applied voltage, the flow rate, the temperature and humidity of the environment, as well as the nature of both the solvent and the polymer [3]. The tip to collector distance (TCD), the viscosity of the solution, and the solvent ratio were all

investigated and varied. **Figure 9.1** shows an example of micrographs (additional pictures shown in the **Appendix A1**) obtained at polymer concentrations less than 26 wt% (**Figure 9a** and **b**). These micrographs show the presence of beads of nanoparticle, which are not ideal for our study.
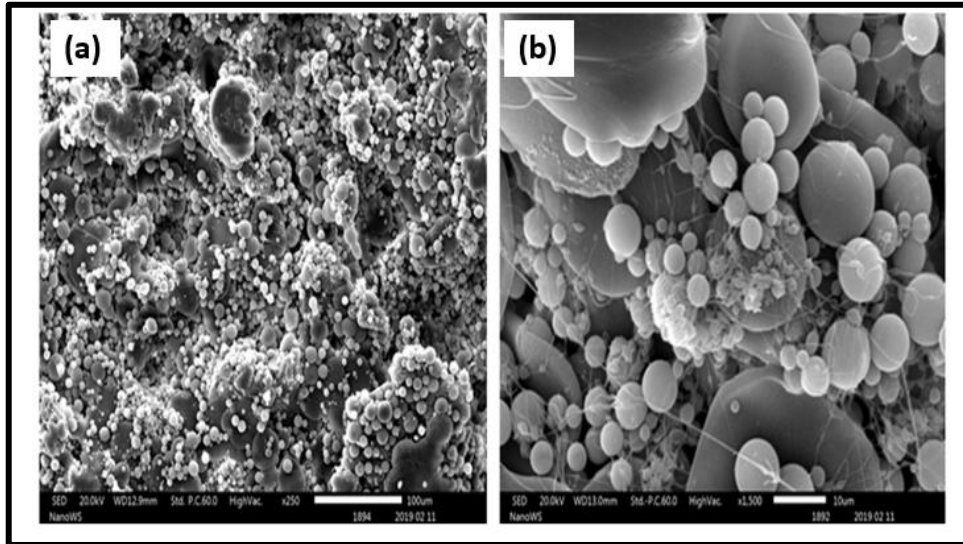
Figure 9.1: SEM micrographs of pristine PES nanofiber at polymer concentration of 20 wt % at (a) lower and (b) higher magnification.

The optimum concentration was found to be 26 wt%, and this was used to incorporate GQDs. The electrospun fibres produced as shown in **Figure 9.2a** were without defects such as nanoparticle beads and droplet formation at this concentration (26 wt%), which was ascribed to low viscosity and fluid jet break [4]. The morphology and diameter of the GQDs-PES ENMs were studied using HR-SEM and ImageJ software was used to calculate the diameters of the ENMs. Unbranched and cylindrical ENMs without GQDs (**Figure 9.2b**) have reasonably smooth surfaces. With nanopores in their matrix, the ENMs without GQDs had an average diameter of 2.1 µm. Upon embeddeding the ENMs with GQDs, some GQDs could be seen embedded inside the membrane, while others were visible on the surface. An increase in diameter to 2.45 µm (**Figure 9.2c**). The diameter of the fibres is said to be dependent on the viscosity of the solution [5]. The addition of GQDs enhanced the viscosity of the solution, and hence the increase in nanofibre diameter.
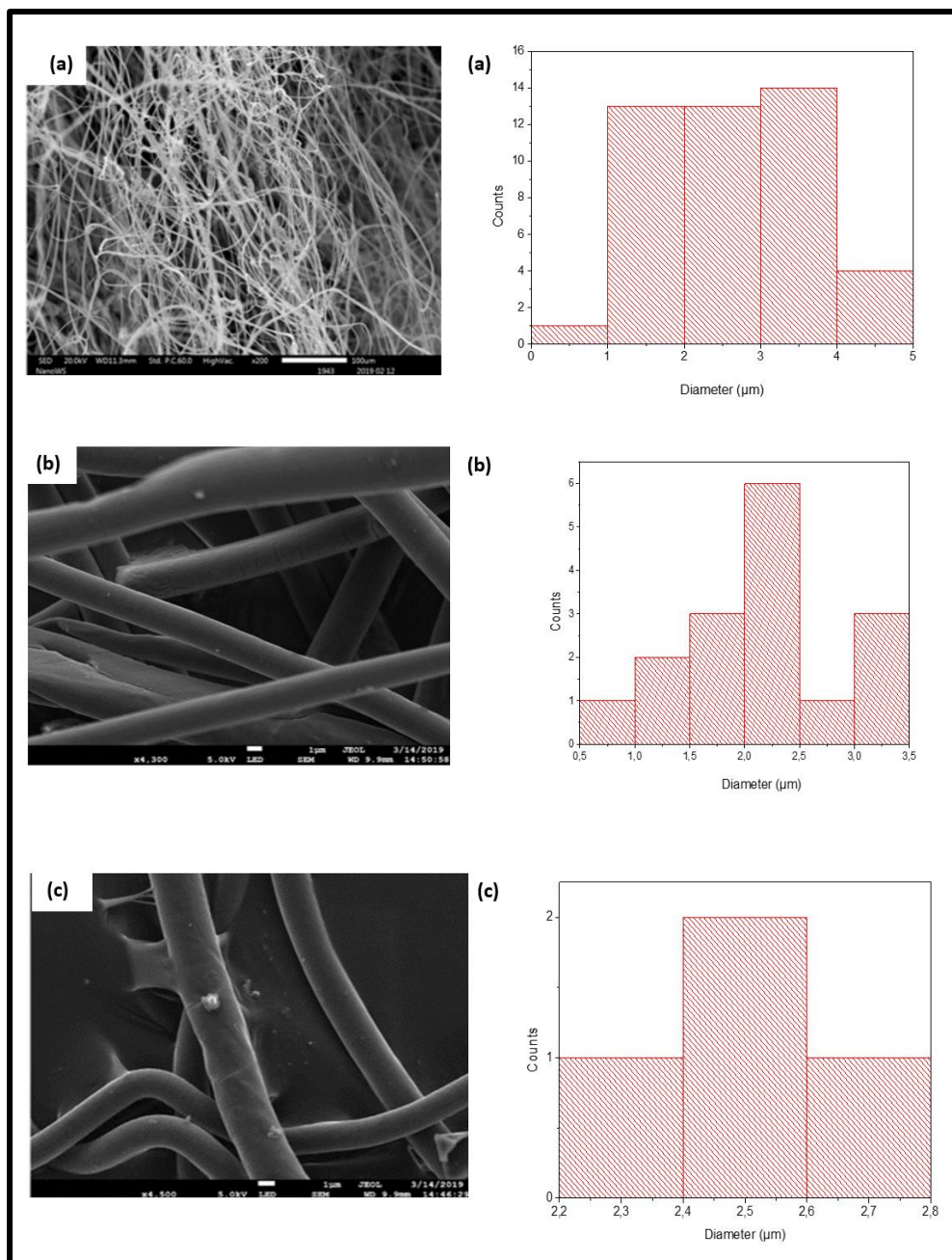
Figure 9.2: SEM micrographs and size histograms of (a) pristine PES nanofiber, HR-SEM micrograph of (b) pristine PES nanofiber and (c) PES-GQDs ENMs.

9.3.2 Functional group identification and optical properties of the PES, GQDs and PES-GQDs ENMs

FT-IR was used to verify whether the GQDs were successfully incorporated into PES to generate PES-GQDs ENMs. **Figure 9.3** illustrates the FT-IR spectra of GQDs alone, bare PES, and GQDs-PES ENMs. The O-H stretching vibrations appear as a widened peak in the region 3100-3600 cm^{-1} in the spectrum of GQDs alone (**Figure 9.3a**). The peaks at 1710 cm^{-1} and 1621 cm^{-1} represent typical stretching vibrations of the carboxylic and/or carbonyl moiety of C=O. The band at 1203 cm^{-1} is likely due to the C-O vibrational deformation [6]. The results of the FT-IR correlates to work previous work by Štengl et al. [7] for reduced GQDs and by Manna et al. [8] for GQDs.

Incorporating GQDs in the PES was marked by changes in the spectrum of the pristine PES (**Figure 9.3b**). The interaction between the GQDs and PES is due to Van der Waals forces. The sharp peak about 3100 cm^{-1} vanished after the GQDs were added. Instead, a wider peak was detected, which was attributed to the O-H stretching vibrations.

The characteristic peaks of the PES, such as benzene rings between -1600 cm^{-1}, ether functional groups at 1296 cm^{-1} - 1319 cm^{-1}, and sulfone vibrations at 1100 -1140 cm^{-1}, remained after the inclusion of the GQDs, indicating that the PES structure was not distorted. The characteristic peaks of the GQDs were also visible in the composite (**Figure 9.3c**), certifying that their incorporation was successful.
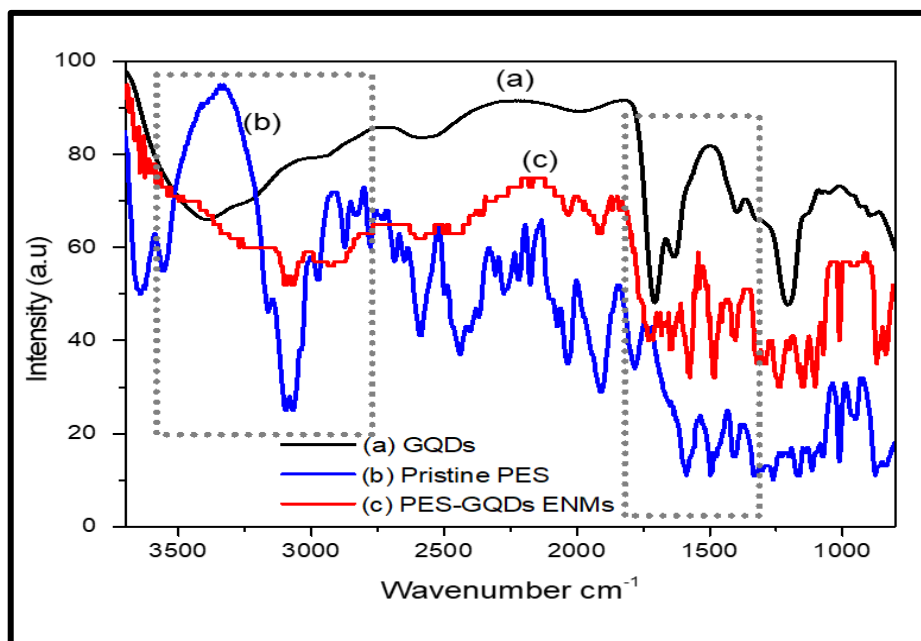
Figure 9.3:   FT-IR of (a) GQDs) (b) pristine PES nanofiber and (c) GQDs-PES ENMs.

9.3.3   UV-Vis analysis

The absorption spectra of the GQDs-PES ENMs, pristine PES ENMs, and GQDs alone were run to verify the inclusion of the GQDs in PES (**Figure 9.4a-c**). The GQDs were incorporated successfully into the PES polymer, as evidenced by a peak with a shoulder at 351 nm, which corresponds to the absorbance of the GQDs alone, as shown in **Figure 9.4**.
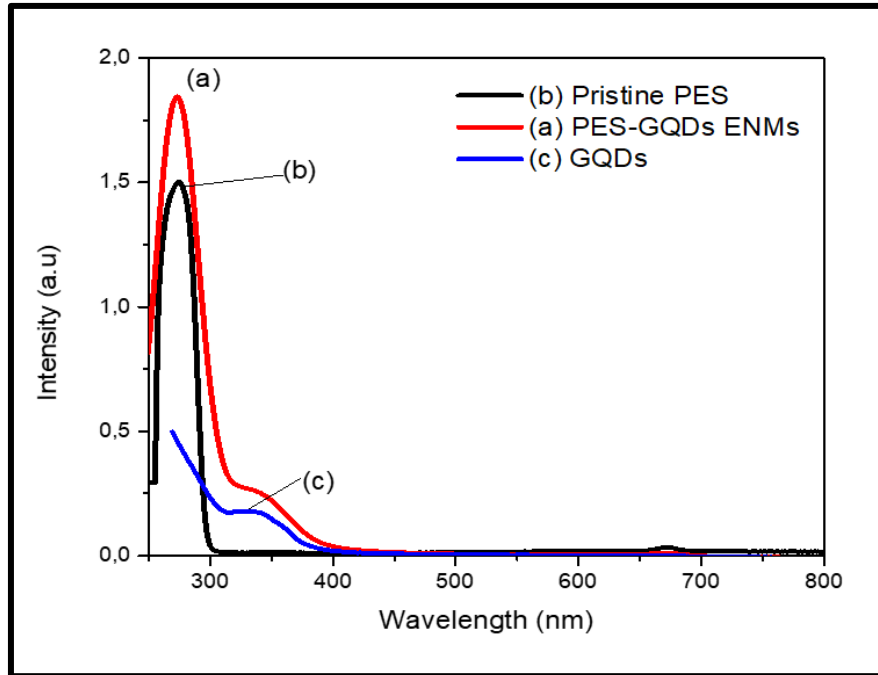
Figure 9.4:   Ground state absorption of (a) GQDs in PES (b) PES alone and the (c) GQDs alone.

9.3.4   Raman spectroscopy analysis

Raman spectroscopy data was utilized to assess the quality of GQDs produced and to validate the successfully incorporation of GQDs into the PES solution. Excitation was provided by a 514-nm laser. **Figure 9.5** shows two noticeable peaks that indicate that the GQDs were successful synthesised. **Figure 9.5a** depicts the presence of the 'D' (1362 cm^{-1}) and 'G' (1611 cm^{-1}) bands, whereas **Figure 9.5b** depicts the 'D' and 'G' values at 1350 cm^{-1} and 1590 cm^{-1}, respectively. These bands are attributed to hexagonal lattice defects and disorder, as well as sp^2 bonding. The ratio of the intensity of the D and G bands (I_D/I_G ratio) is used to represent the amount of sp^2 /sp^3 hybridization of carbon atoms. The I_D/I_G ratio of the GQDs alone (**Figure 9.5a**) was higher than that of the GQDs in the fibre. The findings are in line with the findings of Chhabra et al. [9].
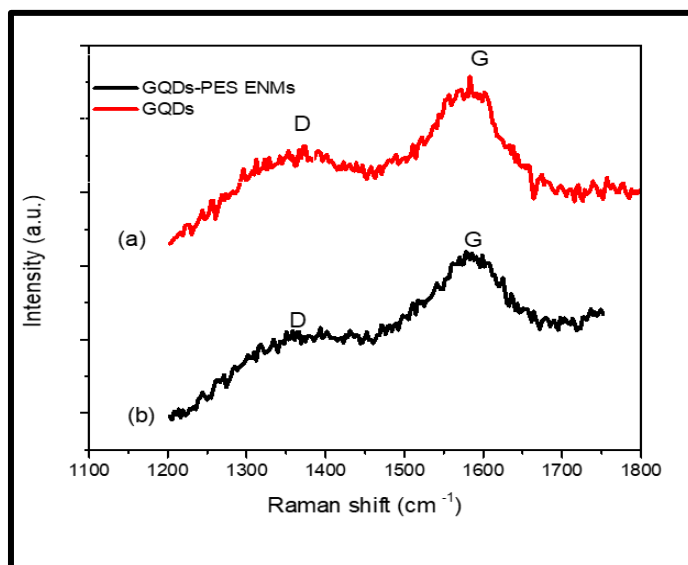
Figure 9.5:   Raman of the (a) GQDs and (b) GQDs-PES ENMs.

9.3.5   **XRD analysis**

The crystalline structure of GQDs and GQDs-PES ENMs was determined using XRD analysis. XRD peaks for GQDs are identical to those previously reported, implying that the GQDs are structurally similar to graphite [10]. **Figure 9.6a** shows that the carbonization of citric acid resulted in GQDs that have a more compact interlayer spacing than the initial graphene, with a broad conspicuous peak at $2\theta = 24$ and an interlayer spacing of 0.36 nm. Pristine PES is an amorphous, highly disordered material with a strong XRD peak at $2\theta = 18$ (**Figure 9.6c**). After incorporating GQDs in the polymer (**Figure 9.6b**), the characteristic peaks of the GQDs and PES were still visible but with a slight shift. The peak belonging to the PES was now seen at at $2\theta = 16$ and $2\theta = 27$ for the GQDs, and this was ascribed to the interaction of the two nanoparticles.
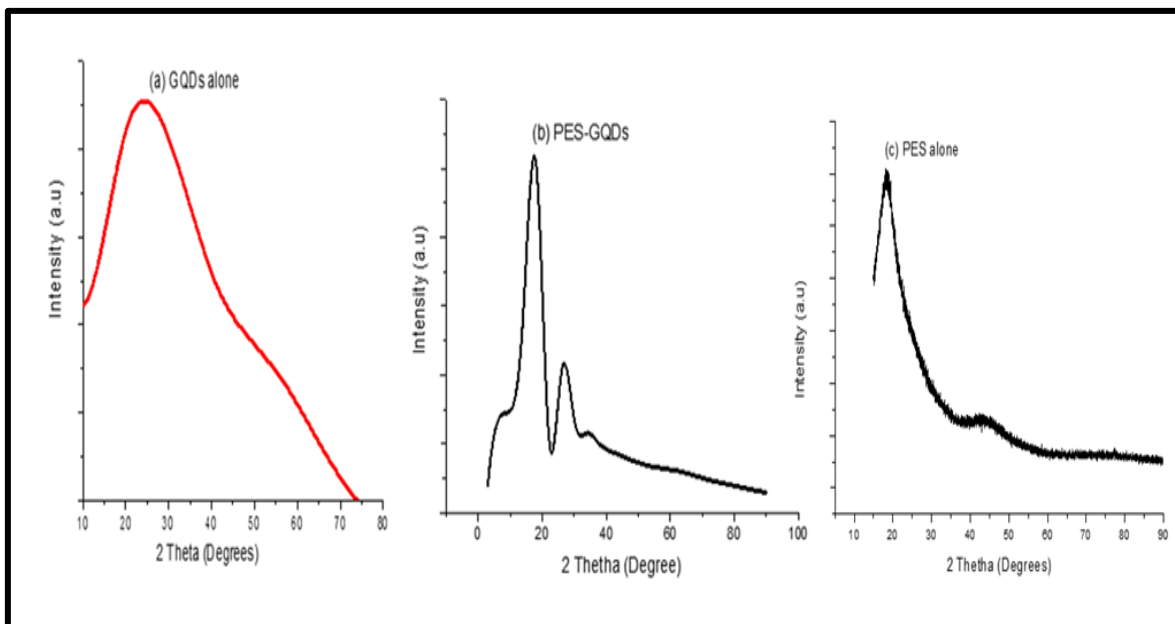
Figure 9.6:   XRD patterns of (a) GQDs (b) GQDs-PES ENMs and (c) pristine PES.

9.3.6   Contact angle measurement

Sessile drop observation was used to determine the surface contact angle of ENMs with and without GQDs. The bare PES ENMs had a surface contact angle of 64.3°, which corresponded to a decreased surface hydrophilicity. The contact angle decreased to 38.5° after embedding with GQDs, which was ascribed to the larger amount of oxygen containing moeities on GQDs that were identified by FT-IR. Other parameters (such as electrospinning voltages) have been shown to influence the contact angle in addition to surface chemical features.

9.3.7   Antimicrobial activity of the PES-GQDs ENMs

GQDs-PES ENMs were evaluated against *E. coli, B. cereus and S. auerus*. The inhibitory effect of the GQDs is depicted in **Figures 9.7** and **9.8**. Pure PES nanofibers were used as the negative control and showed no bacterial activity.Whereas adding different amounts of GQDs (7.0, 7.5 and 10 wt %) in the polymer resulted in sizeable ZOI against *E. coli, B. cereus and S. aureus).* The antibacterial activity of GQDs-PES-ENMs containing 10% GQDs was substantial. The diameter of the ZOI were 36 mm, 39 mm and 40 mm when tested

against *E. coli*, *S. aureus* and *B. cereus* respectively. At 7.5 wt% of the GQDs, the GQDs-PES-ENMs recorded ZOI of 25 mm, 29 mm, 23 mm when tested against *E. coli, S. auerus* and *B. cereus* respectively.
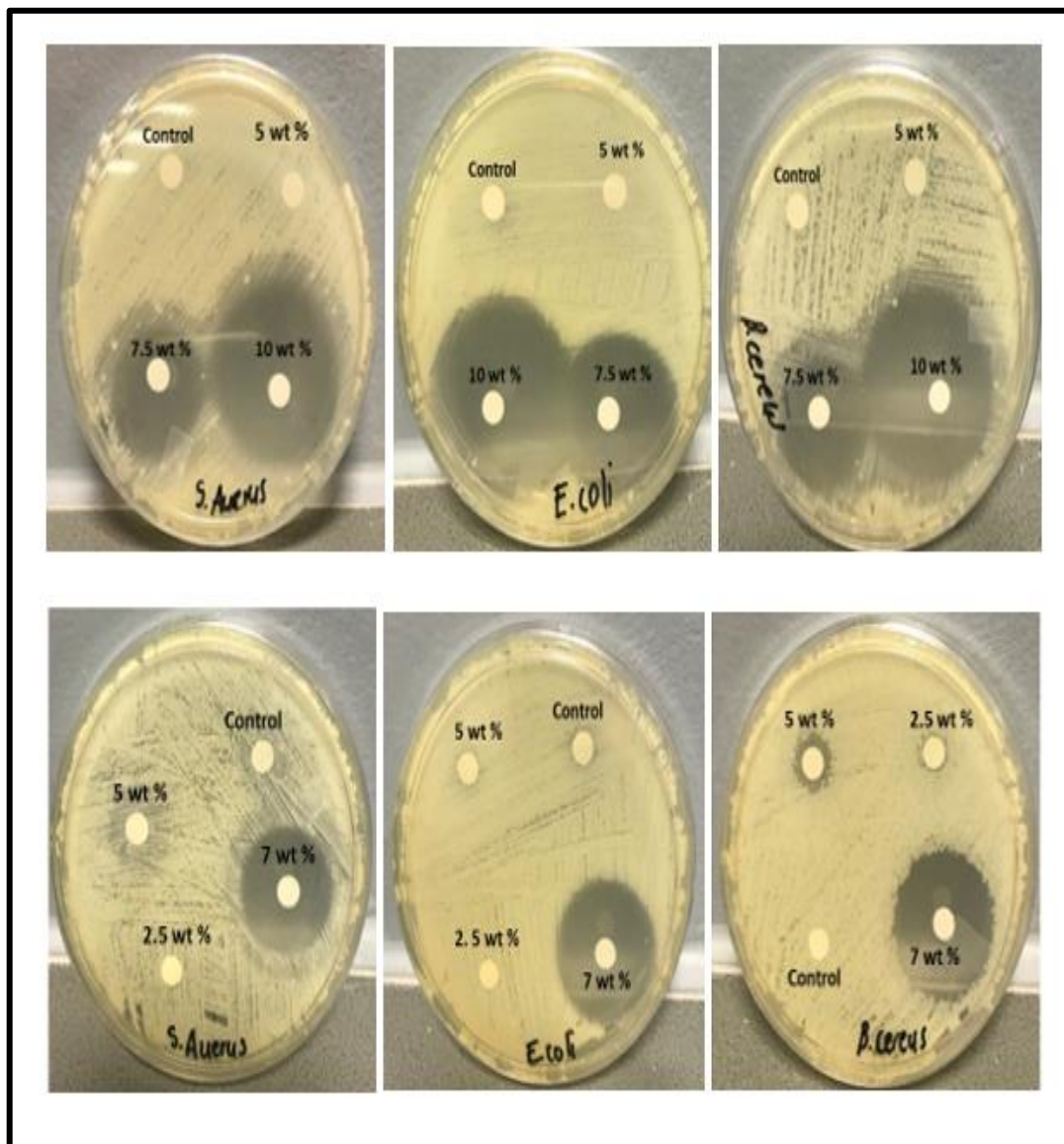
Figure 9.7:   Inhibitory effect of GQDs at varying GQDs concentration.

When the GQDs-PES-ENMs were evaluated at 7.0 wt% of the GQDs, the diameter of the ZOI was recorded as 29 mm, 24 mm, and 23 mm, respectively. With the exception of *B. cereus*, there was no antibacterial activity and thus no ZOI at lower GQD concentrations (2.5 and 5 wt%). A small ZOI of 9 mm was seen. The difference in the morphology of the cell walls of these bacteria may explain why 5 wt% of GQDs inhibited *B. cereus* (very small ZOI in *S. aureus*) but not *E. coli*. Gram-negative bacteria are characterized by an outer cell membrane cmade up of of liposaccharide in the outer leaflet and phospholipids in the inner leaflet, but Gram-positive bacteria do not, possibly making the Gram-positive bacteria more susceptible to GQDs inactivation.
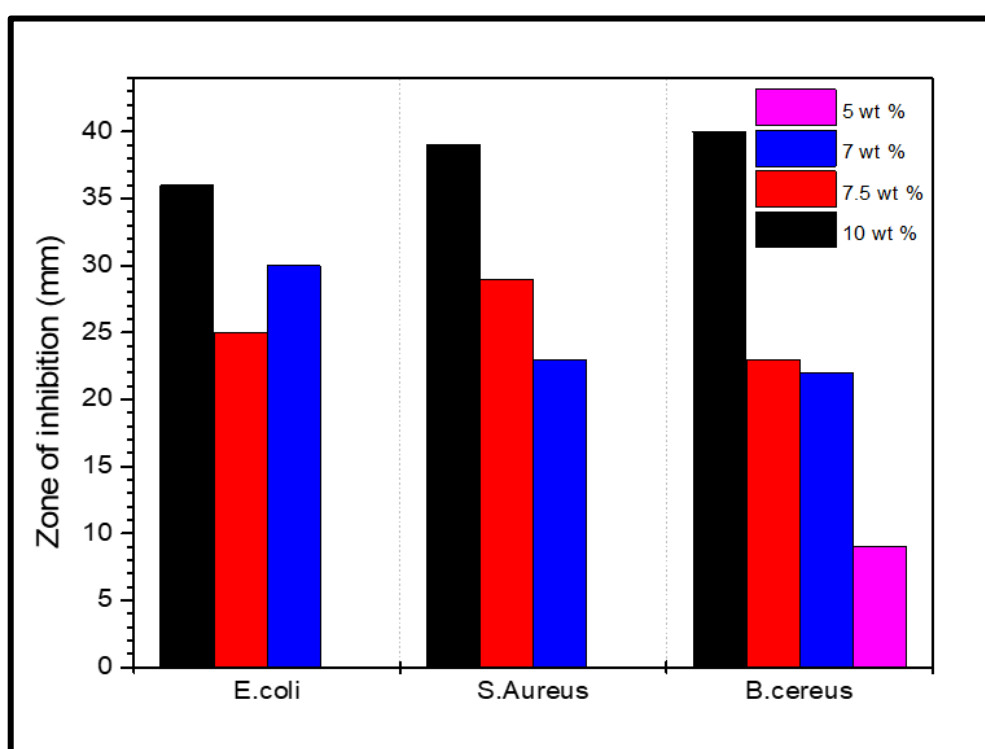
Figure 9.8:   Qualitative data of the diameter of the ZOI of the GQDs-PES-ENMs.

The antibacterial mechanism is thought to be a synergistic combination including (a) oxidative stress and (b) contact inhibition. Initially, the GQDs-PES ENMs improve GQDs' attachment to the cell membrane of bacteria; the large π-conjugated system of GQDs makes attachment easier. GQDs with high specific area will promote contact inhibition which results in the cutting of lipid membranes due the strong forces from the unique sp^2 structure of graphene. This ultimately results in the destruction of the cell membrane [11]. Alternatively, GQDs can cause membrane stress by increasing oxidative stress, in which

GQDs oxidize vital cellular components, causing cell content leakage and death [12]. The antimicrobial activity of polymer modified GQDs has been demonstrated in the literature, and GQDs-coated PVDF membrane effectively inactivated *E. coli* and *S. aureus* cells, resulting in excellent antimicrobial activity (88.9% inhibition rate within 1 hour) and anti-biofouling capability. GQDs-PVDF membrane activity was higher than that for two-dimensional GO sheet and one-dimensional carbon nanotube-modified membranes [13]. Following an 8-hour incubation period, PEGylated GOQDs showed 100% growth inhibition for *S. aureus* (25 g/mL) and *P. aeruginosa* (50 g/mL). The MICs for *E. coli, B. cereus,* and *S. aureus* were found to be 0.5 mg/mL, 0.3 mg/mL, and 0.2 mg/mL, respectively, in this investigation.

9.4   Conclusion

GQDs were added to a PES to form a dope solution that was electrospun and gave rise to GQDs-PES ENMs. Raman microscopy, contact angle, SEM, and FT-IR and XRD spectroscopy confirmed the incorporation of GQDs into the PES membrane to form GQDs-PES ENMs. Significant findings from the chapter were:

- After incorporating the GQDs, the surface ENMs were relatively smooth, unbranched, and with and the average diameter of 2.45 µm.
- The GQDs-PES ENMs were evaluated against three bacterial strains; *E. coli*, *S. aureus*, and *B. cereus* and showed significant zones of inhibition at 7, 7.5 and 10 wt % of GQDs in all three bacterial strains and inhibition at 5 wt% when tested against *B. cereus*. Antibacterial activity was mediated by oxidative stress and contact inhibition, both of which cause cell death.
- *E. coli* had the highest MIC (0.5 mg/mL), followed by *B. cereus* (0.3 mg/mL), and *S. aureus* (0.2 mg/mL).

The findings of this work point to the feasibility of adding GQDs into membranes for wastewater treatment which can be applied in wastewater treatment systems.

References

1. Bernardo P, Drioli, *Pet. Chem.* 50(2010) 271.
2. Feng C, Khulbe K.C, Matsuura T, Tabe S, Ismail A.F, *Sep. Purif. Technol* 102(2013) 118.
3. Carnell L.S, Siochi E.J, Holloway N.M, Stephens R.M, Rhim C, Niklason L.E, Clark R *Macromolecules* 41 (2008) 5345.
4. Darko G, Goethals A, Torto N, De Clerck K, Appl Nanosci 6(2016) 837.
5. Qin X.H, Wan Y.Q, He J.H, Zhang J, Yu J.Y, Wang S, *Polymer* 45(2004) 6409.
6. Huang N, Lim L, Chia C.H, Yarmo M.A, Muhamad M.R, *Inter. J. Nanomed*. 6(2011) 3443.
7. Štengl V, Bakardjieva S, Henych J, Lang K, Kormunda M, *Carbon* 63(2013) 537.
8. Manna S, Bhattacharya S, Sengupta S, Das P, *J. Clean. Prod*. 203(2018) 83.
9. Chhabra V.A, Kaur R, Kumar N, Deep A, Rajesh C, Kim K.H, *RSC Adv* 8(2018)11446.
10. Hashemzadeh H, Hasanzadeh M, Shadjou N, Eivazi-Ziaei J, Khoubnasabjafari M, Jouyban A, J Pharm Anal 6(2016) 235.
11. Zeng Z, Yu D, He Z, Liu J, Xiao FX, Zhang Y, Tan T.T.Y, *Sci. Rep*. 6(2016) 20142.
12. Gopal R, Kaur S, Ma Z, Chan C, Ramakrishna S, Matsuura T, *J. Membr. Sci.* 281(2006) 581.
13. Nasrollahi N, Vatanpour V, Aber. S, Mahmoodi N.M, *Sep. Purif. Technol*. 192(2018)369.

CHAPTER 10

FABRICATION OF POLYETHERSULFONE/GRAPHENE OXIDE QUANTUM DOTS MEMBRANES FOR HYBRID-FILTRATION-ADVANCED OXIDATION PROCESSES FOR TREATMENT OF WASTEWATER

10.1   Introduction

The final chapter of this thesis presents the development of a hybrid-AOPs-filtration system. Based on the previous chapters of this thesis, it was established that GQDs have excellent photocatalytic and antimicrobial features and it was further proven that the synergy between PAA and GQDs significantly enhanced the antimicrobial and photocatalytic properties. Importantly, the GQD/PAA system did not yield any toxic disinfection by-products as was confirmed through Ames test. This chapter seeks to integrate AOPs with membrane technology to achieve the following: (i) simultaneous separation and photodegradation of organic pollutants as the membrane will retain all the un-oxidized organic pollutants, (ii) enhance anti-fouling or self-cleaning properties that are imparted on the membrane and (iii) overall improve membrane fluxes. In the hybrid configuration AOPs (using GQDs as photocatalyst) were applied in the pre-treatment process, followed by passing the feed-water through PES/GQDs membrane and finally post treatment (exploiting the synergy between GQDs and PAA). Further, the performance of the fabricated PES/GQDs was compared to a commercial membrane (Film Tec™NF270). The quality of the wastewater after treatment was assessed by monitoring parameters such as TOC, EC, pH, TDS, turbidity as well as the microbial content.

10.2 Experimental details

10.2.1 Fabrication of PES/GQDs mixed matrix membranes (MMM)

The PES/GQDs membranes were prepared *via* phase inversion method. Pristine membranes (M0) were prepared without the incorporation of GQDs. For the GQDs incorporated membrane 5 wt % (w/w) concentration of GQDs as nanofillers in the PES matrix (M1) was used, details of the composition of the fabricated membranes are detailed in **Chapter 3**.

10.2.2 Membrane characterization

Characterization techniques such as FT-IR, EDX, FESEM, contact angle and zeta potential were carried out as outlined in **Chapter 3**.

10.2.3 Membrane performance

10.2.3.1 Permeation and water retention tests

Permeation tests experiments were conducted using a cell fixed in dead-end mode and the water retention capability tests of the synthesized membranes were performed as discussed in **Chapter 3**.

10.2.3.2 Dye removal tests and rejection studies

Dye solutions of methyl orange (MO) and Rhodamine B (RhB) (15 ppm) were utilized in the dye removal tests employing the fabricated membranes and the rejection studies were conducted using 0.01 M of different salt solutions made up of Na_2SO_4, NaCl and $MgSO_4$ salt as detailed in **Chapter 3**.

10.2.3.3 Antibacterial testing of PES/GQDs membranes against *E.coli* and in real wastewater sample

The antibacterial efficacy of the PES/GQDs membrane was performed using a shake flask method as well as colony counting method as described in **Chapter 3**. After being subjected

to real wastewater effluent, the bacterial content of the fabricated PES/GQDs and the commercial membrane were evaluated, the experimental design is detailed in **Chapter 3**.

10.2.4 Water quality

The quality of the wastewater samples was assessed at the sampling points depicted in (**Figure 10.1**). The sampling points were as follows: before pretreatment **(point 1)**, after pretreatment **(point 2)**, after the membrane filtration step **(point 3)** and after the AOPs step using GQDs/PAA **(point 4)** by measuring the following parameters: pH, turbidity, total dissolved solids (TDS), total organic carbon (TOC) and the electrical conductivity (EC). The removal rate of the water quality parameters was calculated using **Equation 10.1**.

$$R = 1 - \frac{C_P}{C_f} \text{ x } 100 \text{ \%} \qquad \qquad \textbf{(Eq. 10.1)}$$

where C_p is the treated water quality parameter and C_f is the feed water quality parameter.
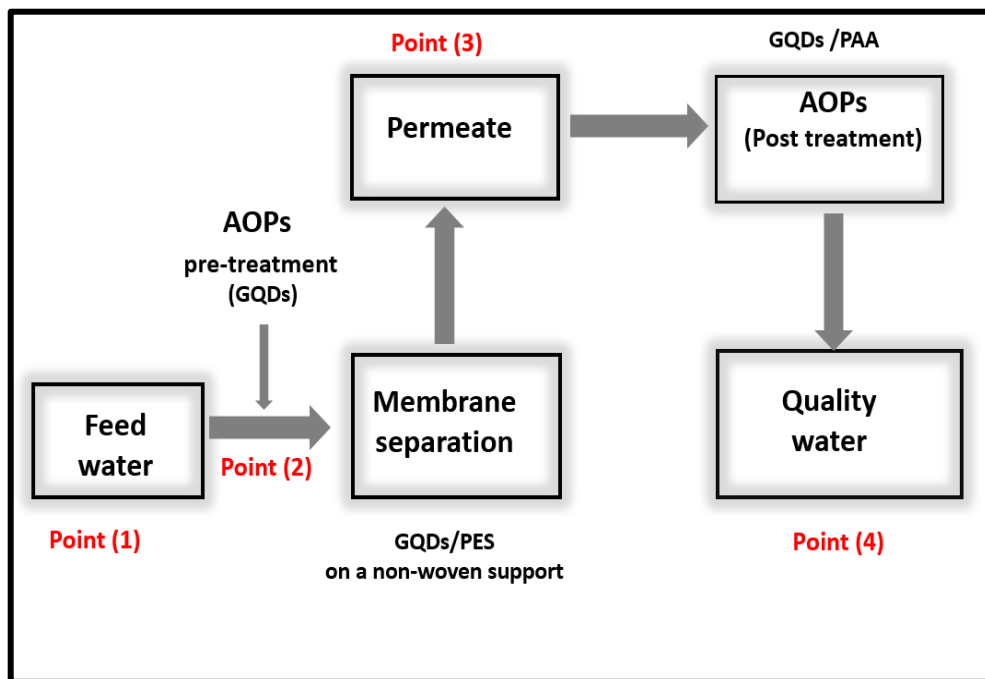

Figure 10.1: Integrated AOPs and membrane technology configuration and the labelled points at which the water quality parameters were determined.

## 10.3	Results and discussion

### 10.3.1	GQDs and PES/GQDs characterization

The GQDs were characterized using TEM and the micrograph shows the synthesized GQDs were not aggregated and were mostly spherical in morphology (**Figure 10.2a**). The particle size was estimated to be 4.8 nm. EDX analysis was used to determine the elemental composition of the GQDs. The EDX spectra (**Figure 10.2b**) shows that the GQDs were composed of C and O which confirmed the successful synthesis of GQDs and as reported in literature [1]. No other elemental peaks were observed confirming the high purity of the GQDs
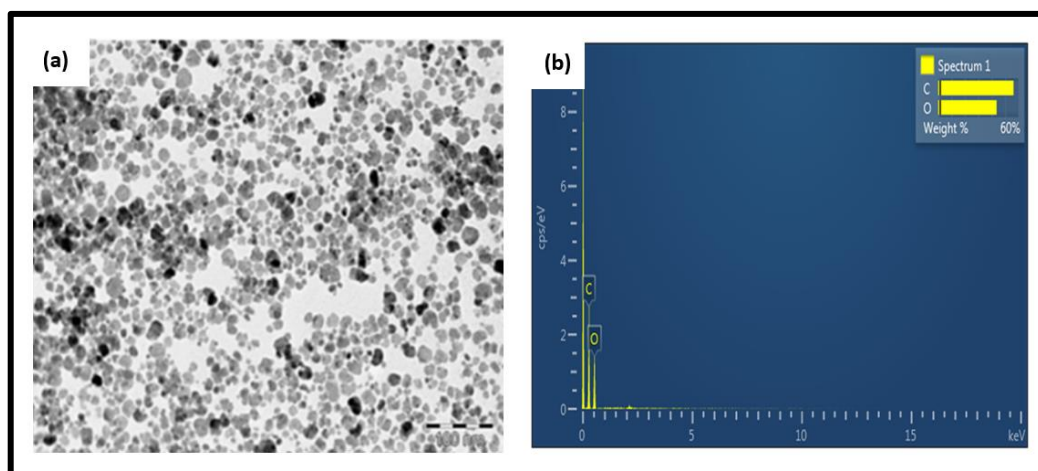
Figure 10.2: (a) TEM micrograph and (b) EDX spectra of the synthesized GQDs.

### 10.3.2	**Functional groups confirmation**

The incorporation of GQDs in the PES membrane was confirmed using FT-IR (**Figure 10.3a-c**); incorporating GQDs in PES resulted in spectral vibrational changes. The sharp peak at 3100 cm^{-1} in PES disappeared and, in its place, a broader peak emerged on PES/GQDs which was assigned to the O-H stretching vibrations. Interestingly, after incorporating GQDs in the polymer the original structure of the PES was not perturbed nor distorted. This was evidenced by the characteristic peaks of the PES i.e benzene rings 1600 cm^{-1}, ether functional groups at 1296 cm^{-1}, 1319 cm^{-1}, sulfone at 1100-1140 cm^{-1} which

were still present indicating that the structure of the PES was not affected neither was the structure of the GQDs.
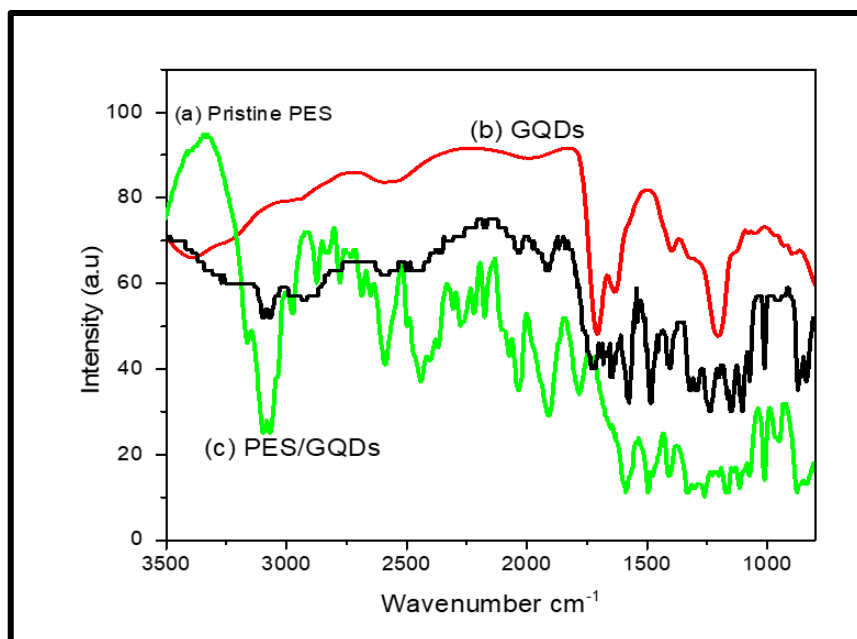

Figure 10.3: FT-IR of the pristine (a) PES (M0) (b) GQDs and (c) PES/GQDs mixed matrix membrane (M1).

10.3.3 Surface and cross-sectional morphology of the membranes

FESEM was used to assess the surface as well as the porosity of the membranes before and after the incorporation of GQDs. **Figure 10.4** shows the surface of the membranes M0 and M1. In M0 the surface is relatively smooth, however, addition of GQDs can be visually seen on the membrane surface. For the cross-sectional view, typical asymmetrical macrovoids were observed in M0. The incorporation of GQDs in the casting solution increased the number of pores as well as wider interlocking channels. Similar observations were reported by Ren et al. [2]. These changes are attributed to the hydrophilic nature of GQDs. By incorporating GQDs in the casting solution, exchange between the solvent (NMP) and nonsolvent (water) is facilitated to yield wider channels with greater porosity and ultimately increased permeability of the membrane [3]. Therefore, the introduction of GQDs increased the membrane porosity, according to FESEM data.
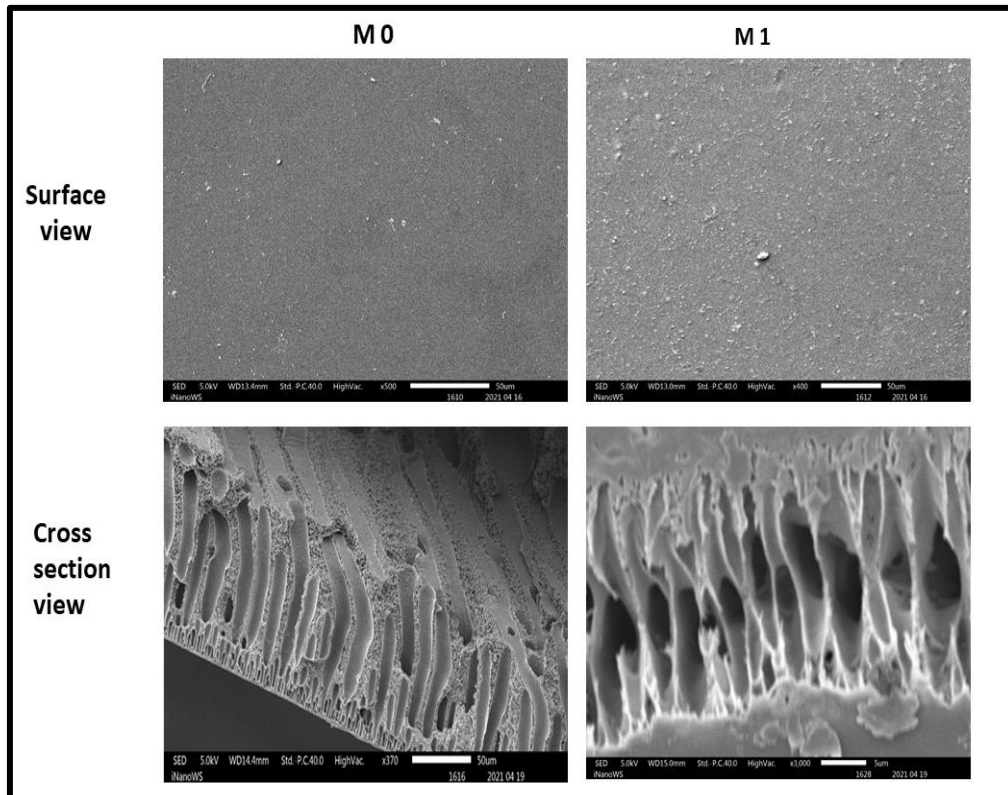
Figure 10.4: FESEM micrographs of the surface and cross-sectional view of M0 and M1 membranes.

10.3.4 **Porosity determination**

In the same vein, the average total porosity of M0 and M1 were calculated as 52 and 69%, representing a 17% increase in the porosity (**Figure 10.5a**). A similar trend was observed for the pore size, wherein the addition of GQDs resulted in the pore size increasing from 23 to 48 nm (**Figure 10.5b**).
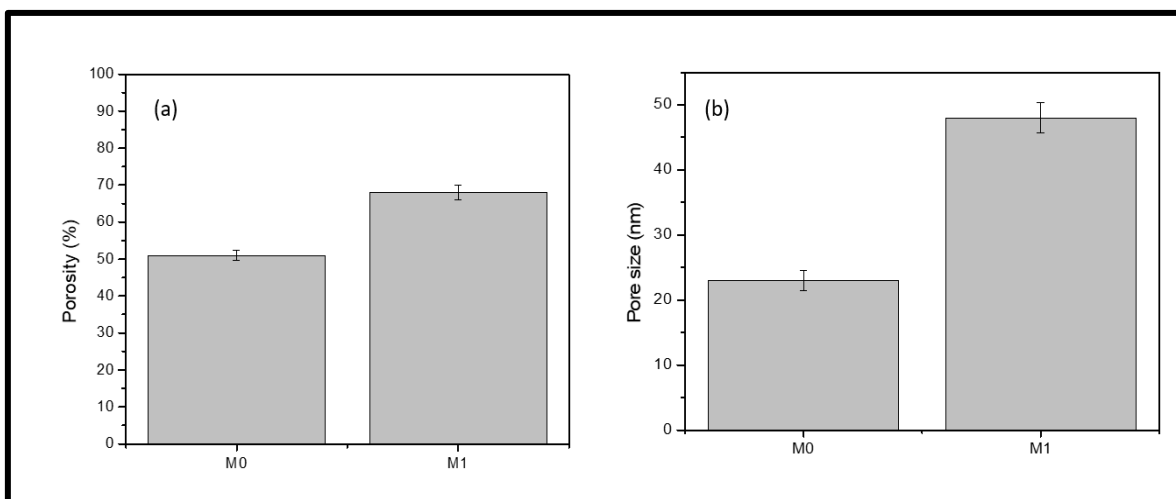
Figure 10.5: (a) Average total porosity and (b) pore size of M0 and M1.

Information relating to the hydrophilic nature of the membrane was determined by looking at two parameters: wettability of the surface membrane as well as the water retention capacity. Due to the hydrophobic nature of PES, a contact angle of 64.8° was recorded for the pristine PES (**Figure 10.6a-c**). As per the Young model [4], the addition of GQDs increased the hydrophilicity of the membrane evidenced by a decrease in contact angle to 36.5°. The exact mechanism of improvement in hydrophilicity is as follows: typically, GQDs have a higher number of oxygens containing functional groups and during the phase inversion process as the solvent and non-solvent exchange, GQDs will have more affinity towards water which will cause them to drift more towards the surface of the membrane [5].
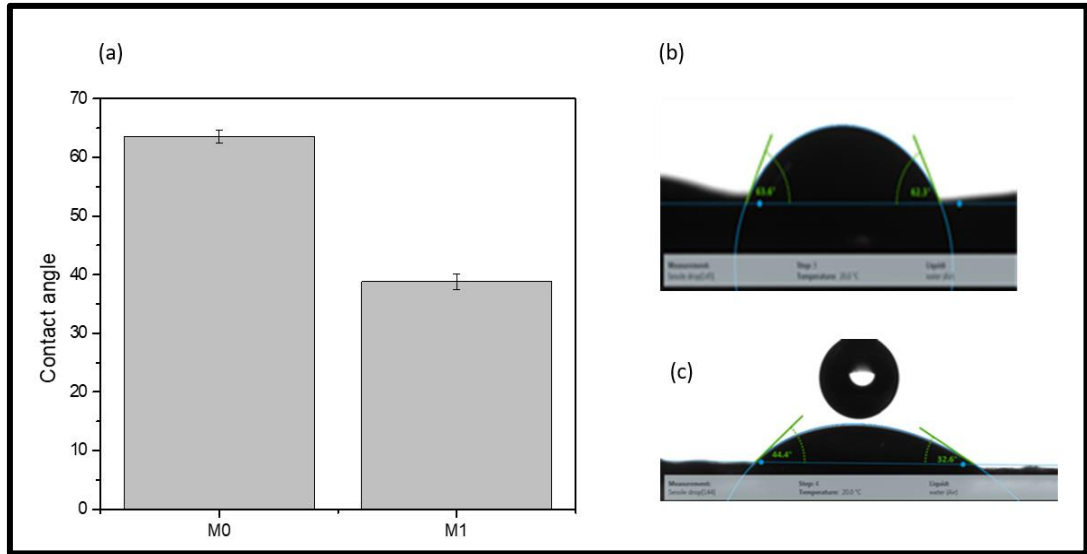
Figure 10.6: (a) Reported average contact angle values for M0 and M1 (b) photographs of contact angle measurements for M0 and M1.

10.3.5 Water flux measurements

The experimental data obtained for the PES/GQDs membrane at different operational pressure (1-6 bar) is presented in **Figure 10.7**. The measured flux for M0 was lower at all pressures which can be ascribed to the hydrophobic nature of PES and the morphological structure of pristine PES membranes that is characterised by small pores and lower pore density as observed in the FESEM image (**Figure 10.4**). The addition of the GQDs in the membrane caused an overall improvement in the flux at all pressures, and this can be explained in relation to the membrane hydrophilicity, porosity and morphological structure. The increase in operational pressure also significantly improved the flux.
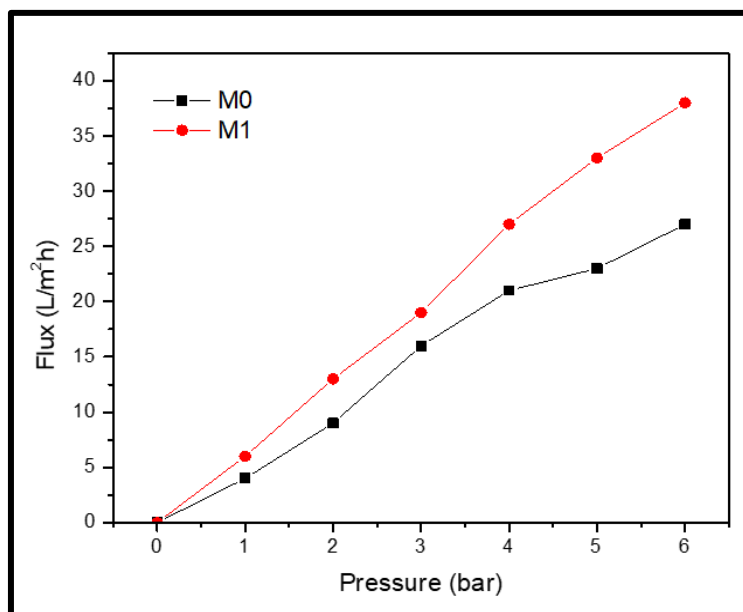
Figure 10.7:   Water flux for PES/GQDs M0 and M1 membranes as function of pressure.

10.3.6   **Salt rejection**

The salt rejection rate of the PES and PES/GQDs membranes is presented in **Figure 10.8**. The addition of GQDs in the membrane slightly increased the salt rejection rate, and this is attributed to the distribution of GQDs which facilitates greater interaction with the ionic $MgSO_4$, NaCl and $NaSO_4$. The salt rejection percentage was in the order; $NaCl > NaSO_4 > MgSO_4$ which was ascribed to the hydration size of ions necessary for mass transfer *via* the pores of the membrane, ion diffusion as well as the electrostatic interaction with the membrane. Elsewhere, using PES/GO membranes; the authors attributed the high salt rejection of the GO incorporated membrane to the great dispersion of GO in the polymer matrix as well as the increased number of active sites on the membranes [6].
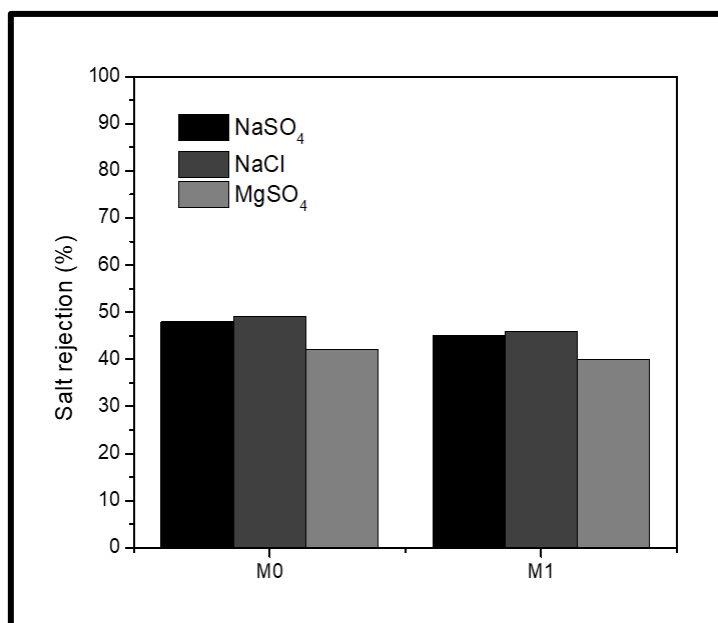
Figure 10.8: Salt rejection percentage PES/GQDs using M0 and M1 membranes.

10.3.7 Performance of M0 and M1 in the removal of dyes

UV-Vis was used to measure the absorbance of each dye solution after filtration through M0 and M1 and the commercial membrane (CM) (Film Tec™NF270) to determine the membrane rejection efficiency. The rejection of the dye solutions is presented in **Figure 10.9**. The CM recorded the highest dye removal (above 80% for both dyes), followed by M1 with a rejection rate of 62% and 65% of MO and RhB respectively. This can be explained using the Donan phenomenon (or the electrostatic repulsion) [7], where the cationic features of MO and RhB dyes and the anionic membrane surfaces result in repulsion.
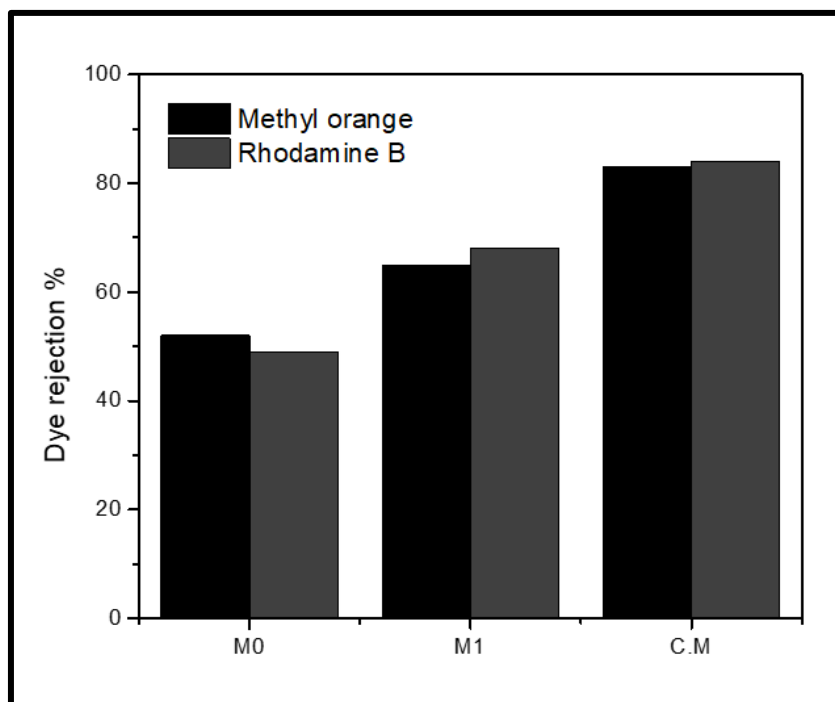
Figure 10.9: Dye rejection percentage of M0 and M1 membranes.

This is further corroborated by zeta-potential data presented in **Table 10.1** which shows that the surfaces of M0 and M1 were negatively charged. The negative charges were ascribed to the presence of the sulfonic group O=S=O groups on the PES [8]. It is a known reality that negatively-charged membranes offer better separation in mixtures as a result of the electrostatic repulsion between the membrane surface and the pollutants in aqueous medium. In contrast, M0 showed the lowest rejection rate of the dyes (47% and 51%) for MO and RhB respectively.

Table 10.1: **Zeta potential as a function of pH for the PES/GQDs membranes.**

Membrane	pH	Charge (mV)
	6.1	-29.3 ± 0.075
M0	8.6	-30.2 ± 0.063
M1	6.7	-33.4 ± 0.052
	8.3	-33.7 ± 0.078

10.3.8 **Antibacterial efficacy of PES/GQDs membranes**

M0 and M1 membranes were incubated in a suspension of *E. coli* overnight for 24 hours at 37 °C on NA and the surface of the membranes were visualized using FESEM (**Figure 10.10**). On the pristine membrane (M0), *E. coli* cells can be seen on the surface of the membrane. In contrast, after the incorporation of GQDs in the membrane (M1) there was a noticeable inhibitory effect resulting in the reduction of *E. coli* cells on the surface of the M1. It is known that all bacteria (both Gram-positive and negative) carry a net-negative charge [9]. In Gram-negative bacteria specifically, the negative charge is ascribed to the phospholipids and polysaccharides that comprise the outer part of the bacterial cell membrane [10]. The contact angle and zeta potential results can be used to elucidate the mechanism of inactivation. The M0 membrane (without GQDs) is hydrophobic in nature which result in the repulsion of water molecules on the surface of the membrane. This is most likely due to the absence of hydrogen bonds on the boundary layer [11]. The vacant space promotes the settlement of bacteria or any other foulants on the surface of the membrane. However with M1, a hydration layer will form and this will prevent the colonization of the *E. coli* cells on its surface.
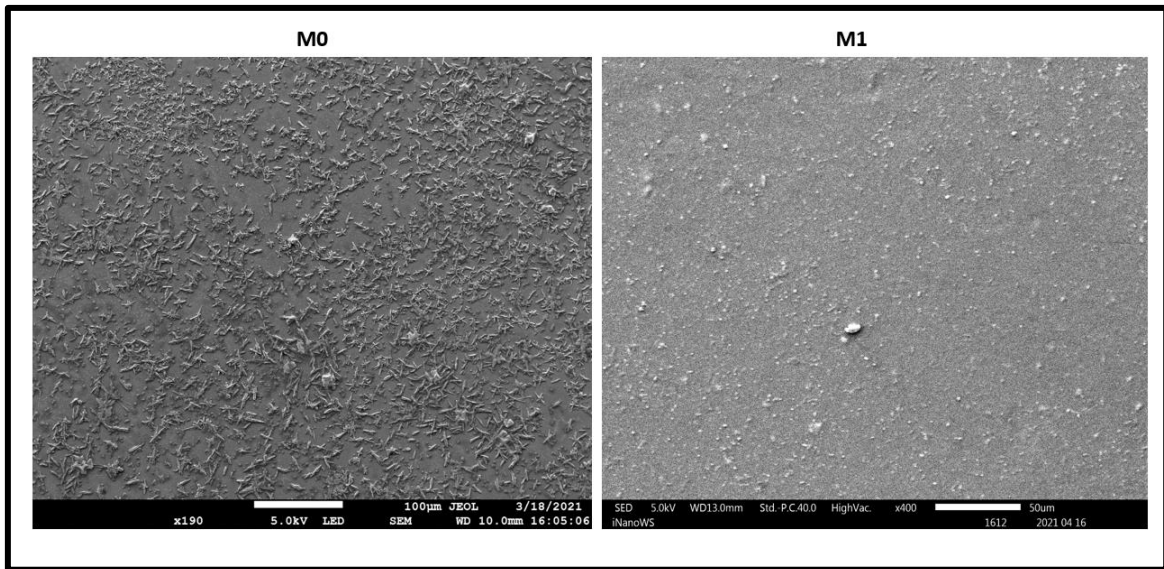
Figure 10.10: Surface of membranes after *E. coli* tests.

In this study we propose the antibacterial mechanism is due to the synergistic combination that occurs either *via* oxidative stress or contact inhibition (trapping, wrapping, or cutting) (**Figure 10.11**). The possible mechanism is based on membranes being able to cut through the *E. coli* cells resulting in the extraction of phospholipids. Alternatively, the *E. coli* cells can be wrapped or entrapped by the polymer or more likely through induced membrane stress which will increase the oxidative stress, where vital cellular components will oxidized and result in cell content leakage and cell death. Observations made in this work are consistent with what has been reported in previous studies [12-14].
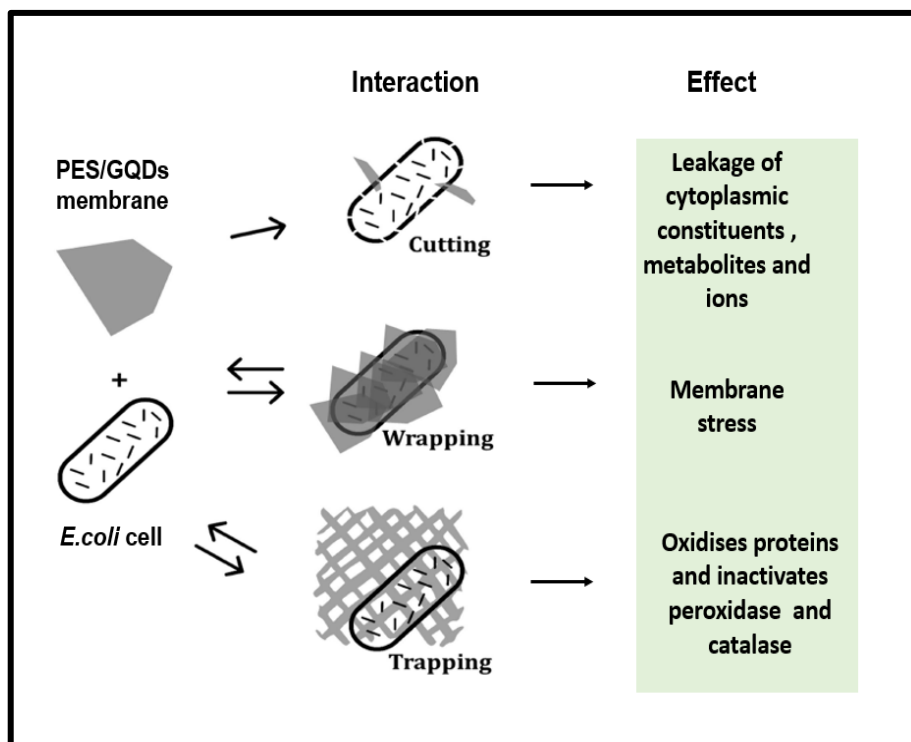
Figure 10.11: Possible inactivation mechanism of PES/GQDs membranes, the interaction and effect on *E. coli* cells.

10.3.9 Changes in the wastewater quality after treatment with hybrid-filtration

The physicochemical properties of the wastewater were assessed before and after the three treatments as described in **Figure 10.1**. The WQPs parameters before and after treatment are summarised in **Table 10.2.** Compared to the PES/GQDs membrane (M1), the recorded percentage removals for the CM were as follows 86.6%, 64.4%, 51.21% and 76.83% for turbidity, TDS, TOC and EC respectively. While M1 recorded 83.45%, 64.12%, 40.76% and 70.36%. Each of the parameters is discussed separately in the subsequent sections.

Table 10.2: **Water quality parameters of the feedwater before and after treatment with integrated with AOPs/membrane techniques.**

	pH	Turbidity (NTU)	Total dissolved solids (mg/L-1)	TOC (mg C.L-1)	Electrical conductivity (µS cm-1)
Point (1)	6.88 ± 0.2	112.± 4.62	354	22.30± 0.0323	743± 5.3
Point (2)	6.82 ± 0.1	18.54 ± 1.44	127	13.21± 0.0454	220±2.8
% Removal	N/A	83.45	64.12	40.76	70.39
Point (3)	6.71 ± 0.2	1.97 ± 0.54	122	12.49±0.052	171±3.2
% Removal	N/A	98.24	77.68	44.00	76.99
Point (4)	6.79 ±0.1	0.48 ± 0.02	34	4.32± 0.012	112±2.0
% Removal	N/A	99.6	90.4	80.63	84.93

10.3.10 **Turbidity**

There was an enhanced removal of the turbidity in the wastewater sample (**Figure 10.12**), suggesting that AOPs (using GQDs as the photocatalyst) were able to remove a significant portion of the dissolved and suspended solids and/or particulate matter. Furthermore, passing

the wastewater sample through the PES/GQDs membrane further reduced the turbidity which can be ascribed to the size exclusion effects of the membranes. It can be postulated that the by-products obtained after AOPs were larger than the pore sizes of M1 so were retained through size exclusion. A similar phenomenon was observed by Maifadi et al. [15], post-treatment in this study, resulted in significant removal of the turbidity.
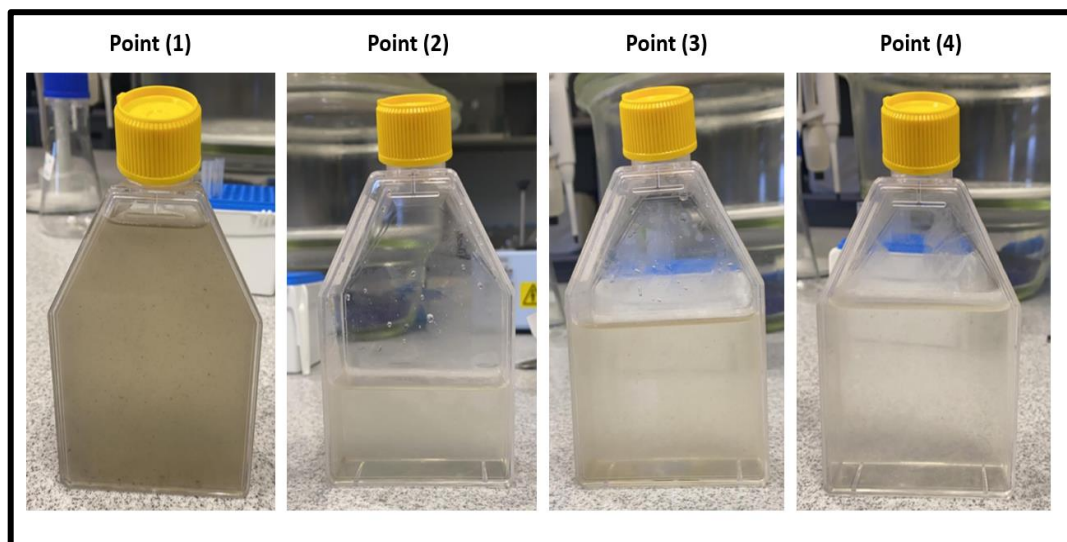
Figure 10.12: Turbidity of the wastewater at different sampling points.

10.3.11 **Total organic carbon (TOC)**

The TOC was reduced after the AOPs marked by a % removal of 40.76, however no significant difference was observed in the TOC after the membrane filtration (% removal of 44). The observation was expected because typically a significant percentage of the organics formed through AOPs may pass through the membrane pores. Conversely, post-treatment the TOC was reduced significantly (% removal 80.63), the results demonstrate that oxidation played a significant role in the degradation of the organic pollutants that had passed through the membrane.

### 10.3.12 **Total dissolved solids and Electrical conductivity**

There was noticeable reduction in EC, and this is ascribed to the complexation that occurs between ions (from dissociated salts in wastewater) with either organic matter or suspended

particulate in the wastewater sample [16] which will often yield larger components which will hinder passage through the PES/GQD membrane pores. TDS removal was recorded to be between 1.38% (lowest) and 29.25% (highest).

10.3.13 Bacterial content after filtration

The total bacterial content of the wastewater permeate was observed visually by incubating the membranes M0 and M1 in LB after use (Figure 10.13). In both bacterial tests (total coliform and total bacterial count), the pristine membrane (M0) had significant bacterial growth whereas no visible bacterial growth was observed on M1. The significant reduction in bacterial growth is attributed to the effect of AOPs and GQDs on the wastewater sample in the pre-treatment subsequently followed by PES/GQDs membrane filtration. A number of studies have since documented the antimicrobial efficiency of GQDs embedded in polymer matrices [17-19].
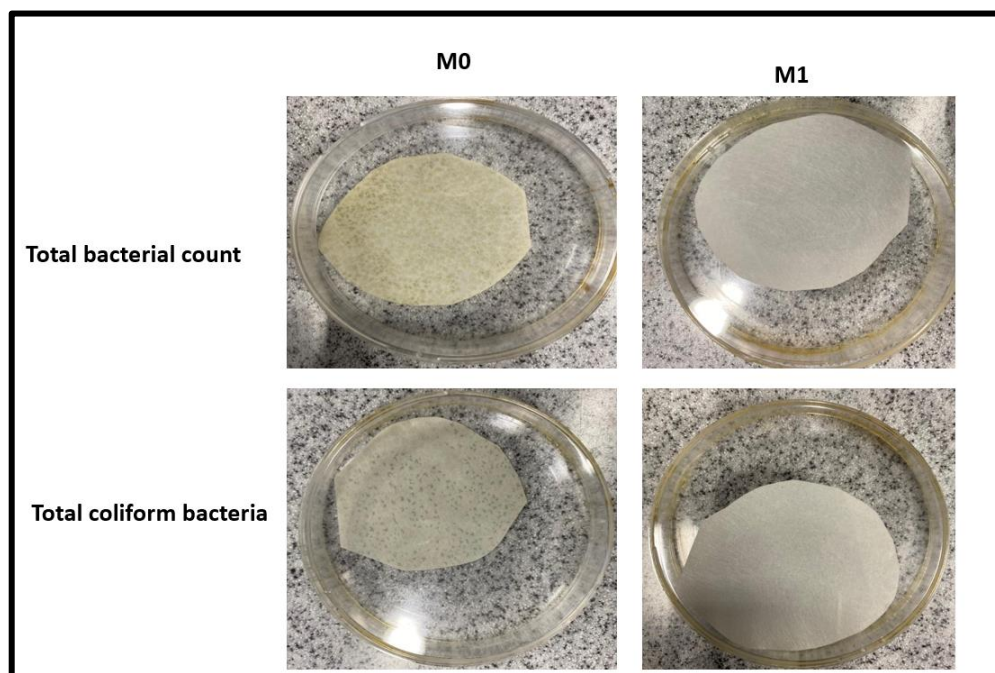
Figure 10.13: Photographs of membranes M0 and M1 after filtration with wastewater sample.

10.4   Conclusion

PES/GQDs membranes were fabricated using phase-inversion method and the key findings from this chapter include:

- The incorporation of the GQDs in the PES matrix increased the oxygen content and further enhanced the hydrophilicity, pore size and porosity of the membrane. The water flux of the membrane was significantly improved.
- The PES/GQDs membrane had better salt rejection capabilities and remarkable dye rejection capabilities compared to the pristine membrane. Superior inhibition of *E.coli* cells were observed coupled with an overall reduction of the total bacterial count and total coliform count.

This study demonstrated that coupling AOPs and membrane filtration has a potential of treating wastewater, as the quality of the wastewater significantly increased after the hybrid treatment. The hybrid treatment process developed in this study is cost-effective, robust and offers advantages over other conventional treatments in that it can remove recalcitrant pollutants in water and thus may contribute substantially to sustainable provision of clean water.

References

1. Liu B., Xie, J., Ma, H., Zhang, X., Pan, Y., Lv, J., Ge, H., Ren, N., Su, H., Xie, X. and Huang, L., 2017.*Small*. *13*(18) (2017)1601001.

2. Jizhong Ren, Rong Wang, in: Membrane and Desalination Technologies, Humana Press, Totowa, NJ, 47(2011)100.

3. Manawi Y.; Kochkodan, V.; Mahmoudi, E.; Johnson, D.J.; Mohammad, A.W.; Atieh, M.A. *Sci. Rep*. 7(2017) 15831.

4. Manawi Y.; Kochkodan, V.; Mohammad, A.; Atieh, M.A. *J. Membr. Sci*. 529(2017)95.

5. Van de Witte P.; Dijkstra, P.J.; Van den Berg, J.; Feijen, J. *J. Membr. Sci*. 1996, 117(1996) 1.

6. Marjani A., Nakhjiri, A.T., Adimi, M., Jirandehi, H.F. and Shirazian, S., *Scientific reports 10*(1)(2020)1.

7. Hamzah S., Ali, N., Ariffin, M.M., Ali, A. and Mohammad, A.W., *J. Eng. Appl. Sci 9* (12)(2014)2543.

8. Ridgway H.F.; Rigby, M.G.; Argo, D.G. J.-Am. Water Works Assoc. 77(1985)97.

9. Blenkinsopp S.; Costerton, *J. Trends Biotechnol*.9 (1991) 138.

10. Kang G.-D.; Cao, Y.-M. *Water Res*. 46 (2012)584.

11. Tshangana C.S., Muleja, A.A., Nxumalo, E.N. and Mhlanga, S.D., *Environ. Sci Pollut. Res. 27*(21) (2020)26845.

12. Zeng Z., Yu, D., He, Z., Liu, J., Xiao, F.X., Zhang, Y., Wang, R., Bhattacharyya, D. and Tan, T.T.Y., *6*(1)(2016).1

13. Zhang W., Yang, Y., Ziemann, E., Be'er, A., Bashouti, M.Y., Elimelech, M. and Bernstein, R. *Environ. Sci: Nano*, *6*(10) (2019)3080.

14. Maifadi S., Mhlanga, S.D., Nxumalo, E.N., Motsa, M.M. and Kuvarega, A.T., *Sep. Purific. Techn. 267* (2021)118618.

15. Tijana Uroˇseviˊc, Katarina Trivuna Current Trends and Future Developments on (Bio) Membranes, Elsevier (2020) 67.

CHAPTER 11

CONCLUDING REMARKS, RECOMMENDATIONS AND FUTURE PERSPECTIVES

11.1   Concluding remarks

GQDs were successfully synthesized from the pyrolysis of citric acid. The quality of the GQDs were confirmed by Raman spectroscopy, and the extent of sp^2/sp^3 hybridization of carbon atoms was expressed using the ratio of the intensity of the D and G bands (I_D/I_G ratio). The synthesized GQDs of average size around 3.1 nm showed spherical morphology and were not aggregated. The topographic height of the GQDs was determined to be ~ 1.2 nm. The structural composition of the GQDs was further probed using XPS and peaks ascribed to C1s, O1$_S$ and the Na auger peak were observed at 286.3, 531 and 495 eV respectively.

The synthesized GQDs were applied in real wastewater treatment through photocatalytic evaluation of degradation of dyes and pharmaceuticals. GQDs were able to efficiently decolourise the BB dye from the spiked real wastewater samples. Furthermore, increasing the initial concentration of the BB dye had a negative impact on GQD photocatalytic activity. The degradation of dye was attributed to a combination of photocatalytic mechanism and photosensitization degradation emanating from self-degradation of photoexcited dyes. This highlighted the significant role of GQDs in the removal of emerging pollutants.

The third objective of this study examined the effect of the shape of the ZnO nanoparticles on both the photocatalytic and antimicrobial properties. Based on the results, ZnO-F showed a high photocatalytic efficiency compared to the ZnO-R and this was ascribed to the larger surface area that allowed better absorption of the organic pollutants. In contrast, the ZnO-R were more efficient at inactivating microorganisms, as the rods could penetrate the surface of the bacteria with much ease compared to the flakes. Therefore, ZnO-F and ZnO-R could be promising low-cost dual nanohybrid materials for potential use in degrading organics and and inactivating microorganisms in wastewater.

This study also reported for the first time, the use of GQDs as activators of PAA. The synergy between GQDs and PAA afforded enhanced photocatalytic efficiency. This study examined to greater detail the degradation kinetics, mechanism and assessed the mutagenic potential of the photodegradation by-products. The results showed that the degradation by-products were not mutagenic. Furthermore, the disinfection properties of the GQD were significantly enhanced and the live/dead assay showed that the cells were inactivated within 3 mins. Based on these results, the synergistic effect of GQDs can be exploited in the field of wastewater treatment for degradation of organics and removal of pathogens and this can be extended to environmental remediation applications.

Finally, the work demonstrated as proof-of-concept, the incorporation of GQDs into a polymeric membrane to develop a hybrid AOPs/membrane filtration configuration. In the configuration GQDs were applied in the pre-treatment step using AOPs, after which the feed was passed through a PES/GQDs membrane and the permeate collected. This study demonstrated that coupling AOPs and membrane separation has a dual advantage in treating wastewater, as the quality of the wastewater significantly improved after the hybrid treatment. The hybrid treatment process developed in this study was offers advantages over other conventional treatments in that it can remove recalcitrant pollutants in water and thus can contribute substantially to the strides made in research on improving conventional wastewater treatment technologies.

11.2   RECOMMENDATIONS AND FUTURE PERSPECTIVES

While this study provided significant insight on the application of GQDs in the removal of emerging pollutants in wastewater, there is still scope for further investigations and any future work in this niche area should incorporate the following suggestions and address the following issues:

- Scaling up and implementing industry-scale methods that can yield large quantities of GQDs that are uniform in size and functionality. This will enable the use of GQDs on a large-scale, as well as testing the efficiency of the GQDs on a pilot scale.

- Extending the photodegradation experiments using GQDs and GQDs-based nanocomposites in the removal of a wide range of emerging pollutants including

pesticides, insecticides, phenols and more pharmaceutical products. To lower the overall costs, the utilization of solar light in all the photodegradation experiments is recommended.

- Extend the cytotoxicity tests using more sensitive pathogenic species such as *V. fischeri* and *S. aurata*.

- Due to the demonstrated anti-microbial properties of the PES/GQDs membrane, they can further be used as point-of-use filters that can be used in communities that rely on surface water or incorporated in filter designs in municipal wastewater treatment plants.

- Use of other oxidants besides PAA (e.g PMS and PDS, Ozone, H_2O_2 etc)

- Exploring other ways of incorporating the GQDs into membranes (e.g Hollow fibre configurations, Thin Film Composites etc)

- Investigating the up-conversion effect of GQDs in order to utilize very low energy light sources for activation during photocatalytic experiments

This thesis clearly demonstrated GQDs are promising materials that offer extraordinary potential in the design of novel GQDs-based nanocomposites for water treatment applications.
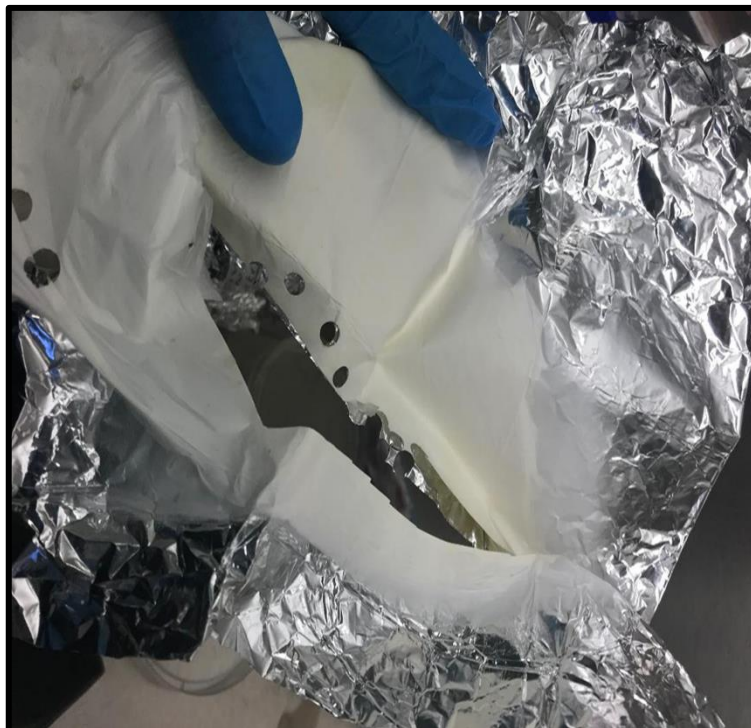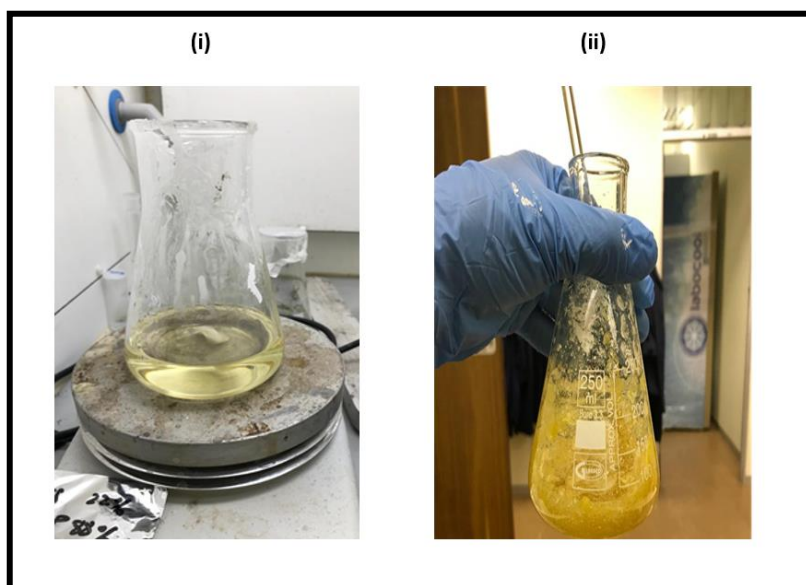
Chapter 3 Appendix
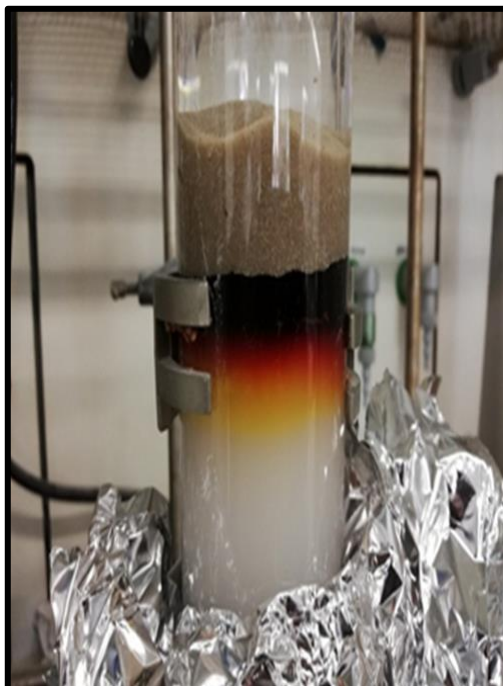
Figure A1: Silica gel column used to obtain pure GQDs (0.01 M NaOH as the developing phase).

Figure A2: Electrospun nanofibrous membranes cut into discs for the Kirby Baüer experiments using a paper puncher.

Figure A3: Polymer solution used to fabricate (i) pristine PES membrane with no GQDs (**M0**) and (ii) 5 wt % GQDs in PES (**M1**).
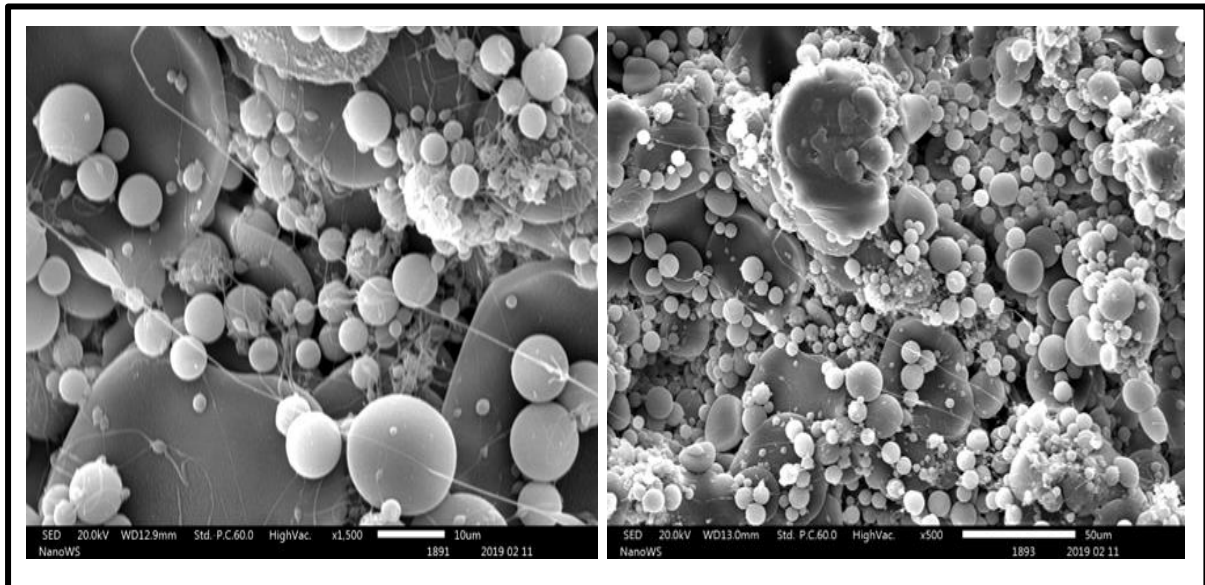
Chapter 5 Appendix

Figure A1: Image of effluent from a WWTP which is alleged to pollute a nearby river accessed on Mail& Guardian online publication.

Chapter 9 Appendix

Figure A1: SEM micrographs at lower viscosity showing the defects on the membrane.